



Proceedings of
International
Symposium

THUNDERSTORMS & ELEMENTARY PARTICLE ACCELERATION



Edited by

A. Chilingarian

Nor Amberd

*Yerevan Physics
Institute*

3-7

October

2016



Proceedings of International Symposium

TEPA 2016

Thunderstorms and Elementary Particle Acceleration



Nor-Amberd, Armenia
October 3 - 7

Edited by A. Chilingarian

Cosmic Ray Division
Yerevan Physics Institute



Published by CRD
(Cosmic Ray Division,
A.Alikhanyan National Laboratory
(Yerevan Physics Institute)
Alikhanyan Brothers Street 2,
Yerevan, Armenia

©All rights reserved by **CRD**
<http://crd.yerphi.am>

Printed by **TIGRAN METS**
2, Arshakouniats Avenue, Yerevan, Armenia
Tel. (37410) 521 775

ISBN 978-99941-0-803-9
March 2017
<https://inspirehep.net/record/1407534>

Copies 150
Pages 152

INTERNATIONAL SCIENTIFIC ADVISORY COMMITTEE

- Ashot Chilingarian,
Yerevan Physics Institute, Armenia,
co-chair
- Lev Dorman,
Israel Cosmic Ray Center and Emilio
Segre' Observatory, Israel
- Joe Dwyer,
University of New Hampshire, USA
- Gerald Fishman,
NASA-Marshall Space Flight Center,
Huntsville, USA)
- Hartmut Gemmeke,
Karlsruhe Institute of Technology,
Germany
- Andreas Haungs,
Karlsruhe Institute of Technology,
Germany
- Johannes Knapp,
DESY, Zeuthen, Germany
- Karel Kudela,
Institute of Experimental Physics,
Slovakia
- Alexandr Lidvanski,
Nuclear Physics Institute, Russian
Academy of Science, Russian
Federation
- Jean Lilensten,
Laboratory of Planetology, Grenoble,
France
- Evgeny Mareev,
Institute of Applied Physics, Nizhny
Novgorod, Russian Federation
- Razmik Mirzoyan,
MPI, Munich, Germany
- Yasushi Muraki,
STE laboratory, Nagoya University,
Japan
- Michail Panasyuk,
Moscow State University, Russian
Federation, co-chair
- David Smith,
INAF and University of California,
Berkeley, USA
- Marco Tavani,
INAF and University of Rome "Tor
Vergata", Italy
- Tatsuo Torii,
Japan Atomic Energy Agency,
Tsuruga, Japan (to be confirmed)
- Harufumi Tsuchiya,
Cosmic Radiation Laboratory, Riken,
Japan.
- Lev Zeleny,
Space Research Institute, Russian
Academy of Sciences, Russian
Federation

Exploring Origin of the High-Energy processes in Earth's Atmosphere

Thunderstorms and Elementary Particle Acceleration (TEPA-2016)

Yerevan, Armenia, 3-7 October 2016

The problem of the thundercloud electrification and how particle fluxes and lightning flashes are initiated inside thunderclouds are among the biggest unsolved problems in atmospheric sciences. The relationship between thundercloud electrification, lightning initiation, and particle fluxes from the clouds has not been yet unambiguously established. Cosmic Ray Division of Yerevan Physics Institute (YerPhI), Armenia and Skobeltsyn Institute of Nuclear Physics of Moscow State University (SINP), Russia already 6th year are organizing Thunderstorms and Elementary Particle Acceleration (TEPA) annual meeting, creating environment for leading scientists and students to meet each other and discuss last discoveries in these fields (see reports of previous TEPA symposia in Fishman and Chilingarian, 2010, Chilingarian, 2013, 2014, 2016).

The CRD have an impressive profile of the investigations in the emerging field of high-energy physics in the atmosphere. New designed particle detector networks and unique geographical location of Aragats station allows observation in last 8 years near 500 intensive particle fluxes from the thunderclouds, which were called TGEs – Thunderstorm ground enhancements. Aragats physicists enlarge the TGE research by coherent detection of the electrical and geomagnetic fields, temperature, relative humidity and other meteorological parameters, as well as by detection of the lightning flashes. An adopted multivariate approach allows interrelate particle fluxes, electric fields, and lightning occurrences and finally come to a comprehensive model of the TGE. One of most intriguing opportunities opening by observation of the high-energy processes in the atmosphere is their relation to lightning initiation. C.T.R. Wilson postulated acceleration of electrons in the strong electric fields inside thunderclouds in 1924. In 1992 Gurevich et al. developed the theory of the runaway breakdown (RB), now mostly referred to as relativistic runaway electron avalanches - RREA. The separation of positive and negative charges in thundercloud and existence of a stable ambient population of the cosmic ray electrons enables the acceleration of the seed electrons in direction of the Earth's surface and to open space (Terrestrial gamma flashes, TGFs). Both TGEs and TGFs precede the lightning activity and can be used for the research of poorly understood lightning initiation processes providing key research instrument – fluxes of electrons, neutrons and gamma rays originated in the thunderclouds. Information acquired from the time series of TGEs along with widely used information on the temporal patterns of the radio waveforms will help to develop both reliable model of lightning initiation and detailed mechanism of electron acceleration in thunderclouds.

TOPICS OF THE SYMPOSIUM:

30 participants from Russia, USA, Germany, Israel, and Armenia present 20 plenary talks and 10 posters in 6 sessions:

1. Research of the Thunderstorm ground enhancements (TGEs) observed by particle detectors located on earth's surface;
2. Research of the Terrestrial gamma-ray flashes (TGFs) observed by the orbiting gamma-ray observatories;
3. Relation of Lightning to the TGE and TGF;
4. Monitoring of TLEs and thunderstorms from the orbit;
5. Cloud electrification and atmospheric discharges: measurements and applications;
6. Instrumentation, muon detection.

2 discussions held:

Databases in high-energy atmospheric physics: description and ways to establish cooperation;

Do lightning discharges produce relativistic particles?

Visit Aragats research station near the south summit of Aragats Mountain coincide with the installation of new detectors measuring UV and IR radiation from the lightning bolt (collaboration YerPhI- SINP).

Among the most important results reported and discussed at symposia was the relation of TGE to lightning:

During numerous thunderstorms on Aragats there were no particles fluxes registered simultaneously with lightning;

In 2015-2016 25 events were detected when lightning abruptly terminate particle flux from clouds;

Investigations of pulse shape from particle detectors and atmospheric discharges prove that all pulses from detectors are electromagnetic interferences (EMI) only.

Observed on Aragats fluxes of electrons, gamma rays and neutrons can be explained with standard RREA + MOS theory with CR electron seeds. Lightning do not generate high-energy particles!

Large TGEs open conductive channel for lightning and usually lightning occurred at large TGEs and stop them. TGE is essential for the lightning initiation.

Symposia participants agree that the topic of High-Energy Physics in Atmosphere (HEPA) is well progressing:

There is big activity in several countries to establish surface particle detectors for research in TGE physics;

RB/RREA model with CR seeds rather satisfactory explains TGE measurements worldwide;

Planned research of TLE and TGF from orbit can be coupled with surface measurements;

The established links with meteorology, atmospheric electricity, Atmospheric Cherenkov Telescopes (ACT) experiments, look very promising;

Planned lightning mapping array will be very important addition to Aragats facilities;

New fast electronics will reveal origin of TGE and TGE-lightning relations;

Broad collaboration with Space and Lightning physics experiments will significantly improve research and understanding in the new emerging HEPA field.

REFERENCE

G. Fishman and A. Chilingarian, (2010) Observations of High-Energy Particles and Radiation. From Thunderstorms, , 91, 47 Eos Trans. AGU, 91, 47.

Chilingarian, A. (2013), Exploring High-Energy Phenomena in Earth's Atmosphere, Eos Trans. AGU, 94(50), 488.

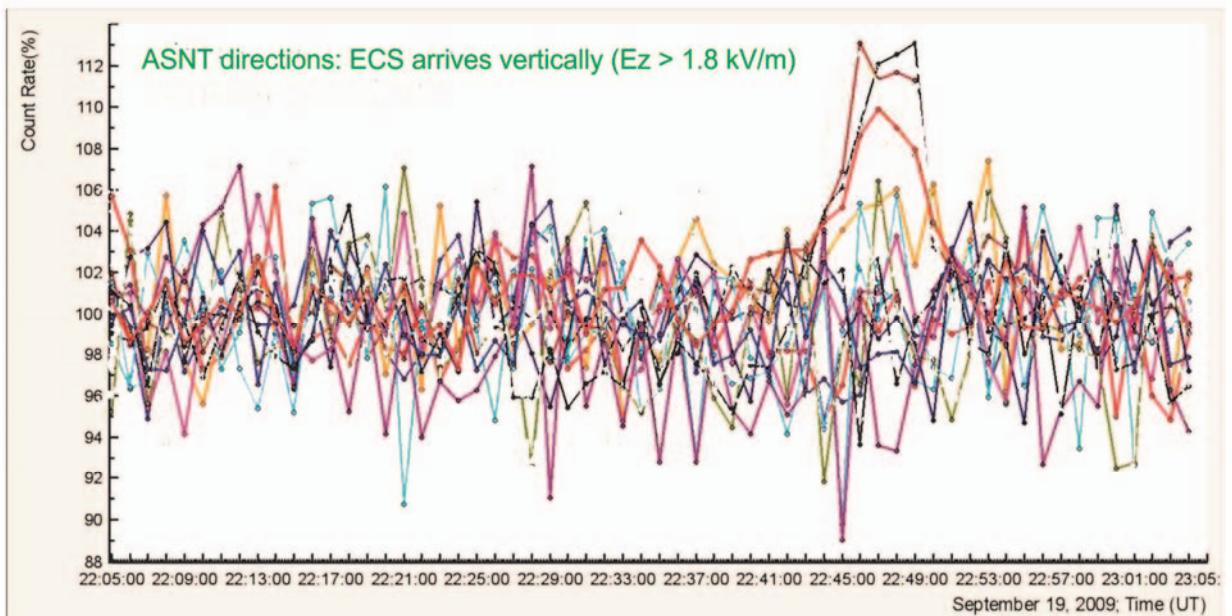
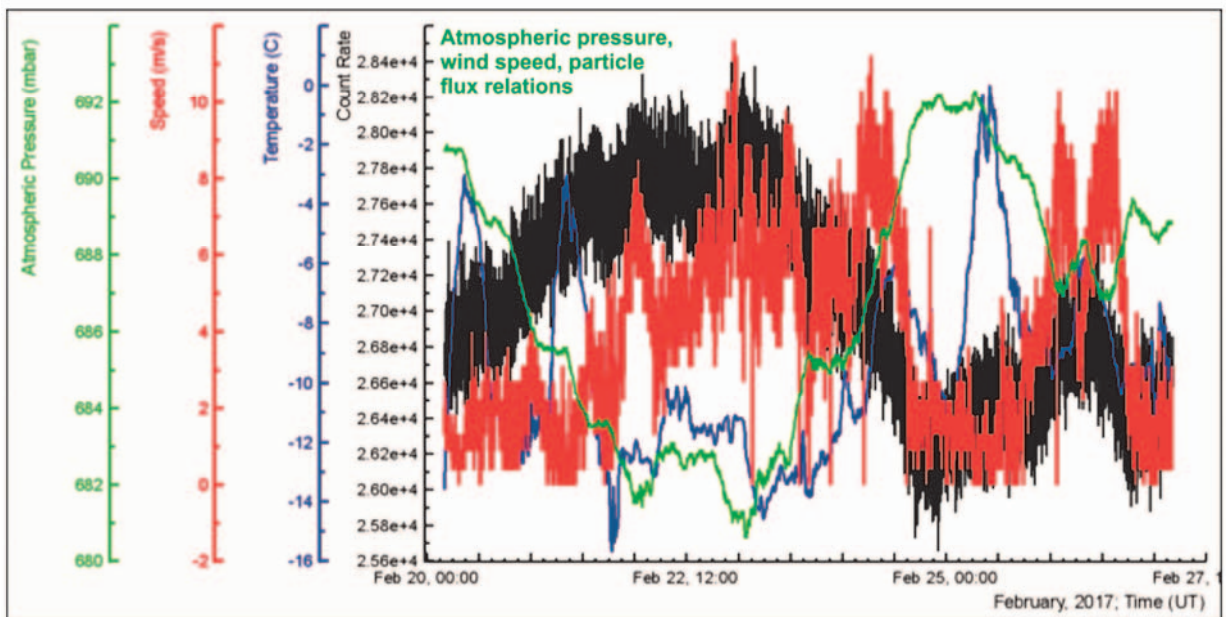
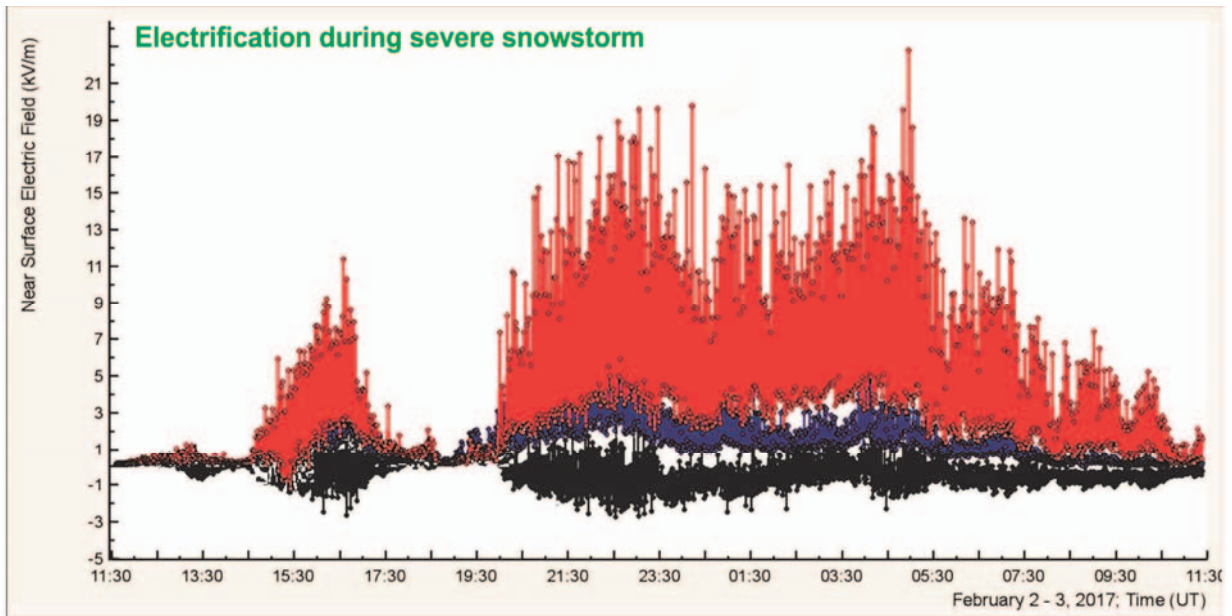
Chilingarian A. (2014) Exploring the Origin of High-Energy Particle Beams in the Atmosphere Eos Trans. AGU 95(46)

Chilingarian, A. (2016), Where does lightning come from?, Eos Trans. AGU, 97Published on 15 April 2016.

Ashot Chilingarian

Table of Contents

Types of Lightning Discharges that Abruptly Terminate Enhanced Fluxes of Energetic Radiation and Particles Observed at Ground Level	1
<i>A. Chilingarian, Y. Khanikyants, E. Mareev, D. Pokhsraryan, V. Rakov and S. Soghomonyan</i>	
On the Origin of Particle Fluxes from Thunderclouds	13
<i>A. Chilingarian, S. Chilingaryan, T. Karapetyan, Y. Khanikyants, D. Pokhsraryan, S. Soghomonyan</i>	
On the Initiation of Lightning in Thunderclouds	20
<i>A. Chilingarian, S. Chilingaryan, T. Karapetyan, L. Kozliner, Y. Khanikyants, G. Hovsepyan, D. Pokhsraryan, S. Soghomonyan</i>	
In Situ Measurements of the Runaway Breakdown (Relativistic Runaway Electron Avalanche) on Aragats: Experimental Data and Models A.	30
<i>A. Chilingarian, S. Chilingaryan, G. Hovsepyan, L. Kozliner, B. Mailyan</i>	
Extensive Air Showers Detected by Aragats Neutron Monitor	38
<i>A. Badalyan, A. Chilingarian, G. Hovsepyan, A. Grigoryan, Y. Kanikyants, A. Manukyan, D. Pokhsraryan, S. Soghomonyan</i>	
Constraining the Source Properties of Individual Terrestrial Gamma-ray Flashes	45
<i>B. Mailyan, M. Briggs, E. Cramer, G. Fitzpatrick, O. Roberts, M. Stanbro, V. Connaughton, S. McBreen, P. Bhat and J. Dwyer</i>	
Results of TGE Study in 0.03-10 MeV Energy Range in Ground Experiments near Moscow and Aragats	50
<i>V. Bogomolov, A. Chilingarian, G. Garipov, G. Hovsepyan, A. Iyudin, T. Karapetyan, A. Kovalenko, I. Maximov, E. Mntasakanyan, M. Panasyuk, K. Saleev, S. Svertilov</i>	
Physical Analysis of Multivariate Measurements in the Atmospheric High-energy Physics Experiments within ADEI Platform	56
<i>K Avakyan, S. Chilingaryan, A. Chilingarian, T. Karapetyan</i>	
Measurements of the Energy Spectra of TGE Gamma Ray Flux on Aragats Mountain	69
<i>A. Chilingarian, G. Hovsepyan, L. Kozliner</i>	
Terrestrial Gamma Flashes at Ground Level -- TETRA-II	75
<i>D. Pleshinger, M. Cherry, C. Adams, S. Al-Nussirat, J. Arias, S. Bai, Z. Baum, P. Bitzer, H. Christian, S. Ellison, D. Granger, T. Guzik, J. Hoffmann, E. Khosravi, M. Legault, M. Orang, R. Ramos, D. Smith, D. Smith, M. Stewart, A. Sunda-Meya, J. Trepanier, A. Ward</i>	
Cosmic Ray Short Time Increases During Intervals with Strong Electric Field at Lomnický Štít: First Experience	80
<i>J. Baše, J. Chum, M. Kollárik, K. Kudela, R. Langer, I. Strhářský, S. Štefánik</i>	
Gamma-Ray and Energetic Electron Flux Short-time Variations Observed in Vernov and Lomonosov Missions	82
<i>M. Panasyuk, S. Svertilov, V. Bogomolov, G. Garipov, V. Barinova, A. Bogomolov, A. Iyudin, V. Kalegaev, M. Kaznacheeva, V. Morozenko, I. Myagkova, P. Klimov, V. Petrov, A. Prokhorov, I. Yashin</i>	
Investigation of Atmospheric High-energy Phenomena onboard International Space Station: Microsatellite "Chibis-AI" and VHF Interferometer "Kite"	89
<i>M. Dolgonosov, V. Gotlib, V. Karedin, A. Kosov, V. Nazarov, L. Zelenyi, S. Klimov</i>	
Space-time analysis of the Seismic Waves propagation and World Wide Lightning Location Network data association with the Terrestrial Gamma-ray Flashes detected by the Fermi Gamma-ray Burst Monitor	93
<i>L. Sorokin</i>	
The First Sprite Observation from Moscow in the Direction of Tver Region Associated with Repetitive Lightning Discharge	100
<i>L. Sorokin</i>	
Muon Flux monitoring in the YerPhi Underground Laboratory	103
<i>A. Aleksanyan, S. Amirkhanyan, T. Kotanjyan, L. Poghosyan, V. Pogosov</i>	
Muon Hodoscope URAGAN as a New Meteorological Tool	106
<i>N. Barbashina, A. Petrukhin, I. Yashin</i>	
Muon Telescope Planned for Operation in Israel Cosmic Ray Observatory on Mount Hermon	112
<i>L. Kozliner, L. Pustynnik, D. Shtivelman</i>	
GEANT4 Simulations of Electromagnetic Showers Initiated by 30MeV γ-Rays Entering the Atmosphere at Different Altitudes	116
<i>N. Akopov, A. Grigoryan, G. Karyan</i>	
First Results on Transient Atmospheric Events from Tracking Ultraviolet Set-Up (TUS) on Board the Lomonosov Satellite	122
<i>P. Klimov, B. Khrenov, S. Sharakin, M. Zotov, N. Chirskaya, V. Eremeev, G. Garipov, M. Kaznacheeva, M. Panasyuk, V. Petrov, A. Shirokov, I. Yashin</i>	
List of Participants	128
Photogallery	129





**Fast Integrated
Synchronized
Sensors
System**

SPECIFICATIONS

Programmable High Voltage Power Supply for PMT

- Voltage programming in two hardware selectable ranges $\pm 900V$ to $2100V$ and ± 1500 to $3000V$ in $2V$ steps
- Output voltage ripple less than $1mV$
- Max. output current $1.2 mA$ for $\pm 900V$ to $2100V$ range; $0.8 mA$ for ± 1500 to $3000V$ range
- Input voltage from $+12V$ to $+15V$
- Absolute output voltage accuracy $\pm 1V$
- Optional temperature sensor
- RS-485 half-duplex 2-wire 9600 baud interface for programming and monitoring the output voltage

8-channel counter board

- 8 programmable threshold analog inputs
- Termination 50-Ohm
- I/O connectors BNC
- Threshold programming range $4mV$ - $1000mV$ with $4mV$ step
- Configurable Time Span $1ms$ - 10 minutes
- LEDs to indicate the input pulses in each of 8 channels

8-channel counter board

Processor	
Processor type.....	Xilinx Z-7010
Processor speed.....	667 MHz
Processor cores.....	2
Memory	
Nonvolatile memory.....	256 MB
DDR3 memory.....	512 MB
DDR3 clock frequency.....	533 MHz
DDR3 data bus width.....	16 bits
FPGA	
FPGA type.....	Xilinx Z-7010
Wireless Characteristics	
Radio mode.....	IEEE 802.11 b,g,n
Frequency band.....	ISM 2.4 GHz
Channel width.....	20 MHz
Channels.....	USA 1-11, International 1-13
TX power.....	+10 dBm max (10 mW)
Outdoor range.....	Up to 150 m (line of sight)
Antenna directivity.....	Omnidirectional
Security.....	WPA, WPA2, WPA2-Enterprise
USB Ports	
USB host port.....	USB 2.0 Hi-Speed
USB device port.....	USB 2.0 Hi-Speed

EFM-100 Hardware Specifications

- Electric Field Range: $-50kV/m$ to $+50kV/m$
- Response Time: 0.1 seconds
- Resolution: $0.01 kV/m$
- RS232: 9600 baud, 8 bits, 1 stop bit, no parity

High-Speed Digitizer

Number of channels 4
 Analog bandwidth 350 MHz (-3 dB)
 Vertical resolution 8 bits (up to 12 in resolution enhance mode)
 Maximum sampling rate :
 5 GS/s (One channel in use)
 2.5 GS/s (wo channels in use)
 1.25 GS/s (Three or four channels in use)
 Buffer size 32 MS
 Hi-Speed USB 2.0



Types of Lightning Discharges that Abruptly Terminate Enhanced Fluxes of Energetic Radiation and Particles Observed at Ground Level

A. Chilingarian¹, Y. Khanikyants¹, E. Mareev², D. Pokhsranyan¹, V. Rakov³,
S. Soghomonyan¹

1. Yerevan Physics Institute, Alikhanyan Brothers 2, Armenia, 0036

2. Institute of Applied Physics, Russian Academy of Sciences,
46 Ulyanov str., 603950 Nizhny Novgorod, Russian Federation

3. Department of Electrical and Computer Engineering,
University of Florida, Gainesville, Florida, USA

Abstract. We present ground-based measurements of thunderstorm-related enhancements of fluxes of energetic radiation and particles that are abruptly terminated by lightning discharges. All measurements were performed at an altitude of 3200 m above sea level on Mt. Aragats (Armenia). Lightning signatures were recorded using a network of five electric field mills, three of which were placed at the Aragats station, one at the Nor Amberd station (12.8 km from Aragats), and one at the Yerevan station (39 km from Aragats), and a wideband electric field measuring system with a useful frequency bandwidth of 50 Hz to 12 MHz. It appears that the flux-enhancement termination is associated with close (within 10 km or so of the particle detector) -CGs and normal polarity ICs; that is, with lightning types which reduce the upward-directed electric field below the cloud and, hence, suppress the acceleration of electrons toward the ground.

1. INTRODUCTION

Thunderstorm Ground Enhancements (TGEs), i.e. enhanced fluxes of electrons, gamma rays, and neutrons detected by ground-based particle detectors during strong overhead thunderstorms and their abrupt termination by lightning discharges have been reported by several research groups (Alexeenko et. al., 2002, Tsuchiya et al., 2013, Chilingarian et al., 2010, 2011, Chilingarian, 2014).

However, some key questions on the origin of TGEs and their relation to lightning discharges still remain to be answered. Among the most important questions are the following: 1) what is the source of accelerating electric field responsible for TGE? 2) What types of lightning can terminate the TGE? 3) At what stage of lightning does the TGE termination occur?

The background flux of energetic radiation and particles at the Aragats station is about 400-600 counts/m² ~s for the plastic scintillators of 3 and 5 cm thick, depending on atmospheric pressure and energy threshold. Flux enhancements (TGEs) are not observed in fair weather, they occur (as the name suggests) only during thunderstorms and, as a rule, are accompanied by upward directed electrostatic field at the ground. Duration of TGE, including a rising part and a falling part, up to the terminating lightning event is 2-5 minutes. The maximum flux enhancement (TGE amplitude) observed to date at Aragats was 240% of the background (October 4, 2014 at 14:12:15 UT). We usually measure the TGE amplitude in the number of standard deviations (from the background, measured before TGE) "contained" in the TGE maximum (Chilingarian et al., 2015).

If the count rate enhancement in the 1-second time series reaches or exceeds 3 standard deviations (~15 %), we accept the event as TGE. We verify our classification using data from other particle detectors installed at Aragats (detailed description of detectors and statistical analysis of TGE occurrences can be found in Chilingarian et al., 2013). In 2008-2012, a total of 277 TGEs were observed at Aragats (Chilingarian et al., 2013); that is about 55 per year (usually,

1-3 per thunderstorm). The catalog of TGEs observed on Aragats in 2013-2016 is under preparation.

In order to gain insights into the physical mechanisms of the phenomenon we performed ground-based measurements of electric field changes caused by lightning flashes that terminated the TGE.

The measurements included the near surface electrostatic field changes and fast wideband electric field waveforms. We also used lightning photography and data from the World Wide Lightning Location Network (WWLLN). This study is based on data acquired at the Aragats Space Environmental Center (ASEC) during the last five years (2012-2016). The rest of the paper is organized as follows. In section 2 we briefly describe the instrumentation used in our study. In section 3 we explain the methodology used for lightning type identification. The data presentation, analysis, and discussion are divided into two parts: in section 4 we present examples of close lightning flashes of known types that were not associated with TGEs, and in section 5 we present 24 TGE-terminating lightning flashes, including their type and electric field signatures. Main results of the study are summarized in section 6.

2. INSTRUMENTATION

Data examined in this paper were acquired at the ASEC located at an altitude of 3200 m above sea level on Mt. Aragats (Armenia). A 52-cm diameter circular flat-plate antenna was used to record the wideband (50 Hz to 12 MHz) electric field waveforms produced by lightning flashes.

The antenna was followed by a passive integrator (decay time constant 3 ms) the output of which was connected via a 60-cm double-shielded coaxial cable to a Picoscope 5244B digitizing oscilloscope. The oscilloscope was triggered by the signal from a commercial MFJ-1022 active whip antenna that covers a frequency range of 300 kHz to 200 MHz.

The record length was 1 s including 200 ms pre-trigger time and 800 ms post-trigger time. The sampling rate was 25 MS/s, corresponding to 40 ns sampling interval, and the amplitude resolution was 8 bit. The trigger-out pulse of the

oscilloscope was relayed to the NI myRIO board which produced the GPS time stamp of the record (detailed description of our fast data acquisition system based on the NI myRIO board can be found in Pokhsrlyan [2015]). The flat-plate and the whip antennas were installed at the same location, within 80 m of particle detectors and two electric field mills. The distance from the antennas to third field mill was 270 m.

The near-surface electrostatic field changes were measured by a network of five field mills (Boltek EFM-100), three of which were placed at the Aragats station, one at the Nor Amberd station at a distance of 12.8 km from Aragats,

and one at the Yerevan station, at a distance of 39.1 km from Aragats (Figure 1).

The distances between the three field mills at Aragats were 80 m, 270 m, and 290 m.

The electrostatic field changes were recorded at a sampling interval of 50 ms. Lightning optical images were captured by a video camera at a frame rate of 30 frames/s. We also used data from the WWLLN, a global lightning location network which detects most intense very low frequency (VLF, 3-30 kHz) signals from lightning.



Figure 1. Locations of the Aragats, Nor Amberd and Yerevan stations.

3. METHODOLOGY FOR LIGHTNING TYPE IDENTIFICATION

Lightning flashes can be grouped into two categories: those striking the ground and those not doing so. It is generally believed that intracloud, intercloud, and cloud-to-air flashes (all of which do not involve ground) comprise around 70-75 % of lightning discharges, and that cloud-to-ground flashes comprise 25-30 %.

The overwhelming majority of cloud-to-ground flashes transfer negative charge from the cloud to ground; they are called negative CGs. About 10 % of ground flashes transfer positive charge to ground; they are referred to as positive CGs.

In our analysis we used the well-known vertical tripole model of the normal-polarity thundercloud charge structure. According to this model, there is a main negative charge region in the middle of the thundercloud, a main positive charge region at the top, and a much smaller positive charge near the cloud bottom. The latter is called the Lower Positive

Charge Region (LPCR). It plays an important role in the initiation and development of lightning discharges. Different lightning scenarios that may arise depending upon the magnitude of the LPCR have been examined by Nag and Rakov (2009). The LPCR usually serves as an igniting cell for initiating -CG and is largely consumed in the course of -CG. On the other hand, the presence of excessive LPCR may prevent the occurrence of a negative CG discharge and facilitate instead an intracloud (IC) discharge between the main negative charge region and the LPCR. Note that the normal-polarity IC flash occurs between the main negative and main positive charge regions, and that the IC flash between the main negative charge region and LPCR is sometimes referred to as the inverted-polarity IC.

Four different lightning types are illustrated in Figure 2 by using the tripolar model of cloud charge structure. Negative cloud-to-ground (-CG) flash occurs between the main negative charge region and the ground. This lightning effectively transfers negative charge from the cloud to the

ground. Positive cloud-to-ground (+CG) flash occurs between the main (upper) positive charge region and the ground and transfers a negative charge from the ground to the cloud (or, equivalently, positive charge from the cloud to the ground). Normal polarity intracloud flash (+IC) occurs in the upper dipole between the main negative charge and main positive charge regions. Inverted polarity intracloud flash (-IC) occurs in the lower dipole between the main negative charge region and the LPCR.

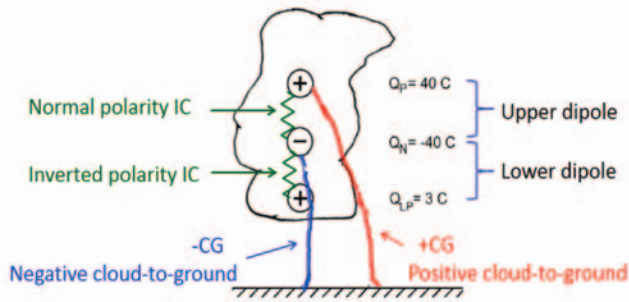


Figure 2. Schematic illustration of the “classical” tripolar charge structure of the thundercloud and four lightning types. $Q_p = +40$ C, $Q_N = -40$ C and $Q_{LP} = +3$ C are typical thunderstorm cloud charges found in the literature, (e. g., Rakov and Uman 2003, Ch. 3). The lower dipole is formed by $Q_{LP} = 3$ C and a portion of Q_N equal to -3 C.

In this paper we use the atmospheric electricity sign convention, according to which the downward directed electric field or field change vector is considered to be positive. Electrons are accelerated downward to the ground by the upward directed electric field which is considered to be negative. Negative CG flashes serve to reduce the negative charge overhead, whereas normal polarity IC flashes reduce (by equal amounts) both the main negative and main positive charges overhead. At close distances, both these lightning types produce electrostatic field changes of the same sign (Rakov and Uman, 2003, Ch. 3). This sign is positive according to the atmospheric electricity sign convention. Correspondingly, the positive CG and inverted polarity IC flashes produce negative electric field changes at close distances. The polarity of electric field changes of CGs is independent of distance, while for IC flashes there is a polarity reversal distance.

The methodology of lightning type identification used in the present study is illustrated schematically in Figure 3. As mentioned above, our analysis is based on the tripolar model of the thundercloud charge structure resulting from normal electrification, which is shown, in Figure 2. First, we check the polarity of electrostatic field change at the Aragats station produced by the close lightning flash. If the field change is positive ($\Delta E > 0$), the flash is considered to be either -CG or normal-polarity IC. If the field change is negative ($\Delta E < 0$), the flash is considered to be either +CG or inverted-polarity IC.

Next, in order to distinguish between CGs and ICs, we check if the polarity of ΔE changes with distance, using our network of field mills. The polarity reversal is expected to occur at a distance of about 10 km for normal ICs and less than 5 km for inverted ICs..

If polarity reversal has been detected, then we identify this lightning as a cloud discharge (normal- or inverted-polarity IC). However, if polarity reversal has not been detected, the lightning-type identification question remains open because the configuration of our field-mill network (see Figure 1) was such that not all polarity reversals could be detected. In order to distinguish between cloud-to-ground and intracloud flashes in cases when the ΔE polarity reversal

was not detected, we examined additional data. These additional data included lightning optical records, fast electric field waveforms, and WWLLN data (when available). Analysis of optical records is relatively simple: the image of luminous channel to the ground is indicative of a cloud-to-ground flash. Unfortunately, optical images were obtained only for two TGE-terminating lightning events (labeled 20 and 24 in Table 1). Fast electric field waveforms were used to search for characteristic return stroke (RS) signatures which are indicative of CGs. Needless to say that not every lightning event could be reliably classified using the methodology described above and illustrated in Figure 3.

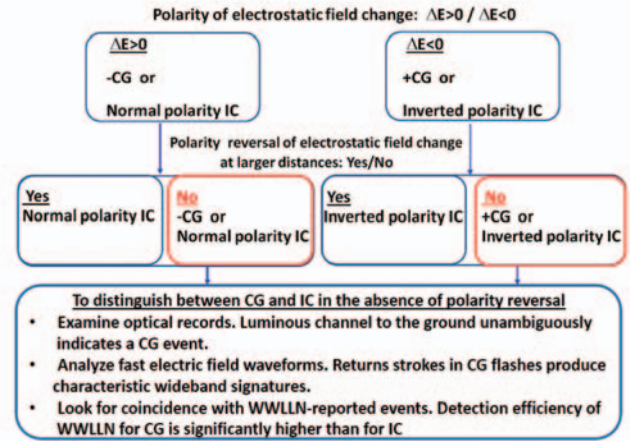


Figure 3. The algorithm of lightning type identification.

In the analysis of fast electric field waveforms, the identification is accomplished by applying waveform criteria to individual electric field pulses. In most cases, RS signatures are readily identifiable in wideband E-field record. Generally, bipolar, radiation-field pulses wider than certain threshold can be interpreted as being produced by return strokes in CG flashes, while narrower pulses are attributed to cloud flashes (Zhu et al., 2016).

For lightning classification and ranging purposes, we also looked for time coincidences of lightning events detected by our recording system with those found in the WWLLN database. It is generally believed that the detection efficiency of WWLLN for CGs is significantly higher than that for ICs (Rodger et al., 2005). Thus, if the flash in question is detected by the WWLLN, we assume that it is likely to be a CG flash.

4. LIGHTNING FLASHES NOT ASSOCIATED WITH TGES

Not all close lightning flashes are accompanied by TGEs. TGE is a rather rare transient process whose occurrence depends on the presence of sufficiently high electric field region of sufficiently large vertical extent in the cloud directly above the particle detector(s) and the occurrence of sufficiently energetic electron in that region, as required for the onset and development of RREA processes. It is the RREA processes that are in the in-cloud “accelerator” that are responsible for TGEs (Chilingarian, 2014). Additionally, the emitting region should remain for several minutes above the particle detectors and be low enough above the earth’s surface, so that the electron-gamma ray avalanche is not faded in the air. Clearly, lightning can occur when the in-cloud accelerator is not present or is not in a favorable position relative to detectors.

Examples of identified relatively close negative (at 9.2 km) and positive (at 13.1 km) cloud-to-ground lightning flashes not associated with TGEs are shown in Figures 4-7. Note that the distances have been estimated by one of the

field mills and are approximate. Figures 4 and 5 show electrostatic field changes produced by those two lightning flashes detected in Aragats and Nor Amberd, separated by a distance of 12.8 km. No polarity reversal of the field change is observed for the lightning flash which occurred at 14:55:45 (Figure 4) and for the flash at 11:19:49 (Figure 5). The polarity of electrostatic field change for the flash in

Figure 4 is positive, and hence it can be either a negative cloud-to-ground flash (-CG) or a normal polarity intracloud flash (+IC). The polarity of electrostatic field change for the flash in Figure 5 is negative, and hence it can be either a positive cloud-to-ground flash (+CG) or an inverted polarity intracloud flash (-IC). Definition of the electrostatic field change ΔE produced by lightning is illustrated, for the Aragats record, in Figure 4.

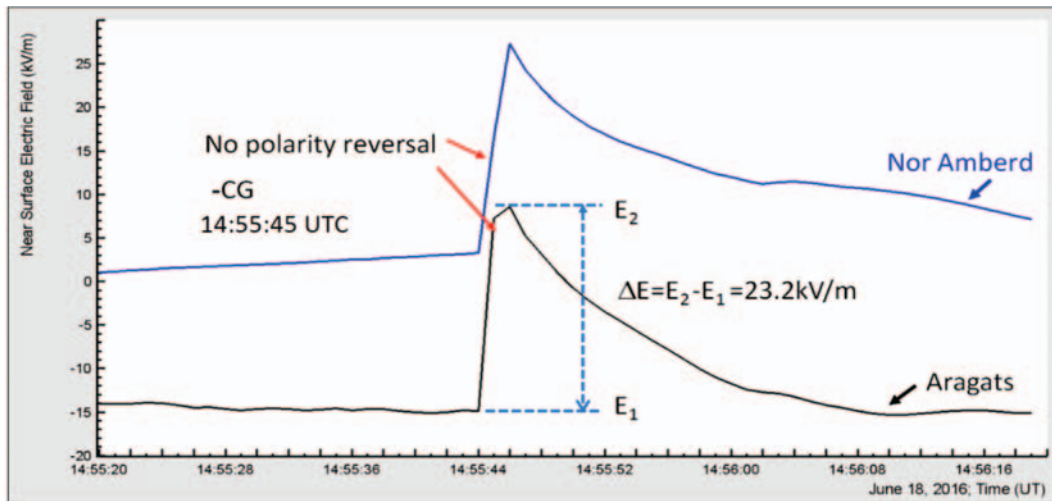


Figure 4. Electrostatic field changes produced by negative CG that occurred on June 18, 2016, 14:55:45 UTC. The field changes are recorded by the field mills located in Aragats and Nor Amberd, separated by a distance of 12.8 km.

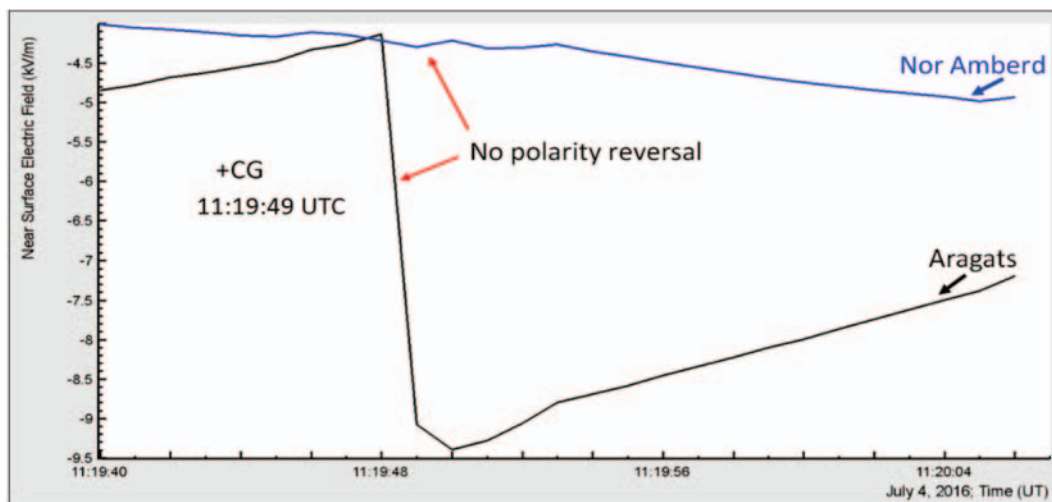


Figure 5. Electrostatic field changes produced by positive CG that occurred on July 4, 2016 11:19:49 UTC. The field changes are recorded by the field mills located in Aragats and Nor Amberd, separated by a distance of 12.8 km.

The polarity of ΔE at the two stations separated by 12.8 km is the same in either Figure 4 or Figure 5, which suggests that both events were CGs (-CG in Figure 4 and +CG in Figure 5). We additionally analyzed fast electric field waveforms of these lightning flashes, which are shown in Figure 6 and Figure 7. The record in Figure 6 contains a relatively long sequence of smaller pulses characteristic of in-cloud discharge activity followed by two strong and relatively wide pulses of positive polarity at 692 ms and 790 ms after the trigger. The risetime of these two pulses is about 7-8 μ s, and the peak-to-zero fall time is 100-110 μ s. The positive initial polarity of these two essentially radiation (judging from the waveforms) pulses is the same as the polarity of electrostatic field changes shown in Figure 4. With a high level of confidence we attribute these two pulses to return strokes of negative cloud-to-ground (-CG) lightning.

The record in Figure 7 does not contain any pronounced pulses indicative of in-cloud discharge activity, only a single

large pulse which has a 10- μ s risetime and a peak-to-zero fall time of 180 μ s. The initial polarity of this pulse is the same as that of the electrostatic field changes shown in Figure 5. We classify this pulse as the return stroke pulse of positive cloud-to-ground (+CG) lightning.

An example of inverted polarity intracloud flash is presented in Figs. 8-10, which show electrostatic field changes produced by this lightning (Figure 8), single frame of optical record (Figure 9), and fast electric field record (Figure 10).

As can be seen from Figure 8, the electrostatic field changes detected by two field mills in Aragats and Nor Amberd have opposite polarities, that is, polarity reversal with distance is detected. Therefore, this lightning can be identified as an intracloud flash, because, as mentioned earlier, the polarity reversal with distance occurs only when an elevated dipole is neutralized.

This classification is supported by the corresponding optical image shown in Figure 9, which clearly shows that

there is no luminous channel to the ground. The polarity of the larger field change detected in Aragats corresponds to a closer distance and is negative, which is indicative of inverted- polarity intracloud flash. Identification of this

event as a cloud flash is further supported by the fast electric field record (see Figure 10) which contains only short bipolar pulses of microsecond and sub-microsecond duration and no signatures characteristic of return strokes.

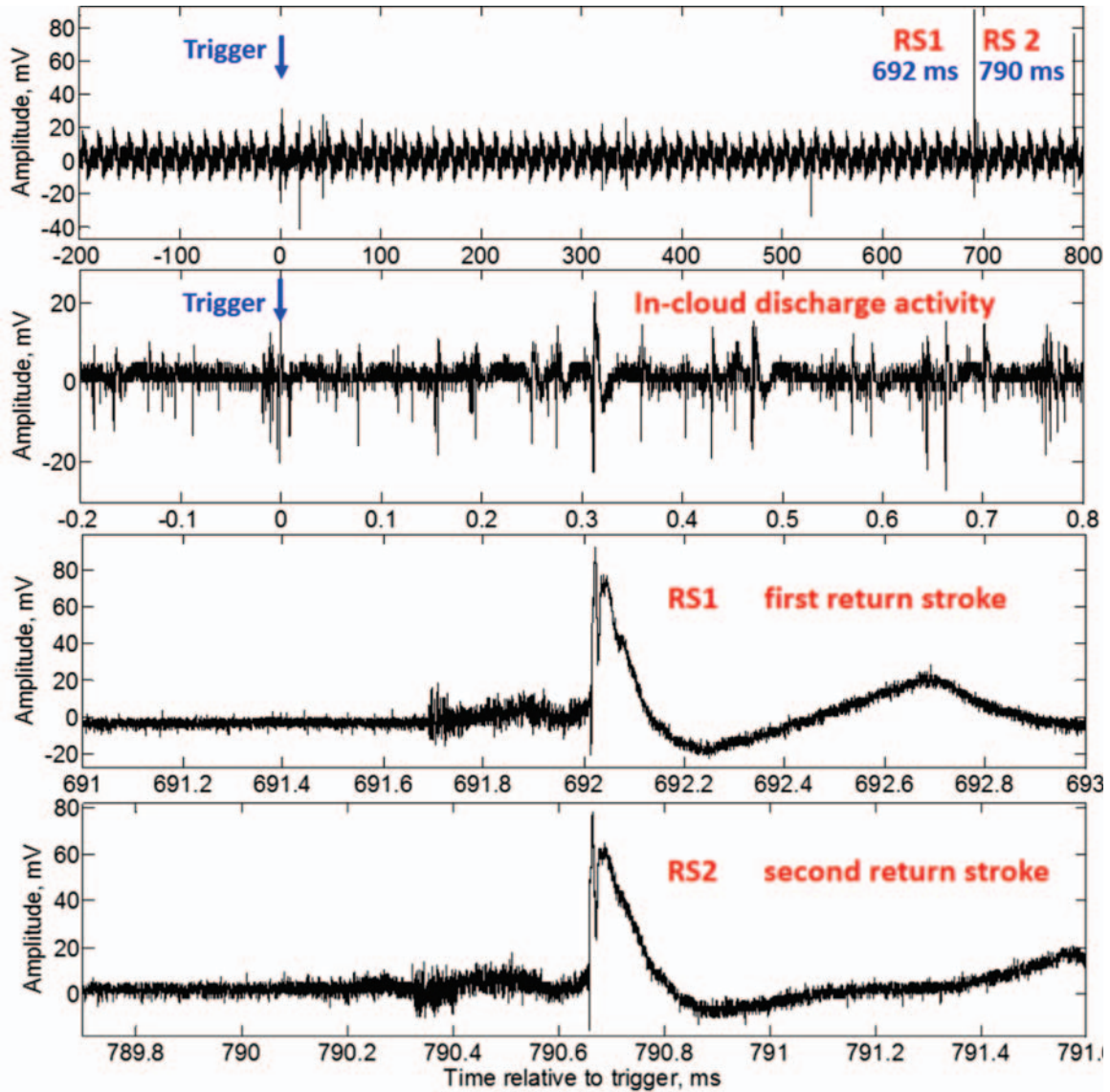


Figure 6. Fast electric field record of negative CG that occurred on June 18, 2016 at 14:55:45 UTC.

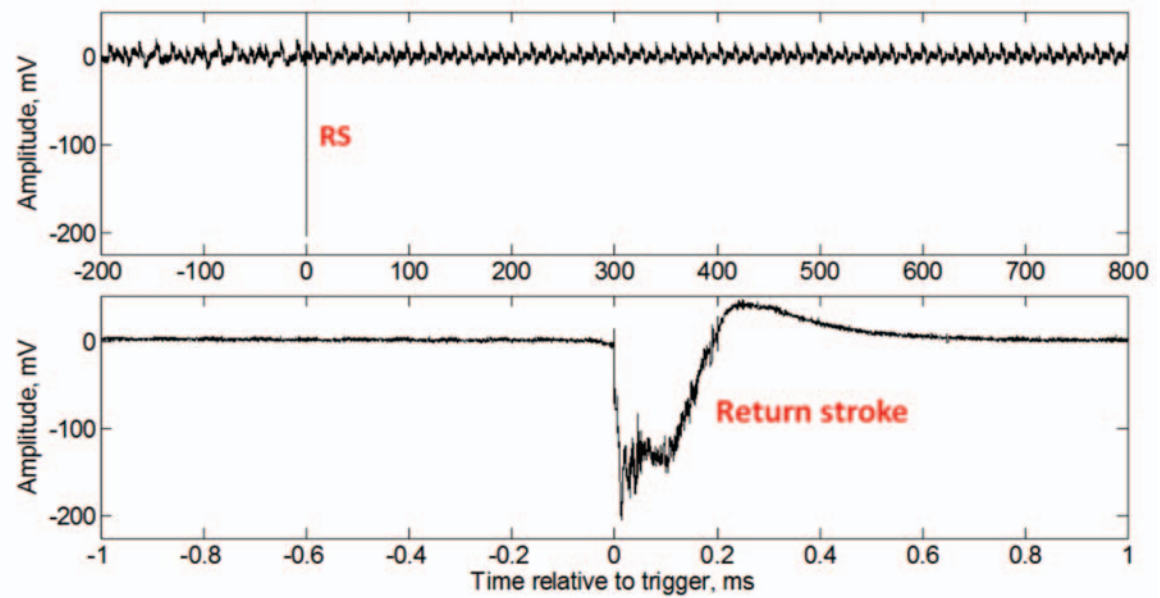


Figure 7. Fast electric field record of positive CG that occurred on July 4, 2016 at 11:19:49 UTC.

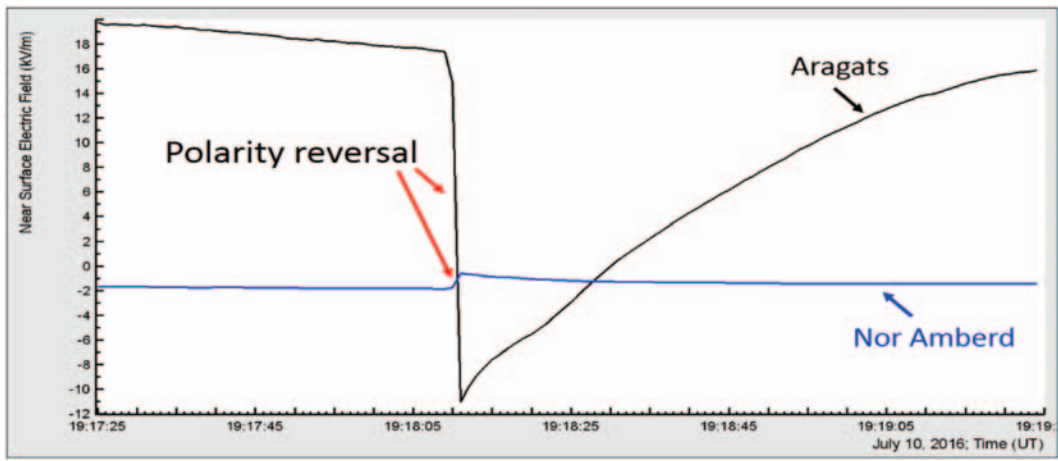


Figure 8. Electrostatic field changes of opposite polarity at Aragats and Nor Amberd, (separated by 12.8 km) produced by inverted polarity IC flash that occurred on July 10, 2016 at 19:18:10 UTC.



Figure 9. Optical image of inverted polarity IC flash, July 10, 2016, 19:18:10UTC.

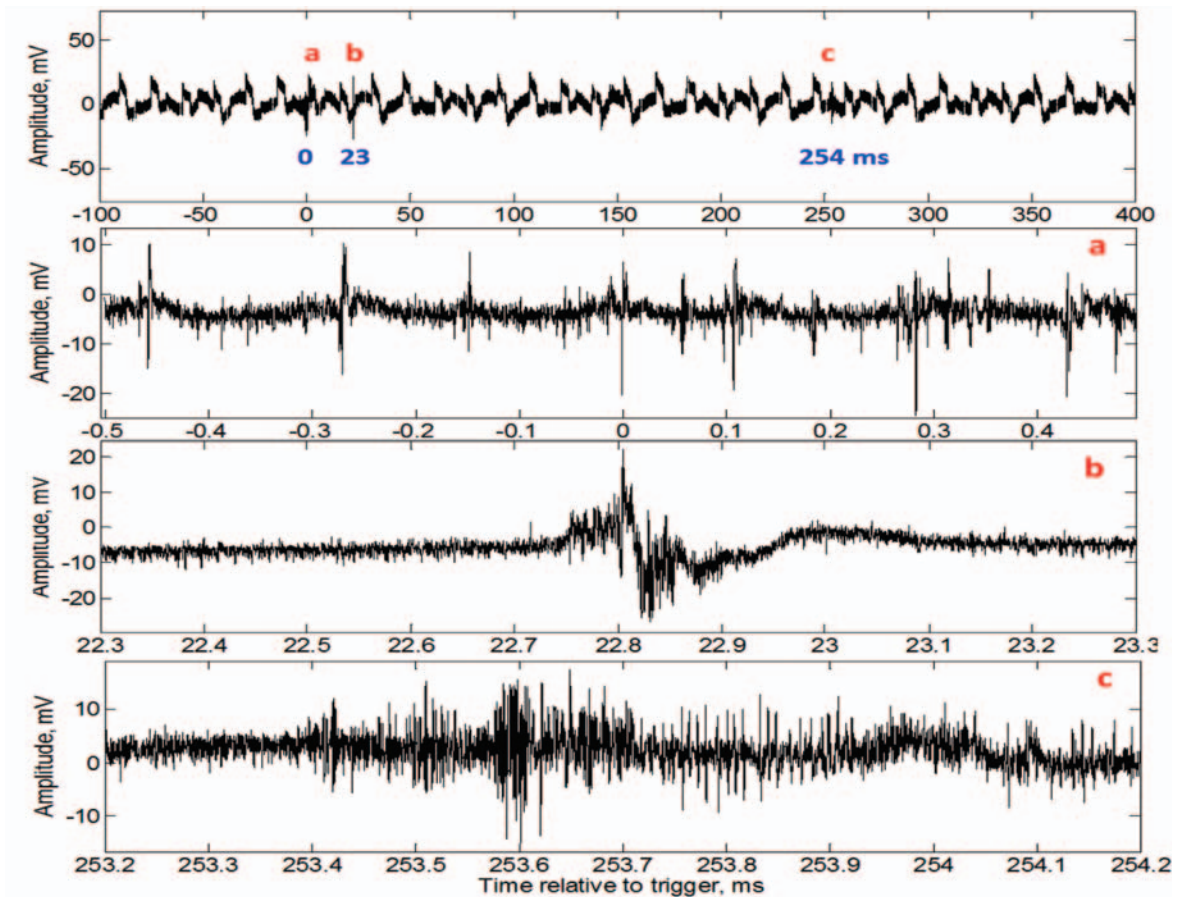


Figure 10. Fast electric field record of inverted polarity IC flash that occurred on July 10, 2016 at 19:18:10 UTC.

5. LIGHTNING FLASHES THAT TERMINATED THE TGE

In this section we will consider 24 lightning flashes each of which appeared to have terminated the TGE. An example of TGE abruptly terminated by lightning flash is presented

in Figure 11. The black curve shows the electrostatic field measured by electric field mill at Aragats, the blue curve shows radiation and particle flux measured by scintillation detector (one-second time series), and the red lines denote the distance to lightning from the detector site.

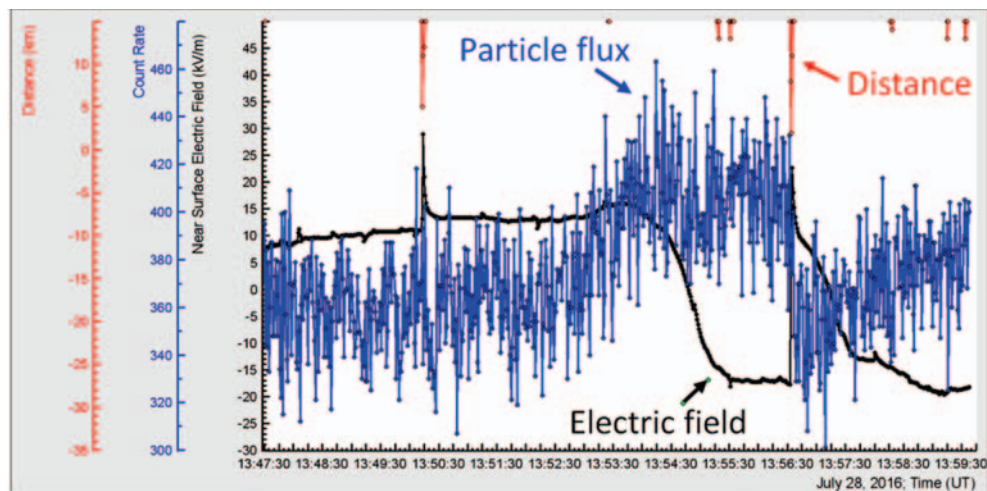


Figure 11. Electrostatic field change and particle flux (count rate) detected at Aragats for TGE (about 20 % above the background) terminated by lightning flash (July 28, 2016, 13:56:34 UTC). Distance to lightning from the particle detector estimated by one of the field mills at Aragats is indicated in red.

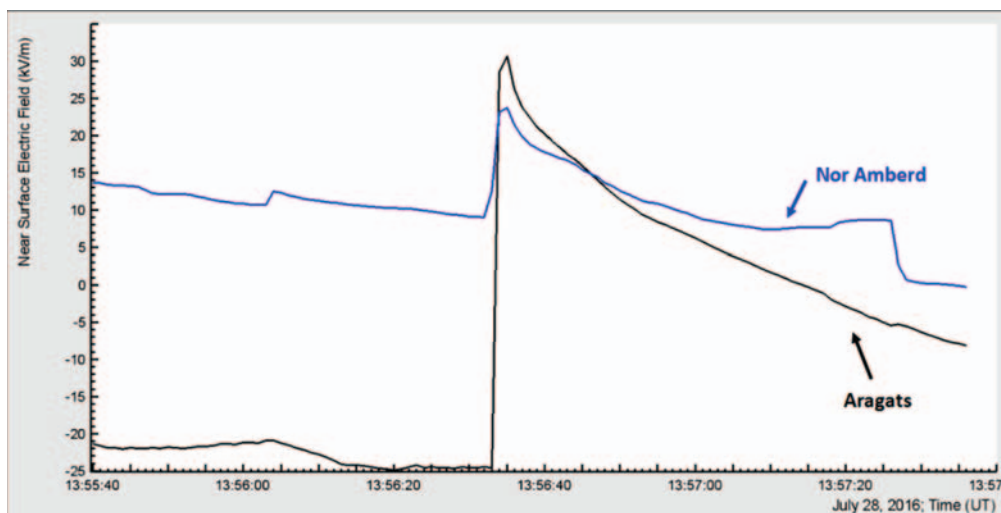


Figure 12. Electrostatic field changes recorded by the field mills in Aragats and Nor Amberd for TGE-terminating lightning flash (July 28, 2016, 13:56:34 UTC) shown in Figure 9.

As mentioned above, the negative upward directed electrostatic field accelerates electrons downward to the ground and initiates an electron avalanche multiplication and gamma rays. This accelerating field can be formed by the main negative charge of the thundercloud and its mirror image in the ground. Inside the thundercloud, this field can be enhanced by the LPCR located below the main negative charge region. The fast change of the electrostatic field sign caused by the lightning discharge leads to abrupt termination of the TGE. The fast positive change of electrostatic field can be associated with -CG that serves to reduce the main negative charge of the thundercloud. Alternatively, it could be a normal-polarity IC, which is shown not to be the case below.

Figure 12 shows electrostatic field changes recorded by field mills in Aragats and Nor Amberd. Distance to lightning estimated by EFM-100 field mill is about 2 km from Aragats, and about 10 km from Nor Amberd. This lightning event has been also detected by the WWLLN. It can be seen from Figure 12 that both field mills detected positive field change. The absence of polarity reversal suggests that this lightning is a negative cloud-to-ground (-CG) flash, as opposed to a

normal- polarity intracloud flash. Optical record of this lightning is shown in Figure 13. Lightning channel in Figure 13 clearly terminates on the ground, strongly supporting our classification of this lightning as cloud-to-ground flash.



Figure 13. Optical record corresponding to lightning flash that terminated the TGE on July 28, 2016 at 13:56:34 UTC (see also Figs. 11 and 12).

A sequence of two TGEs each of which had been terminated by lightning flash is presented in Figure 14 which shows 1-s time series of particle flux (upper blue curve) and electrostatic field (lower black curve). Two abrupt changes of electrostatic field produced by nearby lightning flashes are accompanied by abrupt decreases of particle flux.

Note that after the fast change of electrostatic field caused by the first flash at 14:15:48 the field returns during several seconds to the preceding level of -30 kV/m. The monotonically increasing particle count between the two

flashes can be associated with this strong negative electric field which accelerates electrons toward to the ground. Similar behavior can be seen after the second termination of the particle flux at 14:17:46, when the field returns to its preceding negative value, and the particle count rate tends to increase again. The recovered strong negative field after each of the two lightning flashes on a time scale of a few seconds indicates that intense electrification processes continued in the cloud.

Figure 15 shows the electrostatic field changes produced by these lightning flashes that were recorded in Aragats, and Nor Amberd. It is seen from Figure 15 that both field changes are positive, which suggests that the lightning events were either negative cloud-to-ground (-CG) flashes or normal-polarity intracloud flashes.

In order to distinguish between these two lightning types we examined the corresponding fast electric field record shown in Figure 16. No optical record for this event is available.

As seen in Figure 16, there are only very short pulses with durations less than 1 μ s. The fast field record of the second flash (14:17:46 UTC), not shown here, is similar. There are no pulses that could be attributed to return strokes of cloud-to-ground lightning. Based on the entirety of

information available, we identify these two lightning events as normal-polarity intracloud flashes.

In Table 1, we show the availability of various records for 24 lightning events that terminated TGEs. Lightning types (when identified) and associated particle flux drops are also given.

Classification of lightning flashes for 24 TGEs that were terminated by lightning is summarized in Figure 17. Nearly 50% of the TGE-terminating lightning events were identified as normal-polarity intracloud flashes, and a quarter of them (3 out of 12) have been detected by the WWLLN. About 29% of the events were identified as negative cloud-to-ground flashes, and about 70% of them (5 out of 7) have been detected by the WWLLN. About 21% of the events (5 events observed in 2012-2014; see Table 1) for which no optical or wideband electric field records were available and which were not detected by the WWLLN were classified as not identified.

In Table 2 we compare the distances to lightning from particle detectors estimated by electric field mill EFM-100 at Aragats and those obtained from the WWLLN data.

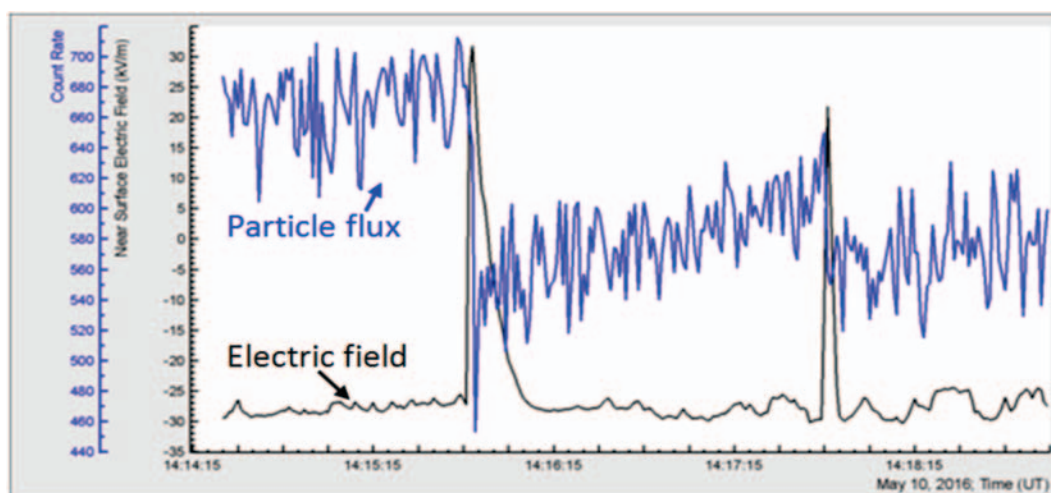


Figure 14. Electrostatic field change and particle flux (count rate) measured at Aragats for a sequence of two TGEs, each terminated by a lightning flash (May 10, 2016, 14:15:48 UTC (left) and 14:17:46 UTC (right)).

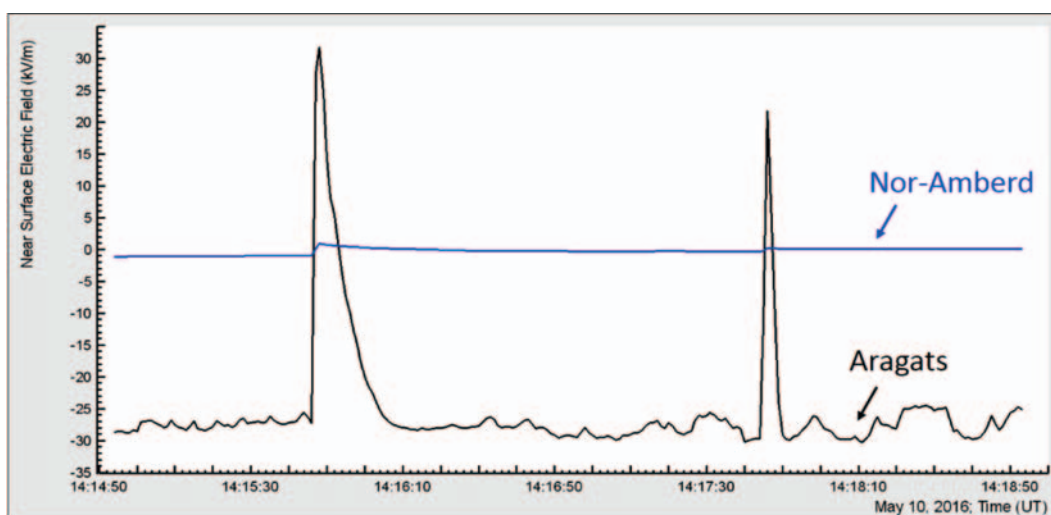


Figure 15. Electrostatic field changes recorded by field mills in Aragats and Nor Amberd for a sequence of two TGEs, each terminated by a lightning flash (May 10, 2016, 14:15:48 (left) and 14:17:46 (right)).

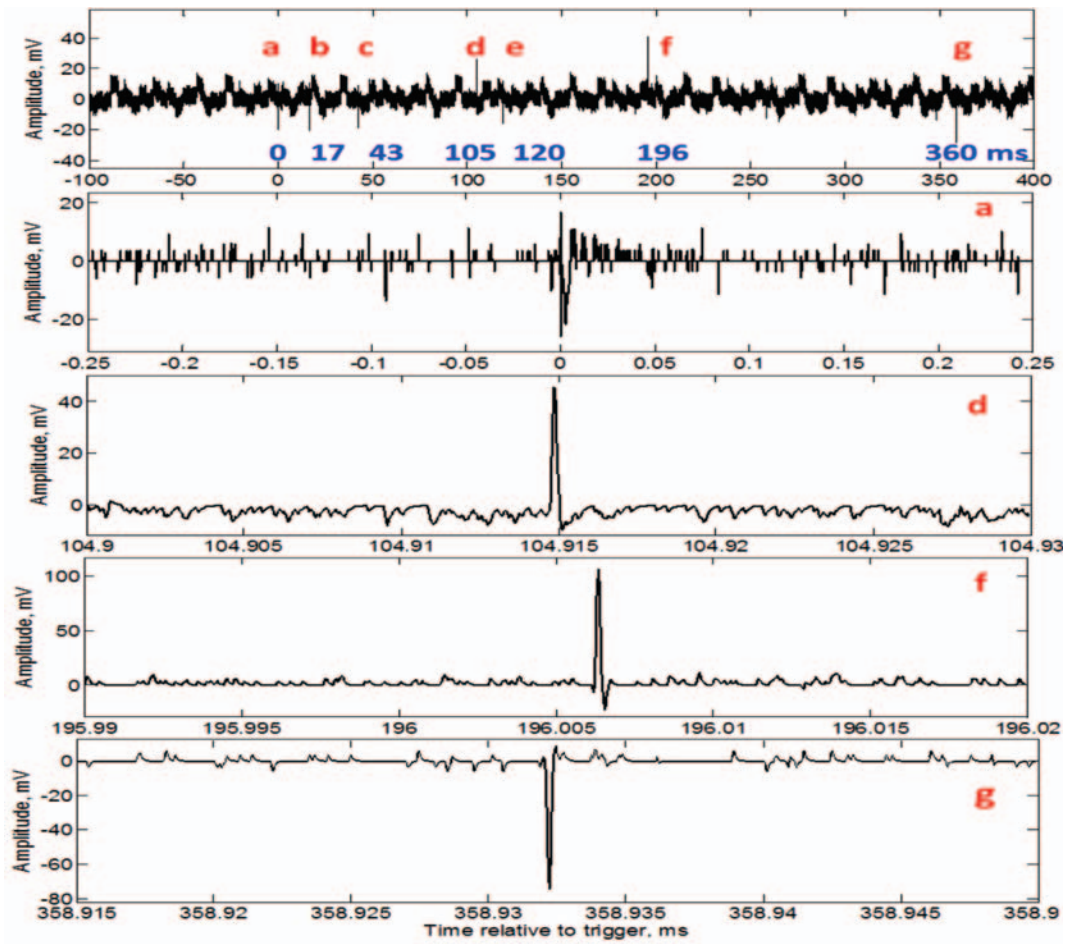


Figure 16. Fast electric field record of lightning flash that occurred on May 10, 2016 at 14:15:48 UTC and terminated the earlier of the two TGEs shown in Figs. 14 and 15. Pulses labeled b), c), and e) in the top panel are similar to pulse a) and are not shown on an expanded time scale.

Table 1. Availability of ΔE records, wideband E-field records, and WWLLN data for 24 lightning events terminating TGEs.

Event ID	Date/ Time (UTC)	ΔE (number)	Wideband E-	WWLLN data	Lightning	Particle flux
1	7-Oct-12, 15:10:53	4	No	No	-	22
2	12-May-13, 06:37:52	3	No	No	-	20
3	19-Oct-13, 11:20:53	4	No	Yes	-CG	58
4	26-May-14, 13:12:41	3	No	No	-	13
5	2-Jun-14, 21:00:11	3	No	No	-	24
6	2-Jun-14, 20:58:10	3	No	No	-	22
7	4-Oct-14, 14:13:32	3	Yes	No	-CG	32
8	20-Apr-15, 18:02:01	4	Yes	No	+IC	25
9	20-Apr-15, 18:00:14	4	Yes	Yes	+IC	91
10	11-May-15, 16:29:36	4	Yes	Yes	-CG	24
11	11-May-15, 16:32:06	4	Yes	Yes	-CG	70
12	11-May-15, 16:35:06	4	Yes	Yes	-CG	44
13	7-Oct-15, 14:45:07	4	Yes	No	+IC	22
14	28-Apr-16, 18:23:02	4	Yes	No	+IC	9
15	28-Apr-16, 18:24:38	4	Yes	Yes	+IC	8
16	4-May-16, 19:04:33	4	Yes	Yes	-CG	20
17	4-May-16, 19:05:58	4	Yes	No	+IC	14
18	10-May-16, 14:15:48	4	Yes	No	+IC	23
19	10-May-16, 14:17:46	4	Yes	No	+IC	13
20	4-Jun-16, 01:25:24	4	Yes	No	+IC	20
21	11-Jun-16, 11:45:23	4	Yes	Yes	+IC	11
22	16-Jun-16, 10:02:11	4	Yes	No	+IC	14
23	16-Jun-16, 10:05:13	4	Yes	No	+IC	12
24	28-Jul-16, 13:56:34	4	Yes	No	-CG	19

Table 2. Distances (km) estimated by electric field mill EFM-100 and WWLLN for 8 lightning events that terminated TGEs.

Event ID in Table 1	10	11	12	9	3	15	16	21	Mean \pm St.Dev
EFM-100	4	7.9	2.9	2.0	11	7.1	6.2	2.2	5.4 \pm 3.2
WWLLN	0.6	13.7	4.2	6.7	4.9	6.0	0.9	6.2	5.4 \pm 4.1

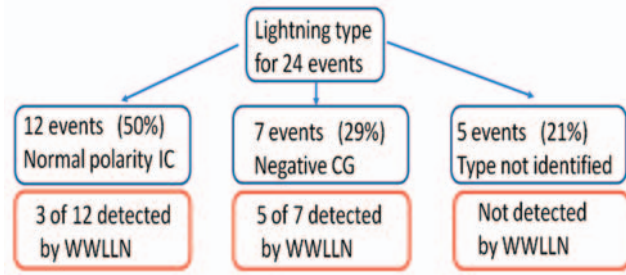


Figure 17. Types of lightning flashes that terminated TGEs.

It appears from Table 2 that, regardless of the source of data (WWLLN or EFM-100), all the distances are within \sim 10 km of the particle detector, with only one exception (event 11). The mean values for both EFM-100 and WWLLN are about 5 km.

It follows from Figure 17 that both negative cloud-to-ground and normal-polarity intracloud flashes can terminate TGEs. We emphasize that at close distances both types of lightning produce net positive changes of electrostatic field resulting from the reduction of negative charge overhead. This corresponds to the reduction of upward-directed (electron-accelerating) electric field below the cloud.

To gain an insight into the temporal evolution of TGE termination by lightning flash, we have analyzed the relative timing of (1) the start of electromagnetic emission from lightning discharge, (2) the start of particle flux decay, and (3) the maximum of electrostatic field change on a millisecond time scale. Two examples of such analysis are presented in Figures 18 and 19, which show 50-ms time series of particle flux and electric field, along with the trigger time of the wideband electric field measuring system.

The start of significant wideband (300 kHz – 200 MHz) electromagnetic emission from lightning was assumed to correspond to the trigger time of the digital oscilloscope, which recorded the fast wideband electric field waveforms. As mentioned in the Instrumentation section, the oscilloscope was triggered by the signal from the antenna operating in the 300 kHz to 200 MHz range (covering the MF, HF, and part of VHF ranges), and the trigger was GPS time stamped. The trigger time is indicated by vertical arrow in each Figures 18 and 19.

For the TGE shown in Figure 18, the wideband electromagnetic emission starts at $t_1=19:04:33.592$, whereas the maximum of electrostatic field change is attained at $t_2=19:04:33.800$; that is 208 ms later. It can be seen from the figure that the decay of particle flux starts in the time interval between the time instants t_1 and t_2 . Uncertainties in the determination of the trigger position and of the maximum of electrostatic field change are about 1 ms, and 10 ms, respectively.

Similar relative timing is observed for another event, as shown in Figure 19. Wideband electromagnetic emission starts at 14:15:47.337, maximum of electrostatic field change is attained at 14:15:47.772, that is 435 ms later, and the decay of particle flux starts in the time interval between these two instants. Such analysis could be performed for a total of 9 TGEs terminated by lightning and showed that the time interval between the start of wideband electromagnetic emission and the maximum of electrostatic field change produced by lightning ranged from 210 ms to 360 ms, with average value of 284 ms and standard deviation of 45 ms. The decay of particle flux invariably started in this time interval.

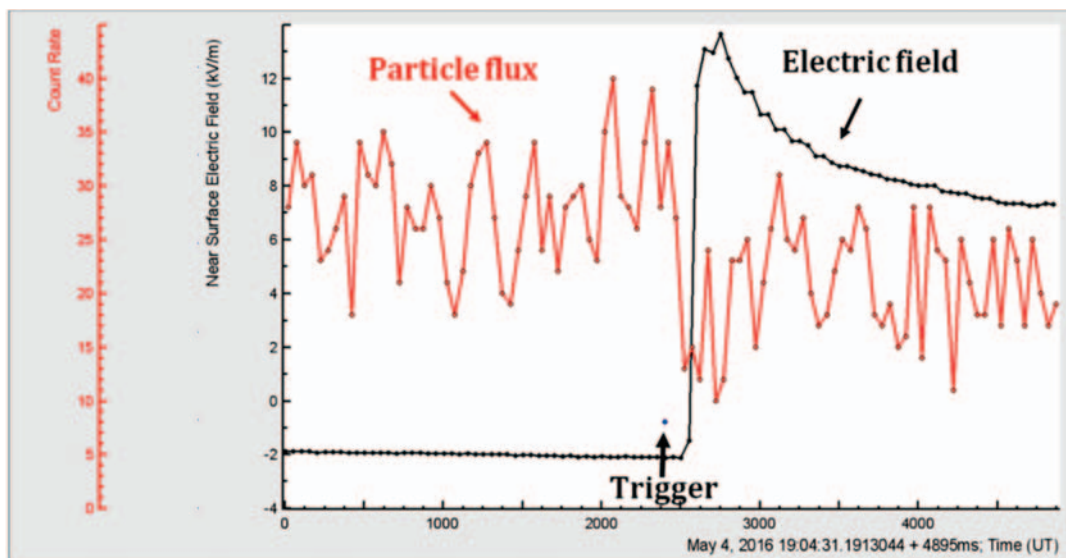


Figure 18. Electrostatic field and particle flux (count rate) for the TGE terminated by lightning flash that occurred on May 4, 2016 at 19:04:33 UTC. The GPS time stamp of the oscilloscope trigger assumed to be a proxy for the start of significant electromagnetic emission from lightning discharge is indicated by vertical arrow, labeled “Trigger”.

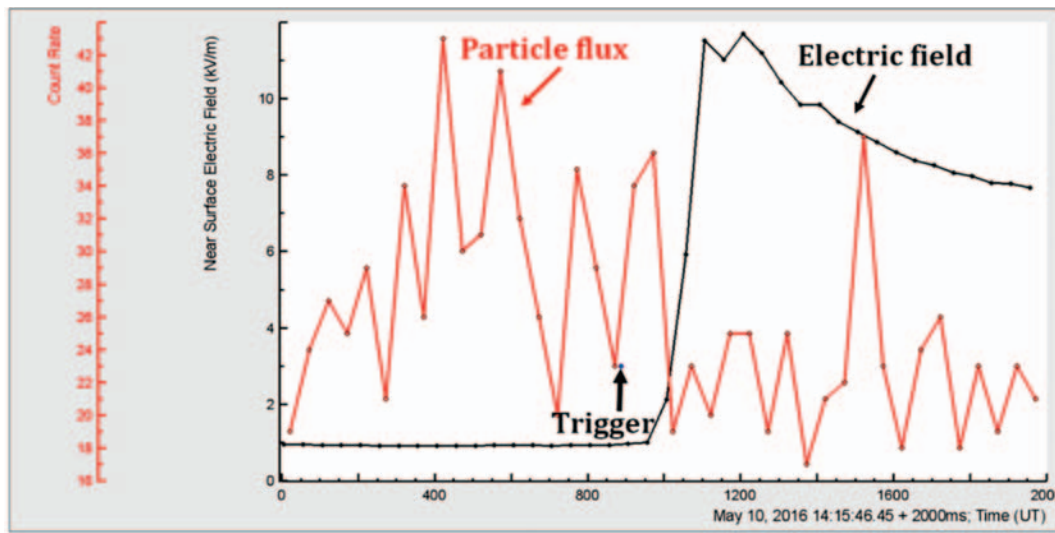


Figure 19. Electrostatic field and particle flux (count rate) for the TGE terminated by lightning flash that occurred on May 10, 2016 at 14:15:48 UTC. The GPS time stamp of the oscilloscope trigger assumed to be a proxy for the start of significant wideband electromagnetic emission from lightning discharge is indicated by vertical arrow.

Parameters of electrostatic field changes and associated particle flux drops for 24 analyzed events are presented in Table 3.

Table 3. Parameters of electrostatic field changes and associated particle flux drops for 24 TGEs terminated by lightning

Parameter	Mean±St.Dev
Rise time of electrostatic field, ms	217±82
Recovery time of electrostatic field	5.5 ± 4.7
Magnitude of electric field change,	61 ± 16
Distance to lightning estimated by	5.6 ± 3.0
Particle flux (count rate) drop, %	29 ± 23

The magnitude of electric field change is defined as the difference between the maximum of electrostatic field and its value at the beginning of abrupt change, as illustrated in Figure 4.

It is important to note that we did not observe any TGE termination by lightning which produced a negative field change, that is, for all TGEs terminated by lightning, the field change was positive. As noted earlier, positive field changes reduce the upward-directed electric field, accelerating electrons toward ground, which leads to a decrease of particle count rate.

CONCLUSION

Main results of the present study can be summarized as follows.

1) The electron-accelerating electric field can be formed by the main negative charge in the cloud and its mirror image in the ground. This field is influenced by other charges in the cloud (and their images) and can be locally enhanced by the LPCR in the cloud and positive corona space charge near ground. TGEs always occur when the electron-accelerating electric field is present at the ground.

2) The electric field both inside and beneath the thundercloud can be abruptly changed by lightning discharges, which can influence the evolution of TGEs, including their abrupt termination.

3) Two types of flashes were observed to terminate TGEs, namely, -CGs and normal-polarity ICs. Both these types reduce the main negative charge in the cloud.

4) Neither +CGs nor inverted-polarity ICs were observed to terminate TGEs. The latter type does reduce the main negative charge in the cloud, but its net effect is to enhance the electron-accelerating field below the cloud due to the accompanying reduction or elimination of LPCR.

5) The decay of particle flux begins in the time interval between the start of significant wideband electromagnetic emission from the lightning discharge and the maximum of electrostatic field change produced by the discharge.

6) Not every TGE-terminating lightning could be reliably classified via lightning-type identification scheme used in the present study. In a follow-up study we plan to improve the classification accuracy via better optical coverage of the detected events and via the use of better instrumentation for measuring wideband E-field waveforms. We also plan to improve the lightning ranging accuracy. Those improvements should allow us to, among other things, estimate the percentages of each type of lightning both terminating and not terminating TGEs.

ACKNOWLEDGEMENT

The authors would like to thank the staff of the Aragats Space Environmental Center for the uninterrupted operation of Aragats research station facilities.

REFERENCE

Alexeenko V.V., Khaerdinov N.S., Lidvansky A.S., Petkov V.B., 2002. Transient variations of secondary cosmic rays due to atmospheric electric field and evidence for pre-lightning particle acceleration Physics Letters A 301, 299–306.

Chilingarian, A., A. Daryan, K. Arakelyan, A. Hovhannisyan, B. Mailyan, L. Melkumyan, G. Hovsepyan, S. Chilingaryan, A. Reymers, and L. Vanyan L., 2010. Ground-based observations of thunderstorm-correlated fluxes of high-energy electrons, gamma rays, and neutrons, Phys. Rev. D, 82, 043009.

Chilingarian, A., Hovsepyan, G., Hovhannisyan, A., 2011. Particle bursts from thunderclouds: natural

- particle accelerators above our heads. *Phys. Rev. D: Part. Fields* 83 (6), 062001
- Chilingarian, A., Karapetyan T, Melkumyan L., 2013. Statistical analysis of the Thunderstorm Ground Enhancements (TGEs) detected on Mt. Aragats. *J. Adv. Space Res.*, 52, 1178.
- Chilingarian A., 2014. Thunderstorm Ground Enhancements - model and relation to lightning flashes, *Journal of Atmospheric and Solar-Terrestrial Physics* 107, 68–76.
- Chilingarian A., Chilingaryan S., Hovsepyan G., 2015. Calibration of particle detectors for secondary cosmic rays using gamma-ray beams from thunderclouds, *Astroparticle Physics* 69, 37–43
- MacGorman, D. R. and W. D. Rust, *the Electrical Nature of Thunderstorms*, 422 pp., Oxford University Press, New York, 1998.
- Nag A. Rakov V. 2009, some inferences on the role of lower positive charge region in facilitating different types of lightning
Geophys. Res. Lett., V. 36, L05815, doi: 10.1029/2008GL036783.
- Pokhsraryana D., 2015, Fast Data Acquisition system based on NI-myRIO board with GPS time stamping capabilities for atmospheric electricity research, *Proceedings of TEPA 2015, Nor Amberd, Tigran Mets* pp.23-27
- Rodger, C. J., Brundell, J. B., and Dowden, R. L., 2005, Location accuracy of VLF World-Wide Lightning Location (WWLL) network: Post-algorithm upgrade, *Ann. Geophys.*, 23, 277-290.
- V. A. Rakov and M. A. Uman, *Lightning: Physics and Effects*.
New York: Cambridge Univ. Press, 2003.
- Torii, T., Sugita, T., Kamogawa, M., et al., 2011. Migrating source of energetic radiation generated by thunderstorm activity. *Geophys. Res. Lett.* 38, L24801.
- Tsuchiya H., Enoto T., Iwata K., et al., 2013. Detection of high-energy gamma rays from winter thunderclouds, *Phys. Rev. Lett.*, 111, 015001.
- Zhu Y., Rakov V., Tran M., and Nag A. 2016 A Study of NLDN Responses to Cloud Discharge Activity Based on Ground-Truth Data Acquired at the LOG. 24th International Lightning Detection Conference. And 6th International Lightning Meteorology Conference., 18-21 April, 2016, San Diego California, USA

On the origin of particle fluxes from thunderclouds

A. Chilingarian^{1,2}, S. Chilingaryan¹, T. Karapetyan¹, Y. Khanikyants¹, D. Pokhsraryan¹,
S. Soghomonyan¹

1. Alikhanyan National Lab (Yerevan Physics Institute), Alikhanyan Brothers 2, Yerevan 0036, Armenia

2. National Research Nuclear University MEPhI (Moscow Engineering Physics Institute), Moscow 115409, Russian Federation

Abstract. We present the observational data on registration of atmospheric discharges simultaneously with the detection of elementary particles performed during thunderstorms at 3200m altitudes above sea level on Mt. Aragats in Armenia. Throughout the 2016 summer campaign on Aragats we monitored lightning occurrences and signals from NaI spectrometers, plastic scintillators, and Neutron Monitor proportional counters, and analyzed the shape of registered pulses. Particle detector signals were synchronized with lightning occurrences on microsecond time scale.

Our measurements prove that all signals registered by particle detectors simultaneously with lightning were Electromagnetic interferences (EMI) and not typical responses of particle detectors on the passage of neutral or charged elementary particles.

1. INTRODUCTION

Copious observations of the Thunderstorm ground Enhancements (TGEs, Chilingarian et al., 2010, 2011), i.e. enhanced fluxes of electrons, gamma rays and neutrons detected by particle detectors located on the Earth's surface and related to the strong thunderstorms overhead, posed the question of their origin. According to the TGE initiation model (Chilingarian, 2014), the electrical field of the lower dipole in the thundercloud effectively transfers field energy to secondary cosmic ray electrons. Electrons by a "runaway" process (Gurevich et al., 1992) generate gamma rays and gamma rays by photonuclear reaction create neutrons (Chilingarian et al., 2012). Large TGEs occur during large negative electric fields near earth's surface (Chilingarian and Mkrtchyan, 2012). To produce large TGEs clouds should be not more than a few hundred meters above particle detectors to allow electrons and gamma rays from Relativistic runaway electron avalanches (RREA) reach the earth's surface. Multiyear observations of particle fluxes and lightning occurrences on Aragats prove that during large TGEs the lightning activity is suppressed; lightning kills particle fluxes and does not boost them (Chilingarian et al., 2015).

Observation of numerous TGEs by the Japanese, Chinese, Slovakian groups (Kuroda et al., 2016, Zeng et al., 2013, Wang et al., 2015, Torii et al., 2011, Tsuchiya et al., 2013, Kollarek et al., 2016) prove that RREA is a robust and realistic mechanism for electron acceleration and multiplication leaving no doubts about correctness of the model of TGE initiation.

However, there is another point of view on the thundercloud particle origination.

Physicists performing experiments at the Tien-Shan Mountain Cosmic Ray Station, Kazakhstan (altitude 3340 m) in several papers reported the existence of the lightning high-energy emissions i.e. the electron, gamma and neutron fluxes obtained simultaneously in multiple lightning events.

Gurevich et al., (2012) "report for the first time about the registration of an extraordinary high flux of low-energy neutrons generated during thunderstorms. The measured neutron count rate enhancements are directly connected with thunderstorm discharges". Gurevich et al., (2016) confirm

that "the intensity both of electrons and gamma rays in lightning discharge prevail the background emission by 1.5 to 2 orders of magnitude"

Lebedev Institute group, Moscow, Russian Federation, reported the emission of neutrons in the energy range up to tens of MeV in a laboratory 1 m long high-voltage discharge. They conclude that "the data obtained allow us to assume that during the discharge fast neutrons are mainly produced" (Agafonov et al, 2013); and that "neutrons were registered within the range from thermal energies up to the energies above 10 MeV. It was found that the neutron generation takes place at the initial phase of electric discharge and is correlated with generation of x-ray radiation" (Agafonov et al, 2016).

Another observation of the lightning-induced gamma ray flux was reported by group from International Center for Lightning Research and Testing (ICLRT, Hare et al., 2016) in North Central Florida. The gamma ray flux on 15 August 2014 was extremely intensive so that by 50 μ s after the system trigger the electronics was completely saturated. The authors claim that the primary factor that triggered the very intensive gamma ray flux was the upward positive leader approaching a negative charge region.

However, the physical model of the particle origination in the thunderbolt is not well explained. Usually, the physical model is not formulated at all, only detection of particles is described:

Gurevich et al., (2015): it is established that the neutrons are generated during thunderstorm atmospheric discharges. Often the neutrons are emitted in short bursts; the burst width is 200-400 μ s.

Agafonov et al., (2013): "Currently, there is no reasonable model or mechanism to explain the generation of neutron bursts during atmospheric discharge in air. A special mystery is the origin of the neutrons with energies above 10 MeV."

Thus, we have 2 models of particle initiation during thunderstorms:

TGE – model: electrons from the ambient population of CR accelerated in the strong electric field in the lower part of cloud, runaway, born bremsstrahlung gamma rays and gamma rays born neutrons via photonuclear reactions;

Lightning model: the electron, gamma and neutron fluxes originated simultaneously in the lightning flashes.

To solve this controversy and select the correct model we need to perform experiment that ambiguously answers the question: do “lightning flashes emit high-energy electrons, positrons, photons and neutrons with single energies of several tens of MeV? (Kohn et al., 2017)”.

To answer this question we perform experiments with pulse shape recording from particle detectors and simultaneously from atmospheric discharges. Direct comparison of synchronized patterns of lightning discharges and particle detector outputs along with examining the typical response of detectors to particle traversal can answer the question of the thunderstorm particle origin.

During summer 2016 campaign on Aragats performed by the staff of Cosmic Ray division (CRD) of Yerevan Physics Institute (YerPhi) several strong storms with numerous lightning flashes were observed, and some of the most violent ones produced Electromagnetic interferences (EMI) in particle detectors and Data acquisition electronics (DAQ). Taking as example huge storms on 15 May, 11 June and 23 September we demonstrate that with new fast electronics we can reliably distinguish EMI from genuine particle registration in variety of particle detectors that are in operation on Aragats.

2. INSTRUMENTATION

The correlation analysis of the TGEs and lightning discharges pose stringent requirements on the time resolution and synchronization of the data flow from particle detectors, near surface electric field sensors and sensors of the fast radio waveforms of atmospheric discharges. Developed fast Data acquisition (DAQ) system, see Fig.1, is triggered by a commercial MFJ-1022 active whip antenna that covers a frequency range from 300 KHz to 200 MHz. A flat-plate antenna followed by passive integrator is used to record fast electric field waveforms. The output of the integrator is directly connected to the digital oscilloscope (2 channel Picoscope 5244B with 25MS/s sampling rate) with 60 cm long RG58 coaxial cable. Data capture length can be chosen from 1 second, including 200 ms pre-trigger and 800 ms post-trigger time with a sample interval 40 ns, or, for instance, 10 ms length with sample interval of 0.4 ns.

The trigger output of the oscilloscope is connected to the input of GPS timing system of MyRio board. Any event recorded by the oscilloscope generates an output trigger, causing the GPS card to trigger at the same instant and produce a timestamp. The duration of the trigger output pulse is 400ns, and its delay in respect to the actual trigger instant is 330ns.

The heart of the DAQ system is NI-myRIO board. It includes eight analog inputs, four analog outputs, 32 digital I/O lines, all programable FPGA (field-programmable gate arrays) and a dual-core ARM Cortex-A9 processor (a high-performance processor implementing the full richness of the widely supported ARMv7-A architecture). With reconfigurable FPGA technology, we perform high-speed signal processing, high-speed control, inline signal processing, and custom timing and triggering. For the control systems, one can also run advanced control algorithms directly in the FPGA fabric to minimize latency and maximize loop rates. “LabVIEW FPGA Module”, which extends the LabVIEW graphical development platform,

provides an alternative to HDL (Hardware description language) graphical programming approach that simplifies the task of interfacing to I/O and communicating data. This greatly improves embedded system design productivity and reduces the time of project accomplishment.

The commercial GPS receiver sends two types of data-stream to the board. The first is RS-232 ASCII data telling what time it is, at what latitude, longitude, and altitude the receiver is, and information about the satellites the receiver is using. An embedded 25 MHz counter on FPGA gives the exact time of the trigger. The (1PPS - one pulse per second) stream of the 5V, 100-ms pulses resets this counter at each second. The leading edges of 1PPS signals from GPS receivers are synchronized within the accuracy of the non-military GPS system (about 100 ns.) This feature allows time synchronization with 100 ns resolution.

8 digital inputs of myRIO board are used for feeding signals from variety of particle detectors operated on Aragats. In the 2016 summer season we attach to myRIO the STAND1 detector comprises from 3 stacked vertically 1 cm thick and 1 m² area plastic scintillators (energy threshold ~ 1 MeV) and 1 stand alone 3 cm thick plastic scintillator (energy threshold ~3 MeV) of the same area, proportional counters of Aragats Neutron Monitor (ArNM) and NaI crystal based detectors (energy threshold ~0.4 MeV). The details of particle detector operation one can find in (Chilingarian, Hovsepian and Mnatsakanyan, 2016, and Chilingarian, Hovsepian and Kozliner, 2016).

The myRIO pulse counting system can provide registration of very short time series (down to 1 millisecond) that will enable investigation the dynamic of TGE development and its relation to the lightning initiation (50 ms time series are stored currently).

Signals from the sensor of “slow” (measurements are made with 20 Hz frequency) electric field sensor (the “electric mill” EFM-100 of Boltek company) are fed to the myRIO board by the TCP-IP connection (WiFi). The firmware application provided by Boltek has a feature to share E-Filed data via a network (it acts as a server for a client running under myRIO). The 8-th channel is reserved for the synchronization pulse (the trigger) from fast waveform recording device or from any of particle detectors.

MyRio board at any triggering signal generates a special output containing current value of particle detector counts, near surface electric field value and precise time of arriving of the trigger signal. Thus, the fast waveform patterns will be synchronized with particle fluxes and, with slow (20 Hz) near surface electric field measurements.

The time series of particle detector count rates, electrostatic field measurements and service information (status of myRIO, time delays, a number of satellites used), as well as the files containing digital oscilloscope data, are transferred via on-line PC to the MySQL database on CRD headquarters in Yerevan. All information is available via ADEI multivariate visualization code by link <http://adei.crd.yerphi.am>; explanations are located in the Wiki section (Chilingaryan et al., 2010).

A web based UI (User Interface) was developed for the monitoring and controlling the fast DAQ system using LabView built-in tools. UI is based on the Microsoft Silverlight web technology and is supported by iOS and Window browsers.

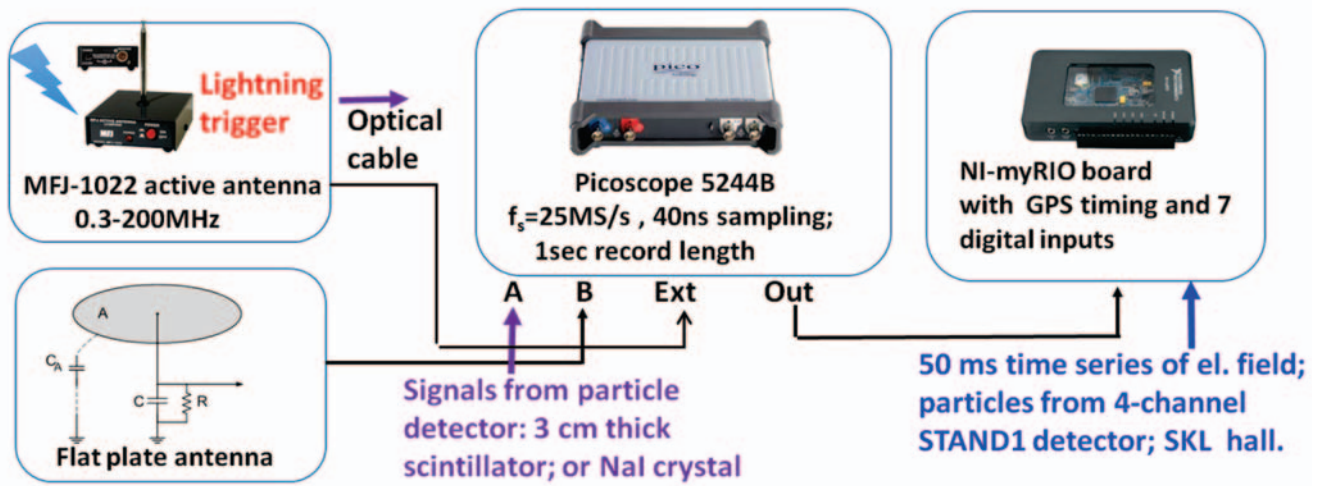


Figure 1. The fast Data acquisition system for the research of particle flux - lightning relations

Without any additional programming, one can configure any LabVIEW application for remote control through a Web browser. The remote user can access the user interface that appears in the Web browser. The acquisition still occurs on the host system, but the remote user has complete control of the application. Other users also can point their Web browser to the same URL for monitoring. To avoid confusion, only one client can control the application at a time, but that control can pass easily among the various clients at run-time.

2 DAQ systems are operated independently in MAKET and SKL experimental halls on Aragats; triggers issued by both fast DAQ systems usually coincide within few ms). However, an optical link can transfer the trigger signal from SKL to MAKET experimental hall located on the distance 100 m. for the joint triggering of 2 networks of particle detectors and field meters.

3. *IN SITU* MEASUREMENTS OF THE THUNDERSTORM PARTICLES ON ARAGATS

On 11 June 2016 large disturbances of the near-surface electrostatic field started at 10:45 UT, see Figure 2a. The atmospheric pressure was 690.8 mbar; relative humidity – 75%; wind speed 3-4m/sec; temperature $\sim 5^{\circ}\text{C}$; no rain was registered. In Figure 2a and 2b we show disturbances of the near-surface electric field; one-minute and one-second time series of count rates of 1 and 3 cm thick plastic scintillators of STAND1 array and distance to lightning in the top of both 2a and 2b Figures. Note the difference in the horizontal axes of 2a and 2b Figures: for one-minute time series it is half of hour, for one-second time series it is 12 minutes. The typical shape of the electrostatic field disturbances (the electrostatic field in the deep negative domain for several minutes possibly accompanied by several short “bursts” touching positive domain and 1-2 negative lightning flashes with large amplitude) shown in Figure 2a indicates the development of the Lower positive charged region (LPCR) in the bottom of cloud (Chilingarian and Mkrtychyan, 2012) and the establishment of the lower dipole accelerated CR electrons downwards. Accelerated electrons unleash multiple relativistic runaway avalanches measured on the earth’s surface (Chilingarian et al., 2010, 2011). The enhanced particle flux (TGE) is shown in Figure 2a by the one-minute time series of count rate of 1 cm thick plastic scintillator of STAND1 detector located near-by MAKET experimental hall (upper detector of 3 stacked

above each other). The count rate enhancement was 26.2% (36.7σ) in percent of the mean count rate and in the number of standard deviations.

A strong lightning discharge occurred at 11:45:22 abruptly terminates TGE. However, after the first lightning flash, the TGE restarted and continuous ~ 4.5 minutes until 11:50 when second strong lightning discharge finally terminates particle flux. After series of strong positive lightning discharges, disturbances of the electrostatic field continues until $\sim 15:00$. Negative lightning depositing negative charge to the ground produces positive electrostatic field change (atmospheric electricity sign convention according to which the downward-directed electric field or field change vector is considered to be positive, is used throughout this paper) as it is shown in the Figure 2a and 2b. Electrostatic field change caused by the lightning has a rise time of few hundreds of milliseconds, and recovery time of several seconds. Abrupt termination of particle flux caused by first lightning is shown in Figure 2b with 1-second time series of the 3-cm thick scintillator of the same STAND1 detector. Count rate decreases from 731 at 11:45:22 down to 592 (19%) at 11:45:23. The negative lightning that terminates TGE is usually very strong and is characterized by very fast enhancement of the near-surface electrostatic field with much steeper recovering. The electrostatic field starts to rise from an initial value of -30.6 kV/m at 11:45:22.48, and shows a maximum of 39.7 kV/m at 11:45:22.58; the amplitude of field change was 70.3 kV/m reached in 100 ms. Field recovery time took much longer time ~ 10 sec.

Strong lightning discharge is a powerful wideband radio-wave emitter inducing pulses in the cables, DAQ electronics, and power lines. To check if the registered pulses are electromagnetic interferences (EMI) or signals from relativistic particles born in the lightning bolt we performed synchronized measurements of the waveforms of fast electric field caused by atmospheric discharges and signals from particle detectors. The Aragats Neutron Monitor (ArNM, see details in Chilingarian, Hovsepyan and Kozliner, 2016) measures one-second time series from 16 proportional counters filled with Boron gas. Neutrons and protons incident the detector’s 5 cm thick lead absorber generate in nuclear reactions numerous secondary neutrons, which enter the proportional counter and registered.

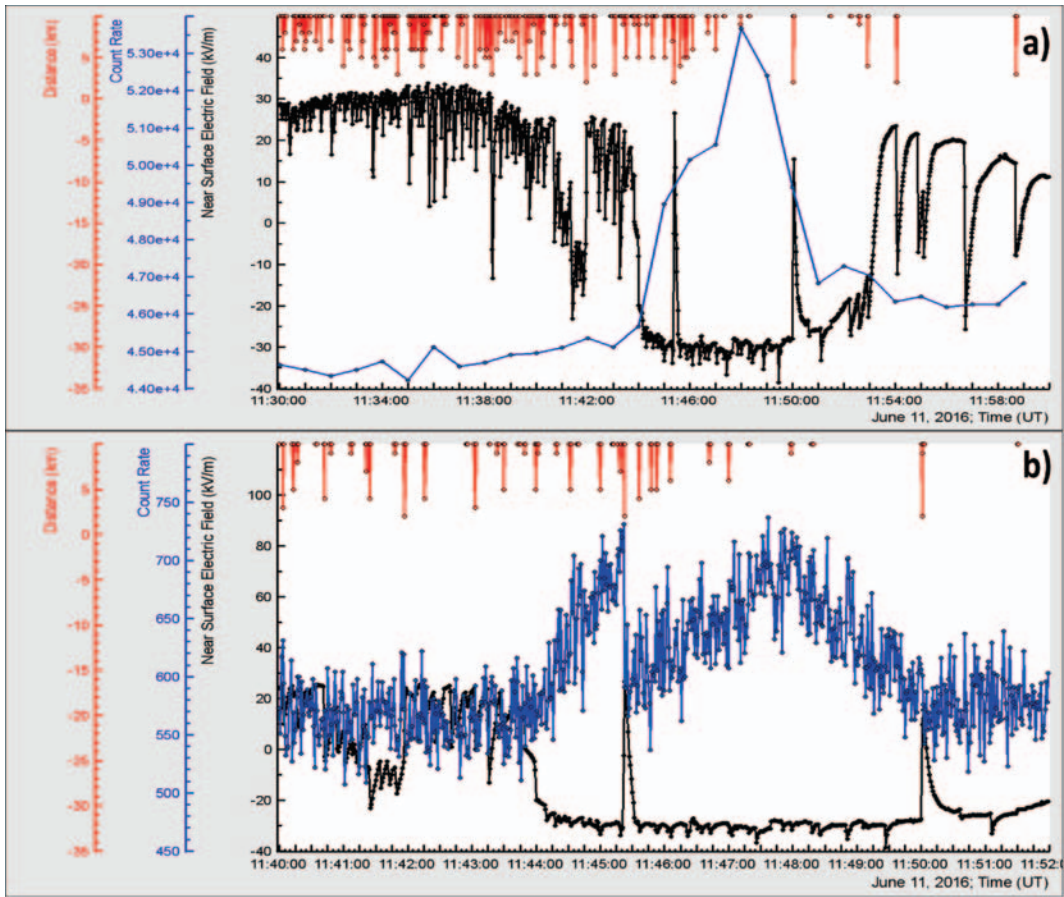


Figure 2. a) disturbances of the near surface electrostatic field, distance to lightning and 1-minute count rate of STAND1 (MAKET) upper scintillator; energy threshold $\sim 1\text{MeV}$; b) 1-sec time series of the 3 cm thick plastic scintillator of the same detector. A strong lightning discharge is seen as a vertical line interrupted TGE.

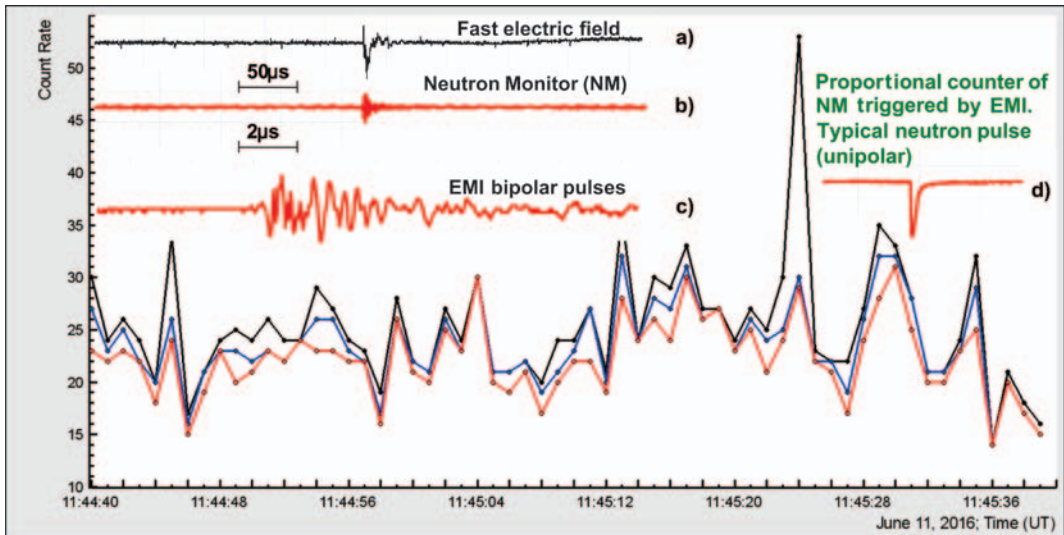


Figure 3. The one-second time series of ArNM. Only time series corresponding to $0.4\ \mu\text{s}$ dead time demonstrates large peak (black curve) due to counting multiple secondary neutrons coming within time span $\sim 1\text{ms}$; the time series corresponding to 750 and $1200\ \mu\text{s}$ dead time demonstrate no peak. Inset is described in the body of the paper.

A hypothetical particle burst from the lightning will be registered by ArNM as a large peak in the one-second time series of detector count rate, see Fig. 3. To distinguish EMI from relativistic particles we need to examine the pulse shape registered by the fast oscilloscope. In the insert of Fig. 3, we demonstrate simultaneous detection of fast electric field waveforms from flat plate antenna (a) and pulses from one of the proportional counters of ArNM (b, and the zoomed version - c). As a reference, a typical shape of the neutron detection is shown in d. Thus, by detecting the large peak at 11:45:23 in time-series of ArNM shown in Figure 3 only, we

can erroneously conclude that simultaneously with atmospheric discharge a large number of neutrons is born in the lightning bolt. However, proceeding from the detailed pattern of the detected during lightning bipolar pulses (Figure 3 c) and from the typical unipolar pulse that neutron generates on the output of the proportional counter (Figure 3d) we should reject the hypothesis of neutron production in the lightning bolt. All additional counts by the proportional counter at 11:45:23 are due to EMI.

On 23 September 2016 on Aragats station was observed severe storm with strong lightning activity and heavy-duty

rain at 13:50 – 14:50 UT. The temperature falls from 3.6 C° down until 1.3 C°; relative humidity was very high – 98%, rain rate during 20 minutes reaches a level of 1 mm/hour. During the storm, several positive lightning flashes trigger the DAQ system in MAKET and SKL experimental halls see Fig.4. In Figure 4 we show the precise timing of the lightning progression. The time of triggers broadcasted by 2 wipe antennas (shown by 2 nearby points in Figure 4) located in the MAKET and SKL experimental halls differ by 23 ms due to different thresholds applied to the signal from atmospheric discharge. 12 GPS satellites determined the precise time-stamp in both DAQ

systems. After 26 ms from the MAKET DAQ trigger, we observe a huge peak in the count rate of bottom scintillator belonging to the STAND1 stacked detector (there were no peaks in the 2 upper scintillators). We relate this peak to EMI from the atmospheric discharge. If it will be peak from genuine particles, it should be detected as well in the 2 upper scintillators. After 224 ms the rearrangement of the electric field in the thundercloud started as it is mapped by changes of the electrostatic field measured on earth’s surface. The field dropped from 23.7 kV/m until -45 kV/m in 50 ms; field recovery took ~ 10 sec.

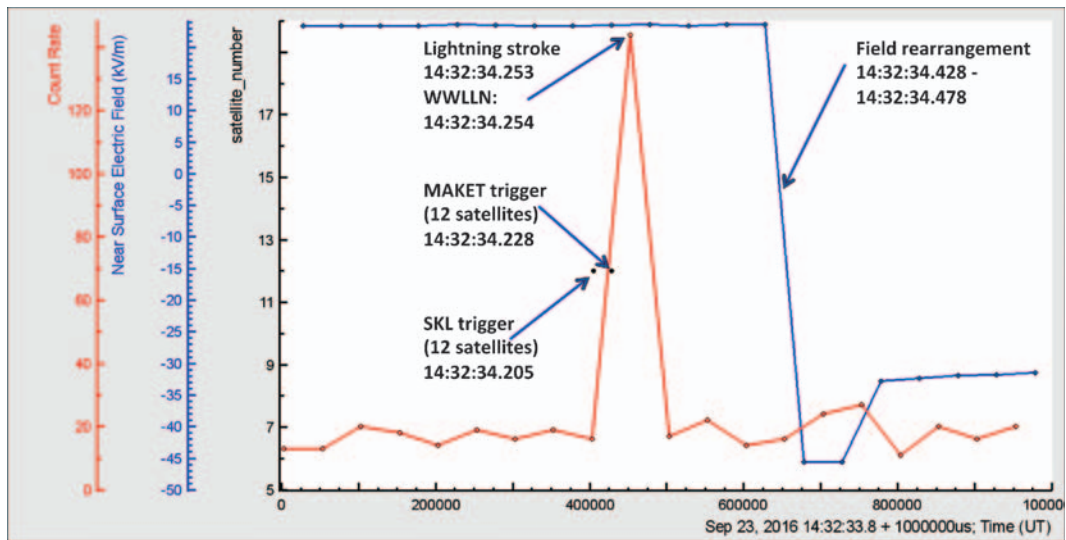


Figure 4. 50 ms time series of the bottoms scintillator of STAND1 detector and electrostatic field disturbances (positive lightning with amplitude 69.3 kV/m).

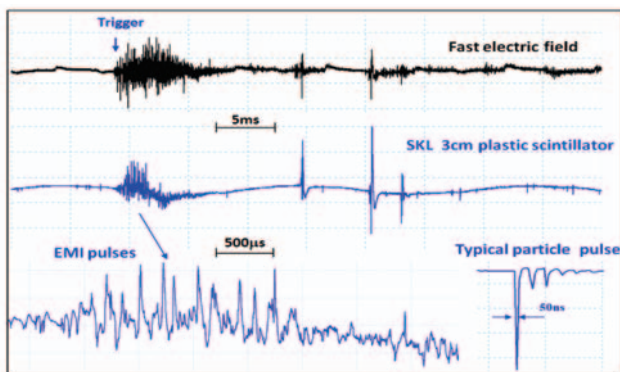


Figure 5. EMI activity Typical EMI signature from atmospheric discharges in the particle detector waveform. Synchronised time-series of the pulses of fast electric field and signals from plastic scintillator.

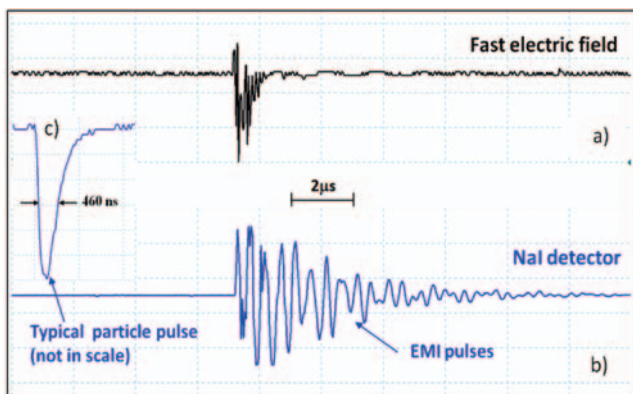


Figure 6. Registration of the lightning occurred on May 15, 2016, 12:48:25; Waveforms of fast electric field a); NaI detector output b); in the insert c) is shown a typical shape of NaI detector response to incident particle.

In Figure 6b we show bipolar pulses registered by another detector, NaI crystal based spectrometer (Chilingarian, Hovsepyan and Mnatsakanyan, 2016) produced by the strong atmospheric discharge (Figure 6a) and not by particle flux from the lightning bolt.

Signals from charged or neutral particles detected by NaI spectrometer are always unipolar (Fig.6c).

Thus, all particle detectors (plastic scintillators, NaI crystals, proportional counters) can be triggered by nearby strong lightning. However, the shape of registered fake pulses can be easily discriminated from the genuine particle pulses.

CONCLUSION

New emerging field of atmospheric high-energy physics is still lacking firmly established concepts and theories. Our paper is an attempt to clarify one of the most important problems: do lightning flashes produce relativistic particles?

In numerous papers this hypothesis was rejected, for instance:

Torii, et all (2011): “Our findings indicate that the energetic radiation is emitted continuously from a downward hemispherical surface without lightning”;

Tsuchiya et al., (2013): “In addition, the present event and the two past observations did not detect any energetic x-ray radiation associated with lightning, mainly its stepped leaders.”;

Chilingarian, 2014: “Simultaneous measurements of the particle fluxes, electrical field disturbances and lightning occurrences at Aragats in the seasons of 2011–2013 do not give any evidence on a causative relation of lightning occurrences to TGEs”.

Alexeenko et al., 2015: “No observations of neutron production during thunderstorms were reported during the three-year period of data recording.”

Furthermore, examining special subclass of TGEs several groups come to a conclusion that the lightning flashes terminate particle flux and not originate it:

Tsuchiya et al., (2013): “...the current results, employing one photon counting with a time resolution of 0.1 ms, demonstrate that 3–30 MeV gamma rays clearly terminate 800 ms prior to the lightning flash”;

Chilingarian (2014): “Proceeding from the described observations (made on Mt. Aragats), we can exclude the second mechanism, i.e., lightning flashes do not initiate TGEs. Particle fluxes started far before the occurrence of lightning flashes when a near-surface electric field is in the negative domain; the time scale of the TGE events is minutes, much larger than typical for lightning flashes; furthermore lightning terminates TGE, did not give rise to it”.

Particle fluxes originated in atmosphere precede lightning flashes; and furthermore they can initiate atmospheric discharges. The airborne experiment f (ADELE) “demonstrate for the first time that glows (particle fluxes of atmospheric origin) can provide a comparably effective channel to lightning for thunderstorm discharge” (Kelly et al., 2015).

Analysis of synchronous shapes of pulses from lightning and particle detectors reveals that all additional detector pulses obtained during lightning flash were the electromagnetic interference signals and not particles originated directly from the atmospheric discharge. Thus we observe no evidence of production of electrons, neutrons or gamma rays during lightning discharge.

We confirm that after pulse shape discrimination only any conclusion on the “lightning origin” of relativistic elementary particles can be considered (Alekseenko et al. 2016).

We also agree with the following comment: “Measurements based solely upon count rates of signals above some discriminator threshold should be viewed with caution, since it is not obvious what is being counted, pulses from energetic gamma rays or, for instance, RF noise from lightning processes. Gain fluctuations due to voltage changes in the electronics may also be an issue when lightning is in the area.” (Dwyer, et al., 2012).

The EMI of nearby lightning can be so strong that no shielding can secure detector and electronics from fake signals. Because EMI can prolong hundreds of microseconds it is rather difficult to “reveal” short duration particle signals (if any) in multiple spurious pulses from atmospheric discharges.

Observed on Aragats fluxes of electrons, gamma rays and neutrons can be explained with standard RREA + MOS theory with cosmic ray electron seeds (Chilingarian, 2014).

Investigations of pulses from particle detectors and atmospheric discharges prove that some of the particle detectors show large enhancements simultaneously with the lightning occurrence. However, the pulse trains registered at a lightning time are bipolar alike the EMI pulses registered by a flat circular antenna, whereas the pulses from genuine particles should have the unipolar shape. During 2016 summer storms campaign we did not observe any lightning producing relativistic particles in any of tested detectors.

Lightning flashes sharply terminate particle fluxes from thunderclouds they do not create them!

ACKNOWLEDGEMENT

The author thanks the staff of the Aragats Space Environmental Center for the uninterrupted operation of Aragats research station facilities. One of the authors (AC) is grateful to Yuri Stenkin for useful discussions and valuable comments.

The data for this paper are available on the WEB page of the Cosmic Ray Division (CRD) of the Yerevan Physics Institute, <http://adei.crd.yerphi.am/adei>. All figures from the paper can be easily reproduced with embedded multivariate visualization on-line program ADEI (Chilingaryan et al., 2010)

The expedition to Aragats high altitude station was supported by the Armenian government grant N13-1C275.

REFERENCE

A.V. Agafonov, A. V. Bagulya, O. D. Dalkarov, et al., Observation of Neutron Bursts Produced by Laboratory High-Voltage Atmospheric Discharge, *Phys. Rev. Lett.* 111, 115003 (2013)^[SEP]

A.V. Agafonov, V.A. Bogachenkov, A.P. Chubenko, et al., Observation of hard radiations in a laboratory atmospheric high-voltage discharge, 2016, e-Print: arXiv:1604.07784 [physics.plasm-ph]

V. Alekseenko, F. Arneodo, G. Bruno, et al., Decrease of Atmospheric Neutron Counts Observed during Thunderstorms, *PRL* 114, 125003 (2015)^[SEP]

Chilingarian, A., Daryan, A., Arakelyan, K., Hovhannisyan, A., Mailyan, B., Melkumyan, L., Hovsepian, G., Chilingaryan, S., Reymers, A., Vanyan, L., 2010. Ground-based observations of thunderstorm-correlated fluxes of high-energy electrons, gamma rays, and neutrons. *Phys. Rev. D: Part. Fields* 82 (4), 043009.

Chilingarian, A., Hovsepian, G., Hovhannisyan, A., 2011. Particle bursts from thunderclouds: natural particle accelerators above our heads. *Phys. Rev. D: Part. Fields* 83 (6), 062001.

Chilingarian, A. and Mkrtchyan, H., Role of the Lower Positive Charge Region (LPCR) in initiation of the Thunderstorm Ground Enhancements (TGEs), *Physical Review D* 86, 072003 (2012).

A.Chilingarian, N. Bostanjan, T. Karapetyan, L.Vanyan, Remarks on recent results on neutron production during thunderstorms, *Physical Review D* 86, 093017 (2012).

A.Chilingarian A., Thunderstorm Ground Enhancements – model and relation to lightning flashes, *J. Atmos. Solar-Terr. Phys.* 107 (2014) 68–76.

Chilingarian A., G. Hovsepian, G. Khanikyanc, A. Reymers and S. Soghomonyan, Lightning origination and thunderstorm ground enhancements terminated by the lightning flash, *EPL*, 110 (2015) 49001.

Chilingarian A., Hovsepian G., and Mantasakanyan E., 2016. Mount Aragats as a stable electron accelerator for atmospheric High-energy physics research, *Phys. Rev. D: Part. Fields*, 93, 052006.

A. Chilingarian, G. Hovsepian, L. Kozliner, Extensive Air Showers, Lightning, and Thunderstorm Ground Enhancements, *Astroparticle Physics, Astroparticle Physics* 82 (2016) 21–35

- S. Chilingaryan, A. Beglarian, A. Kopmann, and S. Vočking, Advanced data extraction infrastructure: Web based system for management of time series data
- J. Phys. Conf. Ser. 219, 042034 (2010). ^[1]_{SEP}
- J.R. Dwyer, D.M. Smith, S.A. Cummer, High-energy atmospheric physics: terrestrial gamma-ray flashes and related phenomena, Space Sci. Rev. 173 (2012) 133–196. ^[1]_{SEP}
- B. M. Hare, M. A. Uman, J. R. Dwyer, ^[1]_{SEP} et al. (2016), Ground-level observation of a terrestrial ^[1]_{SEP} gamma ray flash initiated by a triggered lightning, J. Geophys. Res. Atmos., 121, 6511–6533.
- A.V. Gurevich, G.M. Milikh, R. Rouseel-Dupre, Runaway electron mechanism of air breakdown and preconditioning during a thunderstorm, Phys. Lett. A 1992 V.165 (1992) 463–468.
- Gurevich A.V., Antonova V. P., Chubenko A. P., et.all., Strong Flux of Low-Energy Neutrons Produced by Thunderstorms Phys. Rev. Lett. 108, 125001 (2012). ^[1]_{SEP}
- Gurevich, A.V., Antonova, V.P., Chubenko, et.all. The time structure of neutron emission during atmospheric discharge, Atmospheric Research (2015), V. 164, 339.
- Gurevich, A.V., Almenova A.M., Antonova, V.P., Observations of high-energy radiation during thunderstorms at Tien-Shan, Phys. Rev. D 94, 023003 (2016). ^[1]_{SEP}
- Kelley N. A., Smith D. M., and Dwyer J. R. Et al., Relativistic electron avalanches as a thunderstorm discharge competing with lightning, Nat. Commun 6, 7845 (2015). ^[1]_{SEP}
- M.Kollárik, K.Kudela, R.Langer, I.Strhárský, First results from the measuring equipment SEVAN on Lomnický štít: possible connections with atmospheric phenomena, Proceedings TEPA-2015, TIGRAN METS, 31-34, INSPIRE C15-10-02, 2016.
- Y. Kuroda, S. Oguri, Y. Kato, R. Nakata, Y. Inoue, C. Ito, M. Minowa, Observation of gamma ray bursts at ground level under the thunderclouds, Physics Letters B 758 (2016) 286–291.
- Köhn C., Diniz G. and Harakeh M.N., Leptons, hadrons and photons and their feedback close to lightning leaders, J. Geophys. Res. Atmos., vol. 122, doi: 10.1002/2016JD025445, 2017.
- Pokhsraryana D, 2016. Very fast Data Acquisition system based on NI-my RIO with GPS time stamping capabilities, Proceedings of TEPA 2015, Nor Amberd, Tigran Metz, 23-27, INSPIRE C15-10-02, 2016.
- Torii, T., Sugita, T., Kamogawa, M., et al., 2011. Migrating source of energetic radiation generated by thunderstorm activity. Geophys. Res. Lett. 38, L24801.
- H. Tsuchiya, T. Enoto, K. Iwata, et al., Hardening and termination of long-duration gamma rays detected prior to lightning, Phys. Rev. Lett. 111, 015001 (2013) flashes and thunderstorms, J. Geophys. Res. Atmos., 119, 1492–1503,
- Y. Zeng, F.R. Zhu, H.Y. Jia, For the ARGO-YBJ collaboration, Correlation between cosmic ray flux and electric atmospheric field variations with the ARGO-YBJ experiment, 33ICRC, RIO DE JANEIRO 2013.
- Xinjian Wang, Xunxiu Zhou, Daihui Huang, Huanyu Jia, 2015. Effects of the near-earth thunderstorms electric field on intensity of the ground cosmic ray electron at YBJ, PoS, ICRC2015, 233

On the Initiation of Lightning in Thunderclouds

A. Chilingarian^{1,2}, S. Chilingaryan¹, T. Karapetyan¹, L. Kozliner¹, Y. Khanikyants¹, G. Hovsepyan¹, D. Pokhsraryan¹ and S. Soghomonyan¹

1. Yerevan Physics Institute, 2 Alikhanyan Brothers, 0036, Yerevan, Armenia

2. National Research Nuclear University MEPhI (Moscow Engineering Physics Institute), Moscow 115409, Russian Federation

Abstract. The relationship of lightning and elementary particle fluxes in the thunderclouds is not fully understood to date. Using the particle beams (the so-called Thunderstorm Ground Enhancements – TGE) as a probe we investigate the characteristics of the interrelated atmospheric processes. The well-known effect of the TGE dynamics is the abrupt termination of the particle flux by the lightning flash. With new precise electronics, we can see that particle flux decline occurred simultaneously with the rearranging of the charge centers in the cloud. The analysis of the TGE energy spectra before and after the lightning demonstrates that intense high-energy part of the TGE energy spectra disappeared just after lightning. The decline of particle flux coincides on millisecond time scale with first atmospheric discharges and we can conclude that Relativistic Runaway Electron Avalanches (RREA) in the thundercloud assist initiation of the negative cloud to ground lightning. Thus, RREA can provide enough ionization to play a significant role in the unleashing of the lightning flash.

1. INTRODUCTION

Among top unanswered questions in lightning research J. Dwyer and A. Uman (2014) state as number one: “*By what physical mechanism or mechanisms is lightning initiated in the thundercloud?*” and - number two: “*What physical mechanisms govern the propagation of the different types of lightning leaders?*”.

They also mentioned that “*The problem of how lightning is initiated inside thunderclouds is not only one of the biggest unsolved problems in lightning physics; it is also probably one of the biggest mysteries in the atmospheric sciences.*”

One of the candidates related to initiation and propagation of lightning is considered to be energetic runaway electrons. Electron acceleration in the thunderstorm atmospheres was first recognized by CTR Wilson (1925); then Gurevich et al. (1992) introduced the electron runaway concept (named Runaway Breakdown - RB, now mostly referred as Relativistic Electron Runaway Avalanche – RREA); in 2003 J. Dwyer developed the feedback model of intracloud electron-gamma ray avalanches exponentially enhancing electron number. Recent observations of hundreds of the Thunderstorm ground enhancements (TGE, an abrupt enhancement of the secondary cosmic rays measured on the Earth’s surface in correlation with thunderstorms) on Aragats provide an extensive source for the development of models of particle acceleration and multiplication in thunderclouds (Chilingarian, Mailyan and Vanyan, 2012, Chilingarian 2014).

The electric field strength and spatial extent required for the RB/RREA development was measured during balloon flights in thunderstorm atmospheres at New Mexico. A 1.87 kV/cm field extended 1 km downwards from the height of 5.77 km would give an RREA multiplication factor of about 650 (Marshall and Winn, 1982). *In situ* measurements of the RREA by the network of particle detectors on Aragats (Chilingarian et al., 2010, 2011) allow retrieving the RREA propagation in the thundercloud. Estimated multiplication factor is ~ 330, e-folding length ~250-300 m and maximum energy of RREA electrons in the cloud is 40-50 MeV. The strength of the uniform vertically downward field of 1.5 km

elongation expected to be 1.8-2.0 kV/cm. For the both observed cases, RREA electron flux will significantly increase the electrical conductivity in the cloud and possibly would not only introduce an additional leakage current but also can assist propagation of the lightning leader.

In this study, we analyze a special kind of TGEs, i.e. TGEs abruptly terminated by lightning flashes. To our knowledge, the Baksan group reported the first TGEs of this kind (Alexeenko et al., 2002). They demonstrated that the particle count rate increased at energies of ~30 MeV then quickly returned to the background level when lightning occurred. In (Khaerdinov and Lidvansky, 2005) they correctly deduce that the detected flux enhancements are not directly related to the lightning activity; the lightning flashes serve rather as a switch-off for the electric field. Recently several groups report such special TGEs as well (Tsuchiya H. et al., 2013, Chilingarian et al., 2015, Kelley et al., 2015, Kollarik et al., 2016, Kuroda et al., 2016).

Thus, using additional key observables, the TGEs, we investigate relations between RREA propagation in the cloud and occurrence of nearby lightning flashes and gain insights into the role of energetic runaway electrons in lightning initiation.

The main method of the multivariate data analysis and physical inference consists in the selection of the hierarchical time series of particle count rates along with measurements of the electrostatic electric field, distance to lightning, fast electric field waveforms and other. Precise synchronization of all measurements allows analyzing the time series on millisecond time scales. The one-second and one-minute time series also are very useful for discovering many non-trivial correlations in TGE data. Analyzing numerous TGEs with one and the same sequence of patterns we reveal the repeating structures, typical correlations and finally causal relations between observables. As a result, we come to models and theories of TGE initiation and its relation to the electrical structure of the thunderclouds and lightning initiation and propagation. Multivariate analysis methodology has been made possible by the use of Advanced Data Extraction Infrastructure - a very flexible and powerful tool providing services for the multidimensional visualization, data zooming, comparison, digitizing, statistic analysis and other.

2. METHODS: REGISTRATION OF THE TGES AND ASSOCIATED GEOPHYSICAL PARAMETERS BY THE NETWORKS OF PARTICLE DETECTORS AND FIELD-METERS

The particle detectors of the Aragats Space Environmental Center (ASEC) (Chilingarian et al., 2005) measure the fluxes of the neutral and charged species of secondary cosmic rays. Numerous thunderstorm-correlated events, detected by the ASEC facilities, constitute a rich experimental set for the investigation of the high-energy phenomena in the thunderstorm atmosphere. The new generation of ASEC detectors consists of 1- and 3-cm-thick molded plastic scintillators arranged in stacks (named STAND1 and STAND3) and cubic structures (named CUBE1 and CUBE3); see the appendix. A detailed description of ASEC detectors, including charts with all sizes, is available from the WEB site of the Cosmic Ray Division of Yerevan Physics Institute <http://crd.yerphi.am/ADEI> in the WIKI section of the multivariate visualization platform and from (Chilingarian et al, 2010 and in Chilingarian, Chilingaryan, and A. Reymers, 2015). With networks of these and other operated on Aragats particle detectors, we continuously monitor incident particle fluxes and geophysical parameters. The data on particle fluxes is integrated and stored as 1-minute, 1-second and 50 ms time series of particle counts (number of particles detected each minute, each second, each 50 ms). Measurements of the electric field are performed with frequency 20 Hz; geomagnetic field and meteorological parameters – once a minute; cameras operate with frequency 30 Hz only when electric field strength exceeds a threshold value. When an amplitude of the atmospheric discharges exceeds the threshold the fast digital oscilloscope stores 1-second file with waveforms of atmospheric discharges. The data transfer from Aragats to Cosmic Ray Division (CRD) servers is performed each minute via fast radio-modems and is immediately assessable to users.

The detection efficiency of relativistic charged particle by plastic scintillator is ~99%. The detection efficiency of the neutral particle is proportional to the thickness of the scintillator, ranging from 1 to 20% for scintillators with the thickness from 1 - 20 cm. Detectors are located outdoors or indoors under a minimal amount of matter allowing registration of low energy particles. Lowest energies for neutral particles are ~ 0.4 MeV; for charged ~ 1 MeV. The lowest energy is ~ 0.4 MeV and ~ 1 MeV for neutral and charged particles, respectively.

The data acquisition (DAQ) system counts and stores all coincidences of the detector channel operation. For instance, the coincidence “100” of STAND1 detector denotes a signal in the upper detector only. This combination registered low-energy electrons with an efficiency of ~99%; for the outdoors location of STAND1 detector, the threshold energy is ~1 MeV. The gamma ray detection efficiency of this combination is 1-2%. The coincidence “010” selects mostly gamma rays as the probability to miss charge particle in the upper and bottom scintillators is ~ 0.01. The coincidence “111” means that all three layers register particles; the minimal energy of charged particles giving a signal in all three layers is above 10 MeV.

CUBE detector separates electron and gamma ray fluxes. The 1-cm thick scintillators surround two 20-cm-thick plastic scintillators. Both 20 cm thick and thin scintillators detect charged flux with a very high efficiency (~99%). Thick scintillators can also detect neutral flux with an efficiency of ~20%. The efficiency of detecting neutral flux by thin scintillators is below 2%. Thus, using the

coincidences technique, it is possible to purify the neutral flux detected by inside scintillators, rejecting the charged flux by the veto signals from surrounding thin scintillators. The count rates of two inner thick scintillators and of the surrounding 6 scintillators are measured and stored each minute. In this way we estimate electron fraction in TGE each minute. For the TGEs with a small fraction of electrons, we recover the energy spectra of gamma-ray flux by the network of 7 NaI spectrometers. Each minute the histogram of energy releases in each NaI crystal is stored and transferred to CRD database. During the off-line recovering of the energy spectra, we make energy-release- energy conversion using detector response simulation, taking into account bin-to-bin migration.

With installing a new fast electronics at Aragats (Pokhsrryan, 2016) it became possible to simultaneously investigate time series of the near-surface electric field, fast electric field waveforms of atmospheric discharges and particle fluxes on the millisecond time scale (Chilingarian et al., 2016). The TGE data is related to the atmospheric discharge measurements provided by networks of antennas and near surface electric field sensors located nearby particle detectors. Fast electronics provides GPS stamp on each registered event. The TGE events and lightning occurrences also are supported by measurements of the World Wide Lightning Location Network (WWLLN) and 30 Hz cameras making photos of the skies above Aragats during lightning occurrences.

3. TGE ABRUPTLY TERMINATED BY LIGHTNING: 28 JULY TGE

Spring-Summer on Aragats is the time of very strong thunderstorm activity. On 28 July 2016 large disturbances of the near surface electrostatic field began at 12:00 UT. A severe storm started ~1.5 hours later with numerous positive and negative lightning flashes. The atmospheric electricity sign convention (a downward-directed electric field change vector is considered positive) is used throughout this paper. The field change for negative lightning that lowers negative charge overhead is positive.

At 13:53 UT electrostatic field started to decrease; the same minutes all particle detectors located at Aragats station register enhancement of particle flux (TGE, Figure 1). A strong lightning at 13:56:34 UT terminated TGE. During 5 minutes of the large flux atmospheric pressure was 693 mbar; relative humidity – 90 %, wind speed 2-3 m/sec from ~340° N direction, temperature ~5.9 C°, no rain was registered. Solar radiation was very low, reaching minimum of ~11 W/m² during TGE event. During the maximal flux of TGE the electrostatic field was in negative domain reaching -24 kV/m at 13:56 UT.

We start the analysis of the 28 July TGE event by examining the pattern of correlated measurements of one-minute time series of the STAND1 detector and the disturbances of the electrostatic field at detector site (see Figure 1). From this initial pattern we can observe:

- Direct relation of TGE (sizeable particle fluxes registered by surface detectors) to negative electrostatic field measured at detector site;
- Presence of the negative nearby lightning during TGE; the change of the amplitude of electrostatic field exceeds 50 kV/m;
- Correlation of decreasing electrostatic field and enlarging particle flux;
- Start and rise of TGE occurred before the lightning flash;

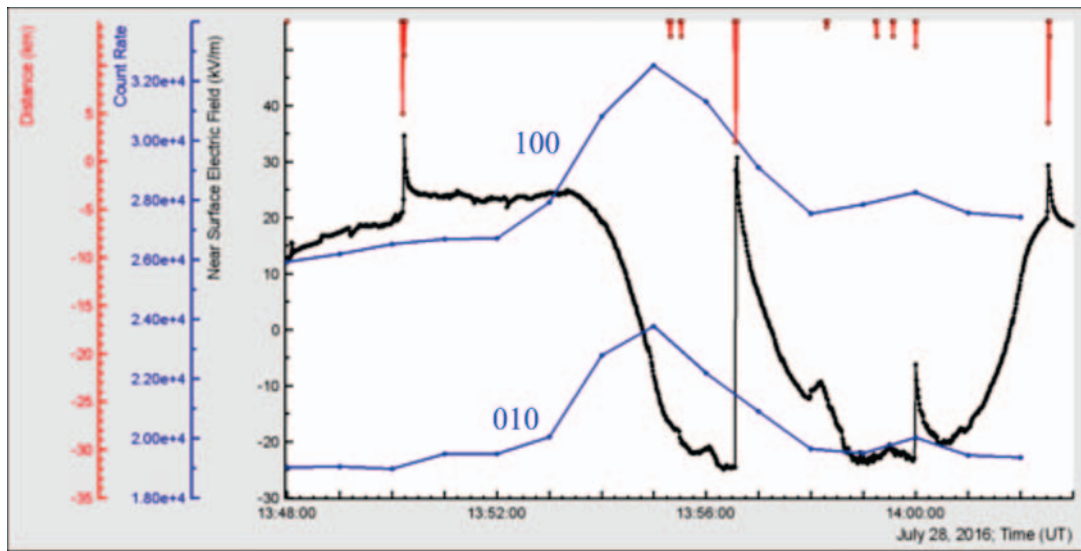


Figure 2. One-minute time-series of STAND1 detector: the count rate combinations 100 and 010 correspond to signals only from upper and middle scintillation detectors, respectively. Flux enhancement at 13:55-13:56 UT is $\sim 34\%$ (44σ). Electric field decreased from $+25$ kV/m at 13:53:25 UT to -24 kV/m at 13:55:25 UT. Distances to 4 nearby lightning flashes measured by the same EFM-100 device are 4.8, 1.9, 11.7, and 3.8 km from left to right, respectively. Other 6 lightning flashes shown in the top of picture occurred at distances more than 10 km.

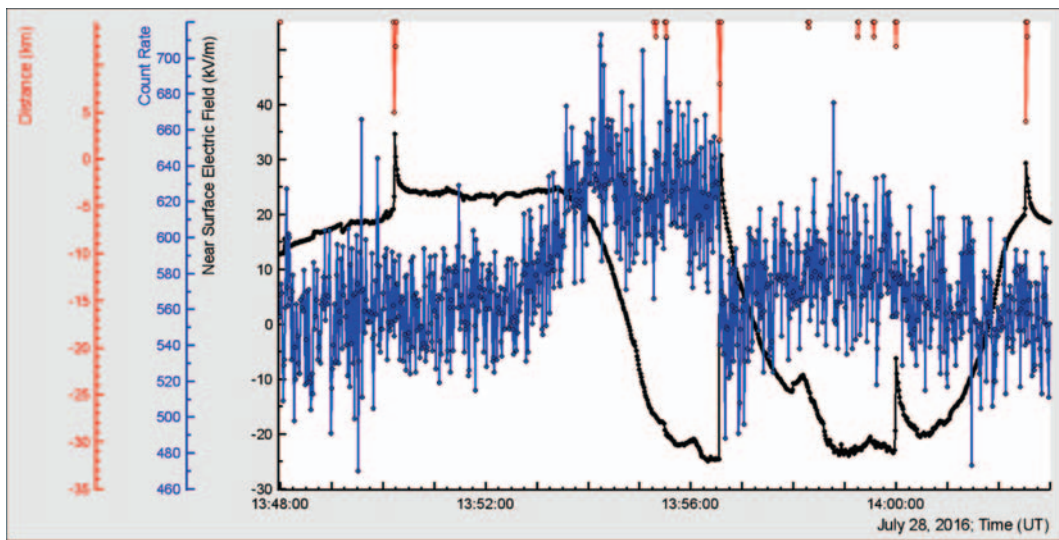


Figure 3. One second time series of 1 cm thick scintillator of STAND1 detector located nearby MAKET experimental hall. Negative lightning abruptly terminates TGE.

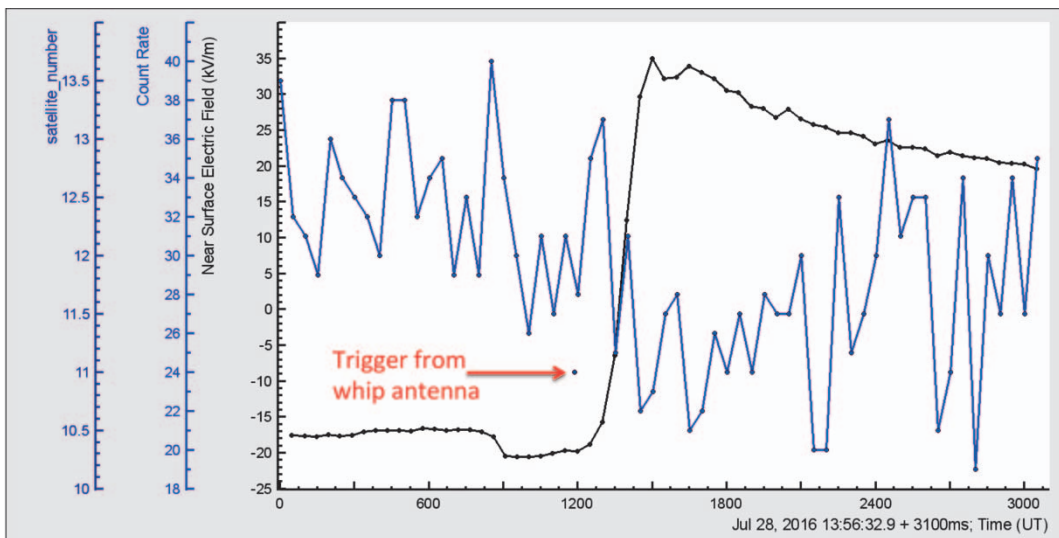


Figure 4. 50 ms time series of MAKET upper 1-cm thick scintillator count rate and electrostatic field. The time of trigger is denoted by a point occurred at 13:56:34.087 UT (calculated by 11 GPS satellites). WWLLN registered lightning at 13:56:34.087 UT. The electric field starts to rise ~ 50 ms after trigger, reaching maximum ~ 200 ms later; the amplitude of the electric field change is ~ 48.6 kV/m. Particle flux starts to decline at 13:56:34.2 UT.

Comparison of 2 time series of STAND1 detector allows to roughly estimate the fraction of electrons in TGE: if amplitudes of peaks of “010” (time series (mostly gamma rays) and “100” (gamma rays and low energy electrons) are more or less coinciding - the fraction of electrons is minimal.

Examining the second pattern with one-second time series (Figure 2) of the outdoors 1-cm thick plastic scintillator we see in much more details the fine structure of TGE.

- The particle flux from the cloud is not uniform on the second time scales, exhibiting several 1-second spikes and deeps during 2 minutes of maximal flux;
- Negative lightning abruptly terminates TGE; in one second starting at 13:56:33 the flux decreases from 654 to 541, that is, by 17.2%. After abrupt termination the flux starts to rise again although does not reach previous maximum;
- The electrostatic field recovery needs much more time ~ 2 minutes.

Next data pattern (Figure 3) includes 50 ms time series of the count rate of 1 cm thick plastic scintillator and disturbances of the electrostatic field, as well as the time of the trigger (shown by an arrow) produced by the signal from a commercial MFJ-1022 active whip antenna. After the trigger signal, which denotes the start of significant electromagnetic emission from lightning, digital oscilloscope generates a file with electric field waveforms produced by lightning (1 s record length, including 200 ms before trigger and 800 ms after trigger).

From this data analysis we can get the following information:

- The exact time of lightning flash reported by WWLLN is 13:56:34.087 UT (same as for the trigger). The 3 cm thick scintillator of STAND1 detector registered large EMI (induced by the lightning stroke) at 13:56:34.1 UT in good agreement with WWLLN time;
- Particle count rate decline occurs after the trigger at 11:56:34.2 UT simultaneously with start of rearrangement of electrostatic field;
- TGE decay started simultaneously with an abrupt increase of the near-surface electrostatic field. Therefore, the termination of TGE is directly connected to the rearranging of charged structures in the thundercloud, which is governed by lightning.

From the presented above patterns (Figs. 1-3), we can see how the RB/RREA process in thunderclouds is related to the disturbances of the electric field (including lightning flash) above particle detectors:

- Particle flux start to rise on declining of the electrostatic field and TGE reaches maximum on the minimum of the field strength;
- On the rising phase of TGE no lightning occurred before the particle flux was abruptly terminated by a strong negative lightning stroke. Lightning flash rise time was ~ 100 ms, recovery ~ 2 minutes;
- The rearrangement of the electric field in the cloud and particle flux decline occurred simultaneously the same time after lightning stroke.

To gain more insights into the avalanche processes in the cloud we measured the intensities of electron and gamma ray fluxes, as well as energy spectra of the gamma rays available from the variety of spectrometers on Aragats. To

select TGEs with small electron contamination we used thick plastic scintillators fully shielded by thin scintillators vetoing charge flux (see CUBE detector description in the attachment). Correcting the fluxes due to possible miscount of gamma rays and electrons caused by not 100% detection efficiency of the scintillators according to techniques described in (Chilingarian, Mailyan and Vanyan, 2012) we readily come to the intensities shown in Table 1. The intensities were recovered separately for 2 vertically stacked 20-cm thick plastic scintillators.

In Table 1 we show a large flux of the high-energy particles at 13:54-13:57 UT; at 13:58 UT the flux abruptly declines; electrons penetrate the CUBE detectors upper thick scintillator and are registered by the bottom thick scintillator within the interval of 13:55-13:56 UT. The high fraction of electrons in the lower thick scintillator is an indication of the intense RB/RREA process in the cloud above the detector. The ultimate check of the presence of the high-energy electrons and gamma rays in TGE is the energy spectra recovered by the network of NaI spectrometers extended up to 30 MeV (see Figure 4).

Table 1. Recovered intensities of the electrons and gamma rays of TGE for the upper and lower 20 cm thick scintillators.

	Upper scintillator			Bottom scintillator		
	e intensity (1/m 2min)	γ intensity (1/m 2min)	e/γ (%)	e intensity (1/m 2min)	γ intensity (1/m 2min)	e/γ (%)
28 July 2016						
13:52-13:53	69	1123	6*	55	425	13*
13:53-13:54	408	3363	12*	0	2172	0
13:54-13:55	460	23328	2.0	0	3524	-
13:55-13:56	992	15608	6.4	760	9532	8.0
13:56-13:57	92	8540	1.1	0	1500	-
13:57-13:58	0	772	-	0	460	-

* for the low intensities the estimate of electron fraction is unstable

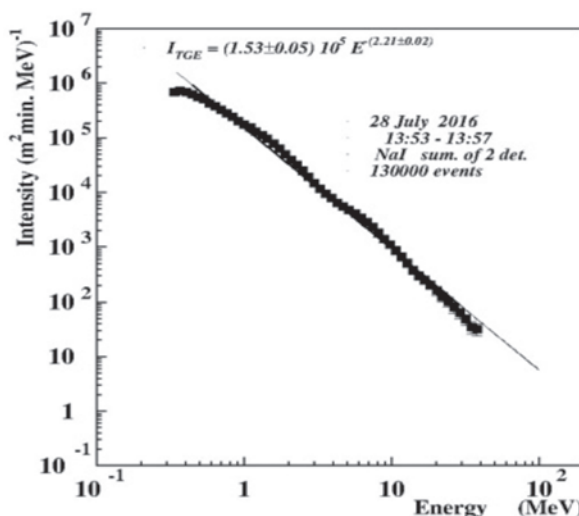


Figure 4. Energy spectrum of TGE extended up to 30 MeV measured by 2 NaI spectrometers

The sizes of NaI crystals are rather small (12 x 12 x 24 cm), and to have a statistically significant number of events in the highest energy bins of histogram we need to keep data collecting time not smaller than 1 minute. With 1 m² area 60 cm thick plastic scintillator we can lower the collecting time

down to 20 sec and register lower intensities, corresponding to highest energies. However, the 60 cm thick plastic scintillator comprises only 1.4 radiation lengths (RL); the thickness of the NaI crystal corresponds to 4.6 RL. Therefore, for the 60 cm thick scintillator we present only energy release spectra and do not recover energy spectra

From Figure 5 it is apparent that maximal energy particles had illuminated particle detectors randomly in the time span of 13:53 – 13:57 UT. Before the lightning occurred at 13:56:34 UT the energy release spectra were extended up to 20 MeV and more. After lightning, the intensity and maximal energy of gamma rays significantly decrease. In (Chilingarian et al., 2011) we have demonstrated that TGE is

a superposition of multiple runaway cascades initiated by the CR electron randomly entering strong electric field region in the cloud. We name such a cascade Extensive Cloud Showers (ECSs); (Gurevich et al., 1999) name it Micro Runway Breakdowns – MRB. On the minute time scale (Figure 1) we see a rather smoothed pattern of the TGE; when we turn to 1-second time scale (Figure 2) we see random fluctuations of the TGE intensity and recognize corresponding changes in the maximal energy (figure 5). RB/RREA is a random process dependent on the fast changing distribution of charge centers in the cloud, on atmospheric discharges, wind speed and other.

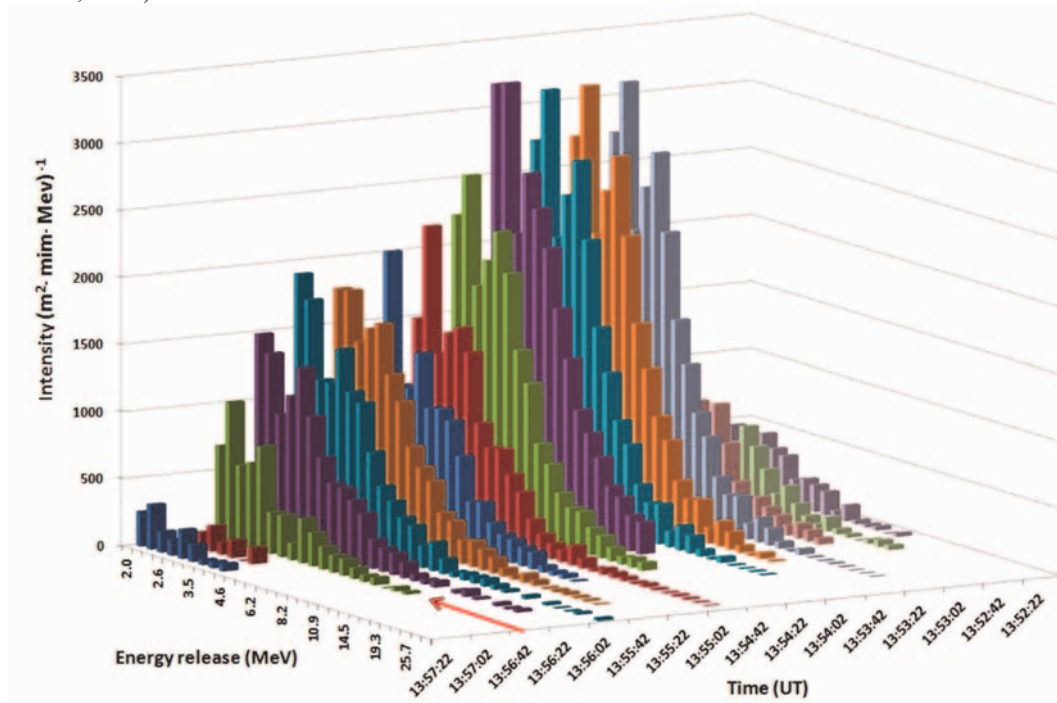


Figure 5. 3-dimensional histogram of the energy release measured by the 60-cm thick plastic scintillator during the time interval from 13:52:22 UT to 13:57:22 UT. The red arrow shows lightning occurred at 13:56:34.

From the recovered overall energy spectrum of TGE (Fig 4) and 20-second energy release spectra (Figure 5) showing the dynamic of changing particle fluxes we can conclude that:

- Maximal intensity of the TGE was observed at 13:54-13:56 UT;
- Recovered energy spectrum by the NaI crystal network demonstrate high-energy particle tail up to 30 MeV;
- Observations of the energy release histograms with 60 cm thick plastic scintillator outline different episodes of the high-energy emission;
- In the energy spectra measured after lightning, at 13:56:42-13:57:22 UT intensities abruptly declined and the highest energy particles vanished.
- The RB/RREE process was developed in the thundercloud and high-energy particles illuminate detectors in the time span of 13:54 – 13:56:34 UT, before the lightning stroke.

We analyzed largest TGE events of spring – summer 2016 mostly abruptly terminated by the lightning discharge, see Figure 6 and Table 2 (TGE data is available from the site <http://www.crd.yerphi.am/adei/>). In Figure 6 we show the TGE's occurred in June, the stormiest month of 2016. As we see from Figure 6 these TGEs share the common features of July 28 TGE. Particle flux increased when the electrostatic

field is in the negative domain; nearby lightning abruptly terminated TGE, after lightning flash the particle flux abruptly terminated and again started to increase (Fig 6, a,c,d). The TGE in Figure 6b smoothly decays after reaching maximum; distant lightning flashes, which occurred more than 10 km apart, do not terminate it.

In Table 2 we show all large TGEs of 2016. In the first column of Table 2 we post the date of the event; in second and third columns - the time of TGE start and time of reaching maximal flux and, and below in the same cells - corresponding values of the electrostatic field strength; in the fourth column - TGE significance in percent of increase related to pre-TGE count rate and in the number of standard deviations (the “100” combination of the STAND1 detector located nearby MAKET experimental hall was chosen as reference count rate); in the fifth– number of lightnings terminating TGE; in the sixth column - drop of TGE flux after lightning (if any); in the seventh – surge of near surface electrostatic field after lightning; in the eighth – distance to lightning estimated by EFM-100 electric mill; in the ninth – total duration of TGE; and in the tenth - maximal energy of differential energy spectra estimated by the network of NaI spectrometers. If two or more peaks are observed in the TGE we show in the Table the time of maximum and corresponding electrostatic field only for the first (usually largest) peak.

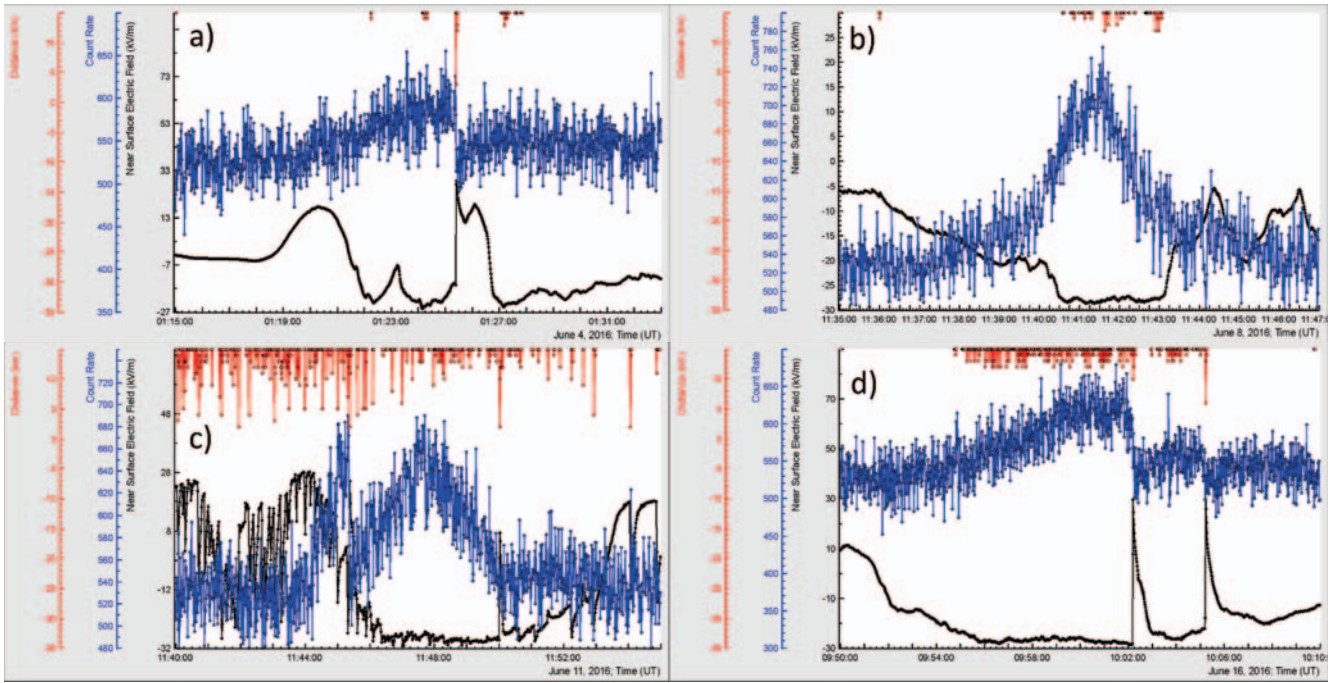


Figure 12. June TGEs abruptly terminated by nearby lightning (a, c, d) and – not terminated (b). The upper 1-cm thick plastic scintillator of STAND1 detector located nearby MAKET experimental hall measures one-second count rate. Electrostatic field and distance to lightning are measured and estimated by the EFM 100 electric mill located nearby GAMMA array.

Table 2. Characteristics of the TGE events detected in Spring-Summer 2016

Date	Start of TGE (UT) and el. field value kV/m	Time of maximum (UT) and el. field kV/m	TGE significance %/N of sigma 100 STAND1 MAKET	time (min)	Drop of flux %	Surge of el. field kV/m	EFM Dist. km	L.	Max. E MeV
28/04	18:19 -6.3	18:23 -13	20.6/22.6 18.5/20.5	4 5:30	13.2 15	60 71	1.9 1.9	2	50
4/05	18:57 -2.4	19:04 -12.3	45.7/56	7 8:30	27 14	54.5 52.5	1.9 2.9	2	40
10/05	14:07 -26	14:14 -29	24/32.6 16.5/22.3	7	29 15	58.5 50.1	7.9 7.9	2	40
12/05	13:40/-15	13:47/-29	13/27	7			10.8		50
15/5	02:21 15	02:27 -27	20.6/17	6 7:20	17.7 16.5	56 57.7	9.7 4	2	40
4/6	01:17/-3.3	01:25/-21.3	17.9/17.6	8	15.9	43.1	3	1	80
8/6	11:37/-15	11:42/-26.5	32.1/37	5			13		50
11/6	11:38 41	11:48 -27	26.2/36.7	10 15	19.2 9.5	51.6 36.1	1.8 1.9		10
16/6	1:53 -15	10:02 -26	18/28	9 12	25 11	57 53.3	9.6 5.8	2	40
28/7	13:50 4	13:55 -16	34/44	5	14.5	38.6	1.8	1	30

One-minute time series of the particle detectors with low energy threshold demonstrate huge enhancements equivalent to tens of standard deviations. The differential energy spectrum of gamma rays extends up to 40 MeV and beyond proving intense RREA process in the thundercloud above the detector site. The strong negative lightning is seen as an abrupt increase of the near-surface electrostatic field with an amplitude of ~ 50 kV/m and more; all observed lightning discharges that terminated TGE events at Aragats lowered the negative charge overhead. Only nearby lightning flashes (within 10 km) terminated TGE. Only in 2 events from 10, we do not register an abrupt decline of TGE flux and nearest lightning flashes for these events were at distance more than 10 km. In 8 events from 10 nearby lightning abruptly terminated TGE.

For our conclusion on the lightning initiation, we use the only small subsample of lightning flashes in the observed storm (flashes terminating particle flux). TGE is a rather rare transient process depending on the coincidence of several random parameters of the electrified atmosphere. The size of the radiation-emitting region in thundercloud is 500-1000 m (Torii, 2012, Chilingarian, 2013) and only by chance this region for several minutes is positioned above the particle detectors. Our particle detectors are not positioned in some specially selected area, as in beam experiments with man-made accelerators. Only by chance the strength of electric field can exceed the RB/RREA initiation threshold in the cloud just above this region. Another key parameter is a vertical extension of the electric field, which must be long enough to provide necessary potential drop. Thundercloud, as well, should be low enough above earth's surface; in other

4. DISCUSSION AND CONCLUSION

Several severe storms were accompanied with intense particle fluxes observed by facilities of Aragats Space environmental Center. By examining TGE events we see that before lightning the intensity of the RB/RREA reaches maximal value and maximal energy of avalanche particles reach 40 MeV and more. After lightning, we detect an abrupt decrease of particle flux caused by the removal of high-energy particles. All these processes occurred within few hundreds of millisecond. All observed TGE-terminating lightning flashes lowered negative charge overhead. Therefore, we can connect by causal relation the RB/RREA process and the lightning initiation, i.e. RB/RREA process in the thundercloud serves as a trigger to the negative lightning.

cases, the electron-gamma ray avalanche will be faded in the air. However, if RREA initiation conditions are fulfilled somewhere in the huge thundercloud, RREA process will be unleashed (see Fig.7). The group from Langmuir Laboratory in central New Mexico during balloon flights on 3 July 1999 measured the maximal field of 1.86 kV/cm (130% of the threshold for a runaway process) at 5.77 km altitude just before nearby lightning flashes (Marshall et al., 2005). Authors conclude that runaway breakdown avalanches have initiated lightning flashes.

So, both our measurements based on particle beam (TGE) detection terminated by a lightning flash and *in situ* measurements of an intracloud electric field along with lightning discharges detection prove that RB/RREA is an apparent mechanism for the initiation of the negative lightning flashes.

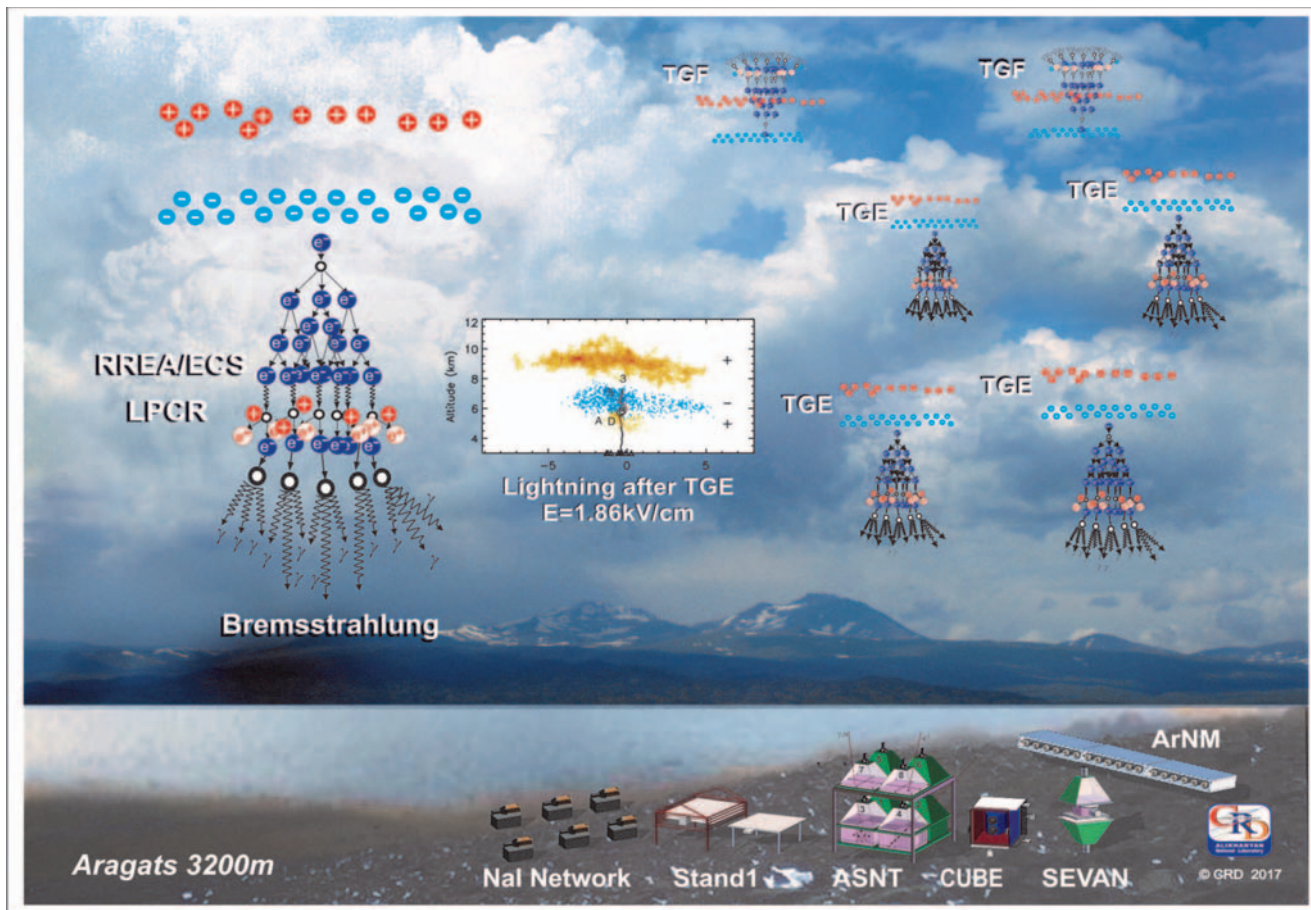


Figure 13. Cartoon of TGE, TGF and lightning initiation above Aragats station. Radar pattern of the charge regions and lightning strokes detected by lightning mapping array are captured from the Figure 1 of (Marchall et al, 2005)

The following scenario of the lightning initiation can be suggested:

1. In the thunderstorm cell randomly emerge extended regions of enhanced electric field with conditions allowing RB/RREA process (for instance electric field of 1.8 kV/cm on 4-6 km heights and ~ 1 km extension); these regions are randomly distributed in the cloud and are continuously moved due to rather strong wind on 4-6 km heights.
2. At the same heights, the flux of secondary cosmic ray (CR) electrons with energies appropriate for the runaway regime (100 KeV - 2 MeV) is significantly high - several thousands of particles per ($s \sim m^2$). These CR seed electrons entering high electric field regions unleash the RB/RREA process producing large particle fluxes.
3. *Charged particles create a random pattern of ionization in a huge 3-dimension storm cell. Due to some, yet unspecified stochastic mechanism (for an example of such a process, see, Iudin 2017) in some place in the cloud a discharge occurred, stopping TGE and initiated lightning.*
4. Due to working charging machine in the cloud at another time in another place points 1-3 will be repeated as a storm prolonged (see Fig.7).

ACKNOWLEDGEMENT

The authors thank the staff of the Aragats Space Environmental Center for the uninterrupted operation of Aragats research station facilities. The data for this paper are available via the multivariate visualization software ADEI on the WEB page of the Cosmic Ray Division (CRD) of the Yerevan Physics Institute, <http://adei.crd.yerphi.am/adei>. One of the authors (AC) is thankful to E.Mareev, D.Yudin, and V.Rakov for useful discussions and valuable comments. The expedition to Aragats high altitude station was supported by the Armenian government grant N13-1C275.

REFERENCE

- Alexeenko V.V., Khaerdinov N.S., Lidvansky A.S., and Petkov V.B., 2002. Transient Variations of Secondary Cosmic Rays due to Atmospheric Electric Field and Evidence for Pre-Lightning Particle Acceleration, *Physics Letters A*, 301, 299-306.
- Chilingarian, A., Arakelyan, K., Avakyan, K. et al., 2005, Correlated measurements of secondary cosmic ray fluxes by the Aragats space-environmental center monitors, *Nucl. Instrum. Methods A* 543 (2-3) 483.
- Chilingarian, A., A. Daryan, K. Arakelyan, A. Hovhannisyanyan, B. Mailyan, L. Melkumyan, G. Hovsepyan, S. Chilingaryan, A. Reymers, and L. Vanyan L., 2010. Ground-based observations of thunderstorm-correlated fluxes of high-energy electrons, gamma rays, and neutrons, *Phys. Rev. D*, 82, 043009.
- Chilingarian, A., Hovsepyan, G., Hovhannisyanyan, A., 2011. Particle bursts from thunderclouds: natural particle accelerators above our heads. *Phys. Rev. D: Part. Fields* 83 (6), 062001.
- Chilingarian, A., Mailyan, B., Vanyan, L., 2012. Recovering of the energy spectra of electrons and

gamma rays coming from the thunderclouds. *Atmos. Res.* 114-115, 1-16.

A. Chilingarian, N Bostanjyan, T Karapetyan, On the possibility of location of radiation-emitting region in thundercloud, *Journal of Physics: Conference Series* 409 (2013) 012217.

Chilingarian A., Thunderstorm Ground Enhancements - model and relation to lightning flashes, 2014. *Journal of Atmospheric and Solar-Terrestrial Physics* 107 68-76.

Chilingarian A., Chilingaryan, S., and A. Reymers, 2015. Atmospheric discharges and particle fluxes, *J. Geophys. Res. Space Physics*, 120, doi:10.1002/2015JA021259.

Chilingarian A., Hovsepyan G., Khanikyanc G., Reymers A. and Soghomonian S., 2015. Lightning origination and thunderstorm ground enhancements terminated by the lightning flash, *EPL*, 110, 49001.

Chilingarian A., Khanikyanc G., Kozliner L. and Soghomonian S., 2016. Fast electric field waveforms and near-surface electric field images of lightning discharges detected on Mt. Aragats in Armenia, *Proceedings of TEPA 2015*, Nor Amberd, Tigran Metz,

A. Chilingarian, G. Hovsepyan, L. Kozliner, Extensive Air Showers, Lightning, and Thunderstorm Ground Enhancements, *Astroparticle Physics* 82 (2016) 21-35

Dwyer J.R., Uman M.A., 2013. The physics of lightning, *Physics Reports Phys. Rep.*, 534(4), 147-241.

Dwyer, J.R., A fundamental limit on electric fields in air. *Geophys. Res. Lett.* 30 (20), 2055, (2003).

Iudin D.I., 2017. Lightning preparation process as a noise induced kinetic transition, accepted for publication in *Radiophysics (Russ)*.

Gurevich A.V., Milikh G.M. and Rouseel-Dupre R., 1992. Runaway electron mechanism of air breakdown and preconditioning during a thunderstorm, *Physics Letters A* 1992, v.165, pp.463 - 468.

Gurevich A.V., Zybin K.P., Roussel-Dupre R.A., Lightning initiation by simultaneous of runaway breakdown and cosmic ray showers, *Phys. Lett. A* 254 (1999) 79.

Kuroda Y., Oguri S., Kato Y., et al., Observation of gamma ray bursts at ground level under the thunderclouds, *Physics Letters B* 758 (2016) 286-291.

Kelley N.A., Smith D.M., Dwyer J.R., et al. 2015. Relativistic electron avalanches as a thunderstorm discharge competing with lightning, *Nature communications*, 6, Article number: 7845, DOI: 10.1038/ncomms8845.

Khaerdinov N.S., Lidvansky A.S., 2005. Cosmic rays and the electric field of thunderclouds: Evidence for acceleration of particles (runaway electrons), *Atmospheric Research* 76, 346-354

Kollarik M., Kudela K., Langer R., Strharsky I., 2016. First results from the measuring equipment SEVAN on Lomnický štít and possible connections with

atmospheric phenomena, Proceedings of TEPA 2015, Nor Amberd, Tigran Metz, 2016, 31-34.

Marshall T.C., Winn W.P., Measurements of charged precipitation in a New Mexico thunderstorm: lower positive charge centers, J. Geophys. Res. D ^[1]_{SEP}87 (1982) 7141–7157. ^[1]_{SEP}

Marshall, T. C., Stolzenburg, Maggio C.R., Coleman L.M. (2005), Observed electric fields associated with lightning initiation, Geophys. Res. Lett., L03813.

Pokhsranyan D., 2016. Very fast Data Acquisition system based on NI-my RIO with GPS time stamping capabilities, Proceedings of TEPA 2015, Nor Amberd, Tigran Metz, 2016, 23-27.

Torii, T., Sugita, T., Kamogawa, M., et al., 2011. Migrating source of energetic radiation generated by thunderstorm activity. Geophys. Res. Lett. 38, L24801.

Tsuchiya H., Enoto T., Iwata K., et al., 2013. Detection of high-energy gamma rays from winter thunderclouds, Phys. Rev. Lett., 111, 015001.

Wilson, C.T.R., The acceleration of b-particles in strong electric fields such as those of thunderclouds. Proc. Cambridge Philos. Soc. 22, 534 (1925).

add ~15 % difference to the particle detector count rates. A significant amount of substance above the sensitive volume of NaI crystals (0.7 mm of roof tilt, 3 mm of aluminum, and 5 mm of MgO) prevents electrons with energy lower than ~3 MeV from entering the sensitive volume of the detector. Thus, the network of NaI spectrometers below 4 MeV can detect gamma rays only.

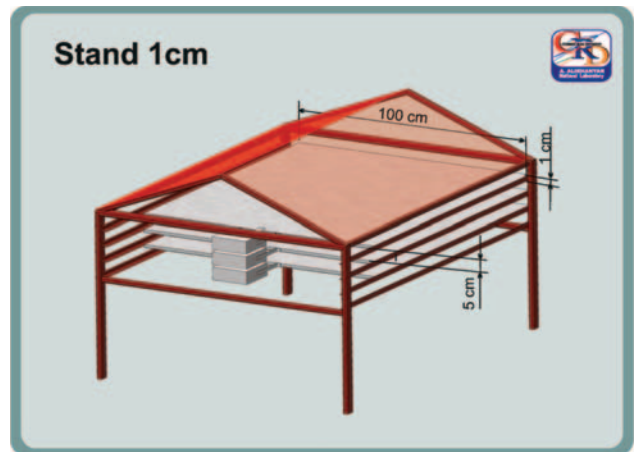


Figure 5. STAND1 detector consisting of three layers of 1-cm-thick scintillators.

APPENDIX

The “STAND1” detector is comprised of three layers of 1-cm-thick, 1-m² sensitive area scintillators fabricated by the High Energy Physics Institute, Serpukhov, Russian Federation; see Figure 8. The light from the scintillator through optical spectrum-shifter fibers is reradiated to the long-wavelength region and passed to the photomultiplier (PMT FEU-115M). The maximum of luminescence is emitted at the 420-nm wavelength, with a luminescence time of about 2.3 ns. The STAND1 detector is tuned by changing the high voltage applied to the PMT and by setting the thresholds for the shaper-discriminator. The discrimination level is chosen to guarantee both high efficiency of signal detection and maximal suppression of photomultiplier noise.

The detector network measuring particle energy consists of 4 NaI crystal scintillators packed in a sealed 3-mm-thick aluminum housing. The NaI crystal is coated by 0.5 cm of magnesium oxide (MgO) by all sides (because the crystal is hygroscopic) with a transparent window directed to the photo-cathode of an FEU-49 PMT, see Figure 3. The large cathode of PMT (15-cm diameter) provides a good light collection. The spectral sensitivity range of FEU-49 is 300–850 nm, which covers the spectrum of the light emitted by NaI(Tl). The sensitive area of each NaI crystal is ~0.0348 m², the total area of the four crystals is ~0.14 m², and the gamma-ray detection efficiency is ~80%. A logarithmic analog-digit converter (LADC) is used for the coding of PM signals. Calibration of LADC and code-energy conversion was made by detecting the peak from exposed ¹³⁷Cs isotope emitting 662 keV gamma rays and by the high-energy muon peak (55 MeV) in the histogram of energy releases in the NaI crystal. The PMT high voltage was tuned to cover both structures (peaks) in the histogram of LADC output signals (codes) and to ensure linearity of LADC in the energy region of 0.4–60 MeV. The count rate of a particle detector depends on the chosen energy threshold of the shaper-discriminator, the size of the detector, and the amount of matter above it. The inherent discrepancy of the parameters of PMTs also can

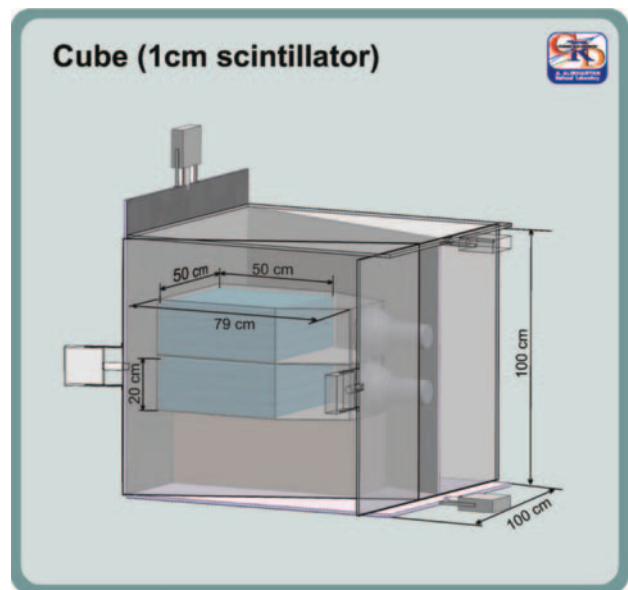


Figure 6. CUBE detector. Six 1-cm thick scintillators are used as a veto system for the charged particles. Inner two 20 cm thick scintillators detect both charged and neutral fluxes.

A 52 cm diameter circular flat-plate antenna was used to record the wideband electric field waveforms produced by lightning flashes. The antenna was followed by a passive integrator the output of which was directly connected with a 60 cm double-shielded coaxial cable to a Picoscope 5244B digitizing oscilloscope. The oscilloscope was triggered by the signal from a commercial MFJ-1022 active whip antenna that covers a frequency range of 300 kHz to 200 MHz. The record length was 1 sec including 200 ms pre-trigger time and 800ms post-trigger time. The sampling frequency was 25 MS/s, and the amplitude resolution was 8 bit. The trigger-out pulse of the oscilloscope was relayed to the NI myRIO board which produced the GPS time stamp of the record (detailed description of our fast data acquisition system based on the NI myRIO board can be found in Pokhsranyan D., 2016).

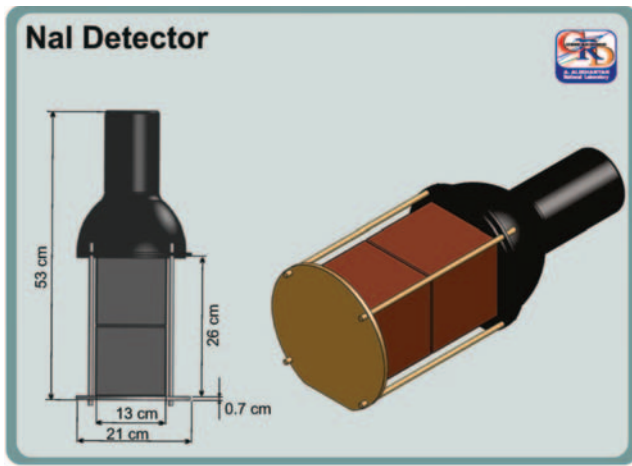


Figure 7. NaI(Tl) crystal assembly.

The near-surface electrostatic field changes were measured by a network of six field mills (Boltek EFM-100), four of which were placed in Aragats station, one in Nor Amberd station at a distance of 12.8 km from Aragats, and another one in Yerevan station at a distance of 39.1 km from Aragats. The electrostatic field measurements were taken with an interval of 50 ms. Lightning optical images were captured by a video camera at a frame rate of 30 frames/s. We used also data from the World Wide Lightning Location Network (WWLLN) which detects very low frequency (VLF, 3-30 kHz) emissions from lightning. Boltek's EFM-100 electric mill also provides estimates of the distance to lightning.

In Situ Measurements of the Runaway Breakdown (Relativistic Runaway Electron Avalanche) on Aragats: Experimental Data and Models A.

A. Chilingarian¹, S. Chilingaryan¹, G. Hovsepyan¹, L. Kozliner¹, B. Mailyan²

Yerevan Physics Institute, 2 Alikhanyan Brothers, 0036, Yerevan, Armenia

Abstract . Acceleration and multiplication of the cosmic ray electrons by strong electric fields in the thundercloud are well-established phenomena comprising the core of the atmospheric high-energy physics. However, the origin and location of charged centers in the thundercloud (one of the most important aspects of the atmospheric physics) and conditions for unleashing the particle cascades in the atmosphere are not clear until now. The majority of experimental data on particle acceleration in the thunderclouds comes from space-born experiments detecting Terrestrial Gamma flashes (TGFs) and from networks of particle detectors located on the earth's surface observing Thunderstorm Ground Enhancements (TGEs). Models for explaining both TGF and TGE are based on the concept of a “runaway” electrons introduced by A. Gurevich. Prove of these models includes registration of the avalanches from the cosmic ray “seed” electrons entering the region of the strong electric field in the thundercloud. We present direct measurements of such an avalanches lasting less than a microsecond; hundreds of such avalanches comprise a TGE lasting few minutes. Our measurements prove that for explaining the TGE it is not necessary to invoke the relativistic feedback discharge model (RFDM) used for the TGF modeling.

1. INTRODUCTION

The high-energy physics in the atmosphere is a new emerging scientific field dealing with electromagnetic cascades originated in the thunderstorm atmospheres. The initial name of the cascade released by a runaway electron—the Runaway breakdown (RB, given by Gurevich et al., 1992), is recently often replaced by the term RREA (Relativistic Runaway Electron Avalanches, Dwyer, Smith, and Cummer, 2012; Dwyer and Uman, 2013). However, the origin and location of charge centers in the thundercloud (one of the most important aspects of the atmospheric physics) are not clear until now. In fair weather conditions, the atmosphere is positively charged and the Earth has an opposite-polarity negative charge. A thunderstorm drastically changed the pattern of the atmosphere electrification. The top layer of the thundercloud has a positive charge with a negative screening layer just above it; the middle layer has a negative charge and a small local region of positive charge usually emerges in the bottom of the cloud (a lower positive charge region – LPCR (Stolzenburg et al., 1998, Chilingarian and Mkrtchyan, 2012). If we use the so-called “physics” sign convention (see discussion of the used sign conventions in Krehbeil et al., 2014), then the near- surface electrostatic field is negative during fair weather (positive ions slowly migrate from the atmosphere to the Earth) and - positive during thunderstorms (electrons are transported by the lightning from the cloud to the Earth). According to the tripole model (quadruple, if we add a negative screening layer above the main positive layer), there are several dipoles of opposite orientation in the cloud, which accelerate electrons downward, in the direction of the Earth and - towards the open space.

Gurevich et al. (1992) showed that when Møller scattering (electron–electron elastic scattering) is considered the runaway electrons would undergo avalanche multiplication, resulting in a large number of relativistic runaway electrons and gamma rays for each energetic seed electron injected into the strong electrical field region. Seed electrons belong to steady population (specific to the height in the atmosphere, latitude, and longitude of detection site) of the secondary cosmic rays, a product of numerous small and large cascades initiated in the atmosphere by copious

protons and fully stripped nuclei accelerated in the Galaxy and bombarded terrestrial atmosphere with a rather stable intensity (Extensive Air Showers – EASs).

Further development of the theoretic knowledge on the runaway process continued with intensive implementations of the Monte Carlo simulation. Sophisticated codes were used to model the propagation of energetic electrons in electric fields (Lehtinen et al., 1999; Babich et al., 2001; Dwyer, 2003, 2007, 2012). The runaway process is naturally embedded in simulations: when you switch on the appropriate electrical field and use incident cosmic ray electron flux as seeds; the electrons gain energy from the field, knock-off atomic electrons and cascade process develops in the atmosphere. Very popular, relativistic feedback discharge model (RFDM, Dwyer, 2003, 2012) was used for explaining Terrestrial Gamma flashes (TGFs, Fishman, 1994, Briggs et al., 2011). When the large-scale electric field in the cloud become relatively high (approaches the relativistic feedback threshold) the backward propagating positrons and backscattered X-rays generate new avalanches. Therefore, according to this model, the avalanche becoming self-sufficient and can prolong until the conditions for the feedback are still effective.

The most difficult and most important part of the model validation is the comparison of competitive hypotheses with the measurements. The high-energy atmospheric physics (HEAP) includes 2 main sources of the experiential data: Terrestrial Gamma Flashes (TGFs) - brief burst of gamma radiation (sometimes also electrons and positrons) registered by the orbiting gamma ray observatories in the space and Thunderstorm ground enhancements (TGEs) -the prolonged particle fluxes registered on the ground level. The central engine initiated TGF and TGE is believed to be RB/RREA mechanism accelerated seed electrons in the terrestrial atmosphere up to 40-50 MeV. The *in situ* observation of numerous TGEs during strong thunderstorms on Aragats resulting in the first simultaneously measured differential energy spectra of TGE electrons and gamma rays (Chilingarian et al., 2010). Further measurements of the gamma ray energy spectra by the network of NaI spectrometers allow to reliably extending energy range of the “thunderstorm” gamma rays up to 100 MeV (Chilingarian et al., 2013) due to another “thunderstorm” gamma

ray production mechanism - MODification of the electron energy Spectrum (MOS, Chilingarian, Mailyan and Vanyan, 2012). The measurements performed on Aragats allow formulating a comprehensive model of TGE (Chilingarian, 2014).

TGFs and TGEs share many common features, as they are results of RREA. The drastic time difference (minutes for TGE and hundred of microseconds for TGF) is not essential because prolonged TGEs are nothing more than a superposition of the short nanosecond scale avalanches, which Aragats group has named Extensive cloud shower (ECS), and Alex Gurevich et. al., Micro runaway breakdown (MRB).

There exist numerous papers on simulations of particle cascades in the atmosphere, but very few of them contain comparisons with experimentally measured parameters. The goal of our paper is to present experimental data in the form that allows validation of the models. We analyze in details the largest TGE event from 19 September 2009 and compare the time distribution of the ECSs with expected results from RDFM and TGE models.

2. INSTRUMENTATION

The Aragats Solar Neutron Telescope (ASNT, previously intended to measure neutrons coming from violent solar flares) is formed from 4 separate identical modules, as shown in Figure 1. Each module consists of forty $50 \times 50 \times 5 \text{ cm}^3$ scintillator slabs stacked vertically on a $100 \times 100 \times 10 \text{ cm}^3$ plastic scintillator slab. Scintillators are finely polished to provide good optical contact of the assembly. The slab assembly is covered by the white paper from the sides and bottom and firmly kept together with special belts. The total thickness of the assembly is 60 cm. Four scintillators of $100 \times 100 \times 5 \text{ cm}^3$ each are located above the thick scintillator assembly to indicate charged particle traversal and separate the neutral particles by “vetoing” charged particles (the probability for the neutral particle to give a signal in 5 cm thick scintillator is much lower than in 60 cm thick scintillator). A scintillator light capture cone and Photo Multiplier Tube (PMT) are located on the top of the scintillator housings.

The main ASNT trigger reads and stores the analog signals (PMT outputs) from all 8 channels if at least one channel reports a signal above threshold. The frequency of triggers is $\sim 4 \text{ KHz}$ due to incident Secondary cosmic rays (SCR) – products of the interaction of galactic cosmic rays with atmosphere; on 3200 m height on Aragats, the intensity of SCR is $\sim 500 / \text{m}^2/\text{sec}$. The flux of particles from thundercloud (TGE) can be 5 times larger than SCR (background) intensity.

The list of available information from ASNT is as follows:

1. 2 second time series of count rates of all 8 channels of ASNT (the integration time of the scintillator counts is 2 seconds);
2. Count rates of particles arriving from the different incident directions: 16 possible coincidences of 4 upper and 4 bottom scintillators;
3. Count rates of the 8 special coincidences, for instance, 1 signal from the upper scintillators and 1 signal from the lower ones, or no signals in upper, and more than 1 signal in the lower, etc.;
4. Estimates of the variances of count rates of each ASNT channel, variances are calculated by 12 five-second counts, i.e. in a minute 12 times (each with 5 sec

integration time) all channel counts are stored; then with stored values the means and variances are calculated;

5. 8×8 correlation matrix of ASNT channels calculated by five-second count rates in 1 minute; with same stored values of the 5-sec time series each minute the correlation matrix is calculated to monitor possible cross-talk of channels;
6. Each minute (after 07.2012, each 20 second) the histograms of the energy releases in all 8 channels of ASNT are stored;
7. The same as in the previous point, but only for particles that do not registered in the upper layer (veto on charged particles to select samples enriched by neutral particles);

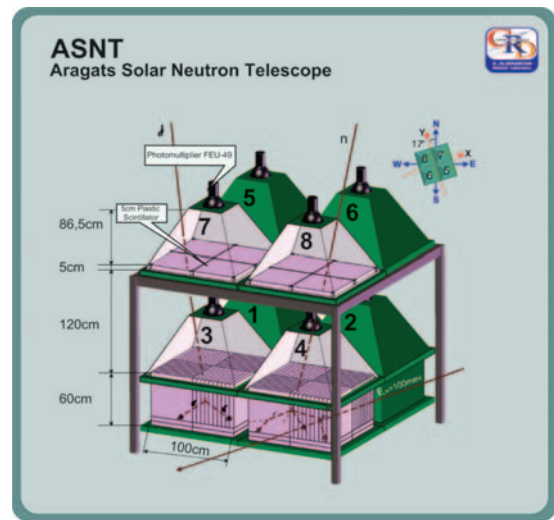


Figure 1. Assembly of ASNT with the enumeration of 8 scintillators and orientation of detector axes relative to the North direction.

A big advantage of ASNT is additional, so called, software triggers, exploiting the information on the energy releases in scintillators. The software triggers are not fixed in electronics and it is possible to add or change them very flexible.

For instance, one of the software triggers used along last 10 years is the selection of the muons traversing the 5 cm thick scintillators horizontally ($0 - 0.5$ degrees). The energy release of such an event should exceed 200 MeV due to a large path of muon in the scintillator. To avoid EAS contamination the condition of horizontal muon selection is the absence of signals in the thick scintillators below

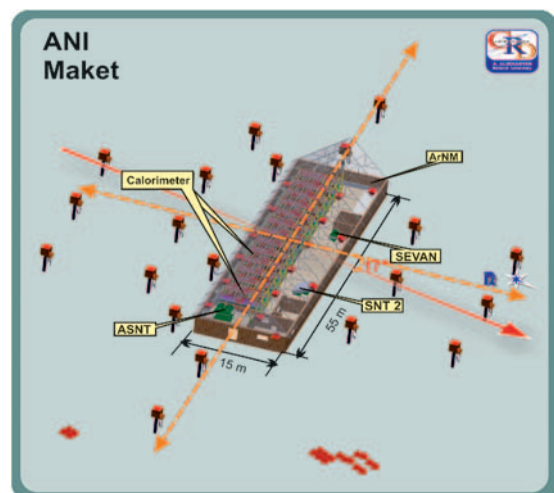


Figure 2. MAKET-ANI Extensive Air Shower (EAS) array

The MAKET-ANI surface array (Figure 2) consists of 92 five cm thick plastic scintillators covering 10,000 m² to measure EAS particles. 24 of them have 0.09 m² area and 68 have 1 m² area. Logarithmic Analog to Digital Converters (ADC) and Constant Fraction Discriminators (CFD) are placed just above the PMT in the light-tight iron boxes. The dynamic range of the registered particle number is $\sim 5 \times 10^3$. During multiyear measurements, the detecting channels were continuously monitored. Data on background cosmic ray spectra was collected for each detector. The slope of the spectra was used for detector calibration. The slope of the background spectra is a very stable parameter, which did not change even during very severe Forbush decreases (abrupt changes of cosmic ray flux intensity due to solar activity) when the mean count rates can decrease as much as 20%.

After publishing the final results of the MAKET-ANI experiment (Chilingarian et al., 2007) the research of high-energy galactic cosmic rays was stopped. Around the ASNT detector was arranged new array consisted of 16 scintillators, which registered EAS events that triggered 8

and all 16 scintillators within a time window of 1 microsecond.

3. *IN SITU* MEASUREMENTS OF THE RB/RREA PROCESS ON ARAGATS

The first observation of the avalanches initiated by the runaway electrons was made at Aragats in 2009 (Chilingarian et al., 2010). MAKET and ASNT detectors (Figs 1 and 2) were used for the *in situ* detection of RB/RREA process in the thundercloud above detector site. In Figure 3, we present the particle abrupt surge observed in the 1-minute time series of ASNT detector on 19 September. This TGE is the one of two largest ever observed on Aragats. On 22:47 the upper scintillators registered 108% enhancement corresponding to 270 standard deviations from the mean value (270σ); the bottom scintillators registered 16% enhancement (60.7σ); the near-vertical flux (coincidences 3 - 7, 5 - 1, 6 - 2, 8 - 4) enhanced by 11.2% (16.8σ). The flux started slow surge, then rockets in 3 minutes to the maximal value and decays in 4 minutes.

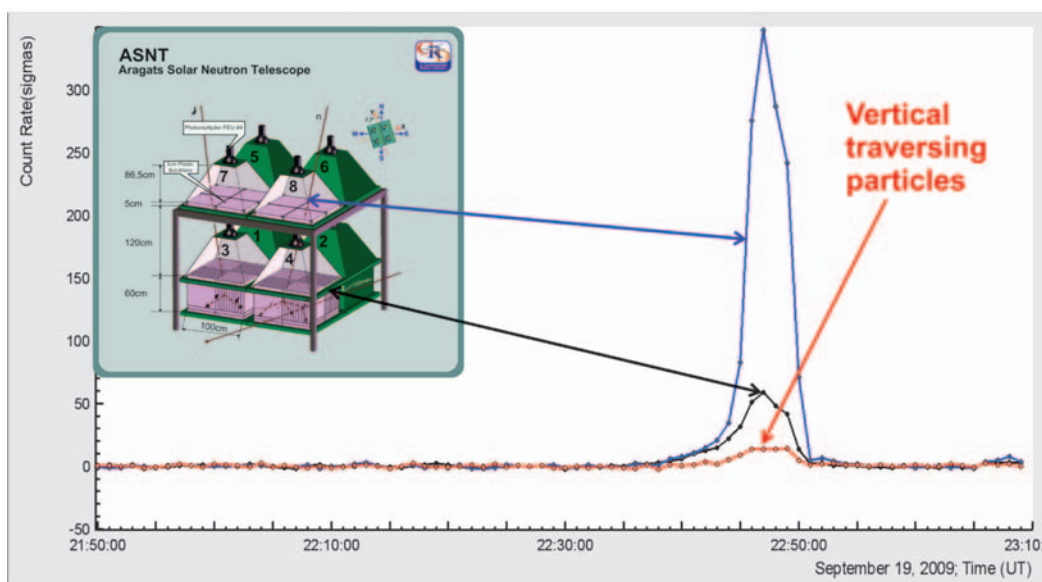


Figure 3. “Significance” of TGE in the number of standard deviations from the mean value of 1-minute time series of count rate. Top curve corresponds to upper scintillators, middle – to lower and the bottom – to vertical particle transition through both scintillators.

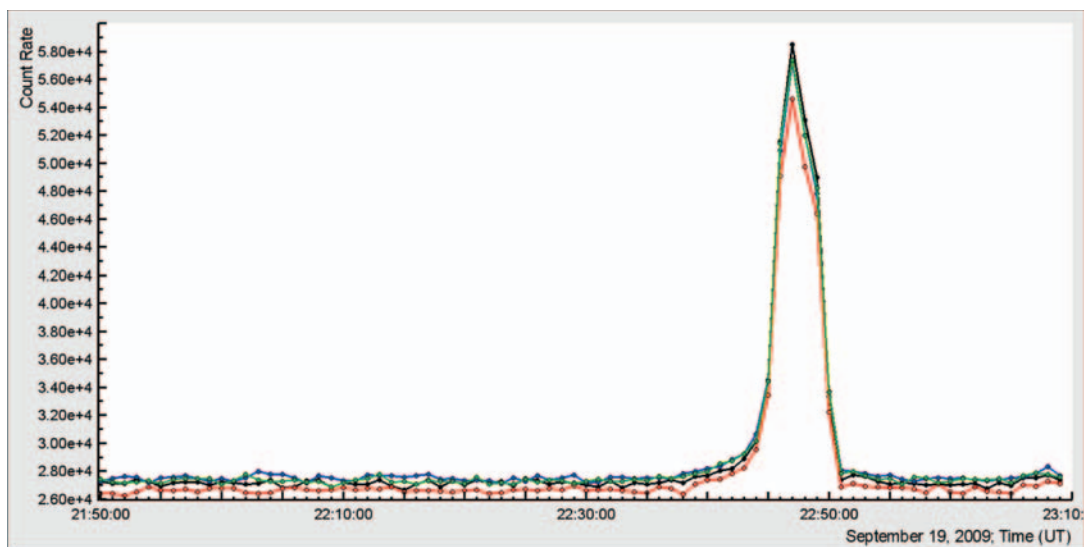


Figure 4. Particle flux enhancement as measured on 19 September 2009 by four 5 cm thick 1 m² area plastic scintillators on top of ASNT detector (Figure 1); energy threshold ~ 7 MeV.

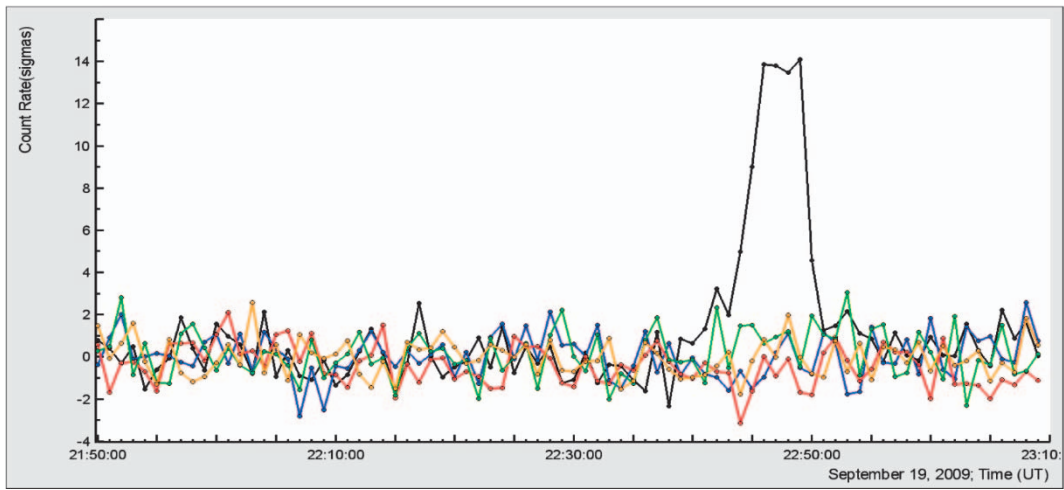


Figure 5. The additional count rate of particles coming from different directions. The 4 minute peak is formed by particles coming from the vertical direction ((coincidences 3 - 7, 5 - 1, 6 - 2, 8 - 4); the particles coming from the inclined directions other combinations of coincidences of upper and lower scintillators, do not show any enhancement

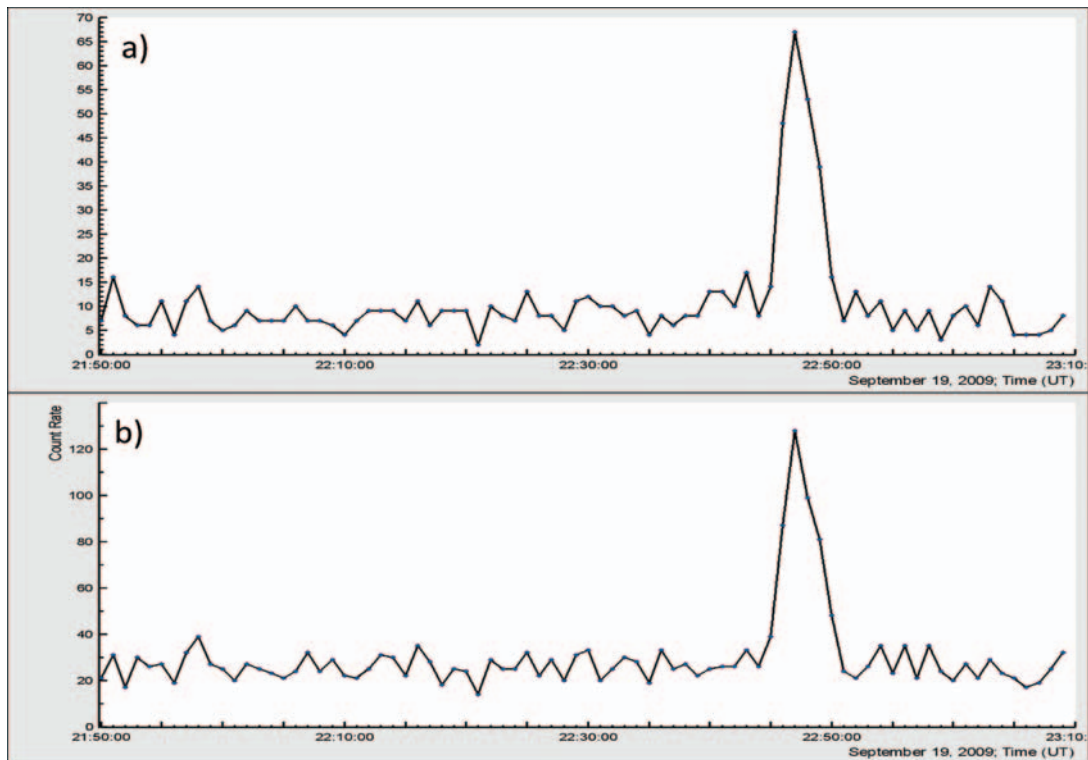


Figure 6. 8 and 16-fold coincidences in the channels of MAKET surface array

In Figure 4 we show rather uniform registration of the particle flux enhancement by the 4 identical 5 cm thick plastic scintillators. Small differences in the count rates are explained by the PMT individual variation. Registered TGE particles flux was rather large $\sim 30,000$ per min per m^2 .

Thus, we observe continuous, several minutes long particle flux. This flux cannot be associated with an active solar event (there was no such an event registered by the gamma ray and X-ray sensors on board of Space Weather monitoring satellites) and with Extensive Air Showers (EAS, only one additional count will be registered on traversal of thousands of EAS particles in a few tens of nanosecond).

Consequently, we decide that it was a particle flux of the atmospheric origin. First of all, we check the direction of incoming particles. As one can see in Figure 5 particles come from near-vertical direction coinciding with the direction of the vertical electric field in the thundercloud.

Another evidence of “thunderstorm” origin of particle flux comes from MAKET array’s 16 and 8-fold

coincidences within trigger window of $1 \mu\text{sec}$ (Figure 6 a and b). The abrupt enhancement the coincidences occurred the same minutes when the flux of particles surges. We observe $\sim 730\%$ enhancement of the 16-fold coincidences, corresponding to $\sim 22\sigma$ (Fig 6a).

The significant excess in shower number observed this minute (~ 100) comparing with showers observed during fair weather (Fig 7a) is due to randomly distributed within this minute ECSs, several times occurred in triplets and quadruplets per second, but never more. If the RB/RREA process will be self-consistent i.e. the RREA will not stop and continuously generate showers via feed back positrons and scattered gamma rays (RDFM model) we should observe much more counts of ECSs. The maximal dead time of the MAKET array is $100 \mu\text{sec}$; thus after each $100 \mu\text{sec}$ another shower can be registered by the surface particle array. Therefore, we can expect up to 10,000 showers per second, however, we register not more than 4.

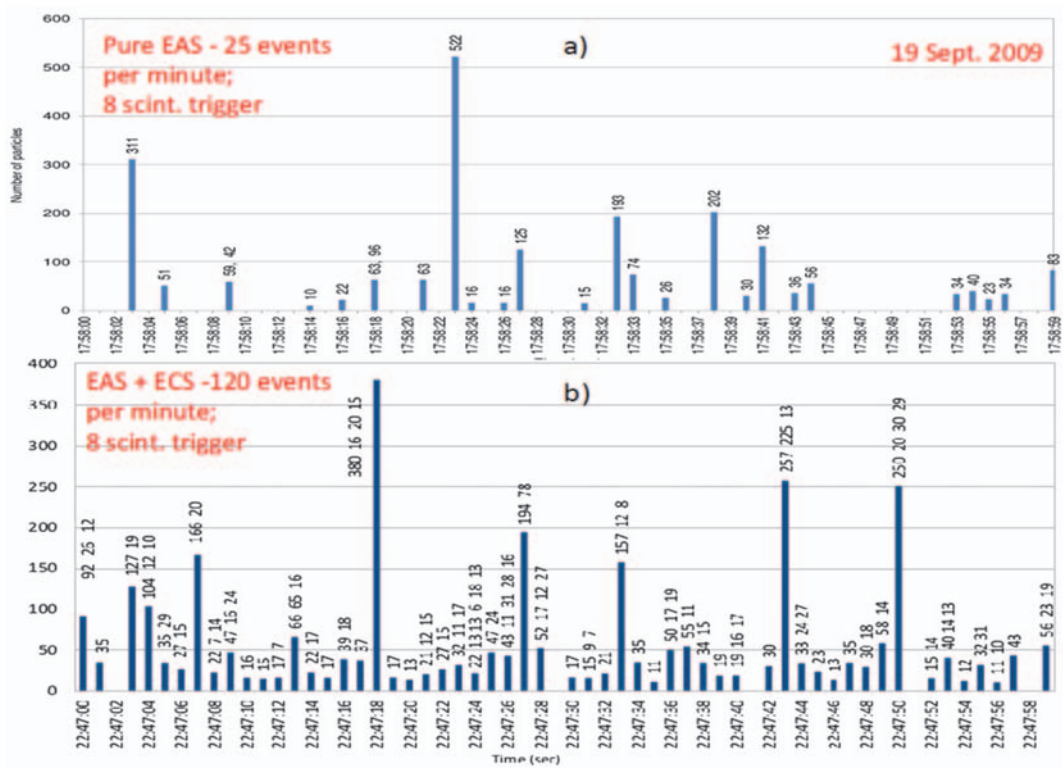


Figure 7. Particle showers detected during 60 seconds of the fair weather a) and during a thunderstorm at maximal particle flux b). Vertical bars show the number of particles in showers. If there were more than one shower in a second the height of a bar is equal to the size (number of particles) of the largest shower, next number after an interval is the number of particles in the next ECS, and so on. Note that maximal number of ECSs in a second is 4.

4. ENERGY RELEASE SPECTRA

ASNT data acquisition system registers energy release histograms both for events with and without veto i.e., if we have a signal in 5 cm thick scintillator this energy release is “vetoed” and do not participate in the histogram. In this way, we obtained the energy spectra of the neutral particles i.e. TGE gamma rays, originated from bremsstrahlung of accelerated in the RB/RREA process electrons. In addition, extracting histogram obtained with veto from the histogram obtained without veto we readily come to the histogram of electron energy releases (Figure 8).

The spectrum of electrons is very shallow, has non-stability below 7 MeV and terminates at 20 MeV; the spectrum of gamma rays is prolonged until 30 MeV. However, TGE particles in order to be registered in the 60-cm thick scintillator have to traverse significant amount of matter above, see Figure 9.

The intensity of electron flux is ~ 20 times less comparing with gamma ray intensity. The maximal energy of electron reaches ~ 25 MeV and, gamma ray - 35 MeV. TGE particles in order to be registered in the 60-cm thick scintillator have to traverse significant amount of matter above, see Figure 10. To estimate maximal electron energy above the roof we calculate energy losses in the matter above the scintillator (~ 10.8 g/cm²) and, considering the minimal required energy release in scintillator ~ 7 MeV, we come to maximal electron energy 40-50 MeV in a good agreement with simulation of TGE (Chilingarian, Mailyan, and Vanyan, 2012). The 4-minute flux of high-energy electrons detected by 60 cm thick scintillator proves a very low location of the thundercloud, possibly just above the roof of the MAKET building.

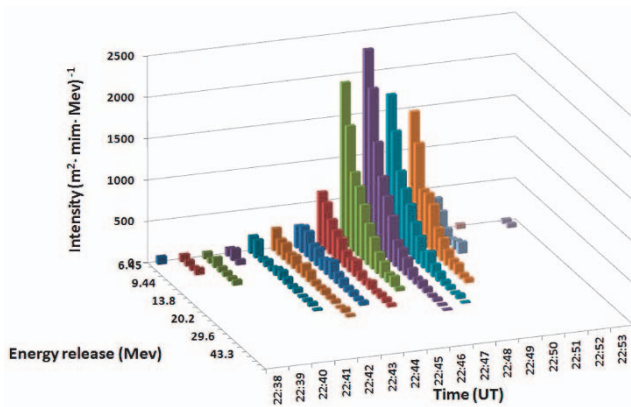


Figure 8. Differential energy release histogram of the TGE gamma rays obtained in 60 cm. thick scintillators of the ASNT array.

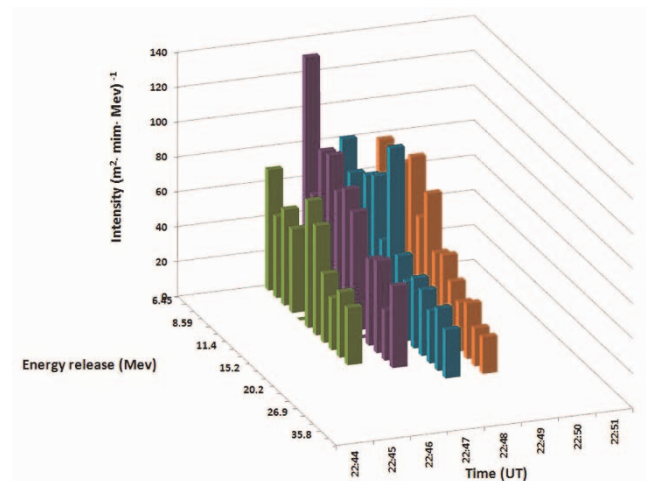


Figure 9. Differential energy release histogram of the TGE electrons obtained in 60 cm. thick scintillators of the ASNT array.

Aragats Neutron Monitor (ArNM, see details in Chilingarian, Hovsepyan and Kozliner, 2016) consists of 18 cylindrical proportional counters of CHM-15 type (length 200 cm, diameter 15cm) filled with BF₃ gas enriched with B¹⁰ isotope and grouped into three sections containing six tubes each. The proportional chambers are surrounded by 5 cm of lead (producer) and 2 cm of polyethylene (moderator). The cross section of lead producer above each section has a surface area of 6m², and the total surface area of three sections is 18 m². The TGE gamma rays produce neutrons in the photonuclear interactions with air atoms. The gamma rays, as well as atmospheric hadrons, produce secondary neutrons in nuclear reactions in lead (Chilingarian et al.,

2012a, 2012b, Tsuchiya et al., 2012). Then, the neutrons slow down to thermal energies in the moderator, enter the sensitive volume of the counter, and yield Li7 and α particle via interactions with boron gas. The α particle accelerates in the high electrical field inside the chamber and produces a pulse registered by the data acquisition electronics.

In Figure 11 we show significant enhancement (> 6σ at 22:47) of ArNM count rate lasting ~ 5 minutes on 19 September 2009; the same hour and minutes as the gamma ray and electron peaks. The count rates corresponding to dead times of 0.4 μs, 250 μs, and 1250 μs are approximately identical; EAS registration leads to enhancement only for the time series obtained with the minimal dead time of 0.4 μs.

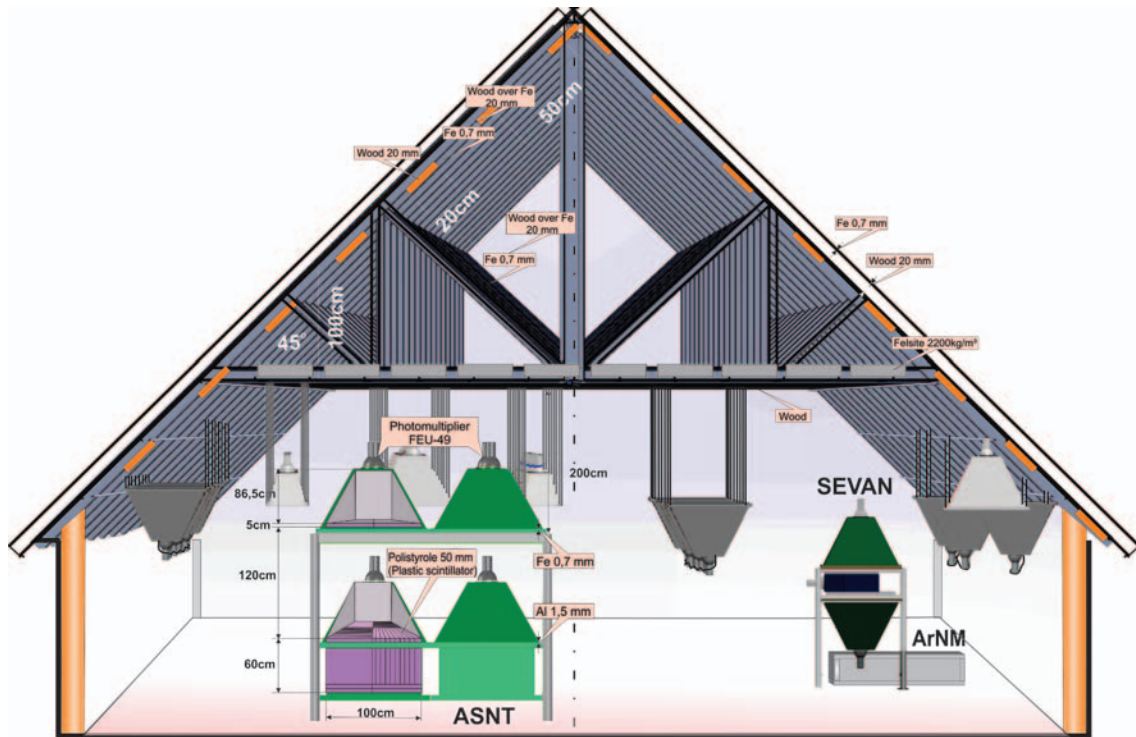


Figure 10. Setup of ASNT detector in the MAKET experimental hall

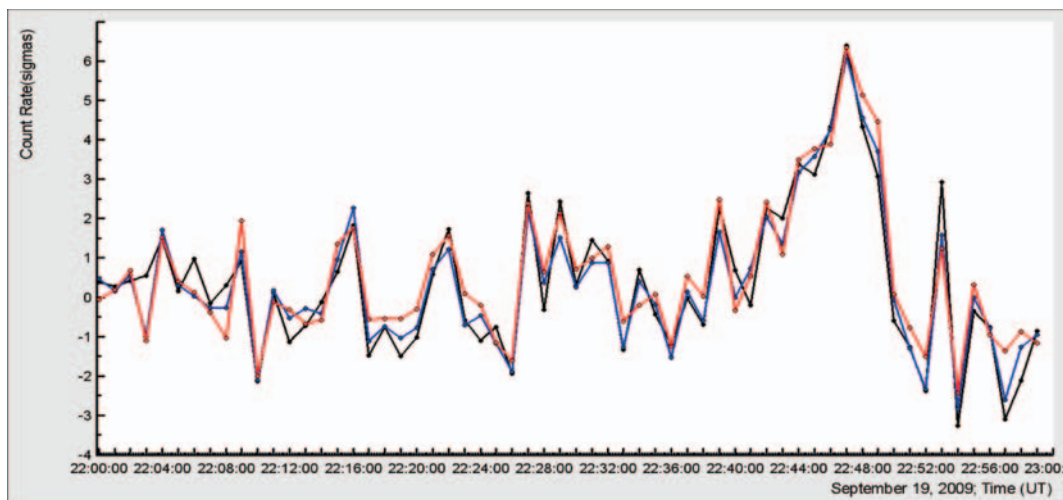


Figure 11. Time series of ArNM 1-minute count rate displayed in the number of standard deviations. Time series corresponding to 3 dead times are approximately identical.

5. DISCUSSION AND CONCLUSION

We measure the energy release histograms of TGE electrons reaching and registering in the 60 cm thick scintillators of the ASNT detector. The energy spectrum prolonged up to 25 MeV. The energy losses in the matter below the roof of the building are ~20 MeV. Taking into

account the amount of matter above the 60 cm thick scintillator we estimate the maximal energy of the electrons above the roof to be 40-50 MeV. Thus, the energy spectra of the super-event occurred on 19 September 2009 is in good agreement with the TGE model (Chilingarian, Mailyan, and Vanyan, 2012, Chilingarian, 2014).

Measured TGE temporal distribution demonstrates (Figure 7) proves that large fluxes of electrons and gamma rays detected during thunderstorms comprise from the numerous very short RB/RREA cascades registered by the particle detectors located on the mountain altitudes. During ~5 minutes of TGE, a large number of very short bursts (individual RRE avalanches, Extensive cloud showers, or Micro runaway breakdowns ECS/MRB, Gurevich et al., 1999) were developed in the thundercloud. For occurring of large TGE, clouds should be low above particle detectors; thus only on near-zero surface temperatures and high humidity, we detect largest TGEs (large negative near surface electric field is also a necessary condition).

The validity of the RDFM model is very difficult to prove with TGF data only; TGF measurements are performed with orbiting gamma ray observatories at the distances hundreds of km from thunderclouds, from which the particle is assumed to reach fast moving satellite. With such an experiment arrangement self-sustained acceleration of electrons does not appear obviously. The detected TGFs are very short, maybe parented by very few seed electrons injected into the strong electrical field region. The TGEs, in contrast, can prolong minutes, 6 orders of magnitude longer than TGFs. The RREA continued down to several tens of meters above detector site. Thus, various RB/RREA models can be validated by *in situ* measurements on Aragats, the natural electron accelerator provided many tens of TGEs each year (Chilingarian et al., 2016).

If the RB/RREA process due to feedback prolonged continuously we can expect much more detections per second (up to 10^4 , as a maximal dead time of MAKET array of ~100 μ sec); however the experimentally measured number of ECSs per second is 4, see Figure 7b). Thus, the temporal distribution of ECSs rejects the hypothesis of continuous acceleration of electrons in the cloud, i.e. the RDFM hypothesis, at least on the timescale of a millisecond and more. Sure TGFs and TGEs are not fully symmetrical processes the first one is propagated in the thin atmosphere becoming thinner as avalanches propagate upward; TGEs are propagating in the dense atmosphere becoming denser as TGE approach Earth's surface. However, the runaway process is in the heart of both and experimental evidence acquired from TGE observations can be used to validate TGF models.

ACKNOWLEDGEMENT

The author thanks the staff of the Aragats Space Environmental Center for the uninterrupted operation of Aragats research station facilities. The data for this paper are available via the multivariate visualization software ADEI on the WEB page of the Cosmic Ray Division (CRD) of the Yerevan Physics Institute, <http://adei.crd.yerphi.am/adei>.

The expedition to Aragats high altitude station was supported by the Armenian government grant N13- 1C275.

REFERENCE

- Babich, L.P., et al., 2001. Comparison of relativistic runaway electron avalanche rates obtained from Monte Carlo simulations and kinetic equation solution. *IEEE Trans. Plasma Sci.* 29 (3), 430–438, 2001.
- Briggs, M. S., et al., 2011. Electron-positron beams from terrestrial lightning observed with Fermi GBM, *Geophys. Res. Lett.*, 38, L02808.
- Chilingarian, A., Gharagozyan, G., Hovsepyan, G., Ghazaryan, S., Melkumyan, L., Vardanyan, A., 2004. Light and heavy cosmic-ray mass group energy spectra as measured by the MAKET-ANI detector. *Astrophys. J.* 603, L29–L32.
- Chilingarian A., Gharagozyan G., Hovsepyan G. et al., (2007). Study of extensive air showers and primary energy spectra by MAKET-ANI detector on Mount Aragats, *Astroparticle Physics*, 28, 58.
- Chilingarian, A., Daryan, A., Arakelyan, K., Hovhannisyanyan, A., Mailyan, B., Melkumyan, L., Hovsepyan, G., Chilingaryan, S., Reymers, A., Vanyan, L., 2010. Ground-based observations of thunderstorm-correlated fluxes of high-energy electrons, gamma rays, and neutrons. *Phys. Rev. D: Part. Fields* 82 (4), 043009.
- Chilingarian, A., Hovsepyan, G., Hovhannisyanyan, A., 2011. Particle bursts from thunderclouds: natural particle accelerators above our heads. *Phys. Rev. D: Part. Fields* 83 (6), 062001.
- Chilingarian, A., Mailyan, B., Vanyan, L., Recovering of the energy spectra of electrons and gamma rays coming from the thunderclouds. *Atmos. Res.* 114–115, 1 (2012).
- Chilingarian A., Bostanjyan N., and Vanyan L., Neutron bursts associated with thunderstorms, *Physical Review D* 85, 085017 (2012a).
- Chilingarian A., Bostanjyan N., Karapetyan T., Vanyan L., Remarks on recent results on neutron production during thunderstorms, *Physical Review D* 86, 093017 (2012a).
- Chilingarian A., Hovsepyan G., and Kozliner L., Thunderstorm ground enhancements: Gamma ray differential energy spectra, *Physical Review D* 88, 073001 (2013).
- Chilingarian A., Thunderstorm Ground Enhancements – model and relation to lightning flashes, *J. Atmos. Solar-Terr. Phys.* 107 (2014) 68–76.
- Chilingarian A., G. Hovsepyan, G. Khanikyanc, A. Reymers and S. Soghomonyan, Lightning origination and thunderstorm ground enhancements terminated by the lightning flash, *EPL*, 110 (2015) 49001.
- Chilingarian A., Hovsepyan G., and Mantasakanyan E., 2016. Mount Aragats as a stable electron accelerator for atmospheric High-energy physics research, *Phys. Rev. D: Part. Fields*, 93, 052006.
- Chilingarian A., Hovsepyan G., Kozliner L., Extensive Air Showers, Lightning, and Thunderstorm Ground Enhancements, *Astroparticle Physics* 82 (2016) 21–35.
- J.R. Dwyer, D.M. Smith, S.A. Cummer, High-energy atmospheric physics: terrestrial gamma-ray flashes and related phenomena, *Space Sci. Rev.* 173 (2012) 133–196.
- Dwyer, J. R. (2012), The relativistic feedback discharge model of terrestrial gamma ray flashes, *J. Geophys. Res.*, 117, A02308.
- J.R. Dwyer, M.A. Uman, The physics of lightning, *Phys. Rep.* 534 (4) (2013) 147–241.
- Dwyer, J.R., 2007. Relativistic breakdown in planetary atmospheres. *Phys. Plasmas* 14 (4), 042901, <http://dx.doi.org/10.1063/1.2709652>.

- Dwyer, J.R., 2003. A fundamental limit on electric fields in air. *Geophys. Res. Lett.* 30 (20), 2055, <http://dx.doi.org/10.1029/2003GL017781>.
- G.J. Fishman, P.N. Bhat, R. Mallozzi, et al. Discovery of intense gamma ray flashes of atmospheric origin, 1994, *Science* V. 264 (5163), 1313.
- Gurevich, A.V., Milikh, G.M., Roussel-Dupre, R., 1992. Runaway electron mechanism of air breakdown and preconditioning during a thunderstorm. *Phys. Lett. A* 165 (5-6), 463–468.
- Gurevich A.V., Zybin K.P., Roussel-Dupre R.A., Lightning initiation by simultaneous of runaway breakdown and cosmic ray showers, *Phys. Lett. A* 254 (1999) 79.
- P. Krehbeil, V. Mazur, W. Rison, Standardizing the sign convention for atmospheric electric field measurements, *Newslett. Atmos. Electr.* 5 (2) (2014) 5.
- Lehtinen, N.G., Bell, T.F., Inan, U.S., 1999. Monte Carlo simulation of runaway MeV electron breakdown with application to red sprites and terrestrial gamma ray flashes. *J. Geophys. Res.* 104, 24,699–24,712, <http://dx.doi.org/10.1029/1999JA900335>.
- Stolzenburg M., Rust W., Marshall T., Electrical structure in thunderstorm convective regions 3. Synthesis, *J. Geophys. Res.* 103 (1998) 14097–14108.
- Tsuchiya H., Hibino K., Kawata K. et al., Observation of thundercloud-related gamma rays and neutrons in Tibet, *Phys. Rev. D* 85, 092006 (2012).

Extensive Air Showers Detected by Aragats Neutron Monitor

A. Badalyan, A. Chilingarian, G. Hovsepyan, A. Grigoryan, Y. Khanikyants, A. Manukyan, D. Pokhsraryan and S. Soghomonyan

Yerevan Physics Institute, Armenia

Abstract. Extensive Air Shower (EAS) duration as registered by the surface particle detectors does not exceed a few tens of nanosecond. However, Neutron monitors containing plenty of absorbing matter can respond to EAS core traversal during 1 \sim ms by registering secondary slow neutrons born by EAS hadrons in the soil, walls of buildings and in the matter of detector itself. Thus, the time distribution of the pulses from the proportional counters of the neutron monitor after EAS propagation extends to \sim 1 ms, \sim 5 orders of magnitude larger than the EAS passing time. The Aragats Neutron Monitor (ArNM) has a special option for the EAS core detection. In general, the dead time of NM is \sim 1 ms that provides the one-to-one relation of incident hadrons and detector counts. The pulses generated by the neutrons possibly entering the proportional chamber after the first one will be neglected. In ArNM, we use several “electronic” dead times, and with the shortest one, 400 ns, the detector counts all pulses that enter the proportional chambers. If ArNM one-second time series corresponding to the shortest dead time contain much more signals (a neutron burst) than with 1-ms dead time, then we conclude that the EAS core hits the detector.

We assume that the distribution of registered burst multiplicities is proportional to the energy of the primary particle. The primary cosmic ray energy spectrum was obtained by the frequency analysis through the counting frequencies of the multiplicities of different magnitudes and relating them to the integral energy spectrum measured by the MAKET array at the same place several years ago.

1. INTRODUCTION

Cosmic Ray (CR) flux incident on terrestrial atmosphere consists mostly of protons and heavier stripped nuclei accelerated at numerous galactic and extragalactic sites. The most exciting questions associated with cosmic rays is the observation of a particular accelerating source and exploring the acceleration mechanism. Due to the bending in the magnetic fields, charged particles lose information about the parent sites during long travel and arrived highly isotropic to the solar system. Thus, cosmic rays cannot map the sites where they born, therefore, only integrated information from all sources are available from measurements of cosmic ray fluxes near Earth and on the Earth’s surface. Energy spectra of the primary particles with energies larger than 100 TeV can be studied only by surface detectors registering numerous secondary cosmic rays (SCR) belonging to the Extensive Air Showers (EASs) developed in the interaction of primaries with atmosphere atoms. The information on the acceleration mechanisms of CR is covered in the shape of the energy spectra of the different species of SCR measured by the particle detectors located on the earth’s surface. Usually, the rather sparse arrays of plastic scintillators overviewed by photomultipliers are used for registration of the shower particles. When trigger conditions are fulfilled (EAS generate predefined particle density or more in the predefined number of scintillators or more) signals from all scintillators are stored and used for estimation of the lateral distribution and then, by integrating it, – the shower size, i.e. the total number of electrons in the shower. The relation of shower size to primary energy (conditioned on primary type) was established by simulations of EAS with sophisticated Monte-Carlo codes. The energy spectrum of different SCR species follows a power law $dN/dE \sim E^\gamma$ over many orders of magnitude. The spectrum recovered by the electron content of EAS steepens at energies around 4-5 PeV from a spectral index $\gamma \approx -2.7$ to $\gamma \approx -3.1$. This feature is commonly called the knee and its explanation is generally believed to be a cornerstone in understanding the origin of cosmic rays, providing answers to one of the key questions of astroparticle physics (Horandel, 2004).

Large fluctuations of the EAS development in the terrestrial atmosphere along with uncertainties of the extrapolation of strong interaction models to yet unexplored with manmade accelerators energy domain make the unfolding (solving the inverse problem) of the measured CR spectrum extremely difficult. However, implementation of the nonparametric multivariate methodology (Chilingarian, 1989), allows the event-by-event-analysis of EAS data (Chilingarian et al., 1991) using Bayesian and Neural Network models. At each stage of the analysis, we estimate the value of the information content of the variables used for EAS classification and energy estimation and restrict the complexity of the physical inference according to this value. The MAKET-ANI experiment (Chilingarian et. al., 2004) is located at 3200 m. above sea level on Mt. Aragats, In Armenia; the quality of reconstruction of the EAS size and shape (shower age) are good enough and we can use these 2 parameters for the EAS classification. The distinctive information contained in distributions of these parameters allows us to classify the EAS with high accuracy into two distinct groups: initiated by “light” or “heavy” nucleolus. In the KASCDE experiment (Antoni et al., 2002), where the muon content of the EAS is measured in addition to shower electron size, it is possible to classify showers into 3 categories adding also the “intermediate” class.

The differences in the spectra slope before and after the knee for different mass groups of the primary cosmic ray flux is the key feature for the solving of the knee origin problem. The available world data confirms the existence of very sharp knee for the CR light component. Energy spectra of KASCADE (Vardanyan et.al., 1999) and MAKET-ANI (Chilingarian, et.al. 2004) experiments are in good agreement in terms of intensities, the shape of the spectra, and spectral indices, Fig.1. HEGRA spectrum (Arqueros et.al.,2000), obtained with completely different experimental methodic, also prove steepening of the light mass group spectra and shift of the knee position to the lower values of primary energy comparing with all-particle spectra, Figure 1.

In Figure 2 we show the energy spectra unfolded by the neural classification methodology (Chilingarian, 1994, 1995). More than million EASs detected in 1999-2004 have been carefully examined and rummage-sale for the estimation of energy spectra of light and heavy nuclei. The efficiency of extensive air shower core selection around geometrical center of the array was >95% for EASs generated by primary particles with energy $\geq 5 \times 10^{14}$ eV. The compact array with well calibrated detectors turned out to be very well suited for the energy and composition measurements at the “knee” of the cosmic ray spectrum.

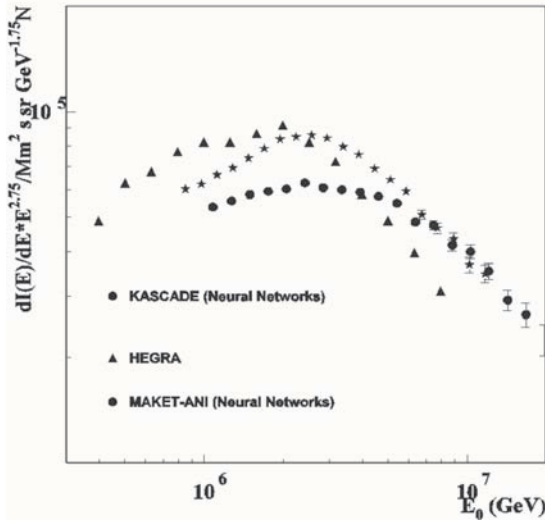


Figure 1. Light nuclei group spectra (Arqueros et al., 2000, Vardanyan et al., 1999, Chilingarian et al., 2004)

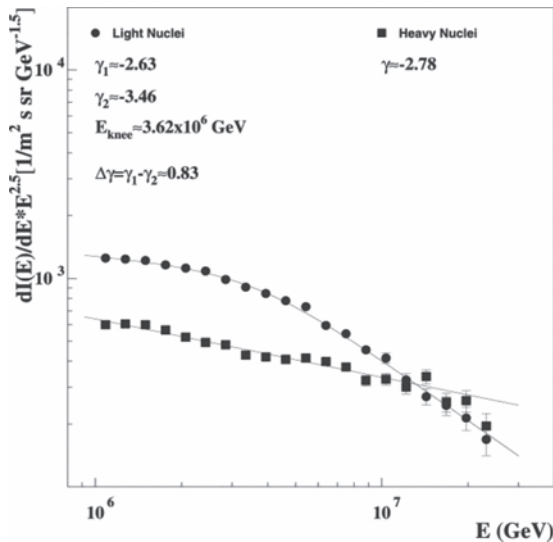


Figure 2 Energy spectra of light and heavy nuclei obtained by neural classification and energy estimation. The EAS characteristics used are shower size and shape (age parameter).

The physical inference from MAKET data can be summarized as follows:

1. The estimated energy spectrum of the light mass group of nuclei shows a sharp knee: $\Delta\gamma \sim 0.9$, compared to ~ 0.3 for the all-particle energy spectra.
2. The energy spectrum of the heavy mass group of cosmic rays shows no break in the energy interval of $10^{15} - 2 \times 10^{16}$ eV.
3. The MAKET results on the rigidity-dependent position of the knee confirm the Super Novae Remnants (SNRs) as a most probable source of

galactic cosmic rays and Fermi-type acceleration as the mechanism of hadron acceleration.

In (Anglietta et al., 2004), the light mass group was isolated using information on the EAS electrons and TeV In (Anglietta et al., 2004), the light mass group was isolated using information on the EAS electrons and TeV muons. Obtained knee position at $E_k \approx 4 \cdot 10^{15}$ eV and difference of the slopes after and before the knee for light component equals to $\gamma_2 - \gamma_1 = 0.7 \pm 0.3$, as compared with all charged particles spectra $\gamma_2 - \gamma_1 = 0.4 \pm 0.1$ again can be interpreted in the standard framework of the rigidity-dependent acceleration. Conclusive evidence from KASCADE experiment has been reached on the knee being caused by light primaries mostly. Furthermore, the data are in agreement with a rigidity scaling of the knee position giving support to an astrophysical origin by either maximum confinement energy or diffusion/drift models of propagation (Kampert et al., 2004).

Thus, the origin of Galactic cosmic rays can be supernovae shock waves as they can explain the intensity of the CR intensity at least up to 10^{15} eV. Direct evidence of shock acceleration in SN shells can be deduced from joint detection of young SNRs in X and γ -rays. To prove that the young supernovae remnant RX J1713.7-3946 is a very efficient proton accelerator Uchiyama et al., (2007) include in the analysis information on broadband X-ray spectra (from 0.4 to 40 KeV) measured by the Suzaku satellite (Takahashi et al., 2008) and - on high energy γ -ray spectra (extending over 10 TeV) measured by HESS Atmospheric Cherenkov Telescope (ACT) (Aharonyan et al., 2007). They exclude the inverse Compton origin of detected high-energy γ -quanta, and taking into account the TeV-KeV correlations validate the hadronic model of detected γ -rays. Thus, the joint analysis of X-ray maps from Chandra and X-ray spectra from Suzaku satellites with high energy γ -ray spectra measured by HESS ACT provide a very strong argument for the acceleration of protons and nuclei with energies 1 PeV and beyond in young SNR shells. The SNR origin of galactic CR has been recently confirmed by the observations of AGILE (Giuliani et al. 2013) and FERMI satellites (Ackermann et al., 2013).

As we mention above, inferring the energy and type of the primary particle from the EAS measurements is a very hard task requiring a priori model of the energy spectrum and chemical composition. In modern experiments, a multivariate approach, based on the simultaneous detection of as much as possible EAS observables and their correlation is used to infer the features of the cosmic ray spectrum (Antony et al., 2002, Chilingarian et al., 2007). Hadronic component of EAS carry important information for multi-parameter correlation analysis and can significantly improve the reliability of CR classification and energy estimation. Recently, instead of very expensive hadron calorimeter, an alternative approach for incorporation hadronic information was proposed (Bartoli et al., 2016). Instead of hadrons, it was proposed to measure neutron content of EAS. Evaporation neutrons are generated abundantly by EAS hadrons, up to 2 orders of magnitude more than parent hadrons. The energy distribution of hadrons in EAS exhibits a very slow dependence on the primary energy; on the other hand, the total number of evaporation neutrons is expected to be proportional to the total number of high-energy hadrons reaching the observation level. A large fraction of the evaporation neutrons thermalized, so that recording thermal neutrons can be exploited to reconstruct the hadron content in the shower. Measurement

of the neutron bursts correlated with EAS with neutron monitors or/and a new EN-detector, made of a mixture of the inorganic scintillator ZnS(Ag) with 6LiF, (Stenkin, 2008) looks very promising for measurements carried out at mountain altitude.

At Aragats research station of Yerevan Physics Institute (3200 m asl) variety of particle detectors are in operation (see details in Chilingarian et al., 2005, Chilingarian et. al. 2016) including 2 Neutron monitors 18NM64 and ~ 300 m² of scintillation detectors. The purpose of this paper is to use these detectors for the detection of EAS neutron content, and - for scrutinizing possibilities of primary CR energy estimation by the registered neutron multiplicities.

2. INSTRUMENTATION

The Aragats neutron monitor (ArNM) consists of eighteen cylindrical proportional counters of CHM-15 type (length 200 cm, diameter 15 cm) filled with BF₃ gas enriched with B¹⁰ isotope and grouped in three sections containing six tubes each (in Figure 3 we show one section of it - 6NM64). The proportional chambers are surrounded by 5 cm of lead (producer) and 2 cm of polyethylene (moderator). The cross section of lead producer above each section has a surface of 6m² and the total surface of three sections is 18m². The atmospheric hadrons produce secondary neutrons in nuclear reactions in lead; then the neutrons get thermalized in a moderator, enter the sensitive volume of the counter, and in interactions with boron gas born Li⁷ and the α particle. The α particle accelerates in the high electrical field inside the chamber and generates enough ionization to be detected by the data acquisition electronics. High- energy hadrons generate a large number of secondary neutrons entering the lead producer, and, if we want to count all pulses initiated by the incident hadrons, we have to keep the dead time of the NM very low (the ArNM has a minimal dead time of 0.4 μ s). If we want to count incident hadrons only (a one-to-one relation between count rate and hadron flux) we have to keep the dead time as long as the whole secondary neutron collecting time (~1250 μ s) to avoid double counting.

The Aragats Muon detector (Figure 4) consists of three vertically stacked plastic scintillators with an area of 1m². The top 3cm thick scintillator is covered by 7.5cm of the lead filter; the middle 1cm thick scintillator is covered by 1.5cm of the lead filter and by ~ 60 cm thick rubber layer (carbon); the bottom 1cm thick scintillator is covered by the 6cm thick lead filter. The energy thresholds to detect muons in three stacked scintillators are ~170 MeV, ~220 MeV and ~350 MeV accordingly. DAQ electronics provides registration of 50 ms time series of all scintillators. ArNM and Muon detectors are located at a distance of ~ 6m from each other in the MAKET experimental hall. The close location of these detectors allows joint detection of large EASs. Outdoors is located the STAND1 detector comprised of three layers of 1-cm-thick, 1m² area molded plastic scintillators and 3 cm thick plastic scintillator of the same type fabricated by the High Energy Physics Institute, Serpukhov, Russian Federation. The light from the scintillator through optical spectrum-shifter fibers is reradiated to the long- wavelength region and passed to the photomultiplier FEU-115M. The maximum of luminescence is emitted at the 420-nm wavelength, the luminescence time being about 2.3 ns.

The heart of the Data acquisition system (DAQ) is NI-myRIO board (see Figure 5). The output pulses from the 7-

channel discriminator board are fed to the FPGA of the myRIO board where the logic of event identifying, pulses counting and GPS time stamping is implemented. The 8-th channel is reserved for the synchronization pulse (the trigger) from any of particle detectors. We use for triggering one of ArNM channels (second or 8-th proportional counter); the “EAS” trigger was generated when 1-second count rate exceeds the mean count rate by 4 standard deviations. The output of the proportional counters (Figure 3) and one of the Muon detector scintillators (Figure 4) were directly connected to the digital oscilloscope (2 channel picoscope 5244B with 25MS/s sampling rate) with 60 cm long RG58 coaxial cable. Data capture length can be chosen from 1 second, including 200 ms pre-trigger and 800 ms post-trigger time with sample interval 40 ns, or, for instance, 10 ms with the sample interval of 0.4 ns.

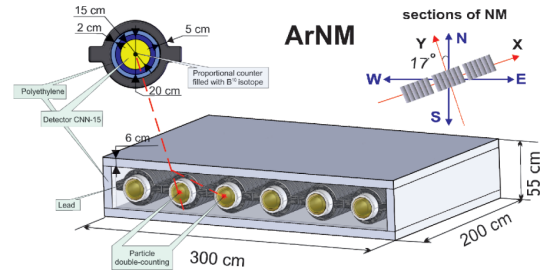


Figure 3. Layout of Aragats Neutron Monitor (ArNM)

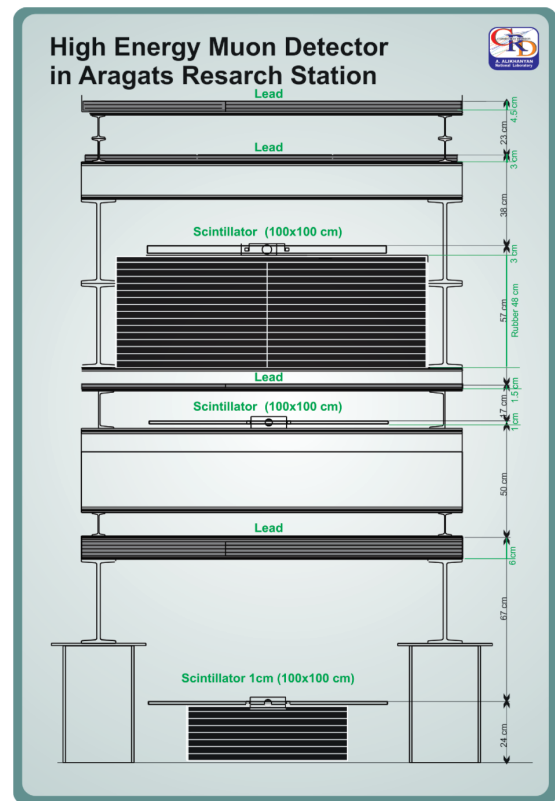


Figure 4. The “muon” stacked detector with large amount of lead and rubber between 3 scintillators

The special file generated by digital oscilloscope at any trigger, time series of particle detector count rates, current electrostatic field strength and service information (status of myRio, time delays, number of satellites used) are transferred to the mySQL database at CRD headquarters in Yerevan. All information is available via ADEI multivariate visualization code by link <http://adei.crd.yerphi.am>; explanations are located in the Wiki section.

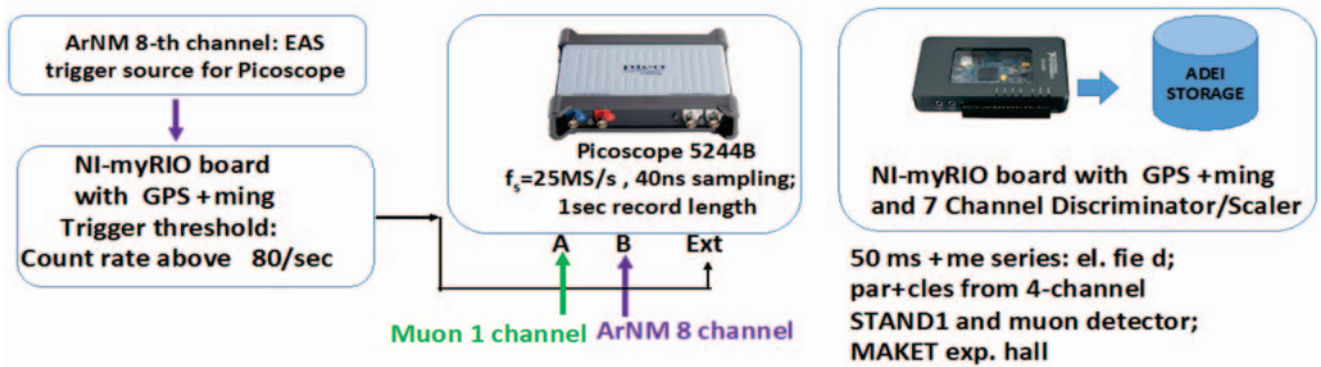


Figure 5. Schematic view of the fast DAQ for the EAS core detection. The particle pulses from first scintillator of Muon detector and 8-th (or second) counter of ArNM are registered and stored when 1-second count rate of ArNM proportional counter exceeds mean count rate by 4σ . The DAQ is continuously registered 50 ms time series of all STAND1 and muon detector channels and electrostatic field as well.

3. THE CORES OF EXTENSIVE AIR SHOWERS DETECTED BY ARAGATS NEUTRON MONITOR AND MUON DETECTOR EAS

Yu. Stenkin suggested slow neutron registration for the EAS studies (Stenkin et. al., 2008). The EAS duration as registered by the surface particle detectors does not exceed a few tens of nanosecond. However, Neutron monitors containing plenty of absorbing matter can respond to EAS core traversal during ~ 1 ms by registering secondary slow neutrons born by EAS hadrons in the soil, walls of buildings and in the matter of detector itself. Thus, the time distribution of the pulses from the proportional counters of the neutron monitor after EAS propagation extends to ~ 1 ms, ~ 5 orders of magnitude larger than the EAS passing time. In the Neutron monitor's 5 cm lead producer the EAS hadrons can generate many hundreds of neutrons and in the polyethylene moderator they slow down to thermal energies before entering the proportional counters. Due to multiple scattering in the absorber and moderator, the time distribution of the secondary neutrons became significantly broader. Thus, the time distribution of the pulses from the proportional counters of the neutron monitor after EAS core propagation extends to ~ 1 ms (Balabin et al., 2011). The measurements on Tien-Shan demonstrated that EASs with energy greater than 10 PeV with axes in 3-10 meters from NM could produce multiplicities above 1000 (Antonova et al., 2002). This, very high number of recorded neutrons are caused by the groups of high-energy hadrons hitting the NM (Stenkin and Valdes-Galicia, 2002).

The Aragats neutron monitor (Figure 3) has a special option for the EAS core detection. Usually, the dead time of NM is set to 1.25 ms for the one-to-one relation of incident hadrons to detector counts. Thus, all neutrons entering the proportional chamber after the first one are neglected; it is expected that during 1.25 ms all delayed secondary thermalized neutrons will enter proportional chamber or will be absorbed in the moderator. In ArNM we use several "electronic" dead times, which artificially block the output of the proportional counter for predefined time span. The shortest one dead time 400 nsec, can count almost all output pulses. Thus, if ArNM with the shortest dead time registers much more pulses than with ~ 1 ms dead time it means that the EAS core is hitting the detector. Within 1 ms, if we assume very large (continuous) pulse train, 2500 pulses can be count. Sure, only extremely energetic EASs (producing numerous hadrons) hitting NM can yield such a large multiplicity.

In Figure 6 we demonstrate 1-second time series of the second (first section) proportional counter of ArNM. On November 26 at 04:08:05 UT the second proportional counter registered neutron burst above trigger level (multiplicity >100) and a file from the digital oscilloscope

with detector pulses shown on the nanosecond scale was stored. In Figure 6 we see the peak corresponding to the shortest dead time of $0.4 \mu\text{s}$; the time series of $250 \mu\text{s}$ and $1250 \mu\text{s}$ demonstrate no peaks.

In Figure 7 we show time series of 7 operating channels of the ArNM.

Only 2 proportional counters belonging to the first section of ArNM (namely the third and fourth) close to the second one demonstrate peaks in 1-sec time series. Accordingly, we can conclude, that EAS core hits the ground near first section of ArNM producing plenty of secondary neutrons, which registered by the proportional counters.

In Tab. 1 we show the mean values, variances and peak values of 1-second time series registered by ArNM at 04:08:20 – 04:08:20. Only in the first section of ArNM we see large enhancements (counters 2, 3, 4). In the second section (counter 8) and in the third section (counters 13, 14, and 18) we see no enhancements. Thus we can relate measured enhancements in 3 close channels of ArNM to high-energy hadron(s) from the EAS core.

Table 1. ArNM registration of the neutron burst

N of Proportional	of n	Mea	σ	Maximum
ArNM #2		41.3	11.	107
ArNM #3		63.0	12.	116
ArNM #4		38.5	9.4	81 (4.48 σ)
ArNM #8		30.7	6.4	46 (2.38 σ)
ArNM #13		22.1	5.3	35 (2.43 σ)
ArNM #14		25.8	6.2	39 (2.12 σ)
ArNM #18		18.5	4.3	29 (2.4 σ)

In Figure 8 we show the pulses from ArNM counter and from plastic scintillator of Muon detector with different time zooming. In the Fig.8a we show the initial full-scale (1 sec) pulse shapes. On the upper line, we can see several charged particle registrations by the plastic scintillator of Muon detector. The muons are entering the muon detector randomly according to the mean count rate of high-energy muons on 3200 m altitude $\sim 500/\text{m}^2\text{s}$. In the time series below we see the multiple detections of slow neutrons entering the sensitive volume of the proportional counter of ArNM. The time distribution of the pulses from the proportional counters of the neutron monitor after EAS core propagation extends several hundreds of μs as we can see in Figure 8b. Plastic scintillator's response to EAS passage is only one pulse. We assume that the first very wide pulse in Figure 8c corresponds to the EAS core passage when a lot of slow neutrons enter the counter simultaneously; following subsequent pulses – are correspond to the delayed neutrons.

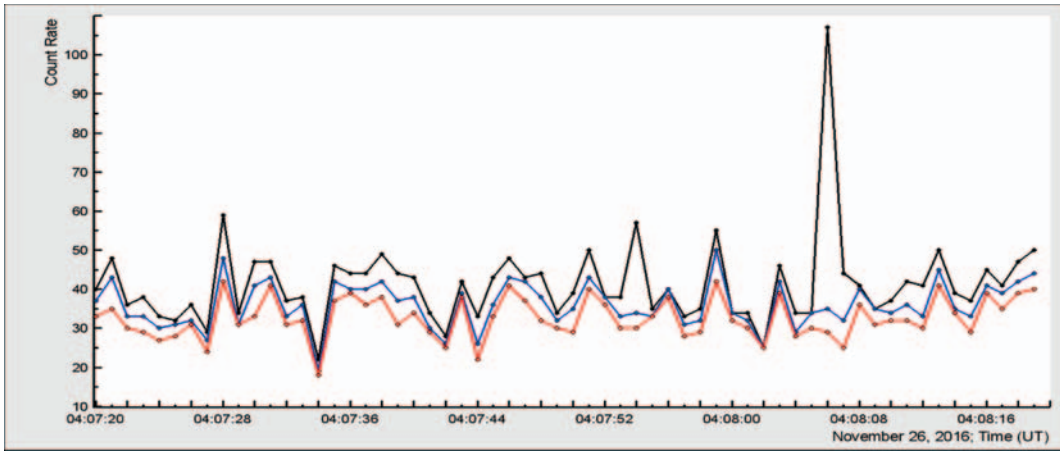


Figure 6. Time series of ArNM second proportional counter corresponding to 3 dead times. Only with shortest dead time of $0.4 \mu\text{s}$ DAQ electronics registered a large neutron burst.

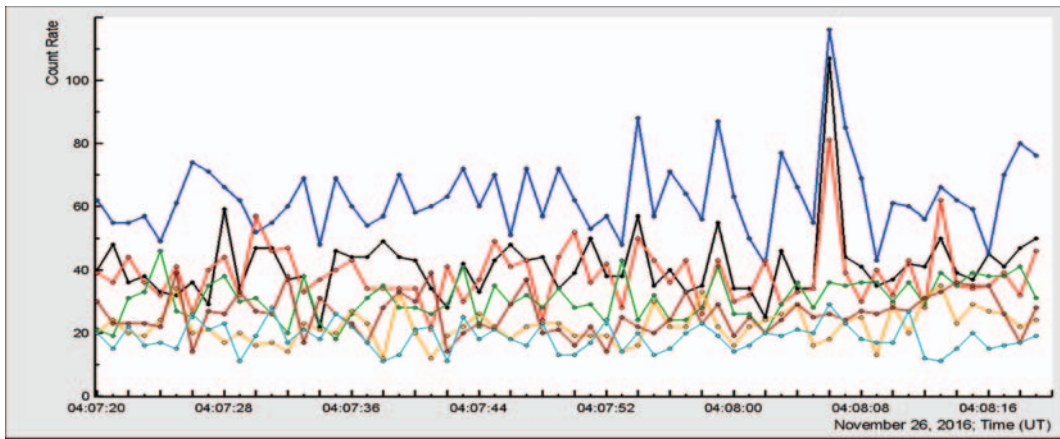


Figure 7. Neutron burst detected by the ArNM with dead time $0.4 \mu\text{s}$. Only counters from the first section (2,3,4) demonstrate peaks.

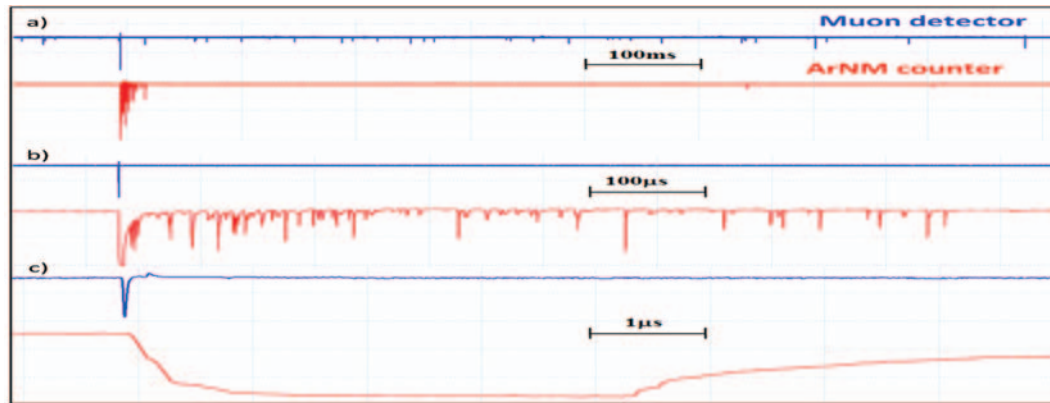


Figure 8. Particle detector output waveforms corresponding to different time zooming scales

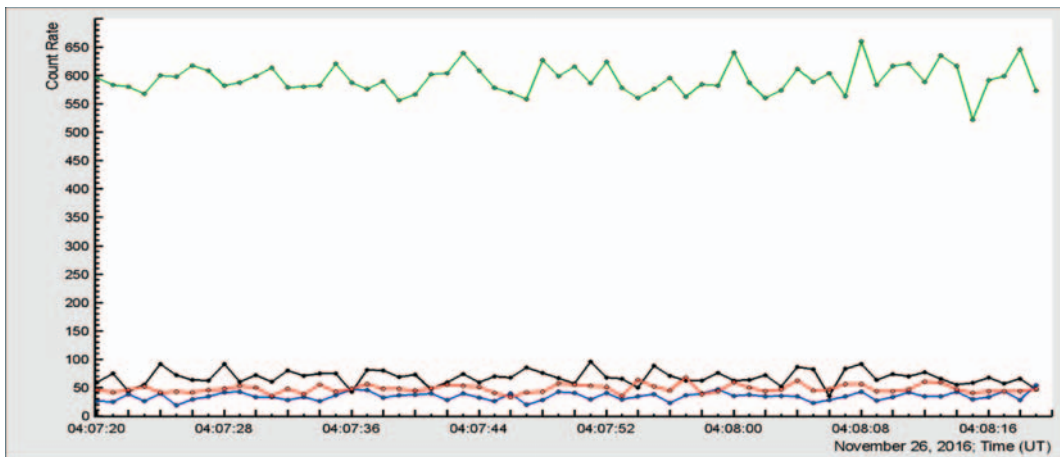


Figure 9. 1-sec time series of 3 scintillators of Muon detector and 3 cm thick outdoor scintillator of STAND1 detector.

In Figure 9 we show 1-second time series of plastic scintillators located under thick layer of lead (Muon detector) and 3-cm thick 1 m² area plastic scintillator located outdoors. No one of them demonstrate any enhancement. EAS do not induce any charged particles even in thick lead; whole thousands of EAS particles are passing scintillators in few tens of nanosecond generating only one pulse in DAQ electronics.

4. ON THE POSSIBILITY OF RECOVERY OF PRIMARY CR ENERGY SPECTRUM WITH ARNM

In (Stenkin and Vald'es-Galicia, 2002) the dependence of neutron burst multiplicity on primary proton and iron nuclei energy was calculated. They found that this dependence can be fitted by a power law with an index ~ 1.3 for protons, and ~ 1.6 for iron nuclei (hadrons were counted inside ~ 1 m around EAS axes). They also found that majority of the neutron bursts are produced by a single hadron. Very high burst multiplicities (>1000), caused by groups of hadrons are very rare: 1-2 per year that coincides with our observations. Such a large multiplicities occurred in all 3 sections of NM, so can be easily distinguished and treated separately. The primary CR energy spectrum was obtained by the frequency analysis of measured multiplicity distribution measured by several proportional counters. The multiplicity spectrum was related to the integral energy spectrum measured by the MAKET array at the same place 10 years ago (see the introduction section and Chilingarian et al., 2004).

MAKET array is a rather compact array comparing with other EAS detectors (the core selection area is only $\sim 10,000$ m²) and was aimed to measure EASs with energies around the "knee" feature of energy spectra, (4-5) PeV. Thus, we can use measured by MAKET array integral spectrum (Figure 10) for the normalization (establish a relation between multiplicity and primary energy) of measured multiplicity distributions (Figure 11).

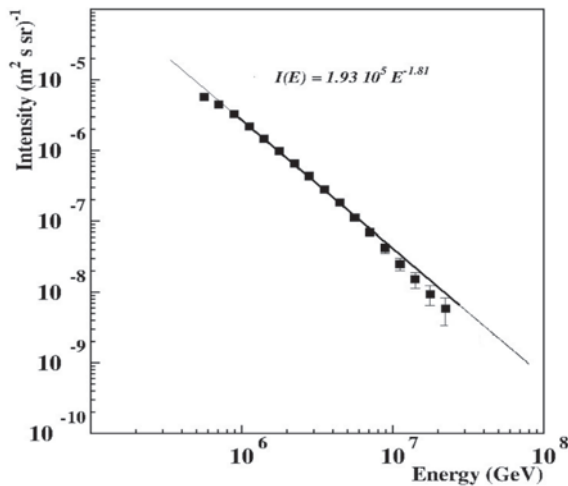


Figure 10. The integral energy spectrum of all particles measured by the MAKET-ANI surface array.

The MAKET-ANI experiment has taken data with exposition time of $\sim 1.46 \cdot 10^8$ s. The total number of the registered shower events was $\sim 1.2 \cdot 10^7$. A smaller sample of the data $\sim 7.2 \cdot 10^5$ (near the vertical EAS, $\theta \leq 30^\circ$) was used for recovering energy spectra. Thus, we proceed from energy spectrum of primary cosmic rays measured by MAKET array:

$I(E) = aE^\gamma$ (Figure 10) and distribution of ArNM proportional counter burst multiplicity:

$J(E) = bE^\beta$ (Figure 11), where E – is energy of primary CR, γ – spectral index of primary flux and β – fitted slope of

the burst multiplicity distribution. Under our assumption of selecting the EASs those core hit the array (area 10,000 m² and the ArNM (18²) we can normalize the multiplicity distribution by the energy spectra measured by MAKET array to tune the arbitrary scale of burst multiplicity distribution to primary energy scale. We can do it simply by equalizing maximal frequencies, i.e. assuming that maximal intensities of both distributions correspond to the one and the same energy of primary particle:

$$I_{max}(E_0) = J_{max}(E_0).$$

In this way we readily obtain integral energy spectra using different proportional counters of ArNM (see Table 2). Fitted power index β can be checked by equalizing frequencies for 2 arbitrary frequencies: $aE_1^{-\gamma} = bE_2^{-\beta}$ and $aE_3^{-\gamma} = bE_4^{-\beta}$.

Table 2. Recovered energy spectra from ArNM proportional counters (numerical values obtained from the fits shown in Figure 11)

$I_1 = 178.5E^{-1.39}$	$I_2 = 5884E^{-1.64}$
$I_3 = 779.3E^{-1.52}$	$I_4 = 5873E^{-1.64}$
$I_8 = 2606E^{-1.589}$	$I_{11} = 130.6E^{-1.369}$

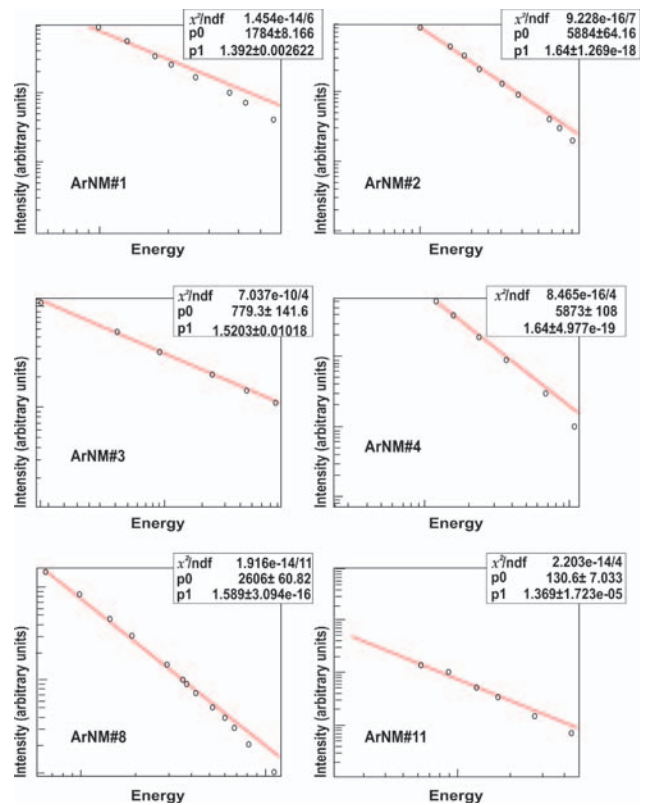


Figure 11. Multiplicity distributions of ArNM proportional counters channels (1,2,3,4,8,11) measured in time span of 1 July 2014 - 1 June 2015.

CONCLUSION

We demonstrate that by measuring the distribution of the bursts multiplicities in NM we can estimate the integral energy spectrum of the primary CR. Obtained multiplicity distribution (Table 2) are in good agreement with previously published estimates (Stenkin and Vald'es-Galicia, 2002). The developed fast electronics techniques could be successfully used in the EAS core studies. Nanosecond accuracy detection of EAS core particle by neutron monitor and scintillation detectors located nearby can reveal fine structure of EAS core.

However, NM is a rather small detector with an area not exceeding 18 m² and cannot collect enough shower axes for

a reliable spectrum recovering. The temporal accuracy of the boron filled proportional counters is rather low and they saturated at high multiplicities (Stenkin et al., 2008). Therefore, NM proportional counters are not suitable for large area EAS experiments.

Bartolli et al.,(2016) suggest using EN-detectors (Stenkin, 2008) for the EAS hadron measurements. The detection of thermal neutrons of EAS by means of proposed quite simple devices deployed over a large area on mountain altitudes is an attractive and a cost effective tool opening a new opportunity to EAS research. Instead of an expensive and complicated hadronic calorimeter, one can spread a number of thermal neutron scintillator detectors over a large area to obtain information on hadrons of EAS.

In this concern, we suggest Aragats research station equipped with advanced technical and scientific infrastructure as a possible site for a new surface array. It is possible to locate EN scintillator within each of ~ 300 housings of plastic scintillators equipped with photomultipliers and high voltage supplies belonging to the finishing it's duty GAMMA array.

ACKNOWLEDGEMENT

The author thanks the staff of the Aragats Space Environmental Center for the uninterrupted operation of Aragats research station facilities. The master students of Yerevan Physics Institute made the calculations of multiplicity distributions. They express gratitude to their teachers introducing them in the EAS physics.

REFERENCE

Aharonyan, F.A., Akhperjanian, A.G., Bazer-Bachi, A.R., et al. Primary particle acceleration above 100 TeV in the shell-type supernova remnant RXJ1713. 7 – 3446 with deep HESS observations. *Astron. Astrophys.* 464, 235–243, 2007.

Ackermann M., et al., FERMI-LAT Collaboration, *Science* 339 (2013) 807.

Aglietta, M., Alessandro, B., Antonioli, P., et al., (2004), The cosmic ray primary composition between 1015 and 1016 eV from Extensive Air Showers electromagnetic and TeV muon data. *Astroparticle Physics*, 20(6),

Antoni T., Apel W.D., Badea F., et al., A non-parametric approach to infer the energy spectrum and the mass composition of cosmic rays, *Astroparticle Physics* 16 (2002), 245-263.

Antonova A.P., Chubenko A.P., Kruychikov S.V., et al., Anomalous time structure of extensive air shower particle flows in the knee region of primary cosmic ray spectrum, *J. Phys. G: Nucl. Part. Phys.* 28 (2002) 251–266.

Bartoli B., Bernardini P., Be X.J., et al., Detection of thermal neutrons with the PRISMA-YBJ array in extensive air showers selected by the ARGO-YBJ experiment, *Astroparticle physics*, 81(2016) 49-60.

Balabin Y.V., Gvozdevsky B.B., Vashenyuk E.V., Dzhappuev D.D., EAS hadronic component as registered by a neutron monitor, *Astrophys. Space Sci. Trans.* 7 (2011) 507–510.

Chilingarian A. A., Statistical Decisions under Nonparametric a priori information, *Computer Physics Communication*, 54, 381, 1989.

A.Chilingarian, G.Zazyan, On the possibility of investigation of the mass composition and energy spectra of primary cosmic ray (PCR) in the energy range

from 1015 to 1017 eV using EAS data, *Nuovo Cimento C, Serie 1* (ISSN 0390-5551), vol. 14 C, Nov.-Dec. 1991, p. 555-568.

A.Chilingarian , G. Gharagozyan , G. Hovsepyan , S. Ghazaryan , L. Melkumyan , and A. Vardanyan, *Light and Heavy Cosmic Ray Mass Group Energy Spectra as Measured by the MAKE T-ANI Detector*, *Astrophysical Journal*, 603:L29-L32, 2004.

Chilingaryan A. A. (1994), Neural Classification Technique for Background Rejection in High Energy Physics Experiments *Neurocomputing*, 6, 497.

Chilingarian A. A. (1995), Detection of Weak Signals Against Background using Neural Network Classifiers *Pattern Recognition Letters*, 16, 333-338.

A.Chilingarian , G. Gharagozyan , G. Hovsepyan , S. Ghazaryan , L. Melkumyan , A. Vardanyan, E.Mamidjanyan, V.Romakhin, and S. Sokhoyan Study of extensive air showers and primary energy spectra by MAKET-ANI detector on Mount Aragats, *Astroparticle Physics*, Volume 28, Issue 1, September 2007, Pages 58–71.

Horandel J., (2004), Models of the Knee in the Energy Spectrum of Cosmic Rays, *Astroparticle Physics* 21 (2004) 241–265.

Giuliani, A., et al., AGILE Collaboration, Direct Evidence for Hadronic Cosmic-Ray Acceleration in the Supernova Remnant IC 443, *Astrophys. J.* 742 (2011) L30.

Kampert, K.H. for KASCADE Grande collaboration, Cosmic rays in the 'knee'-region - recent results from KASCADE - KASCADE Grande Collaboration, *Acta Phys.Polon.* B35 (2004) 1799-1812.

Stenkin Yu.V., Thermal neutrons in EAS: a new dimension in EAS study, *Nucl. Phys. B (Proc. Suppl.)* 175–176 (2008) 326.

Stenkin Yu.V., Valdés-Galicia J.F., On the Neutron bursts origin, *Mod. Phys. Lett. A* 17 (26) (2002) 1745.

Takahashi, T., Tanaka, T., Uchiyama, Y., et al. Measuring the Broadband X-ray spectrum from 400 eV to 40 keV in the southwest part of the Supernova Remnant RX J1713.7-3946.. *Publ. Astron. Soc. Jpn.* 60, S131–S162, 2008.

Uchiyama, Y., Aharonyan, F., Tanaka, T., et al. extremely fast acceleration of cosmic rays in a supernova remnant. *Nat. Lett.* 449 (4), doi: 10.1038/nature06210, 2007.

Vardanyan A., A.Chilingarian, M.Roth for the KASCADE collaboration, (1999), in Proceedings of the workshop ANI 99, Nor-Amberd, 1999, Preprint FZK 672, p.23.

Constraining the source properties of individual Terrestrial Gamma-ray Flashes

B. Mailyan¹, M. Briggs^{1,2}, E. Cramer¹, G. Fitzpatrick¹, O. Roberts³, M. Stanbro², V. Connaughton⁴, S. McBreen³, P. Bhat¹ and J. Dwyer⁵

1. *Center for Space Plasma and Aeronomic Research, The University of Alabama in Huntsville, 320 Sparkman Dr. Huntsville, Alabama 35805, USA*
2. *Department of Space Science, The University of Alabama in Huntsville, 320 Sparkman Dr. Huntsville, Alabama 35805, USA*
3. *School of Physics, University College Dublin, Belfield, Stillorgan Road, Dublin 4, Ireland*
4. *Universities Space Research Association, 320 Sparkman Dr. Huntsville, Alabama 35805, USA*
5. *Department of Physics and Space Science Center (EOS), University of New Hampshire, Durham, New Hampshire, USA*

Abstract. We report on the spectral analysis of two individual Terrestrial Gamma-ray Flashes (TGFs) observed with the Fermi Gamma-ray Burst Monitor (GBM). The large GBM sample provides some events suitable for individual spectral analysis: sufficiently bright, localized by ground-based radio, and with the gamma rays reaching a detector unobstructed. We account for the low counts in individual TGFs by using Poisson likelihood, and we also consider instrumental effects. The data are fit with models obtained from Monte Carlo simulations of the large scale Relativistic Runaway Electron Avalanche (RREA) model, including propagation through the atmosphere.

Two beaming geometries were considered: In one, the photons retain the intrinsic distribution from scattering (narrow), and in the other, the photons are smeared into a wider beam (wide). Large-scale RREA models can accommodate both narrow and wide beams, with narrow beams suggest large-scale RREA in organized electric fields while wide beams may imply converging or diverging electric fields. Wide beams are also consistent with acceleration in the electric fields of lightning leaders, but the TGFs that favor narrow beam models appear inconsistent with some lightning leader models.

1. INTRODUCTION

High-energy atmospheric phenomena include Terrestrial Gamma-ray Flashes (TGFs), which are usually observed with near-Earth low orbit satellites [Fishman et al., 1994; Smith et al., 2005; Briggs et al., 2010; Marisaldi et al., 2010], X-ray bursts from negative cloud-to-ground discharges observed from the ground [e.g. Dwyer et al., 2005], and Thunderstorm Ground Enhancements (TGEs) or gamma-ray glows [Torii et al., 2002; Tsuchiya et al., 2009; Chilingarian et al., 2010, 2012, 2013; Kelley et al., 2015]. A review of the various high-energy phenomena is given in Dwyer et al. [2012a].

TGFs are short, sub-millisecond bursts of gamma-ray radiation, which are believed to be generated due to the bremsstrahlung of electrons that have been accelerated to relativistic velocities in the high electric fields of thunderstorms. The basic idea of particle acceleration in atmospheric electric fields was first suggested by Wilson [1925]. Gurevich et al. [1992] developed the idea further by describing a mechanism by which avalanche multiplication could occur. There are several competing theories for the production of TGFs. To explain the extremely high brightness of TGFs, Dwyer [2012] proposed the large-scale Relativistic Feedback Discharge (RFD) mechanism, which includes the physics of electrons, gamma rays and back-scattering positrons in the avalanche and significantly increases the particle multiplication. In this model, the acceleration occurs in the large scale electric field produced by thunderstorms or by lightning. An alternative theory is that electrons are accelerated at the tips of lightning leaders via the cold runaway process

[Stanley et al., 2006; Carlson et al., 2009; Shao et al., 2010; Celestin and Pasko, 2011; Babich et al., 2015]. There are also models in which the seed electrons are provided by lightning leader tips while the acceleration takes place in

large-scale electric fields [Moss et al., 2006; Dwyer et al., 2012a]. The models differ in whether or not lightning leaders are the sources of the seed electrons, and whether the acceleration takes place in large-scale electric fields or in small-scale regions at the tips of lightning leaders. For our purposes, the more important characteristic is the acceleration site since the beam width can depend on the geometry of the electric field that accelerates the electrons.

As TGFs are observed at large distances (hundreds of km) from the source, only a small number of photons will typically reach the detectors. Often, the data from different TGFs are superimposed to get enough statistics for spectral analysis. Dwyer and Smith [2005] generated such a cumulative spectrum, using 289 Reuven Ramaty High Energy Solar Spectroscopic Imager (RHESSI) TGFs and compared it to Monte Carlo models. The average source altitude of TGFs estimated in this way was 15-21 km, the exact value depending on the beaming of the gamma rays in the Monte Carlo simulations. Xu et al. [2012] estimated a lower source altitude of 12 km for the same dataset, assuming the alternative acceleration mechanism by lightning leaders. Based on the cumulative count spectrum analysis of 130 TGFs observed by Astrorivelatore Gamma ed Immagini Leggero

(AGILE), Tavani et al. [2011] found a significant power law emission component reaching up to 100 MeV. However, Marisaldi et al. [2014] note that such high-energy emission is visible only in ~15 % of the TGFs observed by AGILE.

In this paper, for the first time, we present the individual spectral analysis of two bright TGFs detected by the Gamma-ray Burst Monitor (GBM) on the Fermi satellite. Unlike previous studies, which were adding counts from different events, smearing out the spectral diversity, we fit the individual events using Relativistic Electron Avalanche Model (REAM) [Dwyer, 2003].

2. DATA AND METHODS

The GBM instrument is made up of 14 individual, uncollimated scintillators, 12 thallium-doped sodium iodide (NaI(Tl)) and two bismuth germanate (BGO) detectors [Meegan et al., 2009]. The NaI (Tl) detectors are positioned in clusters of three around the spacecraft, so that any cosmic source unoccluded by the Earth will illuminate at least one cluster. The BGOs are positioned on opposite sides of the spacecraft. The effective energy range is 10-1000 keV and 0.2-40 MeV for the NaI (Tl) and BGO detectors respectively, and the spectra are divided into 128 pseudo-logarithmically spaced energy channels. The relative timing resolution of the measurements is 2 μ s, which is an important factor for studying sub-millisecond bursts like TGFs. The nominal dead time is 2.6 μ s. However, if a count is registered in the overflow channel (>1 MeV for the NaI (Tl) and >40 MeV for the BGO detectors), the dead time is 10.4 μ s.

During the period from 2008-2015, GBM has detected about 3400 TGFs, of which ~ 1200 have associated radio signals that allow their localization. The TGFs without a radio association may occur anywhere within about 800 km of the sub-spacecraft position. The TGF detection rate significantly increased after new data collection modes and analysis methods were introduced in 2012. These include an updated onboard triggering algorithm and off-line search algorithms of the high time resolution data [Briggs et al., 2013]. In this paper, we analyze the spectra of TGFs using the data from BGO detectors, which have a broad energy range and large effective area.

We also made corrections for the effects of dead time and pulse pileup, taking into account the extremely short durations and brightness of the flashes. Spectral distortions may occur caused by multiple photons hitting the detector close in time (within ~ 2.6 μ s for GBM BGO detectors). As the GBM electronics pulse shape is bipolar, the overlapping pulses may be observed as a higher (peak pileup) or lower (tail pileup) energy counts. These contributions are calculated analytically using the method described in Chaplin et al. [2013], which have been verified by Monte Carlo simulations and experiments with radioactive sources

[Bhat et al., 2014]. In addition to this, a more realistic pulse shape was used in the calculations, which is an input for the method described by Chaplin et al. [2013].

The details of the spectral fitting procedure can be found in Mailyan et al., [2016].

3. TGF120120412

In Figure 1, the measured and simulated differential count spectra histograms are presented for TGF120120412, which occurred at a distance of 475 km from the spacecraft nadir. The measurements are compared with 8 different models, which have source altitudes ranging from 11.6 to 20.2 km. When pulse pile-up correction is not used [see the details in Mailyan et al., 2016], the rate is not fit, but is instead calculated so that the model total counts equal the total observed counts.

The observed spectrum is very soft and there are no photons above 3 MeV. This can be explained by the distance from the source to the detectors. Only gamma rays scattered at large distances from the avalanche axis are observed. The effect of the spectral softening with increasing offset distance, was studied statistically in previous works (Hazelton et al. [2009], Østgaard et al. [2008], Gjesteland et al. [2010], Celestin and Pasko [2012], Fitzpatrick et al. [2014]). The expected pulse pileup corrections for this TGF are minor. The analysis of the pulse pileup corrections showed that the incident photon rate was relatively low, and that corrections are not required to obtain a good fit.

For analyses with and without the pulse pileup filter, the narrow models provide the best fit and the wide models can be rejected. Having broader angular distributions, wide models provide more high energy photons at large nadir-source offsets. In narrow models, because of a larger contribution from particles scattered at large angles, the photon spectrum is much softer, which is the case for TGF120120412. In Figure 2, $-2 \log L$ values (the quality function describing the goodness of the fit obtained from the likelihood analysis) are presented for all 8 models after pulse pileup corrections. As we can see all models predict relatively low rates and consequently small pulse pileup effects

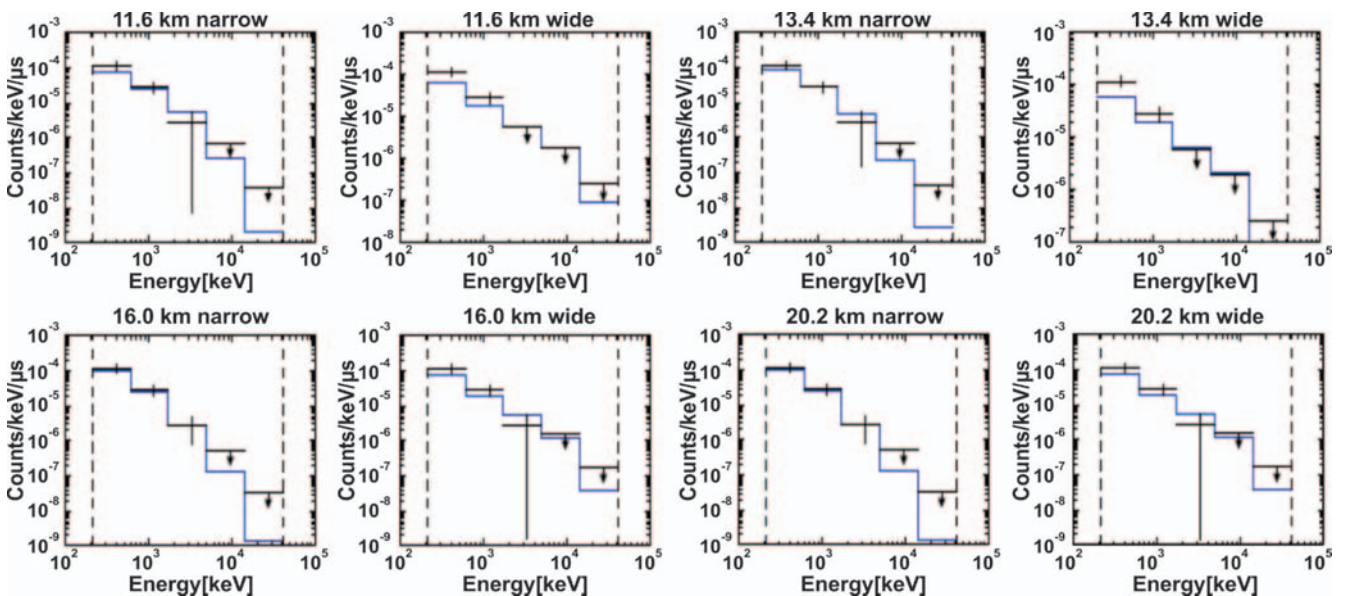


Figure 1. Spectral histograms of the measured TGF120120412 and 11.6, 13.4, 16.0, 20.2 km altitude wide and narrow beam models. Histograms are compared by scaling total number of counts in simulation to be equal the measured number. As data values in some histogram bins for some TGFs are equal to zero, model values are used to estimate the error bars. The narrow beam models are in a better agreement with the data. The corresponding likelihood analysis results are shown in Figure 2.

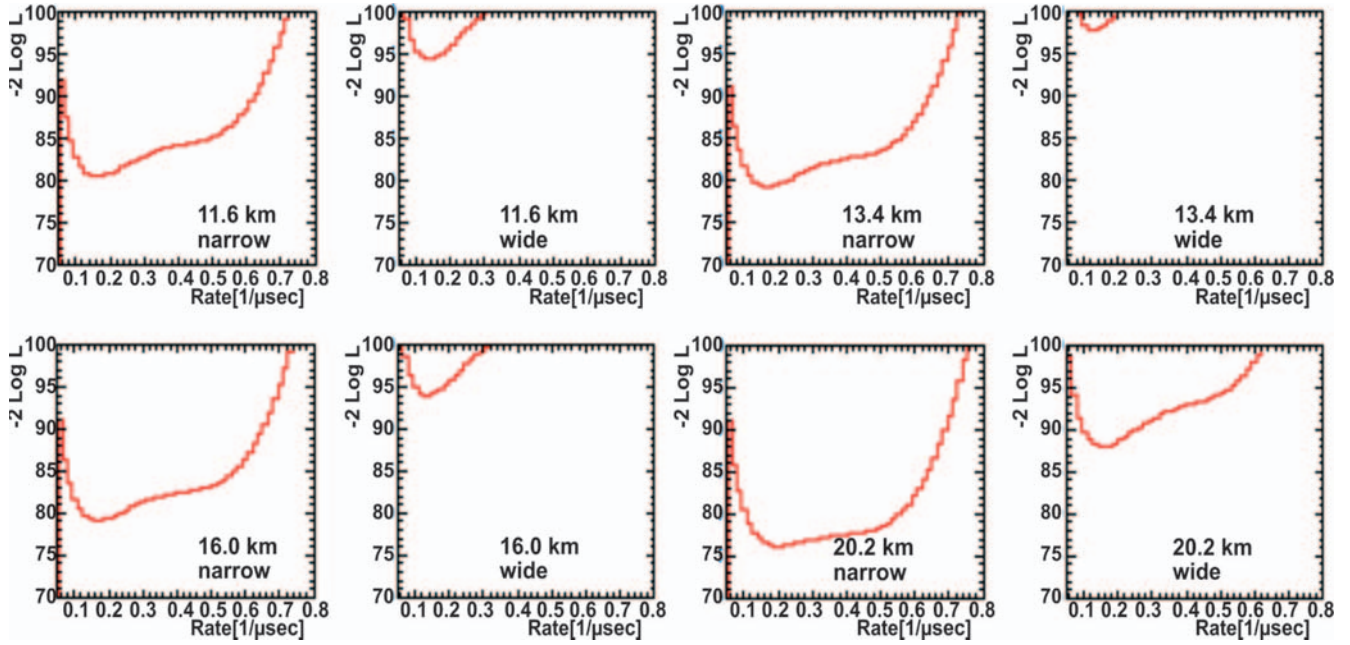


Figure 2. The likelihood analysis results for the different models for the TGF120120412, showing the variation in $-2 \text{ Log } L$ as a function of rate. Smaller values of $-2 \text{ Log } L$ meaning better fits are observed for narrow models. The rate corresponding to the minimum is about 0.15 and 0.2 photons per μsec for 10 and 20 km altitude models respectively. There is a second, less probable minimum at rates higher than 0.5 photons/ μsec .

4. TGF100909539

This bright TGF occurred relatively close to the footprint of Fermi, at a distance of 102 km. In Figure 3, the observed TGF100909539 spectrum and the 11.6 km narrow model spectra with and without pulse pileup are shown. This is a spectrally hard TGF, with 26 counts in BGO-1. The analysis is a more complicated due to the higher count rates and consequent spectral distortion owing to the effects of pulse pileup effects. The model with pulse pileup corrections shows much better agreement with the data, unlike no pulse pileup model, which shows an excess of counts at low energies. The best fit is obtained for an incident rate of $\sim 0.45 \text{ ph}/\mu\text{s}$.

In Figure 4, the measured and simulated differential count spectra histograms are presented for TGF100909539 for all models after pulse pile-up corrections. The best fit is the narrow beam, 11.6 km altitude model. The application of pulse pileup corrections reduces the excess at lower energies, resulting in a better agreement between the models and the data (Figure 3). High source altitude models are less favorable, because of their softness compared to the observed spectrum.

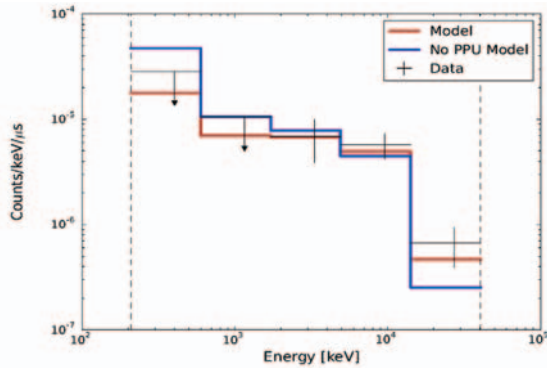


Figure 3. Observed counts spectrum for TGF100909539 (in black), with 11.6 km narrow beam model spectrum overlaid. The red curve is the model spectrum, and the blue is the same curve without pulse pileup effects modelled. As can be seen, taking into account pulse pile-up effects significantly improves the fit.

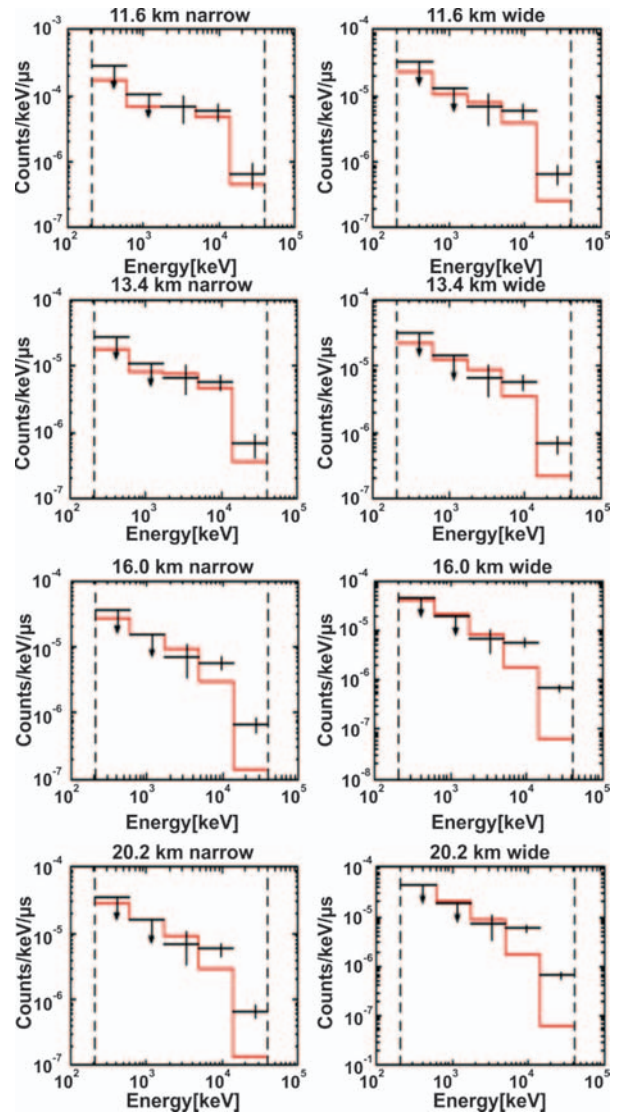


Figure 4. Spectral histograms of TGF100909539, fit with the 11.6, 13.4, 16.0, 20.2 km altitude, wide and narrow models after pulse pile-up corrections. Narrow beam, low altitude models best fit the data.

CONCLUSION

In this work, we have presented the first analysis of individual TGF spectra observed with GBM. The observed spectra are diverse, implying that summed analyses miss important information. Comparisons of Monte Carlo simulations to the data allow us to study the effect of modifying the source altitude and beaming geometry. In spite of the complications arising due to the low statistics and the distortion from pulse pileup, our analysis has placed constraints on the photon beam geometry, altitude and incident rate.

The good agreement of the modeled and measured individual TGFs indicates that the Relativistic Runaway Electron Avalanche (RREA) model [Gurevich et al., 1992; Dwyer, 2003, 2007] is a plausible mechanism for explaining the particle acceleration processes in the Earth's atmosphere. Future work will include the comparative studies of other models, assuming other 517 mechanisms of particle acceleration and electric field parameters.

ACKNOWLEDGEMENT

The Fermi GBM Collaboration acknowledges the support of NASA in the United States and DRL in Germany. We thank NASA for support from Fermi Guest Investigation NNX13AO89G. EC acknowledges NSF support, Grant number 1524533. JRD acknowledges NSF grant AGS-1519236. OR acknowledges support from Science Foundation Ireland under Grant 12/IP/1288. The authors wish to thank the World Wide Lightning Location Network (<http://wwlln.net>), a collaboration among over 50 universities and institutions, for providing the lightning location data used in this paper.

REFERENCE

Babich, L., E. Bochkov, I. Kutsyk, T. Neubert, and O. Chanrion (2015), A model for electric field enhancement in lightning leader tips to levels allowing x-ray and γ -ray emissions, *Journal of Geophysical Research: Space Physics*, 120 (6), 5087–5100.

Bhat, P. N., G. Fishman, M. Briggs, V. Connaughton, C. Meegan, W. Paciasas, C. Wilson-Hodge, and S. Xiong (2014), Fermi gamma-ray burst monitor detector performance at very high counting rates, *Experimental Astronomy*, 38 (1-2), 331–357.

Briggs, M., G. Fishman, V. Connaughton, P. N. , W. Paciasas, R. Preece, C. Wilson-Hodge, V. Chaplin, R. Kippen, A. von Kienlin, et al. (2010), First results on terrestrial gamma ray flashes from the fermi gamma-ray burst monitor, *Journal of Geophysical Research: Space Physics* (1978–2012), 115 (A7).

Briggs, M. S., S. Xiong, V. Connaughton, D. Tierney, G. Fitzpatrick, S. Foley, J. E. Grove, A. Chekhtman, M. Gibby, G. J. Fishman, et al. (2013), Terrestrial gamma-ray flashes in the fermi era: Improved observations and analysis methods, *Journal of Geophysical Research: Space Physics*, 118 (6), 3805–3830.

Carlson, B. E., N. G. Lehtinen, and U. S. Inan (2009), Terrestrial gamma ray flash production by lightning current pulses, *J. Geophys. Res.*, 114, A00E08, doi:10.1029/2009JA014531.

Celestin, S., and V. P. Pasko (2011), Energy and fluxes of thermal runaway electrons produced by exponential growth

of streamers during the stepping of lightning leaders and in transient luminous events, *Journal of Geophysical Research: Space Physics* (1978–2012), 116 (A3).

Celestin, S., and V. P. Pasko (2012), Compton scattering effects on the duration of terrestrial gamma-ray flashes, *Geophysical Research Letters*, 39 (2).

Chaplin, V., N. P. Bhat, M. S. Briggs, and V. Connaughton (2013), Analytical modeling of pulse-pileup distortion using the true pulse shape; applications to fermi-gbm, *Nuclear Instruments and Methods in Physics Research Section A: Accelerators, Spectrometers, Detectors and Associated Equipment*, 717, 21–36.

Chilingarian, A., A. Daryan, K. Arakelyan, A. Hovhannisyan, B. Mailyan, L. Melkumyan, G. Hovsepian, S. Chilingaryan, A. Reymers, and L. Vanyan (2010), Ground-based observations of thunderstorm-correlated fluxes of high-energy electrons, gamma rays, and neutrons, *Phys. Rev. D*, 82 (4), 043,009.

Chilingarian, A., B. Mailyan, and L. Vanyan (2012), Recovering of the energy spectra of electrons and gamma rays coming from the thunderclouds, *Atmospheric research*, 114, 1–16.

Chilingarian, A., L. Vanyan, and B. Mailyan (2013), Observation of thunderstorm ground enhancements with intense fluxes of high-energy electrons, *Astroparticle Physics*, 48, 1–7.

Dwyer, J. (2003), A fundamental limit on electric fields in air, *Geophysical Research Letters*, 30 (20).

Dwyer, J., and D. Smith (2005), A comparison between Monte Carlo simulations of runaway breakdown and terrestrial gamma-ray flash observations, *Geophysical Research Letters*, 32 (22).

Dwyer, J., H. Rassoul, M. Al-Dayeh, L. Caraway, A. Chrest, B. Wright, E. Kozak, J. Jerauld, M. Uman, V. Rakov, et al. (2005), X-ray bursts associated with leader steps in cloud-to-ground lightning, *Geophysical research letters*, 32 (1).

Dwyer, J. R. (2007), Relativistic breakdown in planetary atmospheres, *Physics of Plasmas* (1994-present), 14 (4), 042,901.

Dwyer, J. R. (2012), The relativistic feedback discharge model of terrestrial gamma ray flashes, *Journal of Geophysical Research: Space Physics* (1978–2012), 117 (A2).

Dwyer, J. R., D. M. Smith, and S. A. Cummer (2012a), High-energy atmospheric physics: Terrestrial gamma-ray flashes and related phenomena, *Space Science Reviews*, 173 (1-4), 133–196.

Fishman, G. J., P. N. Bhat, R. Mallozzi, J. M. Horack, T. Koshut, C. Kouveliotou, G. N. Pendleton, C. A. Meegan, R. B. Wilson, W. S. Paciasas, S. J. Goodman, and H. J. Christian (1994), Discovery of intense gamma-ray flashes of atmospheric origin, 625 *Science*, 59, 1313–1316.

Fitzpatrick, G., E. Cramer, S. McBreen, M. S. Briggs, S. Foley, D. Tierney, V. L. Chaplin, V. Connaughton, M. Stanbro, S. Xiong, et al. (2014), Compton scattering in

- terrestrial gamma-ray flashes detected with the fermi gamma-ray burst monitor, *Physical Review D*, 90 (4), 043,008.
- Gjesteland, T., N. Østgaard, P. Connell, J. Stadsnes, and G. Fishman (2010), Effects of dead time losses on terrestrial gamma ray flash measurements with the burst and transient source experiment, *Journal of Geophysical Research: Space Physics* (1978–2012), 115 (A5).
- Gurevich, A., G. Milikh, and R. Roussel-Dupre (1992), Runaway electron mechanism of air breakdown and preconditioning during a thunderstorm, *Physics Letters A*, 165 (5), 463–468.
- Hazelton, B., B. Grefenstette, D. Smith, J. Dwyer, X.-M. Shao, S. Cummer, T. Chronis, E. Lay, and R. Holzworth (2009), Spectral dependence of terrestrial gamma-ray flashes on source distance, *Geophysical Research Letters*, 36 (1).
- Kelley, N. A., D. M. Smith, J. R. Dwyer, M. Splitt, S. Lazarus, F. Martinez-McKinney, B. Hazelton, B. Grefenstette, A. Lowell, and H. K. Rassoul (2015), Relativistic electron avalanches as a thunderstorm discharge competing with lightning, *Nature communications*, 6.
- Mailyan, B. G., M. S. Briggs, E. S. Cramer, G. Fitzpatrick, O. J. Roberts, M. Stanbro, V. Connaughton, S. McBreen, P. N. Bhat, and J. R. Dwyer (2016), The spectroscopy of individual terrestrial gamma-ray flashes: Constraining the source properties, *Journal of Geophysical Research: Space Physics* 121(11), 11346–11363.
- Marisaldi, M., F. Fuschino, C. Labanti, M. Galli, F. Longo, E. Del Monte, G. Barbiellini, M. , A. Giuliani, E. Moretti, et al. (2010), Detection of terrestrial gamma ray flashes up to 40 mev by the agile satellite, *Journal of Geophysical Research: Space Physics* (1978–2012), 115 (A3).
- Marisaldi, M., F. Fuschino, M. , S. Dietrich, C. Price, M. Galli, C. Pittori, F. Verrecchia, S. Mereghetti, P. Cattaneo, et al. (2014), Properties of terrestrial gamma ray flashes detected by agile mcal below 30 mev, *Journal of Geophysical Research: Space Physics*, 119 (2), 1337–1355.
- Meegan, C., G. Lichti, P. N. Bhat, E. Bissaldi, M. S. Briggs, V. Connaughton, R. Diehl, G. Fishman, J. Greiner, A. S. Hoover, et al. (2009), The fermi gamma-ray burst monitor, *The Astrophysical Journal*, 702 (1), 791.
- Moss, G. D., V. P. Pasko, N. Liu, and G. Veronis (2006), Monte carlo model for analysis of thermal runaway electrons in streamer tips in transient luminous events and streamer zones of lightning leaders, *Journal of Geophysical Research: Space Physics* (1978–2012), 111 (A2).
- Østgaard, N., T. Gjesteland, J. Stadsnes, P. Connell, and B. Carlson (2008), Production altitude and time delays of the terrestrial gamma flashes: Revisiting the burst and transient source experiment spectra, *Journal of Geophysical Research: Space Physics* (1978–2012), 113 (A2).
- Shao, X.-M., T. Hamlin, and D. M. Smith (2010), A closer examination of terrestrial gamma-ray flash-related lightning processes, *Journal of Geophysical Research: Space Physics*, 115 (A6).
- Smith, D. M., L. I. Lopez, R. P. Lin, and C. P. Barrington-Leigh (2005), Terrestrial gamma-ray flashes observed up to 20 mev, *Science*, 307, 1085–1088.
- Stanley, M. A., X.-M. Shao, D. M. Smith, L. I. Lopez, M. B. Pongratz, J. D. Harlin, M. Stock, and A. Regan (2006), A link between terrestrial gamma-ray flashes and intracloud lightning discharges, *Geophysical research letters*, 33 (6).
- Tavani, M., M. Marisaldi, C. Labanti, F. Fuschino, A. Argan, A. Trois, P. Giommi, S. Colafrancesco, C. Pittori, F. Palma, et al. (2011), Terrestrial gamma-ray flashes as powerful particle accelerators, *Physical review letters*, 106 (1), 018,501.
- Torii, T., M. Takeishi, and T. Hosono (2002), Observation of gamma-ray dose increase associated with winter thunderstorm and lightning activity, *Journal of Geophysical Research: Atmospheres* (1984–2012), 107 (D17), ACL–2.
- Tsuchiya, H., T. Enoto, T. Torii, K. Nakazawa, T. Yuasa, S. Torii, T. Fukuyama, T. Yamaguchi, H. Kato, M. Okano, et al. (2009), Observation of an energetic radiation burst from mountain-top thunderclouds, *Physical review letters*, 102 (25), 255,003.
- Wilson, C. T. (1925), The acceleration of β -particles in strong electric fields such as those of thunderclouds, in *Mathematical Proceedings of the Cambridge Philosophical Society*, vol. 22, pp. 534–538, Cambridge Univ Press.
- Xu, W., S. Celestin, and V. P. Pasko (2012), Source altitudes of terrestrial gamma-ray flashes produced by lightning leaders, *Geophysical Research Letters*, 39 (8)

Results of TGE Study in 0.03-10 MeV Energy Range in Ground Experiments near Moscow and Aragats

V. Bogomolov^{1,2}, A. Chilingarian³, G. Garipov¹, G. Hovsepyan³, A. Iyudin¹, T. Karapetyan³, A. Kovalenko^{1,2}, I. Maximov^{1,2}, E. Mntasakanyan³, M. Panasyuk^{1,2}, K. Saleev^{1,2}, S. Svertilov^{1,2}

1. Skobeltsyn Institute of Nuclear Physics, Moscow State University. Moscow, Russia

2. Physical Department of Moscow State University. Moscow, Russia

3. A.Alikhanyan National Lab (Yerevan Physics Institute), 2, Alikhanyan Brothers, Yerevan 0036, Armenia

Abstract. Ground-based experiments with scintillator gamma-spectrometers were conducted to study the spectral, temporal and spatial characteristics of TGEs as well, as to search the fast hard X-ray and gamma-ray flashes possibly appearing at the moment of lightning. The time of each gamma-quantum interaction was recorded with ~ 15 us accuracy together with detailed spectral data. The measurements are similar to ones reported at TEPA-2015 but some important improvement of the instruments was done for 2016 season. First, GPS module was used to synchronize the instrument time with UTC. The accuracy of such synchronization allows one to look at the gamma-ray data at the moment of lightning fixed by radio-wave detector or any other instrument. Second, the energy range of gamma-spectrometers was shifted to higher energies where the radiation of natural isotopes is absent. In this case one can see background changes connected with particles accelerated in thundercloud together with the background increases during the rain caused by Rn-222 daughters.

Long-term measurements with two instruments placed in different points of Moscow region were done in 2016 season. First one based on CsI (TI) 80x80 mm has energy range 0.03-6 MeV. The range of the second one based on CsI (TI) 100x100 mm is 0.05-10 MeV. A dozen of thunderstorms with increase of Rn-222 radiation were detected but no significant increase of gamma-ray flux above 3.2 MeV was observed at these periods.

A lot of data was obtained from the experiment with small gamma-ray spectrometer (40x40 mm NaI (TI) at mountain altitude in Armenia at Aragats station. The analysis of readings during the TGE periods indicates on the presence of Rn-222 radiation in low-energy range ($E < 1$ MeV). The detector was improved during TEPA-2016. New 50x50 mm NaI (TI) crystal was used and the energy range was prolonged up to 5 MeV. Exact timing with GPS-sensor was added and fast recording of the output signal at the moments of triggers from UV flash detector was provided. The first results of measurements with this spectrometer in autumn 2016 as well as the data of a new CsI (TI) rectangular detector working with similar electronics will be discussed in the final part of the paper.

1. INTRODUCTION

The gamma-radiation additional to constant background often appears during thunderstorms. The detected gammas are mostly described as the bremsstrahlung radiation of the electrons accelerated in large electric fields existing in thunderclouds. Spectral characteristics can be described in general by the model of relativistic electrons avalanche (Gurevich, 1992, Dwyer, 2012a).

Phenomena in gamma rays connected with atmospheric electricity are observed in wide range of time scale including fast flashes in sub-millisecond range (so-called Terrestrial gamma flashes (TGFs) (Briggs et al, 2013) and such slow phenomena as so-called Thunderstorm ground enhancements (TGEs) lasting up to several hours (Chilingarian, 2014, 2015a). TGFs are usually studied in orbital experiments with gamma spectrometers working in "classical" energy range from several hundreds of keV to several MeV, but there are several observations of TGFs from lightning at the ground level (Dwyer et al, 2012b). It must be noted that the radiation from TGFs is hard up to several tens of MeV. Other fast phenomenon observed in past few years is the termination of TGE at the moment of lightning (Chilingarian et al, 2015b). The flux of hard radiation drops to pre-TGE level during several seconds or even less.

The best conditions for study of TGEs are present in mountains because of low distance between the clouds and the detector leading to less absorption of measured radiation. Many measurements of gamma-ray and electron flux variations were made with large detectors based on organic scintillators specialized for cosmic ray study (Chilingarian, 2015a). These detectors usually measure count rates in high energy range from MeVs to GeVs and unfortunately can't

provide accurate spectral measurements of gamma radiation in energy range of several hundred keV and below (Chilingarian et.al. 2013). To complete the observations in low energy range well-calibrated detectors based on scintillator crystals are needed. It is very important because a lot of gamma-ray flux variations in the range $E < 2.5$ MeV is caused by changes of Rn-222 concentration connected with rainfalls during thunderstorms (Bogomolov et.al. 2015). Energy resolution must be suitable for detection of discrete gamma-ray lines produced by the decay of radioactive isotopes in order to control Rn-222 and its daughter concentration and to make on-line calibration of the spectrometer during the experiment with background lines. The instruments must have stable (up to $\sim 1\%$) characteristics for long-lasting measurements as well as enough time resolution to detect possible short flashes.

In this paper the results of measurements in Moscow region and in Armenia made with gamma-ray spectrometers produced in SINP MSU will be presented and discussed.

2. DESIGN AND CHARACTERISTICS OF GAMMA-RAY SPECTROMETERS

All of the instruments used in this work are scintillator gamma-ray spectrometers based on common non-organic scintillators NaI (TI) or CsI (TI). Electronic circuits used in these spectrometers can work with single-crystal detectors as well as with phoswich multilayer detectors providing determination of the crystal where interaction took place by pulse-shape analysis. Such kind of analysis also allows one to remove imitations of gamma-events by lightning electric pulses. One can read the detailed description of the instrument design in proceedings of TEPA-2015 (Bogomolov et al., 2015)

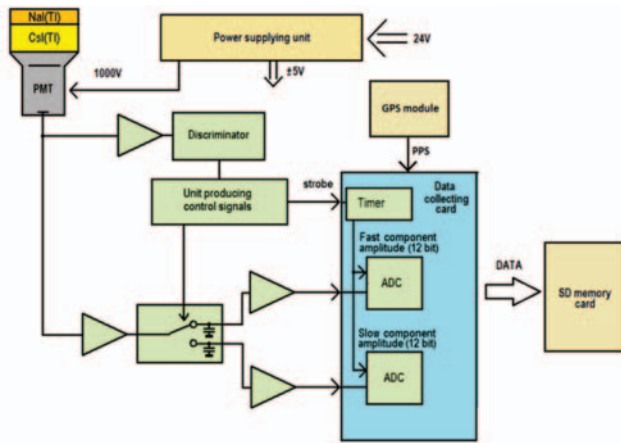


Figure 1. Structural diagram of scintillator gamma-ray spectrometer.

The structural diagram of electronics of gamma-spectrometer is presented at figure 1. It consists of “Power supplying unit” providing high voltage (~1000V) for PMT and low voltage for analog and digital electronics, “Event” card containing analog electronics for event triggering and pulse-shape analysis, and “Data collecting card” based on the board STM32F4DISCOVERY with Cortex M4 microcontroller. GPS module with PPS is used for exact timing providing synchronization of gamma-ray spectrometer readings with the world time with accuracy ~10 microseconds. Every second the output data are recorded to SD card. The data are recorded in gamma-by-gamma mode containing detailed time and amplitude data for each interaction in the detector.

Detailed spectral information present in the data allows one to make calibration with use of background gamma-ray lines observed just during the measurements. The algorithm of data processing finds the position of usually well seen 1.46 MeV background gamma-ray line of K-40. The actual instrumental channel of K-40 is calculated and stored in memory every 300s. Then the energy of each gamma-quantum is calculated in units of energy from correspondent linear formula. Such procedure allows one to minimize the effects of false variations caused by temperature drift of the detector characteristics. It is important for long-lasting observation series because day and night temperature can differ more than 20 degrees. The temperatures taken during sunny day and thunderstorm can also greatly differ.

Several gamma-ray spectrometers were produced. Two of them were used for the study of TGEs and the search for gamma-flashes from lightning in Moscow region. First one has detector based on 80x80 mm CsI(Tl) crystal coupled with Hammamatsu R1307 PMT. Results of the experiment with this spectrometer in low energies (<3000 keV) in 2015 were presented and discussed in TEPA-2015 proceedings (Bogomolov et al., 2015). In May, 2016 the range was extended up to 6000 keV and GPS module was added. So in 2016 it provides measurements in 30-6000 keV energy range with energy resolution 7.2% at 662 keV. The rotating platform and collimator mentioned in (Bogomolov et al. 2015) were not used in 2016 season.

Second spectrometer with even bigger CsI (Tl) crystal was produced. Its energy range is from 50 keV to 10 MeV with ~10% energy resolution. The results of experiments

with both spectrometers placed in summer, 2016 in two different points of Moscow region will be discussed below.

The spectrometer with considerably small NaI(Tl) detector with size 40x40 mm coupled with Russian PMT FEU-176 was used for independent measurements of TGEs on Aragats. It was designed for 20-1000 keV range. The resolution of this instrument is ~12% at 662 keV. A lot of data was obtained from October, 2015 to September, 2016. Several TGEs were detected and preliminary conclusion of presence of Rn-222 component was done. Then during TEPA-2016 the detector was improved. New NaI (Tl) crystal was used as the detecting element and the energy range was extended up to 5 MeV. The output analog signal was prepared for fast recording by “pico-scope” device by the trigger from UV flash detector or any other instrument.

One more set of electronics was designed for work with one of detectors used by the team of Aragats station. In this case no pulse-shape analysis is done and two ADCs are used for measurements with different amplification in order to extend the working range. All other principles of the device functioning are the same as described above. This electronic set was coupled with rectangular CsI (Tl) 100 x 100 x 200 mm detector. The range of the signal from the preamplifier designed by Armenian engineers corresponds to energy range up to 2 MeV. In future the range should be extended to make possible the study of TGEs in the range >3MeV where gamma-radiation from natural radioactivity is absent.

Photos of the detectors are presented at figure 2. All of gamma-ray spectrometers were calibrated with a number of radioactive sources. Some of energy spectra obtained during calibrations are presented at figure 3, 4. One can see similar background peaks corresponding the most intensive radiation of naturally occurring isotopes of K-40, Tl-208 (daughter of Th-232) and Bi-214 (daughter of Rn-222)

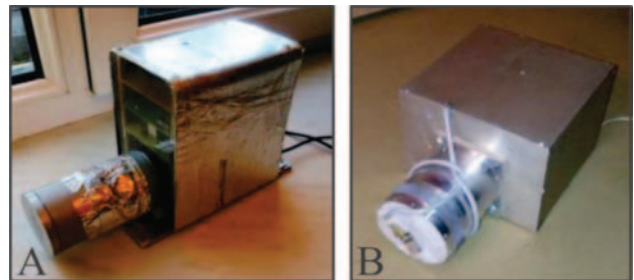


Figure 2. A) Photo of the gamma-spectrometer equipped with 50mm NaI(Tl) detector, B) Photo of the gamma-spectrometer equipped with collimated 80 mm CsI(Tl) detector. GPS sensor is placed on the detectors head.

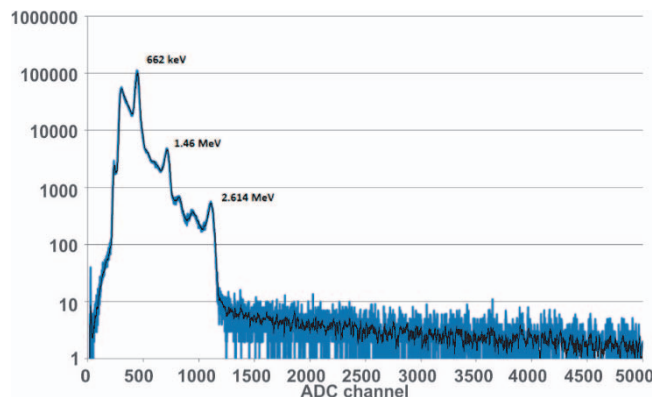


Figure 3. Calibration spectrum of Cs-137 ($E=662$ keV) obtained with 10 cm CsI(Tl) detector. Lines 1.46 MeV and 2.614 MeV correspond to naturally occurred isotopes K-40 and Tl-208.

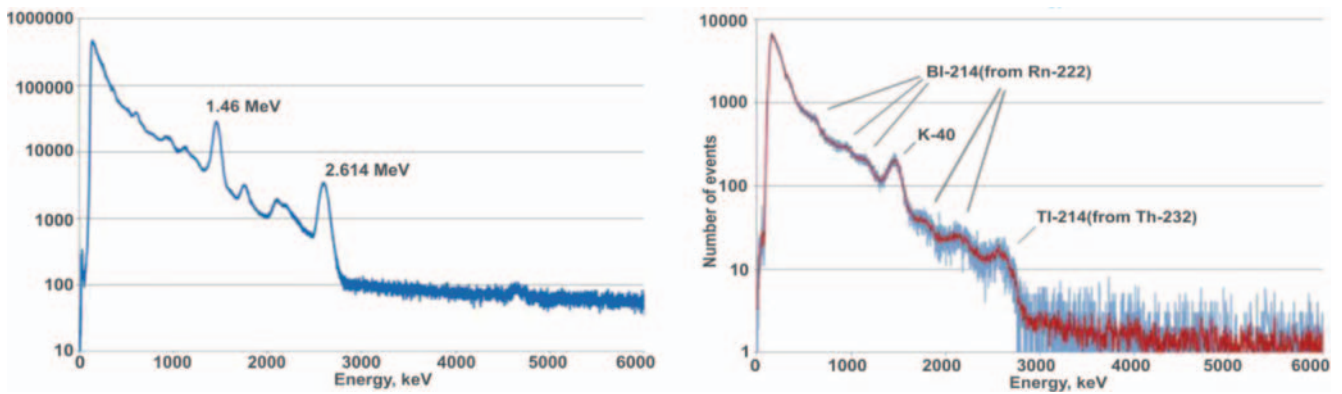


Figure 4. Background spectra obtained with 80mm CsI(Tl) detector in Moscow region (left) and 50mm NaI(Tl) detector at Aragats station (right).

3. RESULTS OF TGE MEASUREMENTS

The measurements in Moscow region were made in two points ~50 km North and North-west from Moscow. There were several thunderstorms in summer of 2016 so it was possible to compare temporal and spectral characteristics of radiation for TGEs caused by the same thunderstorm in neighbor regions. The behavior of hard radiation with energy $E > 3$ MeV is of special interest because there is no gamma-quanta from Radon daughters.

The spectrogram and time sequence of gamma-ray fluxes measured from 13.06.2016 to 17.06.2016 are presented at figure 5. The intensive thunderstorm occurred on 16.06.2016. TGE was observed from 16h to 20h UTC. It can be seen on the spectrogram that intensive additional radiation in 609-keV gamma-ray line of Bi-214 appeared during the thunderstorm. It leads to the conclusion that in this case changes of Rn-222 concentration caused by the shower are responsible for observed TGE in low energy range. One can see that no change of the gamma-ray flux is observed in 3200-6000 keV energy channel.

One more TGE was observed on 18.07.2016. Its time profile in different energy channels are presented at figure 6. One can see the increase of gamma-radiation for more than 3 hours. In most of low-energy channels the amplitude of this TGE reached 100%. The energy spectra obtained for ~10000 s during the flux maximum and during the quiet period before TGE are presented on the upper panel at figure 7. Down panel of figure 7 demonstrates the spectrum of TGE cleaned by subtraction of the background. One can see a lot of Bi-214 gamma-ray lines and conclude that most of low energy radiation was connected with Rn-222 daughters.

The difference between the mean values for TGE and background periods in the most hard channel is <1.4% that

corresponds to not significant value of 1.8 sigma. The upper limit (3-sigma level) of TGE gamma-ray flux in 3200-6000 keV energy range is $2.4 \cdot 10^{-4} \text{ cm}^{-2} \cdot \text{s}^{-1}$.

In autumn, 2016 two instruments equipped with SINP electronics started measurements of gamma-ray flux variations on Aragats station. There were no thunderstorms with lightning in October-December period, but several rainfall and snowfall events took place.

Time variations of gamma-radiation measured during rainy weather on October, 17-18 are presented at figure 8. Upper panel demonstrates the result of long-time TGE observation with NaI (Tl) detectors of Erphi group. The variations of the readings of 5 cm NaI (Tl) detector are presented on down panel of figure 8. One can see 4-hour increase of readings in different energy channels. Energy spectra of the TGE presented at figure 9 demonstrate the presence of 609-keV line that indicates the presence of Rn-222 radiation. Low panel of figure 9 shows that the flux of radiation with energy $E > 3200$ keV remains unchanged.

The time sequences presented at figure 10 show the variations observed during the winter storm. One can see that the flux increase starts together with snowfall and is observable in all detectors demonstrating similar behavior. The energy spectrum of the TGE obtained by CsI (Tl) is similar to the background one. Poor energy resolution of the detector and possible intrinsic background of the crystal do not allow one to conclude about the presence of Rn-222 daughters or other radioactivity. The upper limit of the energy range of CsI (Tl) detector is 2 Mev that is too low to make measurements in the range where the natural radioactivity is absent. It is planned to increase this energy limit in future.

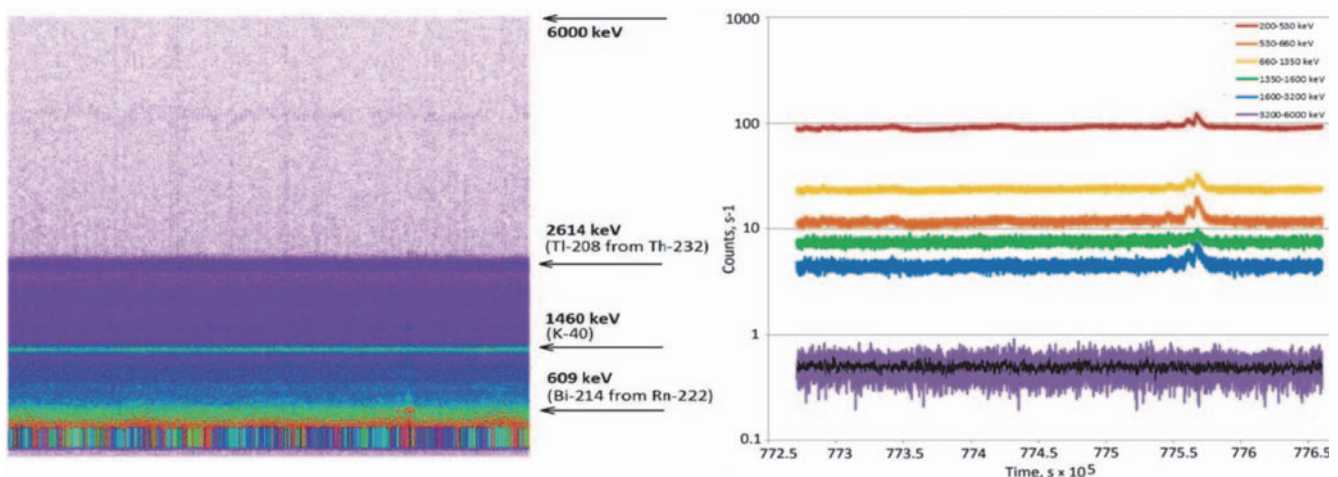


Figure 5. Spectrogram (left) and time profile in several energy channels (right) of gamma radiation measured during thunderstorm in Moscow region.

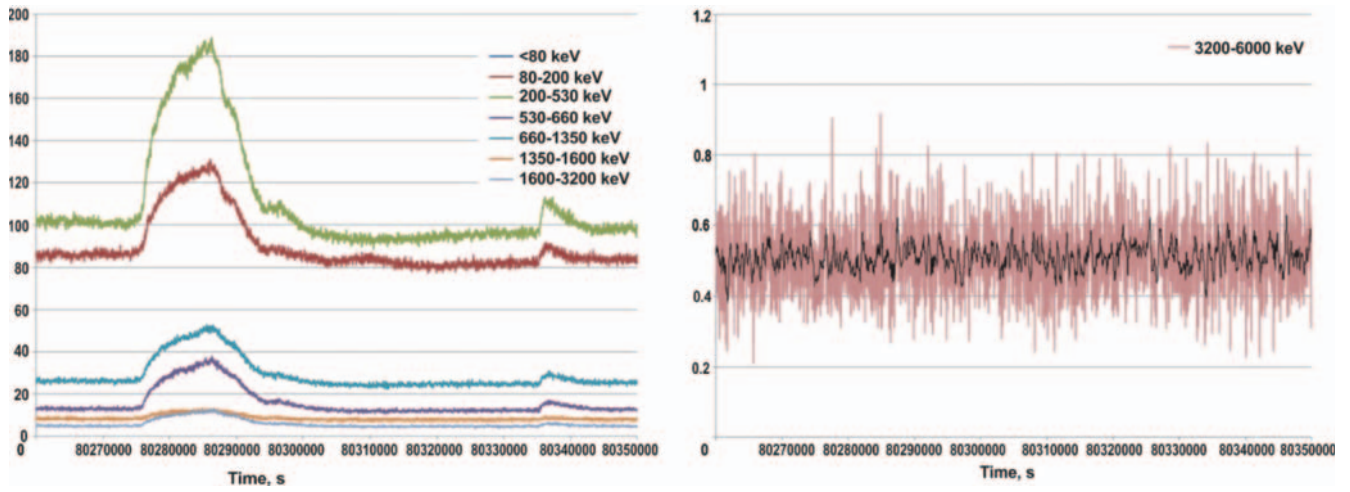


Figure 6. Time profile of TGE observed 18.07.2016

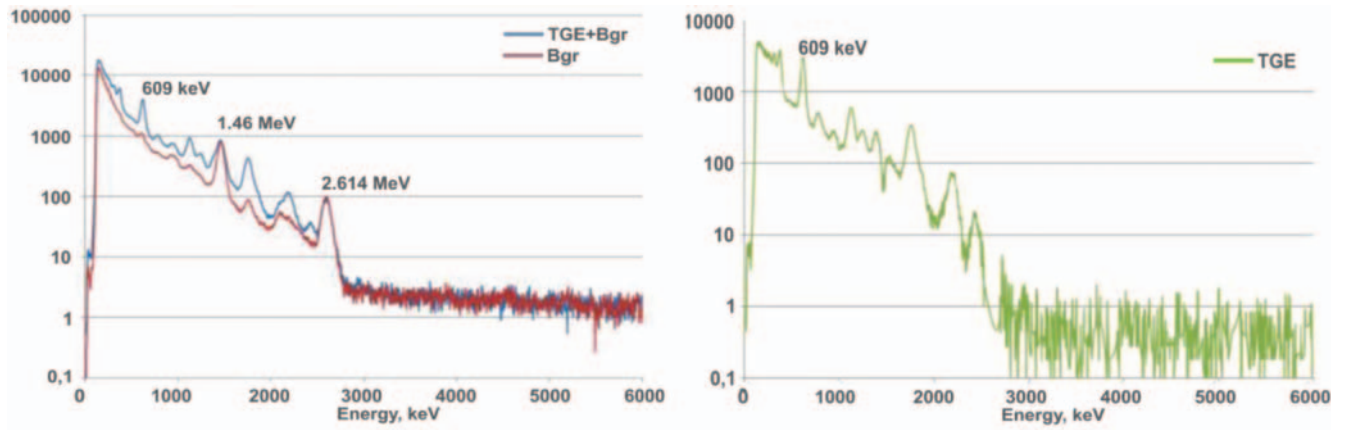


Figure 7. Energy spectra obtained at the period of thunderstorm 18.07.2016 in Moscow region.

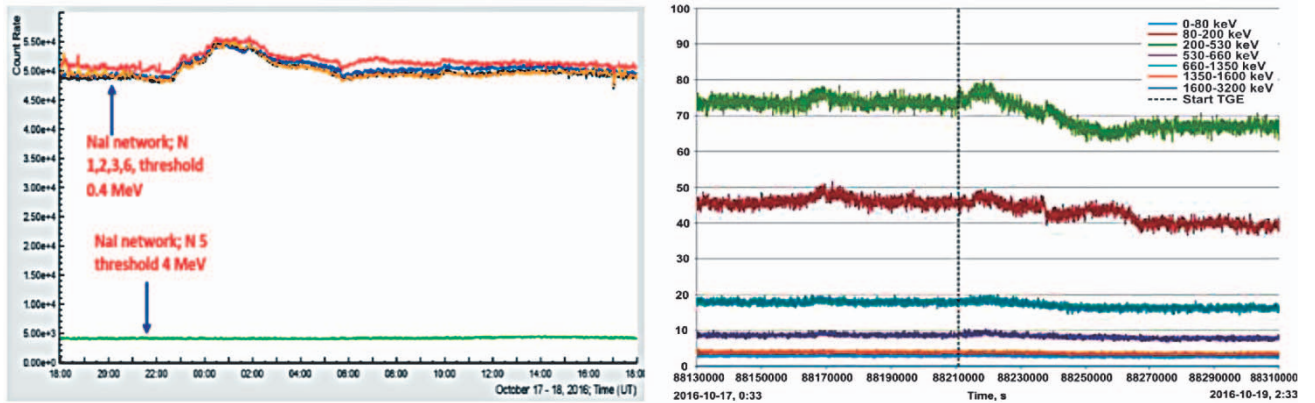


Figure 8. Time variations of gamma-radiation measured during rainy weather on October, 17-18. Right panel: readings of NaI(Tl) detectors of ErPhi group. Left panel: readings of 5 cm NaI(Tl) detector described in this paper.

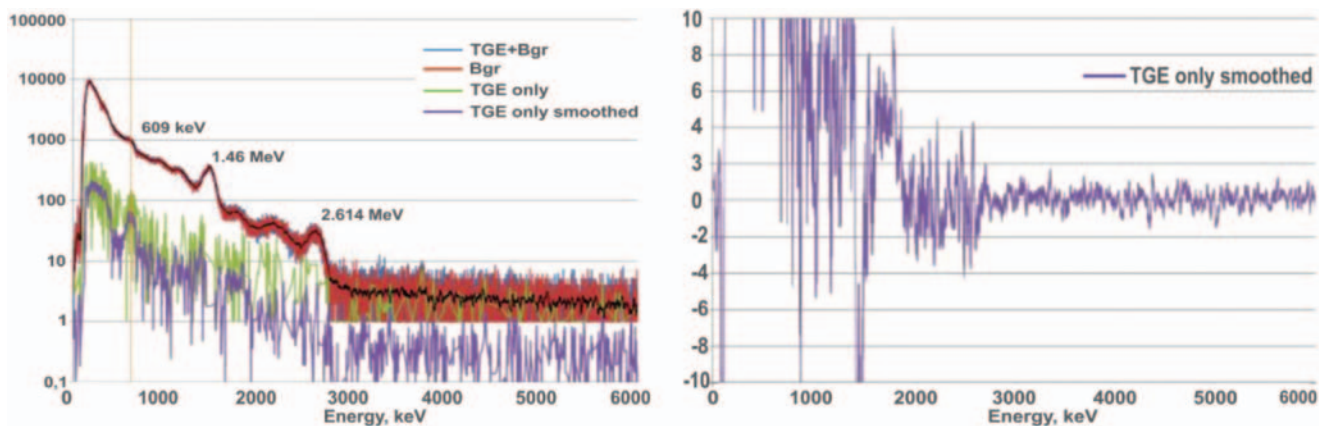


Figure 9. Energy spectra obtained by 5-cm NaI(Tl) detector during 4-hour period of TGE 17-18 of October, 2016.

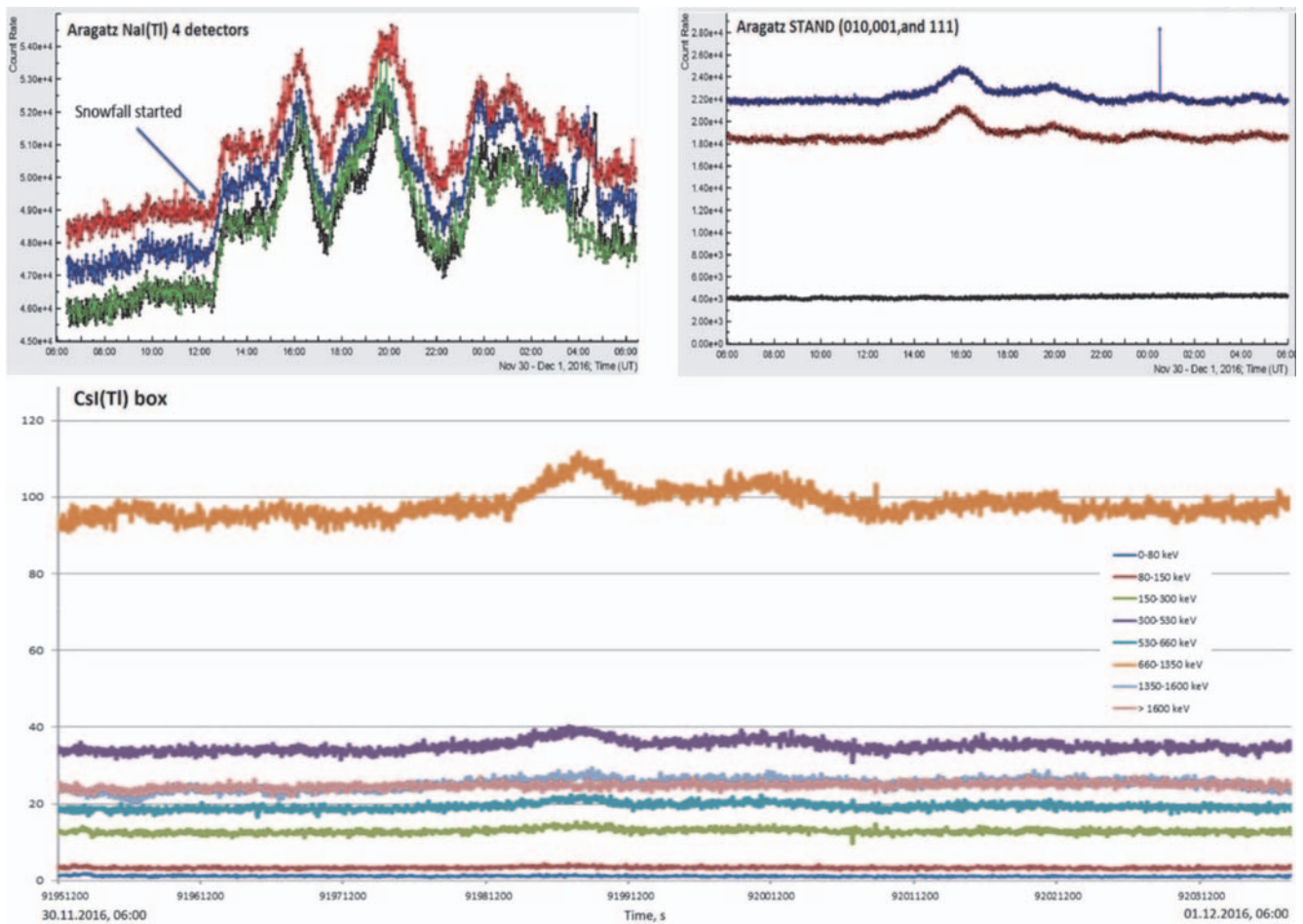


Figure 10. Variations of gamma-ray flux observed during the winter storm of 30.11.2016 – 01.12.2016 by Aragats NaI(Tl) detectors (top left), STAND detectors in different coincidence configuration (top right) and rectangular Csi(Tl) detector equipped with SINP MSU electronics (down).

4. DISCUSSION

One can see that most of energy spectra obtained in 20-3000 keV energy range during thunderstorms in Moscow region show the presence of gamma-ray lines associated with Rn-222 and daughters. The measurements made on rainy days without thunderstorm demonstrate similar variations of Rn-222 concentration. The measurements made on Aragats Mountain also allow to conclude the appearance of Rn-222 background. The variations of Rn-222 gamma-ray background are much greater than ones expected from bremsstrahlung from the electrons accelerated in thunderclouds in the same energy range. However variations of natural radioactivity do not influence on gamma-spectra in the high energies above 3 MeV.

A number of thunderstorms were observed in Moscow region in 2016. All of them do not demonstrate TGE radiation above 3.2 MeV.

Upper limit is plotted together with TGE spectrum, measured by NaI (Tl) detector on Aragats station (Chilingarian et. al, 2015a) at figure 11. One can see that the limit of TGE flux in 3.2-6 MeV range for Moscow region is of the same order as the flux measured on Aragats. These results do not contradict because the distance to thunderclouds in Moscow region is several times greater than one in Aragats region.

Another way to measure TGE spectrum over wide energy range is to compare the readings before and after the lightning abruptly terminating TGE (A. Chilingarian et.al. 2015b). It is important to make fast recording of the readings of gamma-detector around the lightning by triggering from

radio-burst or optical burst detector. Such installation was prepared on Aragats during TEPA-2016. The UV-flash detector DUV (Chilingarian et.al, 2015c) was used as a triggering instrument for “pico-scope” electronic device providing the recording from 4 channels one of which was connected with the analog output of 5 cm NaI(Tl) detector described above. The example of fast record is presented at figure 12. Each negative pulse on the 1s-long oscillogram corresponds to an event in gamma-ray detector. This installation will be used for study fast behavior of TGE radiation at the moments of lightning as well as for the search of fast gamma-flashes in the thunderstorm season of 2017.

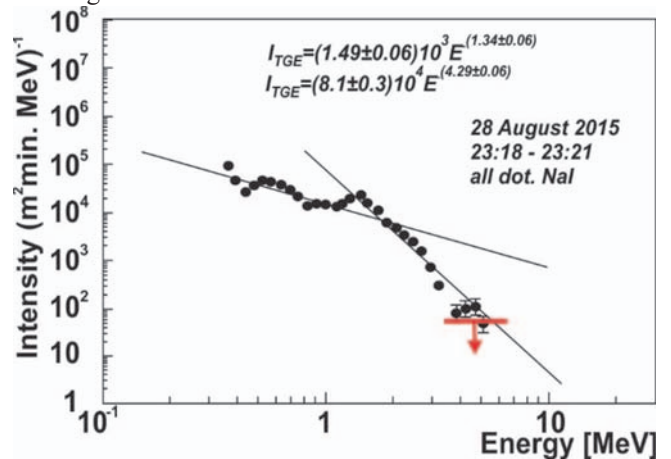


Figure 11. Upper limit for the gamma-ray flux of TGE observed 18.07.2016 in Moscow region (red) and TGE spectrum, measured 28.08.2015 by NaI(Tl) detector on Aragats station (Chilingarian et.al., 2015a) (black)

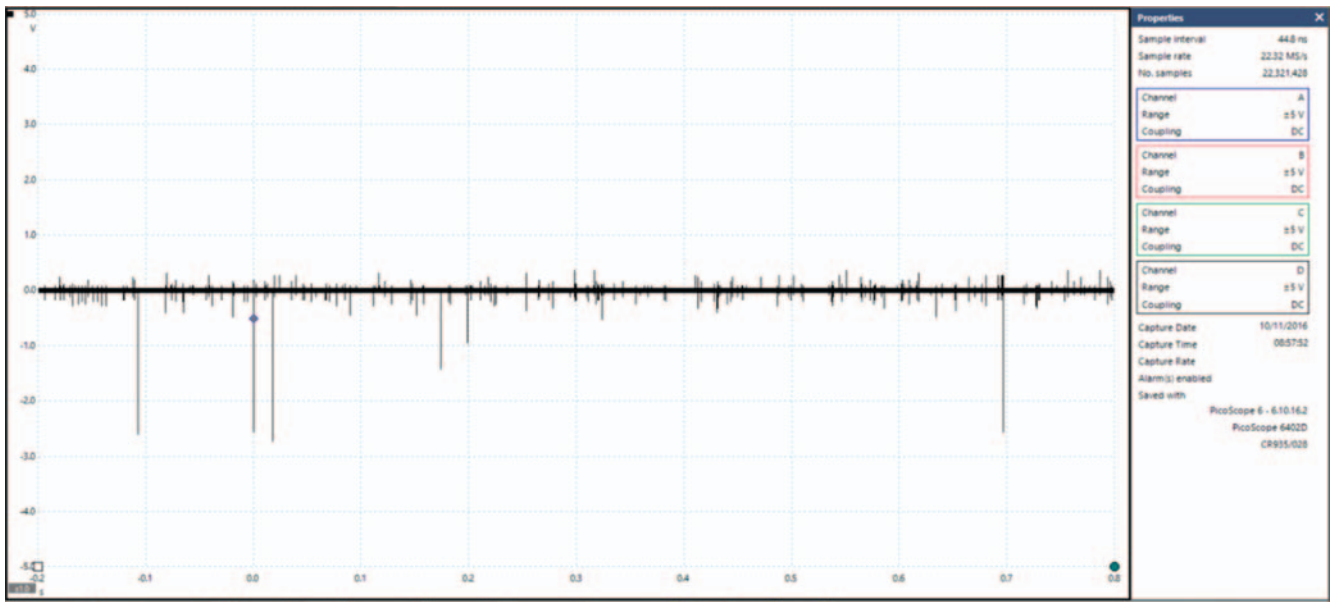


Figure 12. Example of 1-second fast record of 5-cm NaI(Tl) detector readings on Aragats

REFERENCE

Bogomolov V.V., Svertilov S.I., Maximov I.A., et al, (2015) Study of TGEs and Gamma-Flashes from thunderstorms in 20-3000 keV energy range with SINP MSU Gamma-Ray spectrometers, Proceedings of International Symposium TEPA-2015, Nor-Amberd, Armenia, 41-46

Briggs, M.S., Xiong S., Connaughton, V., et al., (2013) Terrestrial gamma-ray flashes in the Fermi era: Improved observations and analysis methods, Journal of Geophysical Research: Space Physics, vol. 118, 3805–3830, doi:10.1002/jgra.50205

Chilingarian A., Hovsepyan G and Kozliner L., (2013), Thunderstorm Ground Enhancements: gamma ray differential energy spectra. Proceedings of International Symposium TEPA-2013, Nor-Amberd, Armenia, 32-41

Chilingarian A., (2014) Thunderstorm Ground Enhancements - model and relation to lightning flashes, Journal of Atmospheric and Solar-Terrestrial Physics 107 68–76.

A. Chilingarian, G. Hovsepyan, E. Mnatsakanyan (2015a) Mount Aragats as a stable electron accelerator for atmospheric High-energy physics research, Proceedings of International Symposium TEPA-2015, Nor-Amberd, Armenia, 2-9

Chilingarian A., Hovsepyan G., Khanikyanc G., et al, (2015b)

Thunderstorm ground enhancements (TGEs) abruptly terminated by negative cloud-to-ground lightnings, Proceedings of International Symposium TEPA-2015, Nor-Amberd, Armenia, 71-78

Chilingarian A., Karapetyan T, Pokhsraryana D., et.al. (2015c), Ultraviolet and infrared emission from lightning discharges observed at Aragats, Proceedings of International Symposium TEPA-2015, Nor-Amberd, Armenia, 58-63

Gurevich A.V., Milikh G.M., Roussel-Dupre R. (1992) Runaway electron mechanism of air breakdown and preconditioning during a thunderstorm. Phys. Lett. A. V. 165, 463– 468.

Dwyer, J.R., D.M. Smith, and S.A. Cummer (2012a), High-energy atmospheric physics: Terrestrial gamma-ray flashes and related phenomena, Space Sci. Rev., 173, 133-196, doi: 10.1007/s11214-012-9894-0.

Dwyer, J. R., Schaal, M. M., Cramer, E. et al, (2012b) Observation of a gamma-ray flash at ground level in association with a cloud-to-ground lightning return stroke, Journal of Geophysical Research, vol. 117, A10303, doi:10.1029/2012JA017810

Physical analysis of multivariate measurements in the Atmospheric high-energy physics experiments within ADEI platform

K. Avakyan¹, S. Chilingaryan^{1,2}, A. Chilingarian¹, T. Karapetyan¹

*1. A. Alikhanyan National Lab (Yerevan Physics Institute), 2 Alikhanyan Brothers, Yerevan 0036, Armenia,
2. Karlsruhe Institute of Technology, Germany*

Abstract. To make transformational scientific progress in Space science and geophysics, the Sun, heliosphere, magnetosphere and different layers of the atmosphere must be studied as a coupled system. Presented paper describes how information on complicated physical processes on Sun, in the heliosphere, magnetosphere and atmosphere can be made immediately assessable for researchers via advanced multivariate visualization system with simple statistical analysis package. Research of the high-energy phenomena in the atmosphere and the atmospheric discharges is of special importance. The relationship between thundercloud electrification, lightning activity, wideband radio emission and particle fluxes have not been yet unambiguously established. One of most intriguing opportunities opening by observation of the high-energy processes in the atmosphere is their relation to lightning initiation. Investigations of the accelerated structures in the geospace plasmas can as well shed light on particle acceleration up to much higher energies in the similar structures of space plasmas in the distant objects of the Universe.

1. INTRODUCTION

In recent years, the interest in using cosmic rays for obtaining information on atmospheric and extra-atmospheric processes is rapidly growing. Cosmic rays are modulated by the solar bursts and can be used as messengers carrying information on upcoming space storms. Precise and continuous monitoring of the secondary cosmic rays with networks of particle detectors can reveal the danger of agents of solar activity (Interplanetary coronal mass ejections and solar energetic proton events). Appropriate scientific infrastructure and analysis methodology was developed at the Cosmic Ray Division (CRD) and tested on the violent events of the 23-rd solar activity cycle (1997-2008, Chilingarian, 2009, Bostanjyan and Chilingarian, 2009, Chilingarian and Bostanjyan, 2010, Mailyan and Chilingarian 2010, Hovhannisyanyan and Chilingarian, 2011, Chilingarian and Karapetyan, 2011). Recently it was discovered that fluxes of cosmic rays detected on the earth's surface also carry information on the parameters of atmosphere, primarily on very difficult to measure atmospheric electricity (Chilingarian et al., 2010, 2011, 2012a). Fluxes of gamma rays and electrons carry information on high-energy processes in the atmosphere and on the net potential of atmospheric electric fields associated with emerging positive and negative charged layers in thunderclouds. Fluxes of the "thunderstorm" neutrons, first reliably detected on Aragats (Chilingarian et al., 2012b and 2012c) are connected with the photonuclear reactions of the gamma rays with atmospheric nuclei and can pose radioactive hazard to crew and passengers of the nearby aircrafts (Drozdov et al., 2012). The muon flux provides the main contribution to the natural ionizing radiation at the Earth's surface. Cosmic ray muons come to the observation point from all directions of the upper celestial hemisphere and are sensitive to any changes in the flux of primary cosmic rays and the meteorological conditions high in the atmosphere. A comprehensive study of all aspects of the impact of atmospheric and extra-atmospheric processes on cosmic rays require as many measurements of various components of cosmic rays as possible.

One of the recognized leaders in contemporary investigations of geophysical phenomena using cosmic ray

is the Cosmic Ray Division (CRD) of the A. Alikhanyan National Scientific Laboratory of Armenia and its Aragats Solar Environmental Center (ASEC). At CRD's Aragats and Nor Amberd research stations the networks of detectors registering electrons, muons, gamma rays and neutrons operate round the clock, providing important information on various geophysical processes. Methods for visualization and analysis of multi-dimensional experimental data developed in the laboratory are successfully used to research solar-terrestrial connections and high-energy phenomena in the terrestrial atmosphere. Modern devices to measure magnetic and electrical fields, meteorological conditions, and lightning occurrences were placed at the Aragats and Nor Amberd research stations. Data from this instrumentation and the associated research gave us important information about the fluxes of electrons and gamma rays from thunderclouds. Detected particles and the penetrating radiation from thunderclouds give information on the local changes of the electric field and other key meteorological parameters. Multivariate analysis of variations of fields, radiation, and particle fluxes can provide new information on the development of thunderstorm anomalies in the atmosphere, including those of catastrophic nature. Such analysis presents a challenge due to the large quantity of acquired data. Huge amount of time series should be processed and identified near on-line for forecasting and alerts, as well as for report and paper preparation. Usually, researchers have no time to access archives if the data stream is pressing and new interesting events appear each new day. Therefore, to support researcher in data mining and finding "new physics" a multivariate visualization platform should be supplemented with tools of elementary statistical analysis (histograms, moments, correlations, comparisons); figure preparation; archiving, i.e. with a data exploration system.

Therefore, we supply the online stream of "big" data from ASEC with an exploration system developed in a collaboration between Karlsruhe Institute of Technology (KIT). The Advanced Data Extraction Infrastructure (ADEI, Chilingaryan et al., 2010) helps researchers in exploring and understanding solar-terrestrial connections, solar modulation effects as well as in understanding high-energy phenomena in the atmosphere. A user-friendly interface interactively

visualizes the multiple time-series and selects relevant parameters for different research objectives. Time series from different domains are joining for a multivariate correlation analysis. The developed software links a multitude of space and geophysical observations into an integrated system and provides analysis tools and services to fully utilize the scientific potential of current space weather/geophysical observations. In this way, we try to fully utilize the new concept of “big” data when an enormous amount of relevant observations culminates in the “new” physics unprecedentedly fast and precise. In this paper, we will focus on the new options of the ADEI that allows not only on-line displaying the multivariate measurements, but also on-line analyze the physical phenomena.

2. ADVANCED DATA EXTRACTION INFRASTRUCTURE (ADEI)

ADEI (Chilingaryan et al., 2010) has been developed to provide data exploration capabilities to a broad range of physical experiments dealing with time series.

All these systems have very different characteristics: an amount of data channels, their types, sampling rates, etc. The data is stored in many different ways utilizing various data formats and underlying database engines. On the other side, users need information in different data formats, which are supported by analysis tools they use for post processing. Besides, operators need a tool providing possibility to examine all collected data checking the integrity and validity of measurements. It is also needed to search and export data possessing specified characteristics.

To provide such a broad coverage ADEI utilizes highly modular architecture. The system consists of backend and frontend parts communicating over HTTP protocol using Asynchronous JavaScript and XML (AJAX, see for references to software used Chilingaryan et al., 2010) approach. The ADEI backend defines few abstract interfaces which are used to implement various capabilities using simple plugins. The data sources are interfaced with dedicated drivers implemented data access abstraction layer. The higher levels of the system are utilizing this abstract interface to get data in a uniform way from arbitrary storage.

The ADEI web frontend is inspired by GoogleMaps interface. Single or multiple time series are plotted using the data from currently selected time interval. Then, the plot could be dragged and zoomed over time and investigated parameters value. The desired region of the plotted variables may be selected for detailed statistical analysis or exported in one of the supported formats.

2.1. ARCHITECTURE

ADEI is designed to deal with the data sampled at high rates and stored for long periods of time. The time span of measurements at ASEC goes back for 20 years and the fastest detectors are sampling the data at rates exceeding 10 Hz. Processing such amounts of data requires enormous computational power. However, the interactive tools should operate in near real-time and extract important information from this enormous amount of data. To achieve this goal ADEI continuously monitors incoming data, performs preprocessing, and caches important information in a high performance database.

The simplified diagram of ADEI architecture is presented on Figure 1. The main logic of ADEI system is

contained in a backend which is implemented purely in PHP programming language. The backend incorporates a data access layer, a caching daemon, an ADEI library. Communication with the web frontend and other client applications is maintained using web services. HTTP protocol is used for data exchange, XML for data encoding.

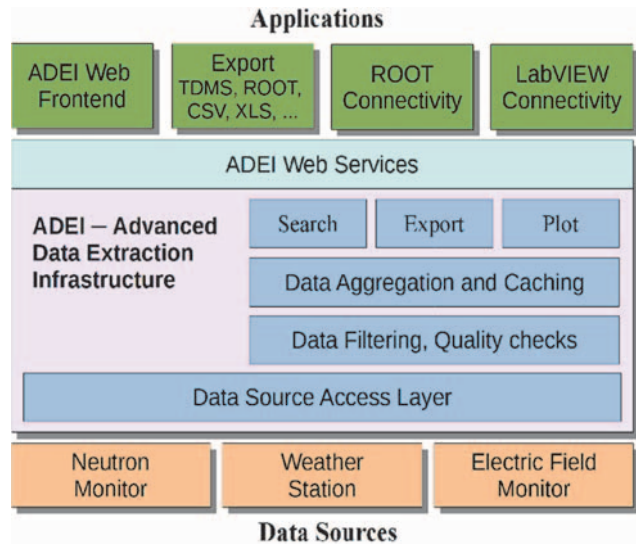


Figure 1. Architecture of Advanced Data Extraction Infrastructure. Data Source Access Layer unifies access to the time series stored in different formats. After data filtering and quality checks the data is aggregated and stored in intermediate caching database. Access to the data is provided by ADEI library and web services are used to communicate with client applications.

The data access layer hides details of underlying data sources providing other components of the system with a uniform way of data access. The data is organized hierarchically. The top level of hierarchy is the data source and ADEI may underline several data sources. The time series provided by the data source is divided in time-synchronized groups, so called *LogGroups*. The current version includes modules to access data stored in relational databases accessible through PDO or ODBC interfaces, several NOSQL databases, RRD (Round Robin Database Tool) data format used by many system monitoring applications. Most of popular databases including MySQL/MariaDB, PostgreSQL, Oracle, Microsoft SQL server, and CouchDB are supported.

The caching daemon is continuously running on a backend server and polls all data sources for a new data. When the data is acquired it piped through series of filters which check the data quality, apply correction coefficients and drop invalid data. Then, the data is aggregated over intervals of few different periods. For each period, called *cache level*, statistical information is gathered and stored in MySQL database (*caching database*) as additional time series. Minimum, maximum, and average values, the total number of recorded records, and the amount of invalid or missing records for each interval of aggregation are stored. Then, this caches are used by ADEI to speed-up searches or provide data averaged over the specified intervals. For instance, the plot module first selects the maximal cache level providing enough points to generate the plot of the specified size. The time resolutions of caching database are selected in the way that between 1000 and 10000 data samples can be extracted for any specified interval. Such an amount of points fulfills most of plotting demands and in the same time the plots could be generated relatively fast. After

selection of cache level is made, the data is extracted from correspondent caching tables and one of supported algorithms is used to convert aggregated values into the graphic points. The data plots are generated with JpGraph on the backend and delivered to frontend as PNG images.

ADEI provides the stored data in multiple formats. We currently support CSV (Comma Separated Values), Microsoft Excel, NetCDF, ROOT (an analysis framework for high energy physics), and TDMS (Technical Data Management Streaming). Additional formats may be implemented in two ways. The ADEI supports custom export plugins. Alternatively, it is possible to filter exported data using system scripts. For example, to generate ROOT output, the data in CSV format is piped to standard input of a simple ROOT application which converts it to ROOT format and prints to standard output. The same mechanism could be used to compress output before returning it to the client application. The chains of filters are supported. This allows to produce archived ROOT files. To limit amount of the exported data, a resampling by averaging or summing up can be requested.

ADEI search engine is implemented with pluggable search modules and is able to search for channels, channel groups, channel values, and time intervals. The channel search is very flexible. The channel names and descriptions are searched for single and multiple words, exact phrases, and regular expressions. The words are matched in three different ways: exact match, words starting with the search term, or words containing search term. The search is case-insensitive and all types of matching can be mixed in a single query. The value search finds a set of time intervals where the values of the given channel are above/below the specified threshold. The two modes are supported: search for time intervals where any value from the interval is above/below the specified threshold and search for time intervals where at least some of the values are above/below the threshold. The data cache is used to accelerate searches over big amounts of data and all searches are executed within few hundred milliseconds. The interval search allows users to quickly position time axes. The search module supports strings like January 2005 or January - March, 2006 and upon submitting of search request the time axis will be set accordingly.

Meteorological information is represented by time series of measurements of automatic weather stations and photographs of lightning discharges in the sky. Though it is impossible to process photographs using standard data aggregation chains in ADEI, we built a "Custom" data chain to provide a uniform access to the images using standard interfaces with minimal restrictions. The data source may optionally provide, so called Custom data, where each data channel is associated with custom array instead of scalar. The module handling the data from relational databases provides such Custom channels from the binary BLOB data stored in the database. As caching for images is currently not available, the visualization modules requests data directly from the database. This limits applicability to rather small time intervals, but allows us to provide additional information in ADEI web interface while analyzing specific atmospheric events. As well, ADEI filtering subsystem is able to create derivative data channels based on the filter output. It allows us to feed images into the chain of filters and extract scalar values characterizing some properties of the recorded data. For example, from the lightning

discharges picture we can extract number and length of lightning and make it available to the scientists via ADEI.

2.2. FRONTEND

The main view of ADEI web frontend is represented on Figure 2 and the numeric labels from 1 to 12 are used to reference interface elements in the description below. The main window (label 1) contains plot depicting measurements of 7 sensors on a voltage, temperature, and default axes.

The channel to axis mapping can be defined either by the source database or in the ADEI configuration. All unmapped channels are displayed using optional default axes. There is no hard limit on a number of supported axes, but rather the size of the browser window is only factor restricting the number of axes which can be reasonably displayed.

The data for period of approximately two weeks is shown. During this period, the registrations of sensors were sampled into the database approximately ten times in a second what gives about 12 millions of data records over two week interval. For visualization, this data is aggregated and approximately a few thousand data points are extracted from the caching database to render the graph. The system is optimized in a way that complete time of rendering does not exceed a few hundred milliseconds on a standard desktop hardware. Sometimes, however, the collected information includes periods when no data was recorded or existing recordings are invalid. Due to aggregation, the short outtages is impossible to see on the low zoom levels. In order to handle such situations, ADEI includes a quality indication line on a top of the data plot (just below a plot title). On the screenshot it is possible to see a tiny line indicating short period when the data was not recorded due to power outage (see label 5).

The ADEI is configured using various controls in the sidebar. The lower part (label 7) allows to set various options controlling behavior of export subsystem, data aggregation and visualization modes, etc. The top part (label 6) includes 3 tabs controlling which data is displayed on the plot. The Source tab allow to select one of the pre-configured groups of channels. More flexibility can be achieved with Source Tree tab of the bottom sidebar (label 7) which allows to select individual channels from the hierarchical tree. The Axes tab allows to tune the axes by specifying their ranges and switching between standard and logarithmic modes. Time tab is used to configure the time interval of interest. Few different modes are supported. The data source may provide a list of time intervals when something important was happening. It is possible to select a desired interval from this list and apply it to the time axis. Alternatively, the beginning and the end of time axis could be set manually with a microsecond precision. Other options include visualization of all stored data or just last quantity of seconds (i.e. plot for last minute, hour, day, week, etc.). In the last case the plot will be periodically updated to display incoming data.

It is also possible to zoom into the regions of interest on the plot using mouse. The subarea of plot can be selected using mouse pointer while holding left button (label 2). After selection is made it still can be fine tuned: resized or positioned using mouse or keyboard arrows. The buttons in the right-bottom part are used to export data within selected time interval (label 3) or to zoom into the selection (label 4). Additional functional buttons can be implemented using custom plugins. Also, the current plot on display can be zoomed in and out by scrolling mouse wheel. The default

action is to zoom along time axis at the position of mouse pointer. However, the key modifiers may be used to zoom over value axis or zoom in the center of the plot. The adjustments of plot position on the time and value axes are achievable by scrolling mouse over the correspondent axis. The double click on considered axis will restore it into the automatic mode and the general overview will be displayed again. Finally, the ADEI supports navigation history. Forward and Back buttons of the browser could be used to go back and forth in the history. The URL in the navigation bar is always precisely describing current position, selected time series, and all configured properties. This URL could be sent to the colleagues over e-mail and exactly the same plot will be displayed on their PC.

A status bar (label 10) is used to provide status and contextual messages to the user. Currently performed actions, their completion status, contextual help, emerging error messages are reported using status bar. On mouse movement the position of mouse pointer along all axes is reported as well. An example could be seen on the provided screenshot. The color coding is used to help with association of axes. ADEI also provides possibility to investigate graphics passing in the specified area of the plot. A legend window (label 10) is popped up when the left mouse button

is clicked. It contains a list of all graphics on the plot which are passing near position where mouse was clicked. The short name, description, and a range of values possessed in the neighborhood are presented on the legend.

ADEI provides advanced search and simple integrated WiKi engine. Upon entering a search string (label 11), the bottom sidebar (label 7) is opened and results are reported in the Search tab. The example on screenshot displays results of searching for temperature sensors. The WiKi engine is normally used to describe the data channels available in the system and provides several specific extensions on top of standard WiKi syntax. [preview] - generates a preview plot. The channel group, time interval, image size, aggregation mode, and other standard properties may be specified. The preview is linked and upon a click will switch to the plotting view and display appropriate graph. [grouplist] - generates linked previews for all channel groups available in the system. [channels_by_name] - includes alphabetical listing of all channels in the system. Upon a click the selected channel will be plotted. [channels_by_group] - includes hierarchical listing of all channels in the system. The selected channel will be plotted upon a click as well. The example Wiki pages are depicted on Figures 3 and 4.

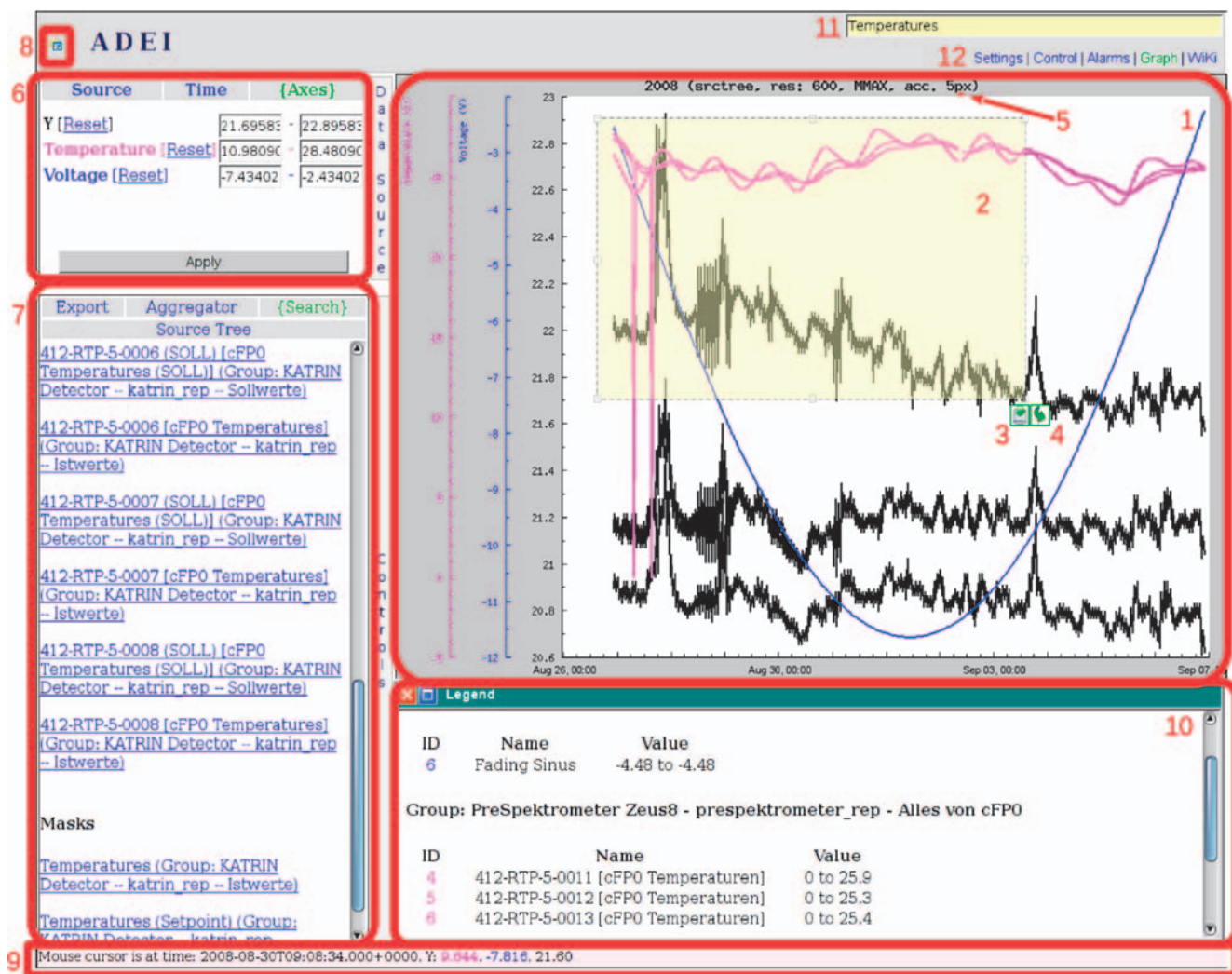


Figure 2. Screenshot of ADEI Web Frontend. The data outage is indicated using a small line on top of the plot (see 5). Legend contains description of displayed graphics. The selected part of plot may be zoomed or exported using buttons 3 and 4. Axes controls and results of search are located in the left sidebar.

Advanced Data Extraction Infrastructure of Aragats Space Environmental Center (ADEI of ASEC)

Dear user, welcome to the ASEC Advanced Data Extraction Infrastructure! The ASEC ADEI is loaded and ready to work. Please select the data *Source* and *Time* interval from the *Data Source* popup on the left sidebar, or use the pull-down menu in the top-left corner.

Navigation through the data done with the mouse:

- Drag with left mouse button to select a region.
- Click on the arrow button to zoom inside a region.
- Use the mouse wheel shift current window left and right.

To **download** selected data open choose the *Export* tab from *Controls* popup. You can export data to the multiple supported formats. Please be patient, as exporting data may take a while.

More detailed information about how to use ADEI can be found in the [ADEI Users' Guide](#). To find more information about ADEI system and report bugs, please, visit [project home page](#). Please read [this](#) publication to get more information how is working ADEI.

[The Efficiencies of the ASEC particle detectors used in Thunderstorm Ground Enhancement \(TGE\) research \(Bagrat Mailyan\)](#)

Below you will find **descriptions of the monitors** and their data.

[Aragats Research Station \(40.47N, 44.18E, 3200m a.s.l.\)](#)

[AMMM](#) - Aragats Multichannel Muon Monitor
[ArNM](#) - Aragats Neutron Monitor
[ASNT](#) - Aragats Solar Neutron Telescope
[Cube](#) - Neutral Cosmic Ray Monitor
[MAKET](#) - MAKET-ANI Extensive Air Shower Detector
[NaI](#) - NaI(Tl) Monitor
[SEVAN](#) - SEVAN Monitor at Aragats
[Stand 1cm](#) - Plastic Scintillator Monitor for Low Energy Particles
[Stand 3cm](#) - Plastic Scintillator Monitor with Spectral Analysis
[Electric Field](#) - Electric Field Monitor at Aragats
[Lightning Detector](#) - Lightning Detector at Aragats
[LEMI-417](#) - Magnetotelluric Station (MTS)
[Weather Station](#) - Davis Wireless Vantage Pro2 Plus

[Yerevan CRD headquarters \(40.205N, 44.486E, 1090m a.s.l.\)](#)

[SEVAN](#) - SEVAN Monitor at Yerevan
[Electric Field](#) - Electric Field Monitor at Nor-Amberd
[Lightning Detector](#) - Lightning Detector at Nor-Amberd
[Cube 3cm](#) - Magnetotelluric Station (MTS)
[Weather Station](#) - Davis Wireless Vantage Pro2 Plus

[Sevan Lake \(40.619N, 45.028E, 1910m a.s.l.\)](#)

[Stand 1cm](#) - Plastic Scintillator Monitor for Low Energy Particles
[Electric Field](#) - Electric Field Monitor at Nor-Amberd
[Lightning Detector](#) - Lightning Detector at Nor-Amberd

[SEVAN Monitors](#)

[SEVAN Aragats](#) - SEVAN Monitor at Aragats
[SEVAN Nor-Amberd](#) - SEVAN Monitor at Nor-Amberd

Figure 3. Screenshot of ADEI Wiki page (left part of the screen). The list of ASEC detectors and links on the pages with detailed detector description.

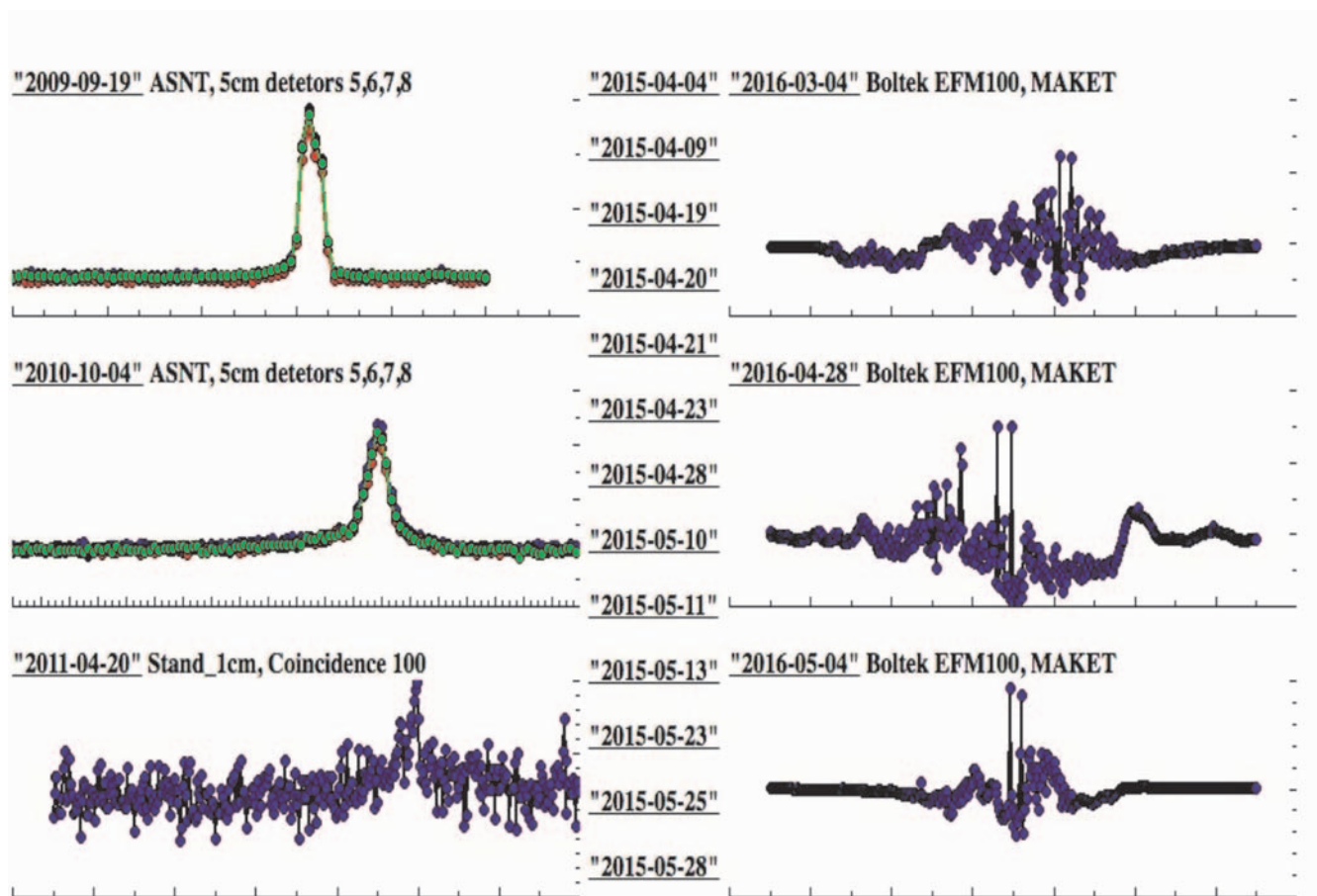


Figure 4. Screenshot of ADEI Wiki page (right part of the screen). Previews of most interesting events (event catalog). By clicking on the preview, the appropriate analysis session for the selected event will be opened in the main ADEI screen.

2.3. ADEI SECONDARY MODULES (PANELS)

More information in textual and visual forms may be provided in ADEI using so called secondary views. The secondary views are implemented with plugins which get all information about current ADEI screen on the display and all configured options. Based on this information, the relevant information is requested from ADEI backend and presented to the user in variety of forms. If necessary the views may interact with users by adding additional forms in the generated HTML content.

A set of secondary modules is available for ADEI to extract statistical information from the time series and provide basic insight in cross-correlations between different channels. The particle detectors at ASEC measure modulation of the stable galactic cosmic ray “background” by solar and local weather phenomena. Therefore, ADEI is often used to find a peak in a noisy random environment. A “background” module is a core component of the analysis platform. Using ADEI standard display, it allows the user to select an interval before an interesting event happened (for instance a particle flux from thunderclouds originated large peak in the time series) and extract the required statistics from it. For each of the data channels in ADEI, the module provides standard statistical information about the selected background to the users and other ADEI modules. For instance, the mean value and standard deviation on fair weather. Using calculated values it will be possible to show the time series in percent to the “background” value or in the number of standard deviations from the mean value. These options allow comparing and correlating variables with significantly different mean values on the one and the same frame. To verify correctness, additionally, the module shows a histogram and applies a Gaussian fit to the count rate histograms.

There are as well other secondary ADEI modules, which provide statistical information on the data, which is on display in the main ADEI window. First of all, for each channel the “channel list” module reports minimum, maximum, average and standard deviation of measurements in the selected interval as well as the minimum and maximum in the units of percent and standard deviation. For optimal performance, for larger time intervals an estimated value of standard deviation is computed using the averages from the ADEI cache. The “histogram” module show the histogram of the selected channel currently on display. The module supports normalization of the histogram and allows the user to perform Gaussian fit of the displayed data. In the upper right corner of the plot, the user sees the mean value of a variable in the selected data interval, the standard deviation, and Pearson’s chi-square test value. The number of bins is configured automatically or may be specified by the user.

The “scatter plot” module is for visualization of the relation of 2 variables. The linear correlation coefficient of the selected pair of variables is calculated and depicted on the plot as well. Delays between signals registered by different detectors can be found out using the “correlation plot” module. It allows viewing the dependence of the correlation coefficient depending on the added delay of one of time variables related to the second one. The user is expected to specify a step in the seconds, minutes, hours, or days.

3. USING ADEI FOR DATA MINING AND PHYSICAL ANALYSIS

Experiments in the field of the atmospheric high-energy physics produce the continuous high-volume stream of data from monitoring of neutral and charged particle fluxes, from high-speed cameras, field meters and lightning mapping arrays. Gaining insights from enormous volumes of such diversity of observations poses a number of challenges to data analysis chain and physical inference techniques.

The adopted method of the multivariate data analysis and physical inference consists in the selection of the hierarchical time series of particle count rates along with measurements of the electric field, distance to lightning, fast electric field waveforms and other. Precise synchronization of all measurements allows analyzing the time series on millisecond time scales. The one-second and one-minute time series also are very useful for discovering many non-trivial correlations in TGE data. Analyzing numerous TGEs registered on Aragats with one and the same sequence of patterns we reveal the repeating structures, typical correlations and finally causal relations between observables. As a result, we come to models and theories of TGE initiation and its relation to the electrical structure of the thunderclouds and lightning initiation and propagation. Multivariate analysis methodology becomes possible only with the use of ADEI - a very flexible and powerful tool providing services for the multidimensional visualization, interactive decision support, data zooming, comparison, digitizing, statistic analysis and other. We demonstrate how instrumental is the ADEI platform in physical inference taking as an example analysis of one of most intensive TGEs measured by facilities of the ASEC.

We illustrate ADEI procedures implementing visualization/analysis methods to TGE occurred on 16 June 2016 (Fig 5). First considered frame contains exhausted information on the storm, including time series of electrostatic field disturbances, the 1-minute count rate of the particle flux, solar radiation, rain rate and distances to lightning flashes. Storm started $\sim 7:30$ UT and continued until 11:30. All this time electrostatic field significantly differs from the fair weather value of ~ 140 V/m. At the depths of negative field we see enhancements of count rate measured by 1-cm thick outdoors plastic scintillator with energy threshold to measure charged particles ~ 1 MeV. The deepest negative field of -21.5 kV/m coincides with largest peak in particle detector count rate. The solar energy decreased from ~ 500 W/m² down to less than 100 W/m² due to thundercloud screening earth’s surface from sun. No rain was detected, thus the charges were not washed out from the cloud and separated differently charged layers in the cloud continuously induce significant electric field and potential drop. Nearby lightning flashes influence electric field and particle flux; these effects will be investigated with more detailed frames later.

Thus, the start of TGE event analysis started from the frame shown in Figure 7. We see how the thundercloud is reaching the skies above detectors location site; how the particle flux start to rise and how it was terminated by lightning.

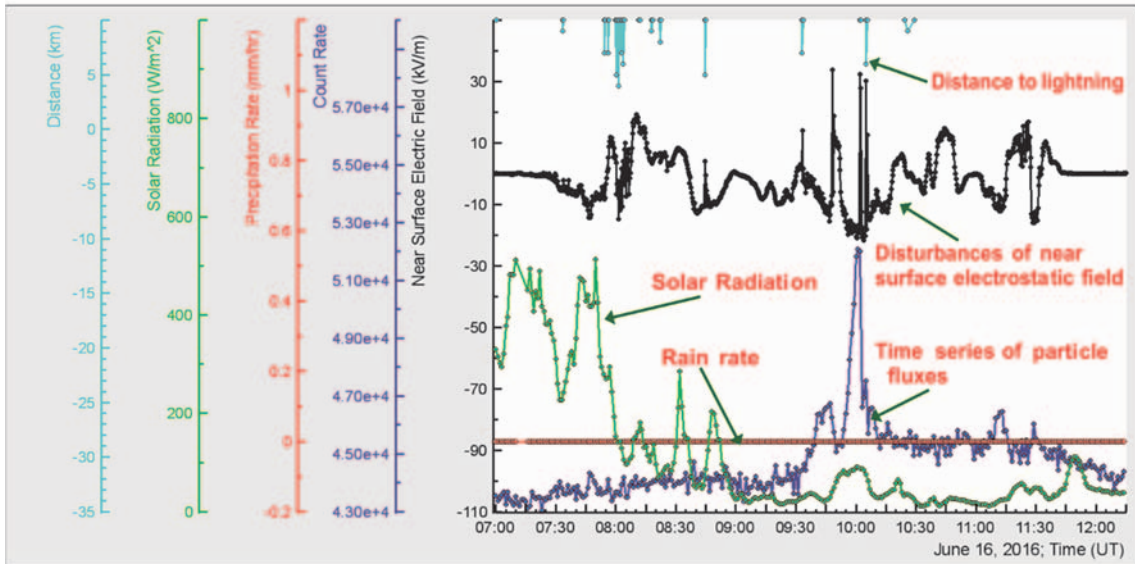


Figure 5. Meteorological and radiation information on the severe storm on Aragats.

Analysis of the next frame gives us more information on particle fluxes (Figure 6). In Figure 6c we show time series of, so called, coincidences or combinations of particle detector STAND3 comprised from stacked vertically 3-cm thick plastic scintillators. Data acquisition electronics of particle detectors provide not only counting of a number of particles hitting each scintillator, but also – coincidences of “firing” of different detector channels. For instance “1000” combination corresponds to the signal only in the upper scintillator i.e. low energy particle (less than 4-5 MeV) stopping in the 3 cm of plastic in the first scintillator. Following coincidences select particles of higher energies. The pattern of all coincidences shown in Figure 6c gives information on TGE energy spectra. The count rate is shown not in the absolute rates, but in the number of standard deviations. First of all, only in this way we can compare time series with drastically different mean values. Moreover, in this way we can estimate the statistical significance of detected peaks and compare different TGEs by, so called, σ criteria. The largest peak, as we can see in Figure 6c is $\sim 20 \sigma$. Certainly, we cannot calculate the chance probability (probability that peak is a fluctuation of the Gaussian population only) for such a gigantic significance; values of the σ criteria will be used for comparative purposes only. The type of count rate presentation is selected from the special menu located in the left side of ADEI layout.

Analysis of the next frame gives us more information on particle fluxes (Figure 6). In Figure 6c we show time series of, so called, coincidences or combinations of particle detector STAND3 comprised from stacked vertically 3-cm thick plastic scintillators. Data acquisition electronics of particle detectors provide not only counting of a number of particles hitting each scintillator, but also – coincidences of “firing” of different detector channels. For instance “1000” combination corresponds to the signal only in the upper scintillator i.e. low energy particle (less than 4-5 MeV) stopping in the 3 cm of plastic in the first scintillator. Following coincidences select particles of higher energies. The pattern of all coincidences shown in Figure 6c gives information on TGE energy spectra. The count rate is shown not in the absolute rates, but in the number of standard deviations. First of all, only in this way we can compare time

series with drastically different mean values. Moreover, in this way we can estimate the statistical significance of detected peaks and compare different TGEs by, so called, σ criteria. The largest peak, as we can see in Figure 6c is $\sim 20 \sigma$. Certainly, we cannot calculate the chance probability (probability that peak is a fluctuation of the Gaussian population only) for such a gigantic significance; values of the σ criteria will be used for comparative purposes only. The type of count rate presentation is selected from the special menu located in the left side of ADEI layout.

The “scatter plot” option is selected from statistical analysis menu that appears at the left side of the ADEI layout. In the inserts, we show scatter plots revealing the interrelation of selected variables. The scatter plot 6a showing large positive correlation is rather trivial: high-energy particles after hitting upper scintillator are hitting and registering by other scintillators located just below and, certainly, correlation should be positive. The scatter plot 6b revealing the negative correlation between 1111 and 1100 combinations is a somewhat surprising, illuminating interesting physical phenomenon. Due to the dominant positive charge of galactic cosmic rays, the positive muons are prevailing the negative ones. This important for many physical applications effect is evident for the muons with energies below 100 MeV; the increase can reach $\sim 10\%$ and more. Most of the particles counted as “1111” coincidence are muons (both positive and negative, we can not distinguish them); the probability that gamma ray is responsible for such a combination is $\sim 10^{-7}$ and there can be only very few electrons with energies above 20-25 MeV reaching surface detectors from the thundercloud. Thus, during TGE the electric field in thundercloud that accelerates and multiplies electrons will decelerate the positive muons diminishing the count rate of 1111 combination. The 1100 combination during TGE will certainly enhance. Thus, we explain the negative correlation and, moreover, we can pose interesting physical problem acquiring data from the Figure 6. We can try to estimate the electric field strength that accelerates electrons and stop the positive muons. And we can try to estimate the charge ratio of cosmic ray muons. Both problems are very important for the atmospheric and cosmic ray physics.

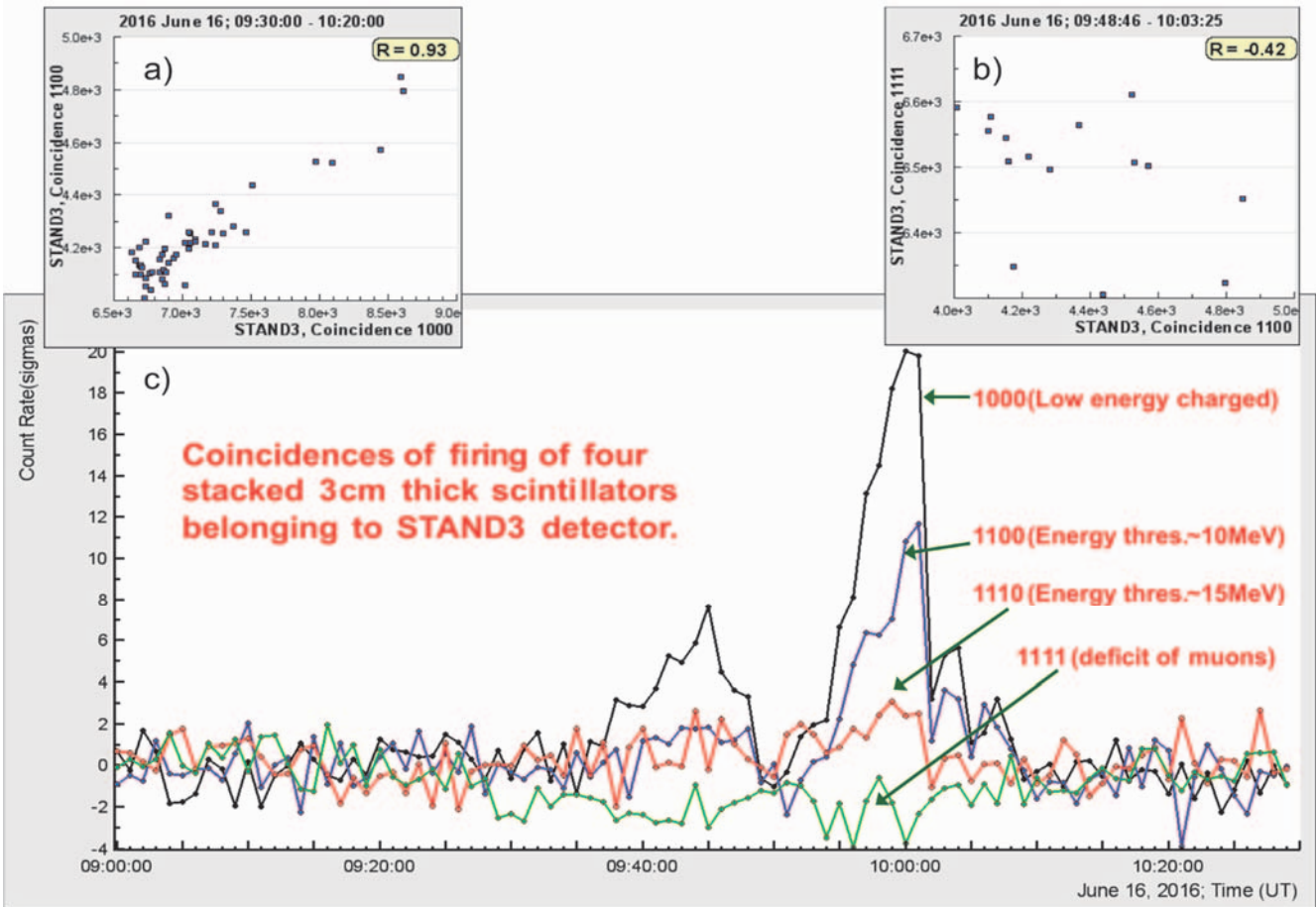


Figure 6. Time series of STAND3 detector coincidences in the “number of standard deviation” scale. Rough estimate of energy spectra. In the insert we demonstrate correlation analysis of the STAND3 detector coincidences.

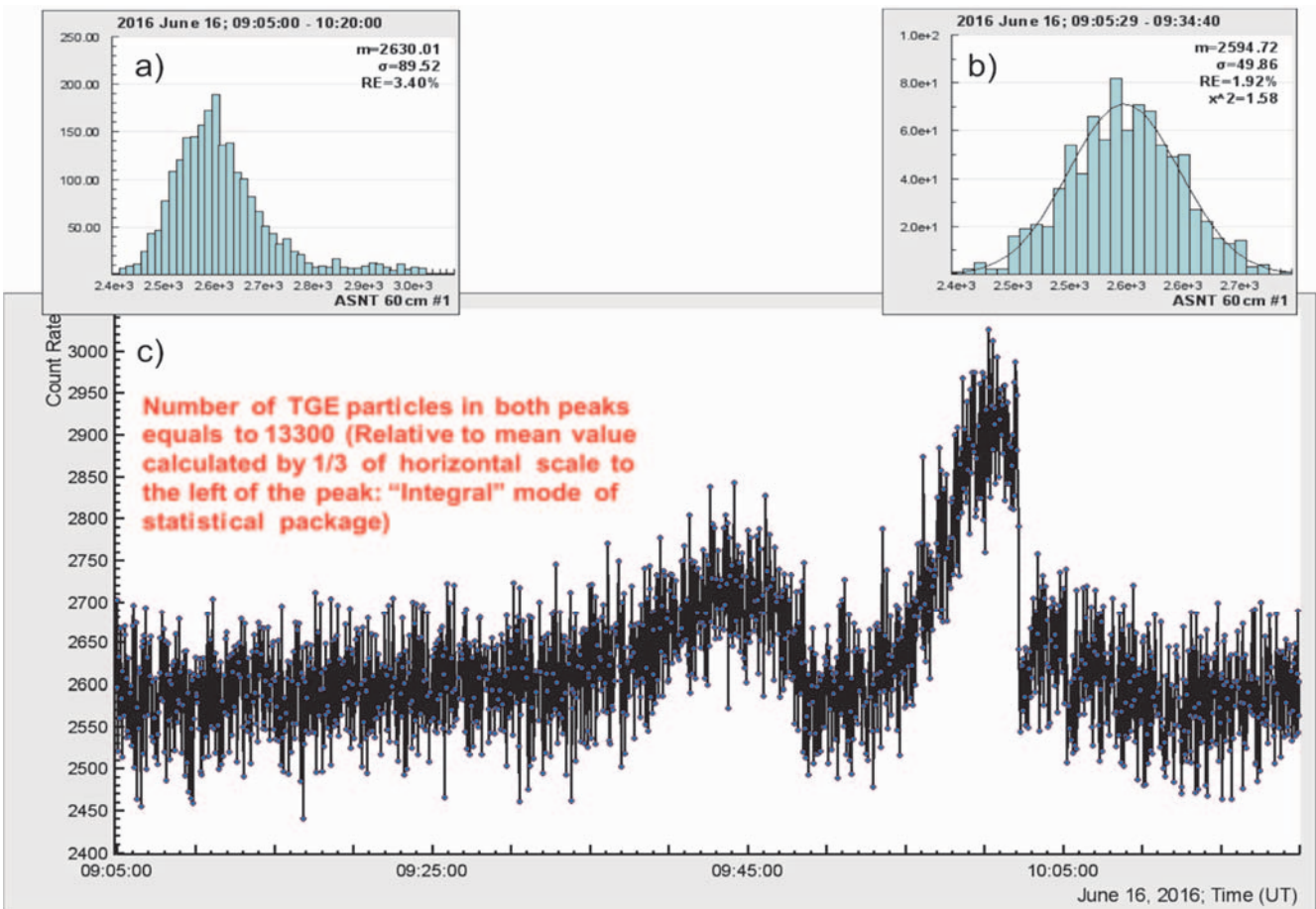


Figure 7. Enumeration of number of additional (relative to mean) particles detected during TGE. In insert histograms of count rates of 60 cm thick plastic scintillator of whole and one third of horizontal scale are shown.

Another statistical procedure is “Histogram”. In Fig 7a we show the histogram of count rates of the 60 cm thick plastic scintillator of ASNT detector shown below in the Figure 7c. Due to peaks in time series (TGEs) histogram significantly diverges from the Gaussian shape. In Figure 7b we show the histogram of count rates of the same scintillator but including only left third of the horizontal scale. The variations of count rate in the selected time span include background fluctuation only and corresponding count rates are rather good described by Gaussian function as we can see from the goodness of fit positioned in the upper right corner of the Figure.

For calculation of the number of particles comprising TGE we use “Integral” mode of ADEI statistical package. Preceding from the calculated mean value of count rate this mode returns the total number of additional particles exceeding the mean (particles containing in the 2 peaks shown in Figure 7c).

In Figure 7c we can see an abrupt termination of the TGE possibly connected with nearby lightning. To uncover the correlation of particle fluxes and atmospheric discharges (one of the most important and yet unsolved problems of atmospheric physics) we use frames shown in Figure 8-10. In Figure 8 we show the one-minute time series measured by the 1-cm thick upper scintillator of STAND1 detector along with electrostatic field measurements by the electric mill EFM 100. Data from the electric mill allows as well estimation of the distance to lightning. We can see 2 nearby (distances 5.8 and 2 km) lightning flashes occurred during TGE.

The exact shapes of the TGE and electrostatic field disturbances are shown in Fig 9. From Figure 9 we can directly obtain the count rate decline due to lightning flashes occurred at 10:02:11 and 10:05:13 (decline of 22% in 3 sec and 10% in 1 sec correspondingly).

To specify the lightning exact time and amplitude we need more detailed time series shown in Figure 10. The new fast DAQ electronics installed at Aragats in 2015 allows synchronization of particle fluxes and atmospheric

discharges and exact determination of the atmospheric electric field disturbances (we show data only for the first lightning). The electrostatic field starts to rise at 10:02:11.488 from -16 kV/m until 10:02:11.638 to 48.1 kV/m. Thus the amplitude of the negative lightning was 64.1 kV/m achieved in 150 ms, field recovering took rather long ~48 sec.

Another important problem of the TGE atmospheric high-energy physics is research of the electron-gamma ray avalanches in the thundercloud. The energy spectra of electrons and gamma rays as measured by surface spectrometers can highly assist in this problem solving. To separate and estimate electron and gamma ray fluxes we use the CUBE detector consisted of two 20 cm thick plastic scintillators (upper N 7 and bottom N 8) fully covered by the 1 cm thick scintillators. This shielding provides “veto” for charged particles. Thus, 20-cm thick scintillators simultaneously register total flux (without veto) and neutral flux. Certainly, due to the non-zero efficiency of 1-cm plastic scintillators to miss charged particles (1-2%) and as well non-zero efficiency to detect neutral particles (2-3%) the flux separation is not absolute. However, according to techniques described in (Chilingarian, Mailyan and Vanyan, 2012) we can take into account scintillator efficiencies and calculate separate fluxes of TGE species. In the insert to Figure 11 we show the 1-minute count rates of upper and bottom 20-cm thick scintillators; in the body of Figure 11 we show the same time series, but in units of “number of standard deviations”. The mean values of all four time series are calculated before the first peak.

ADEI allows export of data in as PNG pictures with controlled parameters (font size, size, number of ticks, resolution and other) and in the numerical form supporting most of standards. In table one we show the count rates from previous figure in numerical form. Also in last two columns, we show the ratio of 2 measurements for 2 scintillators. As we will, show below this ratio is sensitive to TGE amplitude in the case when most of TGE particles are gamma rays.

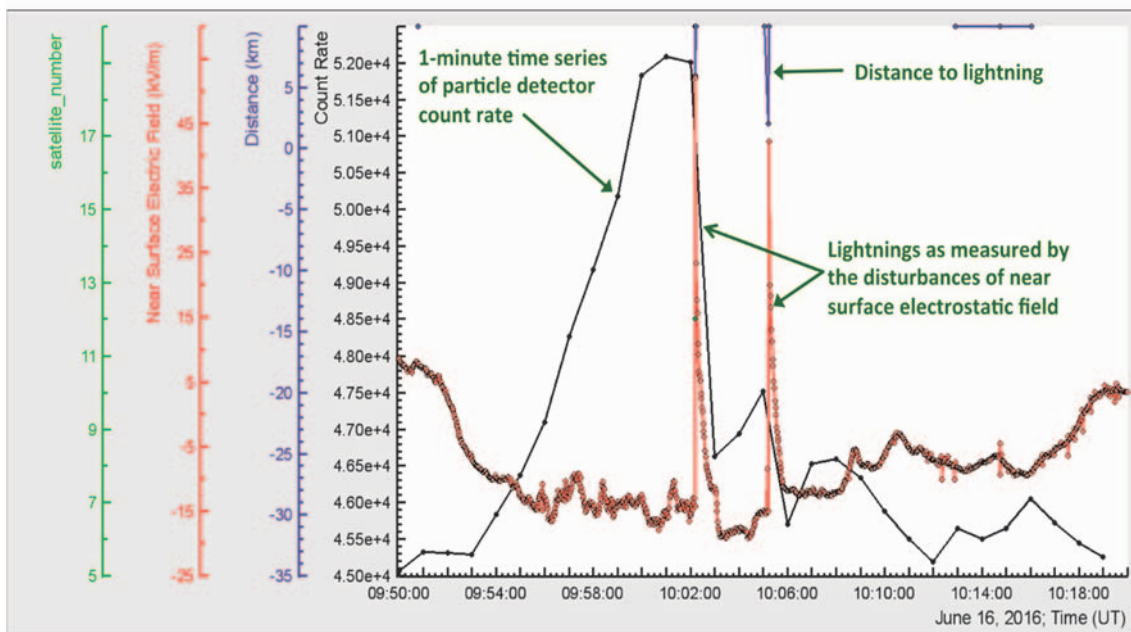


Figure 8. One minute time series of count rate of the 1-cm thick plastic scintillator belonging to STAND1 detector (upper, located nearby MAKET experimental hall) along with disturbances of the electrostatic field and distances to atmospheric discharges.

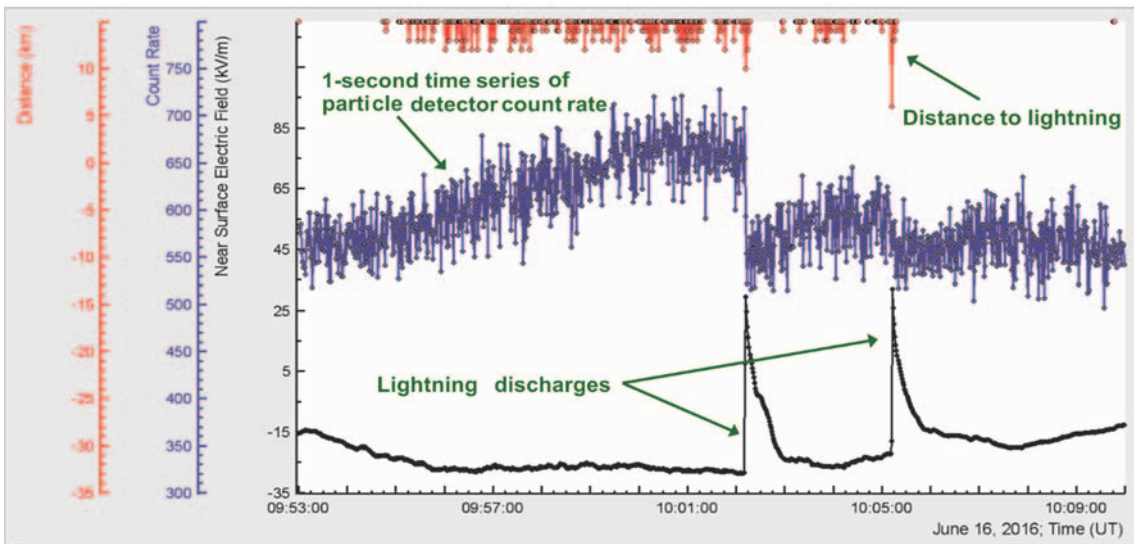


Figure 9. One second time series of count rate of the 3-cm thick plastic scintillator belonging to STAND1 detector (located nearby MAKET experimental hall) along with disturbances of the electrostatic field and distances to atmospheric discharges.

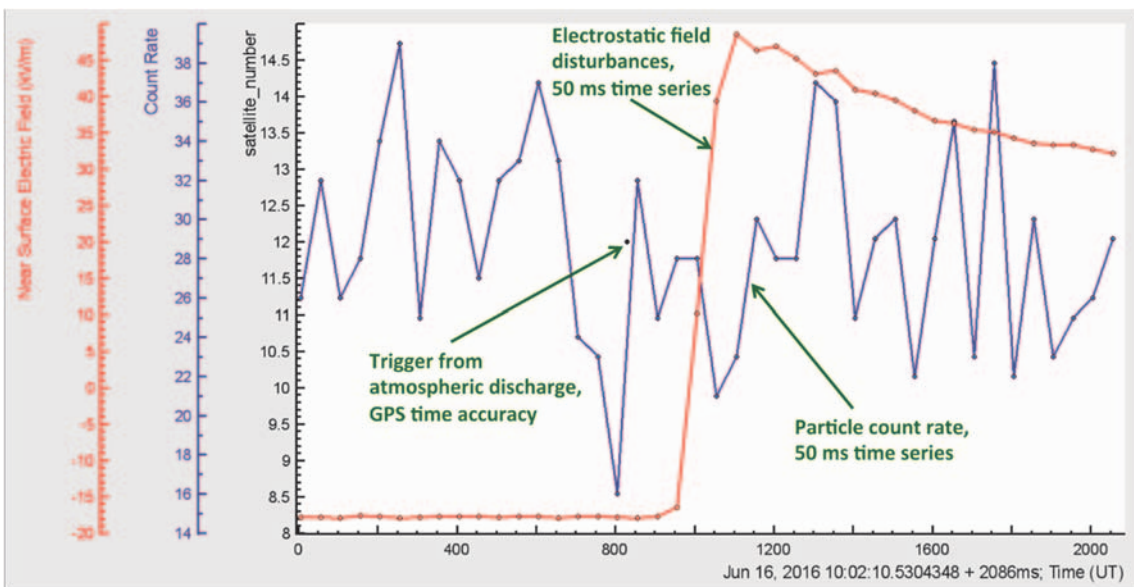


Figure 10. 50 ms time series of count rate of the 1-cm thick plastic scintillator belonging to STAND1 detector (upper, located nearby MAKET experimental hall) along with disturbances of the electrostatic field and distances to atmospheric discharges.

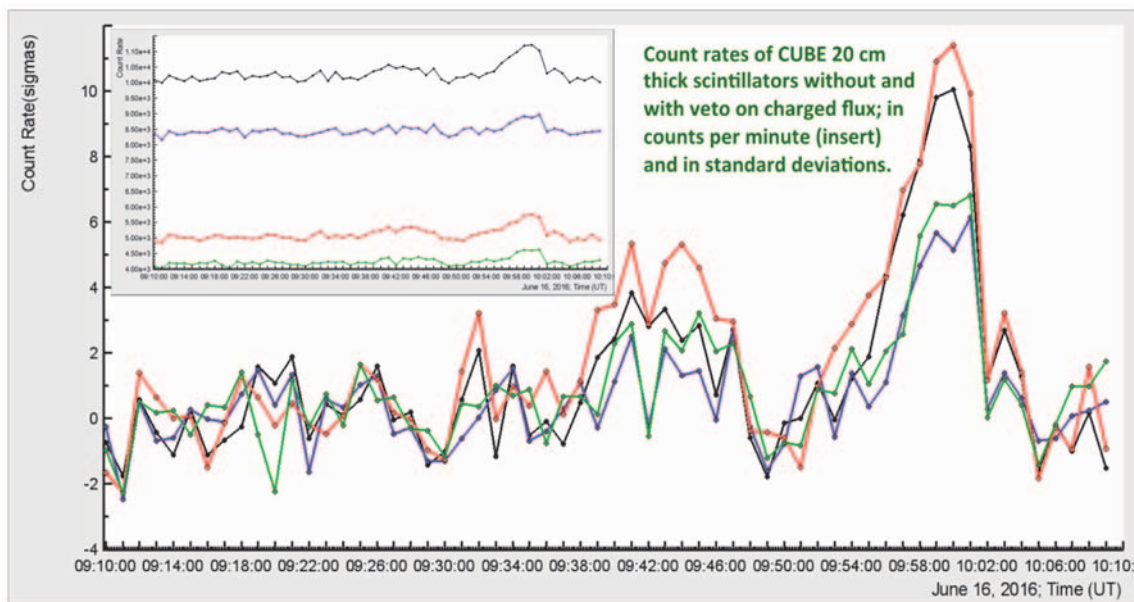


Figure 11. 1-minute time series of 20-cm thick plastic scintillators of CUBE detector. In insert – natural units; main body – in number of standard deviations ($N\sigma$).

In Table 2 we show the mean values of CUBE time series of count rates with and without veto at a fair weather and their ratio. The ratio is rather constant and differs from the ratio measured at 10:00-10:01 by 2.9σ (upper) and 3.7σ (bottom). Thus the ratio of count rates (with a veto to without veto) is a good indicator of TGE and its electron content.

In Table 3 we demonstrate the recovered by upper 20 cm scintillator intensities of electrons and gamma rays and fraction of electrons. Electrons attenuate in the air much faster than gamma rays. And sizable electron fraction in TGE is explained by the proximity of the cloud to earth's surface.

The NaI spectrometers and 60 cm thick plastic scintillators measure the energy release histograms from particles traversing detector. The radiation length of the NaI crystal is rather large ~ 5 and it is possible from the energy

release histograms collected each minute recover the energy spectra of TGE as is shown in the Figure 12. The maximal energy of spectra >30 MeV is reached at 10:01 -10:02.

To relate the TGE fading due to declining of the electric field after lightning we measure energy release spectrum with 60 cm thick scintillators each 20 sec (Figure 13). The radiation length of 60 cm scintillator is ~ 1.6 , thus we cannot recover energy spectra because a significant part of particle energy may not be released in the scintillator. However, the information from this scintillators allows us to notice that the high energy part of TGE disappeared after lightning occurred at 10:02:11. Thus lightning kills the avalanche process in the thundercloud. The low energy Compton scattered gamma rays are still registered but on a much lower scale.

Table 1. CUBE detector one minute time series. 2 inner 20 sm thick plastic scintillators with and without veto and their ratio.

16 June 2016	Upper scint. without veto	Bot. scint. without veto	Upper scint. with veto	Bot. scint. with veto	Upper with veto/without	Bottom with veto/without
9:54:00.0	10297	8522	5191	4310	0.504	0.506
9:55:00.0	10365	8428	5249	4239	0.506	0.503
9:56:00.0	10624	8495	5285	4305	0.498	0.507
9:57:00.0	10817	8683	5462	4341	0.505	0.5
9:58:00.0	10990	8825	5516	4543	0.502	0.515
9:59:00.0	11191	8916	5722	4608	0.511	0.517
10:00:00.0	11215	8867	5755	4605	0.513	0.519
10:01:00.0	11035	8961	5657	4626	0.513	0.516
10:02:00.0	10297	8420	5078	4169	0.493	0.489
10:03:00.0	10449	8522	5213	4248	0.499	0.498
10:04:00.0	10303	8451	5093	4195	0.494	0.496
10:05:00.0	10007	8331	4879	4072	0.488	0.489

Table 2. The mean values of 4 count rates measured by CUBE detector on fair weather on 16 June 2016 and their ratio.

	Mean	σ	7 with veto/ 7without veto	8 with veto/8 without veto
Cube #7, 20cm	10168	103	0.493 +/- 0.007	0.497 +/- 0.006
Cube #8, 20cm	8389	87		
7 with veto	5013	62		
8 with veto	4172	61		

Table 3. The recovered electron and gamma ray fluxes and fraction of electrons in TGE flux on 16 June 2016.

Time	e intensity ($1/m^2min$)	γ intensity ($1/m^2min$)	e/ γ (%)
9:57-9:58	824	8896	9.3
9:58-9:59	1308	9928	13.1
9:59-10:0	1296	14048	9.2
10:00-10:01	1256	14716	8.5
10:01-10:02	920	12788	7.2
10:02-10:03	268	1248	21.5

In Figure 14 we demonstrate another option from ADEI statistical package. Some variables are “delayed” correlated, i.e. there is some inertia (several minutes or even several hours) when the influence of one of the variables becomes apparent on another one. For instance, we show in Figure 14c time series of outside temperature and count rate of NaI crystal located just under the roof of the SKL experimental hall. NaI crystal is sensitive to outside temperature and only after the metallic tits are heated enough they transfer heat to

NaI crystals and count rate goes up. Certainly, the solar radiation is a key parameter influencing both temperature and then count rate. The simple correlation analysis is not applicable for such a dependences (Figure 14a). Therefore we include in ADEI stat package the delayed correlation option Figure 14c. From Figure 14b we can see that we need at least 3 hour of sun radiation till the particle detector “feel” the heat from the roof tilts.

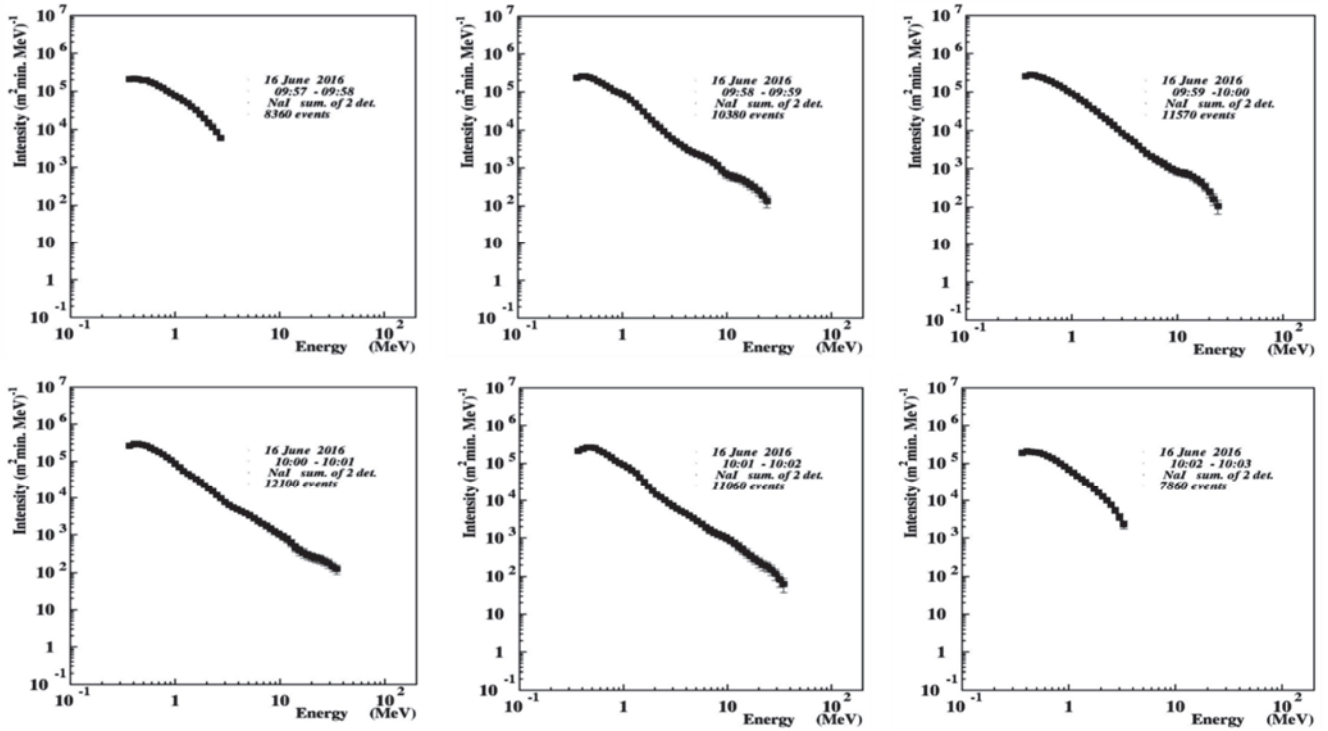


Figure 12. Energy spectra of TGE measured by the the network of NaI spectrometers.

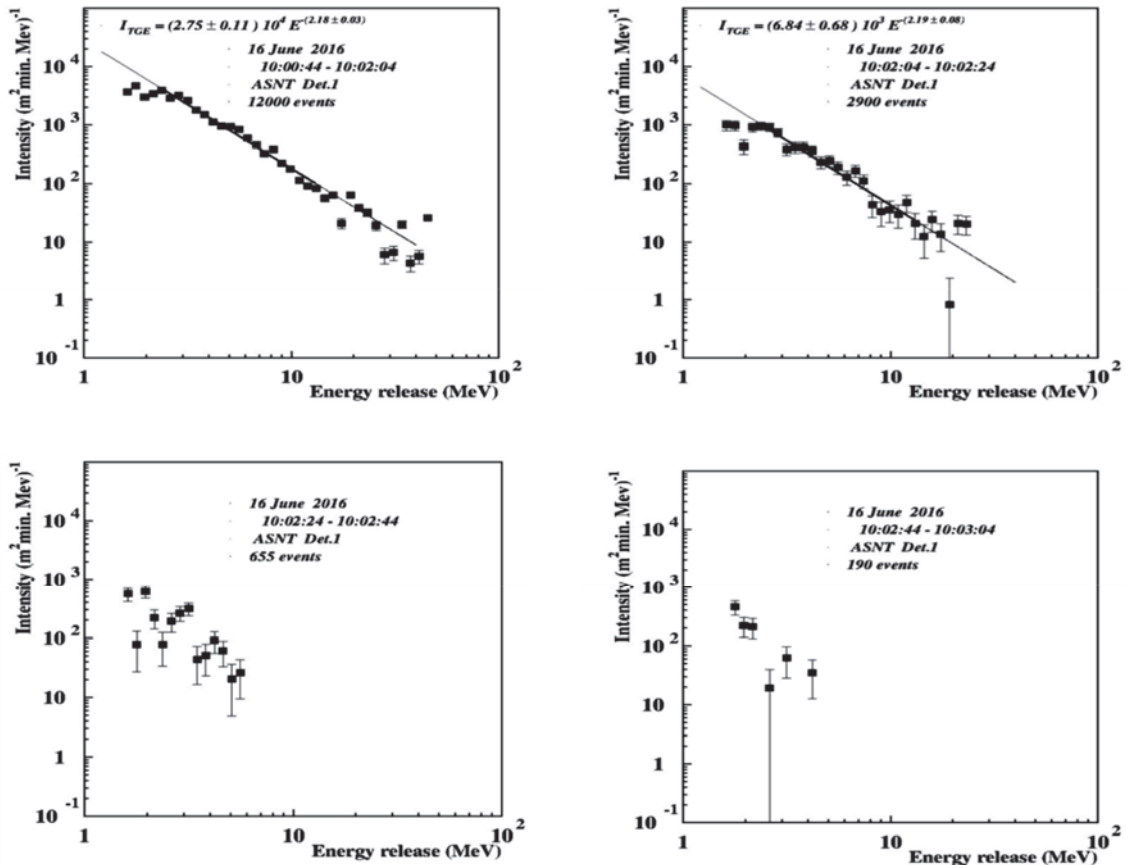


Figure 13. Energy release spectra measured by the the 60 cm thick plastic scintillator

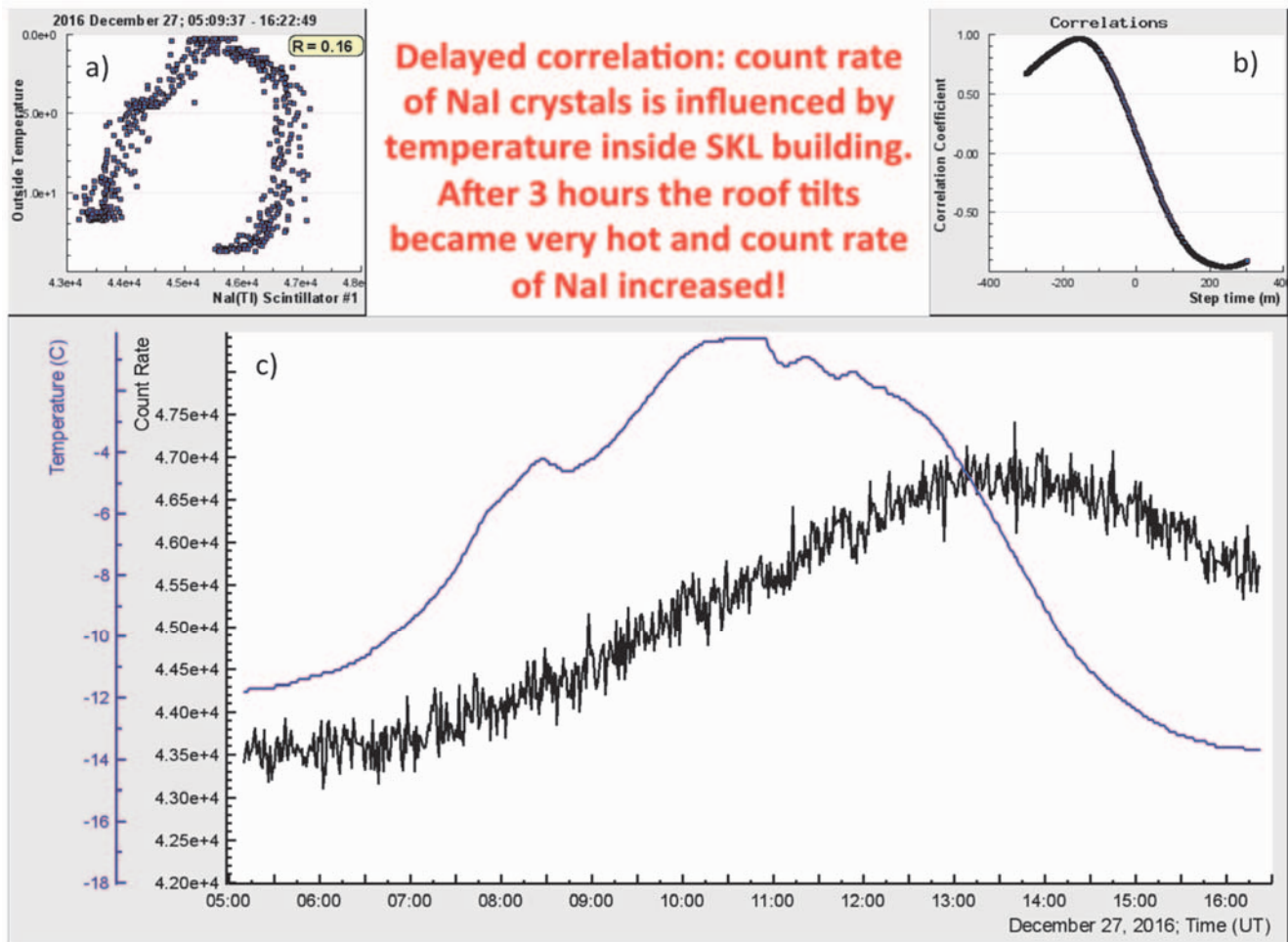


Figure 14. The 1-minute time series of outside temperature and NaI crystal count rate. In insert are shown results of simple correlation analysis and delayed analysis.

CONCLUSION

We describe in details how to apply ADEI procedures for analysis and physical inference in the atmospheric high-energy physics experiments. With the growing archives of the time series from the monitoring of the various cosmic ray fluxes and atmospheric electric field at ASEC, the need to establish a new type of infrastructures for using and comparing the data from numerous sources becomes more and more urgent. ADEI with new statistical modules meets this needs. To acquire the expected new knowledge, data samples from different domains are joining to make possible a multivariate correlation analysis. The developed methodology provides analysis tools and services to integrate a multitude of space and geophysical observations into a system that fully utilized the scientific potential of current and future geophysical observations. ADEI is used as well for the Space Weather and Solar physics research and we can present a set of ADEI layouts for physical inference in these domains. Physicists of Cosmic ray division prepare and publish in high-rank scientific journals near 20 articles heavily using ADEI platform in 2013 – 2016 (see the reference list). ADEI allows performing research projects very fast and comprehensive. ADEI tools make analytical work on the sophisticated problems rather easy; one can try and test many hypotheses very fast and come to definite conclusion allowing crosscheck and validation.

REFERENCE

- S. Chilingaryan, A. Beglarian, A. Kopmann, and S. Vočking, Advanced data extraction infrastructure: Web based system for management of time series data, J. Phys. Conf. Ser. 219, 042034 (2010).
- Chilingarian A. and Reymers A., Investigations of the response of hybrid particle detectors for the Space Environmental Viewing and Analysis Network (SEVAN), Ann. Geophys, 26, (249- 257), 2008.
- Chilingarian; Statistical study of the detection of solar protons of highest energies at 20 January 2005, Advances in Space Research 43 (2009), pp. 702-707.
- Chilingaryan S., Chilingarian A., Danielyan V., et al; Advanced data acquisition system for SEVAN, Advances in Space Research 43 (2009) 717–720.
- Chilingarian A., G. Hovsepyan, K. Arakelyan, et al; Space Environmental Viewing and Analysis Network (SEVAN), Earth, Moon and Planets: Volume 104, Issue 1 (2009), page 195.
- Chilingarian A. and Bostanjyan N., Cosmic ray intensity increases detected by Aragats Space Environmental Center monitors during the 23rd solar activity cycle in correlation with geomagnetic storms, 2009, J. Geophys. Res., Vol. 114, No. A9, A09107
- Chilingarian and N. Bostanjyan; On the relation of the Forbush decreases detected by ASEC monitors during the 23rd solar activity cycle with ICME parameters, Advances in Space Research, Volume 45, Issue 5, 1 March 2010, Pages 614-621

- Mailyan, A. Chilingarian; Investigation of diurnal variations of cosmic ray fluxes measured with using ASEC and NMDB monitors, *Advances in Space Research*, 45, (2010) 1380–1387.
- Chilingaryan S., Beglarian A., Kopmann A., and Voćking S., *J. Phys. Conf. Ser.* 219, 042034 (2010).
- Chilingarian A., A. Daryan, K. Arakelyan, A. Hovhannisyanyan, B. Mailyan, L. Melkumyan, G. Hovsepyan; Ground-based observations of thunderstorm-correlated fluxes of high-energy electrons, gamma rays, and neutrons (2010), *Phys Rev D*. 82.043009
- Chilingarian A., Hovsepyan G., and Hovhannisyanyan A., Particle bursts from thunderclouds: Natural particle accelerators above our heads, *Physical review D* 83, 062001 (2011).
- Chilingarian A., Karapetyan T., Calculation of the barometric coefficients at the start of the 24th solar activity cycle for particle detectors of Aragats Space Environmental Center, *Advances in Space Research* 47 (2011) 1140–1146.
- Chilingarian A., Bostanjyan N., and Vanyan L., Neutron bursts associated with thunderstorms, *PHYSICAL REVIEW D* 85, 085017, 2012.
- Chilingarian A., Bostanjyan N., and Vanyan L., Neutron bursts associated with thunderstorms, *Physical Review D* 85, 085017 (2012b).
- Chilingarian A., Bostanjyan N., Karapetyan T., Vanyan L., Remarks on recent results on neutron production during thunderstorms, *Physical Review D* 86, 093017 (2012c).
- Chilingarian, A. and Mkrtchyan, H., Role of the Lower Positive Charge Region (LPCR) in initiation of the Thunderstorm Ground Enhancements (TGEs), *Physical Review D* 86, 072003 (2012d).
- Chilingarian A., Mailyan B., Recovering of the TGE electron and gamma ray energy spectra, *Journal of Physics: Conference Series* 409 (2013) 012214.
- A Chilingarian, N Bostanjyan, T Karapetyan, On the possibility of location of radiation-emitting region in thundercloud, *Journal of Physics: Conference Series* 409 (2013) 012217.
- Avakyan K., Arakelyan K., Chilingarian A., et al., NaI Detector Network at Aragats, *Journal of Physics: Conference Series* 409 (2013) 012218.
- Chilingarian A., Bostanjyan N., Karapetyan T., Vanyan L., Neutron production during thunderstorms, *Journal of Physics: Conference Series* 409 (2013) 012216.
- Chilingarian A., Thunderstorm Ground Enhancements (TGEs) - New High- Energy Phenomenon Originated in the Terrestrial Atmosphere, *Journal of Physics: Conference Series* 409 (2013) 012019
- Chilingarian A., Hovsepyan G., Extensive Cloud Showers (ECS) – New High-Energy Phenomena Resulting from the Thunderstorm Atmospheres, *Journal of Physics: Conference Series* 409 (2013) 012221.
- Chilingarian A., Vanyan L., Simulations of the secondary cosmic ray propagation in the thunderstorm atmospheres resulting in the Thunderstorm ground enhancements (TGEs), *Journal of Physics: Conference Series* 409 (2013) 012215.
- Chilingarian A. and Mkrtchyan H., Lower positive charge region (LPCR) and its influence on initiation of Thunderstorm ground enhancements (TGEs) and cloud-to-ground (CG-) and intracloud (IC-) lightning occurrences, *Journal of Physics: Conference Series* 409 (2013) 012219
- Chilingarian A., Karapetyan T., Melkumyan L., Statistical analysis of the Thunderstorm Ground Enhancements (TGEs) detected on Mt. Aragats. *J. Adv. Space Res.*, 52, 1178 (2013),
- Chilingarian A., Mailyan B., Vanyan L., Observation of Thunderstorm Ground Enhancements with intense fluxes of high-energy electrons, *Astropart. Phys.*, 48, 1 (2013)
- Chilingarian A., Hovsepyan G., and Kozliner L., Thunderstorm ground enhancements: Gamma ray differential energy spectra, *Physical Review D* 88, 073001 (2013).
- Chilingarian, A., Exploring High-Energy Phenomena in Earth's Atmosphere, *Eos Trans. AGU*, 94(50), 488 (2013).
- Chilingarian A., Thunderstorm Ground Enhancements - model and relation to lightning flashes, *Journal of Atmospheric and Solar-Terrestrial Physics*, 107, 68-76, 2014.
- Chilingarian A., Hovsepyan G., Vanyan L., On the origin of the particle fluxes from the thunderclouds: energy spectra analysis, *EPL*, 106 (2014) 59001
- Chilingarian A., Exploring the Origin of High-Energy Particle Beams in the Atmosphere, *Eos*, Vol. 95, No. 46, 18 November 2014
- Chilingarian A., Chilingaryan S., Hovsepyan G., Calibration of particle detectors for secondary cosmic rays using gamma-ray beams from thunderclouds, *Astroparticle Physics* 69 (2015) 37–43
- Chilingarian A., Hovsepyan G., Khanikyanc Y., Reymers A. and Soghomonyan S., Lightning origination and thunderstorm ground enhancements terminated by the lightning flash, *EPL*, 110 (2015) 49001
- Chilingarian, A., Chilingaryan S., and Reymers A., Atmospheric discharges and particle fluxes, *J. Geophys. Res. Space Physics*, 120, 5845–5853 (2015), doi:10.1002/2015JA021259.
- Chilingarian A., Hovsepyan G., and Mantasakanyan E., Mount Aragats as a stable electron accelerator for atmospheric High-energy physics research, *Phys. Rev. D: Part. Fields*, 93, 052006 (2016).
- Chilingarian, A. Where does lightning come from?, *Eos*, 97 (2016), doi:10.1029/2016EO050097.
- Chilingarian A., Hovsepyan G., Kozliner L., Extensive Air Showers, Lightning, and Thunderstorm Ground Enhancements, *Astroparticle Physics* 82 (2016) 21–35.
- Drozdov, A. Y., A. Grigoriev, and Y. Malyshkin (2012), Assessment of thunderstorm neutron radiation environment at altitudes of aviation flights, *J. Geophys. Res.*, doi:10.1029/2012JA018302, in press.
- Hovhannisyanyan A., A. Chilingarian; Median filtering algorithms for multichannel detectors, *Advances in Space Research* 47 (2011) 1544–1557

Measurements of the Energy Spectra of TGE Gamma Ray Flux on Aragats Mountain

A. Chilingarian, G. Hovsepyan, L. Kozliner

Yerevan Physics Institute, Armenia

Abstract. In 2011 a network of five thallium-doped sodium iodide NaI(Tl) spectrometers was installed on Aragats Space Environmental Center (ASEC) for the research of a new discovered phenomenon, Thunderstorm ground enhancements (TGEs) – an intensive flux of electrons, gamma rays and neutrons originated in the thunderstorm atmospheres. NaI (Tl) crystals measure energy release of gamma rays, most penetrable and intensive specie of TGE. We perform calibration of the NaI(Tl) detectors and data acquisition electronics (DAQ) with gamma rays from the decay of the Caesium-137 (^{137}Cs) isotope and with energy release corresponding to the peak in the energy spectrum of the ambient population of secondary cosmic ray (CR muons with energy ~ 60 MeV). Thus, the gamma ray energies used for calibration cover two decades in energy range from 0.662 until 60 MeV. As well, a simulation-based procedure for reconstruction of gamma energy spectrum was developed and influence of a-priory information used in simulation on the accuracy of recovered energy spectra was investigated.

1. NAL(TL) NETWORK OPERATED ON ARAGATS, 3200 M ABOVE SEA LEVEL

Research of the Thunderstorm ground enhancements (TGEs) – an intensive flux of electrons, gamma rays and neutrons originated in the thunderstorm atmospheres gradually becomes a main scientific activity on the high-altitude Aragats stations of Yerevan Physics Institute (Chilingarian et al., 2005). The energy spectrum of the TGE gamma rays provides key information on the models of TGE origination (Chilingarian, Mailyan and Vanyan, 2012, Chilingarian, 2014). The NaI(Tl) spectrometers are located just below the tilt roof of the SKL experimental hall on Aragats 3200 m above sea level (Figure 1). The pulses from photomultiplier (PMT) optically connected to the crystal are fed through a preamplifier to an amplitude-to-digital converter (ADC).



Figure 1. NaI(Tl) spectrometers installed beneath the tilt roof of the SKL experimental hall at Aragats station

DAQ electronic specifications are described in detail in (Chilingarian et al., 2008, Arakelyan et al., 2014). The ADC dynamic range is expected to be ~ 200 and a scale factor d is used for the code-to-amplitude conversion.

$$K = d * \ln(E/E_0) + K_0 \quad (1)$$

where K is the ADC code, E is energy deposited in the spectrometer, K_0 is the code corresponding to the known incident energy E_0 (calibration with radioactive isotope). To determine parameter d , we need at least two calibration points with known ADC code values. The calibration was made with decay gamma rays from Caesium-137 (^{137}Cs) isotope and with energy release corresponding to the peak in the energy spectrum of the ambient population of secondary cosmic rays (CR muons with energy ~ 60 MeV). Thus, the gamma ray energies used for calibration cover two decades in the energy range from 0.662 until 60 MeV (see Figs 2 and 3).

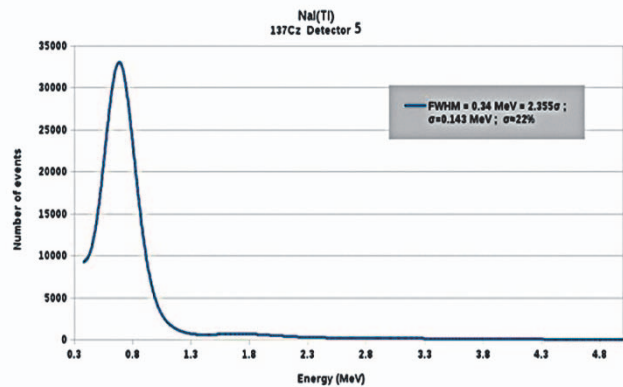


Figure 2. Energy deposited from 662 keV gamma rays from ^{137}Cs isotope decay; 1 minute exposure time.

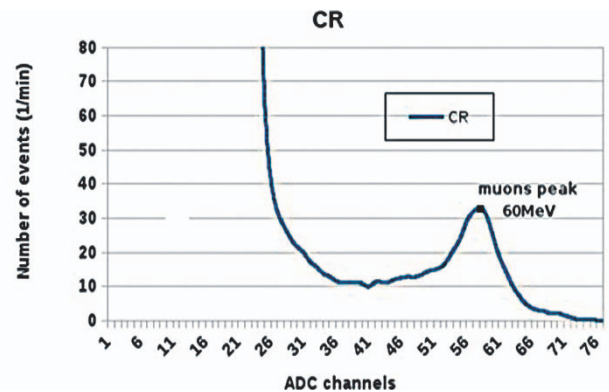


Figure 3. Energy deposited in detector by ambient cosmic rays (peak is corresponding to muons with energy ~ 60 MeV).

Table 1. Energy resolution of NaI (Tl) spectrometers at 662 keV and the ADC scale factor d .

Det.	σ	RE (%)	d
1	0.187	29	11.2
2	0.168	25	10.9
3	0.168	25	11.1
4	0.143	22	11.4
5	0.143	22	11.2

The distributions of the energy deposited in four NaI (TI) spectrometers from 662 keV gamma rays are shown in Figure 4.

The estimates of the energy resolution (the variance σ and relative error RE) and d scale factor values of 5 spectrometers comprising the NaI network are shown in Table 1.

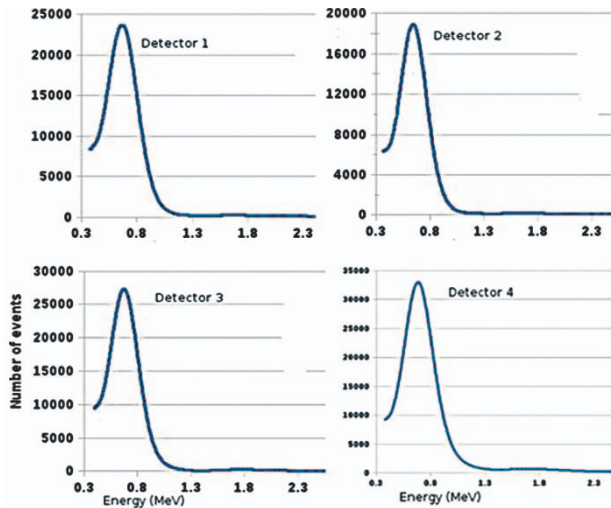


Figure 4. Energy deposited from 662 keV gamma rays in four NaI (TI) spectrometers.

The Log ADC's linearity was tested with a B&K Precision 4064 pulse generator which can generate signals of arbitrary shape with frequency 120 MHz. Because of the variations of parameters the 12-channel ADC board, we determine scale factor d for each channel separately. One should also check the linearity of energy determination within the whole range of measured energies. For this, negative rectangular pulses with amplitudes of $A_1=50$, $A_2=500$ and $A_3=1500$ mV and a width of $t=15$ ns were fed to the tested channels. The code values (k_1 , k_2 , k_3) as a function of the pulses fed to different channels are presented below.

Table 2. The code values corresponding to the different generator pulses

Channel	k1 (50mv)	k2 (500mv)	k3 (1500mv)
1	11	37	49
2	6	32	43
3	14	43	55
4	15	32	43
5	8	35	47
6	6	30	42
7	6	31	43
8	8	33	44
9	10	37	49
10	8	33	45
11	13	42	53
12	9	35	47

By two measured codes of ADC for different pulse amplitudes we calculate d values for each channel by

$$d_i = (k_i - k_j) * \ln(A_i/A_j), \quad (2)$$

where $i, j = 1, 2, 3$ and $i \neq j$.

The values of obtained in such a manner scale factor d are presented in Table 3.

Table 3. Scale factor d s for each ADC channel.

Channel	d_1	d_2	d_3
1	11.29	11.17	10.92
2	11.29	10.88	10.01
3	12.59	12.05	10.92
4	10.86	10.58	10.01
5	11.73	11.47	10.92
6	10.42	10.58	10.92
7	10.86	10.88	10.92
8	10.86	10.58	10.01
9	11.73	11.47	10.92
10	10.86	10.88	10.92
11	12.59	11.76	10.01
12	11.29	11.17	10.92

As one can see, the scale factor d differs from channel to channel and also depends on the pulse amplitude. Thus, before operating the DAQ electronics one should carefully certify and calibrated all ADCs and use a mean scale factor d , different for each channel.

2. LINEARITY OF ADC

The linearity of ADC was tested with pulses with a width of $t=100$ ns and different amplitudes. The results are presented in Figure 5. They show rather a satisfactory linearity (linear correlation coefficient equals to 0.78).

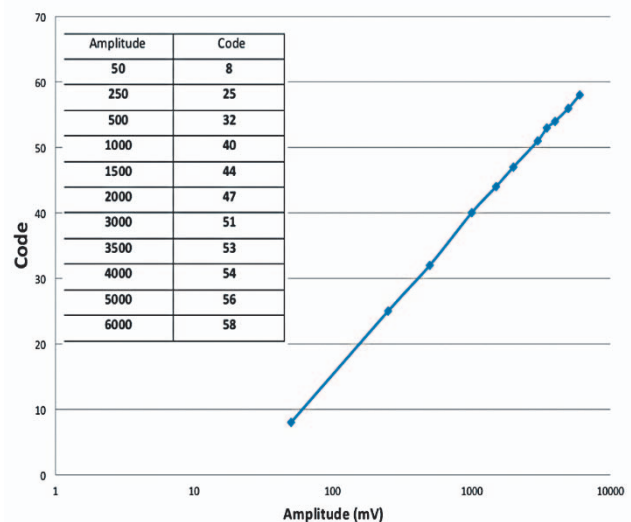


Figure 5. ADC linearity test, in the insert we show the pulses amplitude fed to ADC and registered code.

3. SPECTRUM CALCULATION. IMPACT OF BACKGROUND FLUCTUATION ON THE CHARACTERISTICS OF RECOVERED TGE SPECTRA.

During thunderstorms, the detectors register copiously secondary cosmic rays as well as TGE (signal). Each minute the histogram of energy releases from each spectrometer is stored in the database and is immediately assessable for the users via ADEI multivariate visualization platform (see Avagyan et al., 2017). As well, we measure and store 20-second histograms of energy releases in the 60 cm thick plastic scintillator of the ASNT detector (Chilingarian et al., 2017). To obtain a pure signal (TGE) the cosmic rays background measured at fair weather just before TGE is bin-by-bin deducted from the joint histogram containing both background (CR) releases and TGE releases. After deducting, the remained histogram of TGE releases is fitted by an analytical distribution function (usually power law function). The accuracies of the obtained parameters of the fit functions depend on the background fluctuations.

We have to keep background estimate time as much as possible near to TGE time not too large, because of possible biases due to changing atmospheric pressure and outside temperature.

Thus, we have to determine optimal size of a sample by which we will calculate the mean one-minute background. We start with a minimal time span of 20 seconds. Then the background was estimated by the 100, and 200-second data. The differential energy release spectrum was approximated by the power law function.

$$dJ/dE = A * E^{-\gamma} \quad (3)$$

The parameters of spectrum A and γ were determined by minimizing χ^2 function with CERN MINUIT code (CERN Program Library, 1993). We perform background estimation and power law parameter estimation for the 10 independent samples of size 20, 100 and 200 seconds see Table 4. The last row in Table 4 shows the average and root mean square errors for each case. Obviously, the smaller the background fluctuations are the higher is the accuracy of determination of the fit parameters.

Table 4.. Parameters of the TGE spectra approximated by a power function for 3 different modes of background estimation

20 sec		100sec		200sec	
A	γ	A	γ	A	γ
5.06E+03	1.47	3.09E+03	1.33	3.58E+03	1.29
3.17E+03	1.28	3.05E+03	1.24	3.65E+03	1.31
3.78E+03	1.27	3.67E+03	1.28	4.23E+03	1.36
3.80E+03	1.24	3.64E+03	1.34	3.75E+03	1.31
5.00E+03	1.44	4.21E+03	1.44	4.97E+03	1.43
7.96E+03	1.81	4.34E+03	1.35	4.54E+03	1.39
3.97E+03	1.33	3.97E+03	1.41	4.30E+03	1.38
4.43E+03	1.38	2.93E+03	1.21	4.02E+03	1.30
6.02E+03	1.41	5.55E+03	1.49	4.80E+03	1.42
5.20E+03	1.43	4.44E+03	1.39	4.33E+03	1.33
Average \pm rmse					
4.46E+03 \pm 1.95E+03	1.406 \pm 0.154	3.89E+03 \pm 7.58E+02	1.348 \pm 0.084	4.22E+03 \pm 4.48E+02	1.352 \pm 0.049

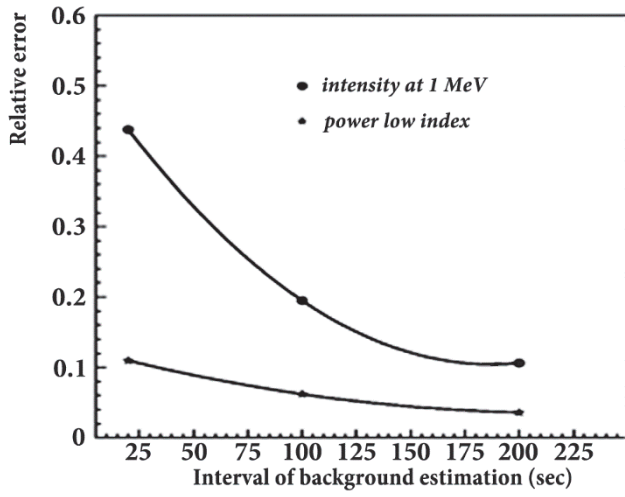


Figure 6. Relative errors of spectrum parameters for three modes of background estimation

The decreasing of the relative errors of parameters A and γ for three modes of background estimation are shown in Figure 6. Further increase of the background accumulation time (larger than 200 sec) does not decrease the errors of spectral parameters and is apparently determined by fluctuations of the TGE itself.

4. RECONSTRUCTION OF THE DIFFERENTIAL TGE ENERGY SPECTRA

No one spectrometer is ideal and there occurred migrations of events from bin-to-bin. If we have uniform spectrum such a migration will not distort approximation nction shape. However, all cosmic ray spectra are very steep and we have to introduce correction procedure for the recovering genuine spectral shape. It is well known, that due to errors of registering devices the measured and true values may differ significantly. The response function that allows the correction of spectra is mathematically expressed as

$$f(x) = \int_{-\infty}^{\infty} W(x,y)\varphi(y)dy, \quad (4)$$

where $f(x)$ is the measured distribution of the physical quantity, $\varphi(y)$ is a true distribution and $W(x,y)$ is the core function. With the help of this first-class Fredholm equation one can solve the inverse problem, i.e. using the measured distribution $f(x)$ and known kernel $W(x,y)$ one can find the true distribution $\varphi(y)$, i.e. solve the inverse problem of cosmic rays. For reconstructing of the energy spectra of the TGE gamma rays the discrete form of the Fredholm equation is used:

$$x_k = A_{i,k}y_i, \quad (5)$$

where x_k are the experimentally observed intensities and y_i are the its "true" value. The task is to recover the true y_i values using the measured values x_k and the known values of A_{ik}^{-1} . The A_{ik}^{-1} values had been determined by solving direct problem of cosmic rays i.e. by simulation of the gamma ray traversal through the detector. For it the GEANT3 simulation program was used (CERN Program Library, 1993). The adequacy of the experimentally observed calibration distributions to the simulated ones is discussed in (Arakelyan et al., 2014).

The energy deposit Edep (MeV) in the spectrometer was simulated for a given energy of gamma ray, E_i ($i=1, \dots, 130$) by a logarithmic uniform scale with a step $s=1/26$. Selected

energy range covers near five decades of energy beginning at $E_0=0.2343$ MeV. Conversion of energy to ADC codes was done according to Eq.(1), where $E_0=60$ MeV and K_0 is the code corresponding to the maximum of muon energy deposit in the detector (see Figure 3). When calculating Edep in 60 cm thick plastic scintillator, the specific light yield function dependent on the "deepness" of gamma ray interaction in scintillator slab was taken into account. $N=105$ events had been simulated for each E_i . The obtained matrix $B_{i,k}$ contains the number of gamma rays with energy E_i detected under a code k ($k=1, \dots, 127$). Figure 7 shows a fragment of that matrix. Column "A" represents the energies E_i of gamma rays. The rows present the number of events registered under code k . By summation of the matrix over k index we get the full number of detector responses to the gamma rays of a given energy. This procedure yields the gamma ray registration efficiency as a function of the energy (Figure 8). Transition from $B_{i,k}$ to $A_{i,k}^{-1}$ matrix is done by normalizing it in accordance with the number of events for each index k . When normalizing, the a priori information on the recovered spectrum had been taken into account, namely, we took the power law spectrum (3) with the probability density $F(E_i) = ((\beta - 1)/E_0) * (E_i/E_0)^{-\beta}$, where $E_0=0.2343$ MeV is the imulated threshold energy and E_i is the current gamma ray energy (see Figure 7); index β is an unknown spectral index:

$$A_{i,k}^{-1} = B_{i,k} * F(E_i) / \sum_{i=1}^{130} B_{i,k} * F(E_i) \quad (6)$$

So, $A_{i,k}^{-1}$ is the probability for the ADC's k code to be triggered by gamma ray with E_i . Ultimately, the real number of gamma rays having energy E_i is

$$y_i = \sum_{j=1} A_{i,k}^{-1} * x_k, \quad (7)$$

where x_k is the number of the events observed in the k -th channel of ADC. So, the true intensity is

$$J_i = \frac{y_i}{(E_{i+1}-E_i)*T*S*F(E_i)}, \quad (8)$$

where $F(E_i)$ – is the efficiency of the gamma registration (see Figure 8), T and S are exposition time and detector area, respectively.

Thus, in recovering the energy spectrum we need during solving direct CR problem in simulation, to specify the spectral index, which we have to estimate in the measurements. To resolve this contradiction we have to demonstrate that using a priory information on the spectral index β , is not curtail for obtaining matrix A, and – in recovering the experimental spectra. This check was performed for the TGE event registered at on 4 March 2016. By the other ASEC detectors, we see that the contamination of electrons is less than 5%.

Three versions of $A_{i,k}^{-1}$ matrix were obtained for the values of $\beta = 1.5, 2.0$ and 2.5 . In each case, the spectrum was approximated by the power-law function (3), as it was described above. The observed and corrected spectra parameters are shown in the Table 5 and Figure 9. As one can see from Table 5, the change of the spectral index ("Reconstructed " columns) leads to changes in the parameters of the restored spectrum ~5% in A coefficient and ~2% in γ index, i.e. this errors should be noted as additional methodical errors in final presentation of results.

	A	B	C	D	E	F	G	H	I	J	K	L	M	N	O	P	Q
1	Energy	k=1	2	3	4	5	6	7	8	9	10	11	12	13	14	15	16
2	0.23431	17632	14958	8730	3305	755	111	9	0	0	0	0	0	0	0	0	0
3	0.25661	15370	17851	14894	8698	3209	766	97	11	0	0	0	0	0	0	0	0
4	0.28103	10412	15396	17845	14865	8745	3345	812	116	7	0	0	0	0	0	0	0
5	0.30778	5964	10470	15559	17744	14759	8541	3369	821	93	11	0	0	0	0	0	0
6	0.33707	3121	5946	10463	15333	17616	14692	8600	3325	815	100	10	0	0	0	0	0
7	0.36915	1810	3214	5865	10550	15110	17548	14673	8459	3366	785	123	10	1	0	0	0
8	0.40428	1322	2019	3241	5856	10288	15162	17385	14491	8263	3349	789	105	8	0	0	0
9	0.44275	1061	1407	1955	3289	5959	10074	15150	17179	14314	8386	3191	699	103	6	1	0
10	0.48489	798	1029	1501	2061	3246	5727	10013	14805	16999	14259	8252	3145	757	102	7	1
11	0.53103	707	869	1175	1555	2161	3285	5797	9765	14485	16586	13929	8121	3152	775	110	6
12	0.58157	586	718	951	1205	1611	2266	3499	5746	9969	14019	15813	13531	7991	3059	696	104
13	0.63692	553	697	772	1007	1293	1662	2203	3381	5832	9633	13626	16090	13238	7750	3012	667
14	0.69754	604	657	792	888	1099	1371	1716	2361	3364	5804	9377	13632	15431	12796	7533	2903
15	0.76392	610	709	754	836	1017	1123	1441	1715	2349	3450	5647	9252	13261	14845	12663	7384
16	0.83662	610	677	692	759	975	1065	1303	1484	1820	2342	3535	5564	9218	12766	14697	12176
17	0.91624	576	640	727	822	871	1017	1153	1305	1526	1824	2374	3538	5523	8884	12534	14458
18	1.0034	605	624	650	709	865	888	1105	1200	1396	1632	1914	2440	3485	5659	8757	12337
19	1.0989	565	615	657	710	797	888	1003	1087	1306	1491	1752	2065	2524	3494	5433	8686
20	1.2035	567	563	647	700	748	799	877	1074	1226	1311	1488	1670	1948	2562	3560	5524
21	1.3181	549	563	583	634	690	751	895	997	1057	1161	1305	1535	1710	2015	2560	3540
22	1.4435	451	527	549	591	612	688	789	887	943	1113	1183	1385	1518	1767	2040	2643
23	1.5809	427	496	496	531	620	633	742	770	895	990	1099	1189	1341	1517	1720	2127
24	1.7313	454	432	501	511	563	581	631	724	824	883	1027	1095	1235	1372	1535	1738
25	1.8961	376	428	515	465	485	557	576	719	733	788	947	990	1125	1153	1312	1531
26	2.0766	394	381	415	426	466	497	531	598	723	786	826	860	1027	1066	1239	1306
27	2.2742	295	362	397	422	457	422	529	563	595	704	793	790	925	960	1064	1218
28	2.4906	311	294	337	376	386	407	479	469	550	593	658	683	768	792	962	1057
29	2.7276	261	292	294	319	314	373	425	426	510	530	584	613	665	758	816	826
30	2.9872	226	245	282	261	305	331	336	389	481	471	497	576	600	647	697	800
31	3.2715	185	222	268	260	262	275	306	366	433	478	500	494	556	574	602	716
32	3.5829	166	202	227	220	252	258	265	318	322	420	425	418	455	456	596	569
33	3.9238	125	146	195	203	204	225	252	246	344	353	388	372	385	438	447	503
34	4.2973	158	139	167	206	195	208	230	256	321	329	344	286	338	370	425	422
35	4.7062	106	121	148	147	172	178	174	247	283	259	315	291	285	328	323	382
36	5.1541	100	119	147	166	135	161	157	187	232	277	226	255	250	299	277	321

Figure 7. Fragment of B_{ik} matrix. Column "A" represents the energies E_i of gamma-quanta. The rows show the number of events registered under code k at the given energy.

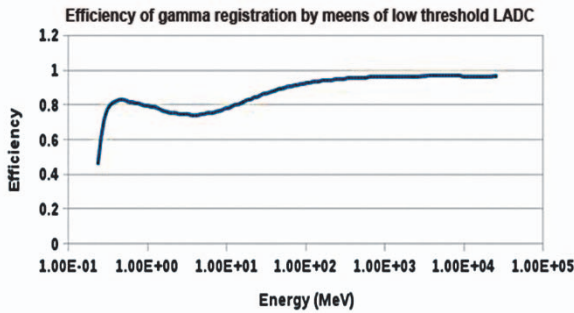


Figure 8. NaI(Tl) detector's gamma registration efficiency as a function of energy.

Table 5. Parameters of the 10 June 2014 and 04 March 2016 observed and reconstructed events spectrum.

Date	Observed	Reconstructed			
		$\beta=1.5$	$\beta=2.0$	$\beta=2.5$	
04 March 2016	A	$(8.42 \pm 0.07) 10^4$	$(1.09 \pm 0.47) 10^5$	$(1.07 \pm 0.42) 10^5$	$(9.72 \pm 0.42) 10^4$
	γ	2.16 ± 0.02	2.08 ± 0.05	2.12 ± 0.05	2.17 ± 0.05

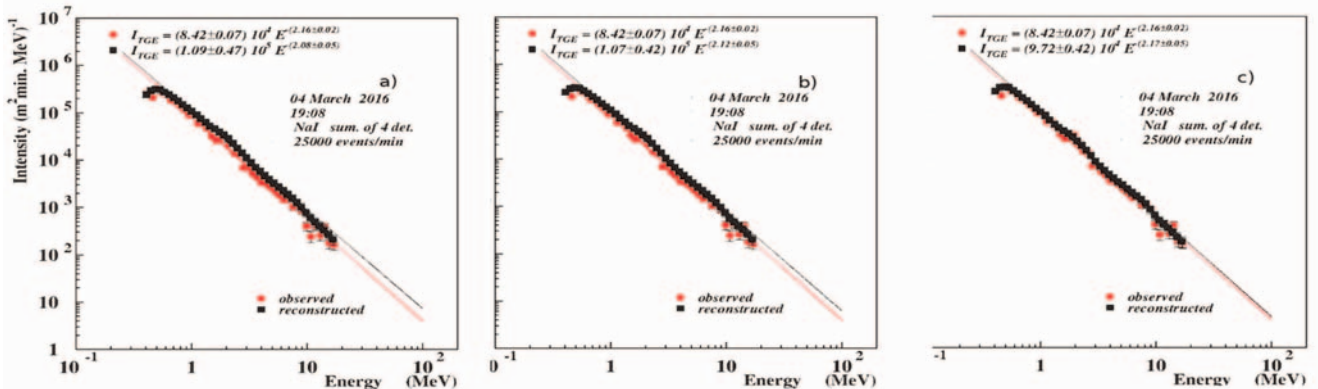


Figure 9. Registered on the 10 June 2014 at 17:29-17:32 TGE spectrum. The observed (red) spectra compared with reconstructed with inverse matrix obtained with a) $\beta = 1.5$; b) $\beta = 2.0$ and c) $\beta = 2.5$.

CONCLUSION

The network of NaI(TL) spectrometers reliably measure TGE differential energy spectra. The energy resolution of spectrometers is 20-30% at 662 KeV. The scale factor d for all 5 spectrometers was measured by calibrations experiments with ^{137}Cs isotope and secondary CR flux. Parameters of 12-channel ADC board were precisely estimated with high-frequency signal generator in the pulse amplitude range (50 – 1500 mv), maximal deviation from the linearity do not exceed 10%.

The influence of the background fluctuation on the accuracy of the recovered TGE energy release spectra was investigated; the optimal time span of 200 sec for the estimation background spectrum measured by the 60 cm. thick plastic scintillator was found. If we use background estimate by 20 sec energy release histogram the errors of power law coefficient and index are 44% and 11%; for the 100 sec – 20% and 7%; for 200 sec – 11% and 3%. Further increase does not lead to the diminishing of errors.

For the recovering of the differential energy spectra measured by NaI network, the spectrometer response function was calculated with CERN GEANT package. To avoid uncertainty and additional errors connected with a selection of the energy spectra shape in recovering of the spectra, 3 different spectral indices were used. The power law coefficient and index varied by 5% and 2% correspondingly when a priory spectral index got values 1.5,, and 2.5. Thus, this methodical error should be mentioned in presenting TGE spectra along with statistical one.

REFERENCE

Chilingarian, A., Arakelyan, K., Avakyan, K. et al., 2005, Correlated measurements of secondary cosmic ray fluxes by the Aragats space-environmental center monitors, Nucl. Instrum. Methods A 543 (2–3) 483.

Chilingaryan S., Chilingarian A., Danielyan, Eppler W., *The Aragats data acquisition system for highly distributed particle detecting networks*, Journal of Physics: Conference Series 119 (2008) 082001.

Chilingarian, A., Daryan, A., Arakelyan, K., Hovhannisyan, A., Mailyan, B., Melkumyan, L., Hovsepyan, G., Chilingaryan, S., Reymers, A., Vanyan, L., 2010. Ground- based observations of thunderstorm-correlated fluxes of high-energy electrons, gamma rays, and neutrons. Phys. Rev. D: Part. Fields 82 (4), 043009.

Chilingarian, A., Hovsepyan, G., Hovhannisyan, A., 2011. Particle bursts from thunderclouds: natural particle accelerators above our heads. Phys. Rev. D: Part. Fields 83 (6), 062001.

Chilingarian, A., Mailyan, B., Vanyan, L., Recovering of the energy spectra of electrons and gamma rays coming from the thunderclouds. Atmos. Res. 114–115, 1 (2012).

Chilingarian A., Thunderstorm Ground Enhancements – model and relation to lightning flashes, J. Atmos. Solar-Terr. Phys. 107 (2014) 68–76.

Chilingarian A., Chilingaryan S., Hovsepyan G., Kozliner L., Mailyan B., In situ measurements of the Runaway breakdown (Relativistic Runaway Electron Avalanche) on Aragats: experimental data and models, *Ibid*

Avakyan K., Chilingaryan S., Chilingarian A., Karapetyan T., Physical analysis of multivariate measurements in the Atmospheric high-energy physics experiments within ADEI platform, *ibid*.

Arakelyan K, Daryan A., Hovsepyan G., Kozliner L., Reimers A., Design and response function of NaI detectors of Aragats complex installation Nuclear Instruments and Methods in Physics Research A763 (2014) 308–313

MINUIT: CERN Program Library Long Writeup D506, CERN (1993)

Agnostelli, S., Allison, J., Amako, K., et al., 2003. GEANT4—a simulation toolkit. Nucl. Instrum. Methods Phys. Res., Sect. A 506, 250–303.

Terrestrial Gamma Flashes at Ground Level -- TETRA-II

D. Pleshinger¹, M. Cherry¹, C. Adams¹, S. Al-Nussirat², J. Arias³, S. Bai⁴, Z. Baum¹, P. Bitzer⁵, H. Christian⁵, S. Ellison¹, D. Granger¹, T. Guzik¹, J. Hoffmann¹, E. Khosravi⁴, M. Legault⁶, M. Orang⁴, R. Ramos⁷, D. Smith⁸, D. Smith¹, M. Stewart¹, A. Sunda-Meya⁹, J. Trepanier⁸, A. Ward⁹

1. Dept. of Physics & Astronomy, Louisiana State Univ., Baton Rouge, LA 70803 USA

2. Dept. of Physics, Univ. of Alabama, Huntsville

3. CENAMEP, Panama City, Panama

4. Dept. of Computer Science, Southern Univ., Baton Rouge

5. NSSTC and SWIRLL, Huntsville

6. Dept. of Physics, Univ. of Puerto Rico, Bayamón

7. Programa de Ciencias Sociales, Univ. of Puerto Rico, Utuado

8. Dept. of Geography & Anthropology, Louisiana State Univ., Baton Rouge

9. Dept. of Physics, Xavier University of Louisiana, New Orleans

Abstract. An upgraded version of the TGF and Energetics Thunderstorm Rooftop Array (TETRA-II) consists of an array of BGO scintillators in four separate locations: the campus of the University of Puerto Rico at Utuado; the campus of Louisiana State University in Baton Rouge, Louisiana; the Severe Weather Institute and Radar & Lightning Laboratories in Huntsville, Alabama; and the Centro Nacional de Metrología de Panama (CENAMEP) in Panama City, Panama. TETRA-II began operation in May 2016. The original TETRA-I array of NaI scintillators at Louisiana State University detected 37 millisecond-scale bursts of gamma rays at energies 50 keV-2 MeV associated with nearby (< 8 km) thunderstorms. When TETRA-II is fully operational, it will have approximately an order of magnitude greater sensitivity than TETRA-I. The ability to observe ground-level Terrestrial Gamma Flashes from close to the source allows a unique analysis of the storm cells producing these events. A brief description of the TETRA-I observations, a description of TETRA-II, and preliminary results will be presented.

1. INTRODUCTION

Lightning provides the most powerful natural accelerator available on Earth for the production of high-energy particles. Satellite instruments have detected gamma ray bursts at energies in excess of tens of millions of electron volts as a result of this acceleration. Initially, these Terrestrial Gamma Flashes (TGFs) were detected by the Burst and Transient Source Experiment (BATSE) onboard the Compton Gamma Ray Observatory [1], and have since been detected by other satellites, including RHESSI [2, 3], AGILE [4, 5,6], and the Fermi Gamma Ray Telescope [7]. These observations, associated mainly with positive polarity intracloud lightning to generate the upward trajectory of the electrons and photons, were correlated with regions of intense lightning typically at 10-25 km above the ground.

The TGF events observed from space are extremely intense even at such a great distance. Observations of TGFs from the ground give a unique opportunity to study these events. Being significantly closer to the flashes allows for the detection of lower flux events that can be mixed in with the background in the satellite data. Also, detection from the ground gives the ability to associate TGFs with the detailed Evolution of the thunderstorm and specific lightning strikes occurring in the area.

In 2010 the TGF and Energetic Thunderstorm Rooftop Array (TETRA) began operation at Louisiana State University with sensitivity for downward directed TGFs known as Thunderstorm Ground Enhancements (TGEs) [8] associated with negative polarity lightning. In its first four years of operation, 37 millisecond-scale bursts of gamma rays were detected associated with nearby lightning. An overview of the project, its analysis and results are presented. The new TETRA-II detectors were deployed in 2016 with increased size and sensitivity, and with the main sites located

in regions where Fermi has detected many of its events. An overview of TETRA-II, its current status, and initial event candidate results are presented.

2. TETRA I EXPERIMENT

The TGF and Energetic Thunderstorm Rooftop Array (TETRA) consisted of twelve 19 cm x 19 cm x 5 mm NaI (TI) scintillators spread across the Louisiana State University campus in 4 separate boxes to detect gamma ray emissions during thunderstorms in the 50 keV to 2 MeV energy range. Each box contained 3 NaI scintillators that were each viewed by individual photomultiplier tubes (PMTs) and operated in a self triggered mode [9].

The data, consisting of individual phototube pulse heights and times, were binned in 2 millisecond bins with the electronics capable of detecting events at a sustained rate of 30 kHz and a burst rate of up to 70 kHz. Triggers at a level of 20 standard deviations or more above the daily average were flagged, with days containing excessive noise, calibrations, or other instrumental problems removed.

Possible events were then compared with commercial lightning data from the United States Precision Lightning Network (USPLN) and with radar data during the storm.

Figure 1 shows an event that was detected in multiple boxes on 18 August 2011, and its correlation with lightning and cloud density. In the top panel, multiple triggers are seen above the 20 σ threshold around 18:00 CST. In the next panel, a spike in the number of lightning strikes per second within 5 miles is seen at the same time. The third panel shows the distance from the TETRA experiment of all lightning strikes detected by USPLN within 120 miles. Here the storm can be seen starting at a distance around 60 miles out, approaching and reaching Baton Rouge at the time of the triggers, and then moving out again. The final panel shows the cloud density overhead throughout the day.

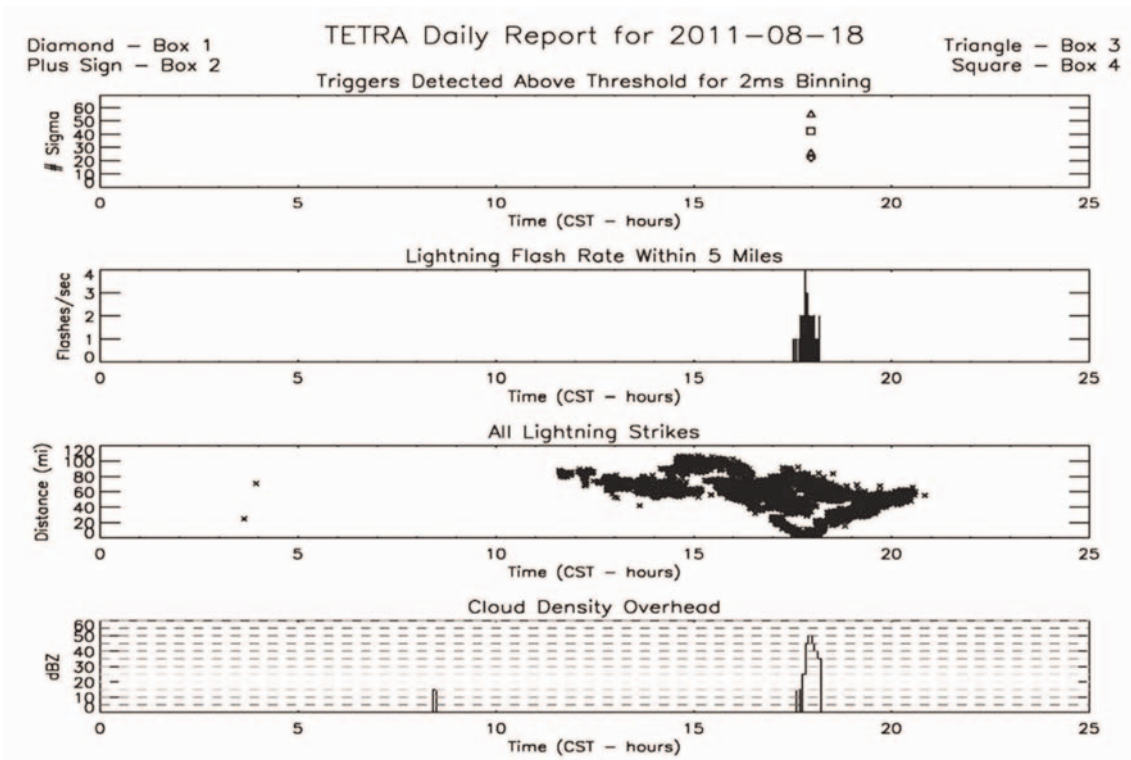


Figure 1. TETRA Report for 18 August 2011 event. Top panel shows triggers detected above 20σ threshold. Second panel shows rate per second of lightning strikes within 5 miles from USPLN. Third panel shows the distance to each lightning strike detected by USPLN within 120 miles. Bottom panel shows the overhead cloud density.

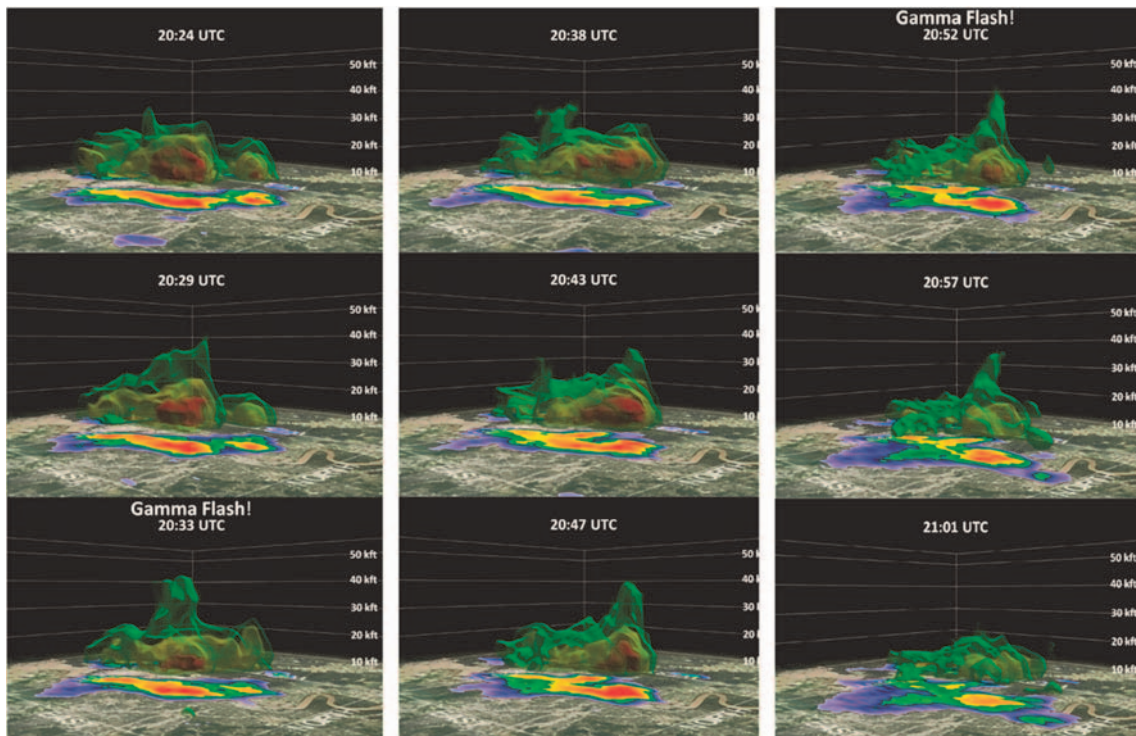


Figure 2. Three dimensional radar images of the thunderstorm on 22 June 2013 that produced two TETRA TGFs. The size of each panel is roughly 30 km by 30 km.

Along with the comparison of the event candidates with lightning, radar images were also obtained. Figure 2 shows a time lapse sequence of radar images every 5 minutes for the thunderstorm that produced two TGFs on 22 June 2013. The colored cloud surfaces correspond to the decibel levels of a standard radar map, with green depicting rain and red for more intense cloud and storm structure. The panels are read down the left, then the middle, and finally down the right, for a total of roughly 40 minutes of time during the storm. Each panel has a timestamp, heights marked in thousands of feet, and a flattened radar image on the base centered over TETRA. The images begin with the storm beginning to intensify, with an updraft reaching almost 14 km in the third panel. Here the gamma flash is observed and the cloud collapses back down. By the sixth panel, another updraft is

seen reaching approximately the same height, and again this cloud collapses as a second gamma flash is seen in the seventh panel. By 21:00 UTC in the final panel the storm is seen to cease. Fourteen of the eighteen storms producing TGFs in the TETRA catalog were found to occur at approximately the same time as the collapse of the updraft in the radar images.

TETRA detected 37 millisecond bursts of gamma rays associated with thunderstorms in its approximately 4 years of full operation. Table 1 lists the events observed by TETRA with lightning strikes observed within 5 miles and 5 minutes of the event. Typically, a T90 duration on the order of hundreds of microseconds is seen with a range of 7 to 45 photons detected in each event and currents ranging from -19 to -158 kA [9].

Table 1. Table of TETRA gamma ray events. [9]

Date	Trigger Time (CST) (hh:mm:ss)	Timing Error (μ s)	Max Lightning Rate within 5mi. (sec^{-1})	Cloud Density (dBZ)	Storm Type	# Flashes within 5mi. and 5min.	Trigger-Lightning Difference (ms)	Lightning Distance (mi)	Lightning Current (kA)	T ₉₀ Event Duration (μ s)	Total γ Rays Detected	Total Energy (MeV)	σ Above Mean	Probability of CEC
31 Jul 2011	16:21:44.976	3950	2	45	Coastal	12	-6	1.4	-43.6	702	19	8.8	25.1	1.7E-06
31 Jul 2011	16:21:45.300	3950	2	45	Coastal	12	-4	1.8	-29.1	1326	23	9.6	25.1	1.7E-06
18 Aug 2011	17:57:38.986	3449	4	50	Coastal	40	6741	1.3	-23.4	1318	38	16.5	22.4	1.2E-13
24 Feb 2011	23:11:15.787	2328	3	45	Front	1	-6	2.9	-20.9	953	20	1.7	24.6	-
29 Jul 2011	10:38:58.932	775	6	45	Coastal	42	5	0.4	-57.7	153	8	4.8	22.6	-
18 Aug 2011	17:57:39.202	3196	4	50	Coastal	40	6525	1.3	-23.4	24	7	3.6	23.8	-
12 Mar 2012	11:30:16.500	1676	6	45	Front	4	5	1.6	-81.3	1997	7	3.2	20.7	-
2 Apr 2012	12:29:30.554	1980	3	50	Coastal	8	6	0.6	-29.9	464	21	15.8	90.0	-
4 Apr 2012	02:49:21.900	1240	5	55	Front	21	-3	1.9	-158.4	515	24	21.3	77.2	-
5 Aug 2012	14:43:35.661	-	7	40	Coastal	16	-849	0.6	-56.5	392	11	6.1	35.3	-
6 Aug 2012	19:17:33.359	-	5	50	Coastal	1	1017	0.8	-23.1	465	10	4.5	21.8	-
9 Aug 2012	15:27:29.804	4832	4	50	Front	21	2	0.4	-27.8	2412	12	2.9	25.6	-
9 Aug 2012	15:28:36.070	4832	4	50	Front	27	80	0.9	-36.7	4217	24	7.4	35.7	-
9 Aug 2012	15:28:36.560	4832	4	50	Front	27	2	0.8	-19.2	146	12	8.0	29.7	-
6 Jun 2012	15:37:31	-	6	55	Coastal	40	-	-	-	759	36	17.5	85.3	-
6 Jun 2012	15:44:18	-	6	55	Coastal	16	-	-	-	609	14	8.5	46.9	-
6 Jun 2012	19:29:43	-	6	55	Coastal	33	-	-	-	2376	24	9.7	51.9	-
6 Jun 2012	19:31:21	-	6	55	Coastal	19	-	-	-	746	31	16.2	45.6	-
6 Jun 2012	19:36:41	-	6	55	Coastal	18	-	-	-	604	28	21.1	57.7	-
14 Apr 2013	01:26:02.390	0.037	4	45	Coastal	2	-493	0.7	-46.9	1552	9	3.9	51.4	-
24 Apr 2013	07:11:37.894	0.024	5	50	Front	24	6595	1.9	-64.8	616	7	1.6	25.6	-
10 May 2013	03:51:57.412	0.034	5	55	Front	166	969	1.3	-23.9	1032	29	-	101.3	-
10 May 2013	03:51:58.116	0.047	5	55	Front	163	265	1.3	-23.9	80	6	2.1	25.2	-
22 Jun 2013	14:31:28.794	0.058	5	50	Coastal	7	-292	1.7	-33.8	159	8	1.9	25.8	-
22 Jun 2013	14:52:49.063	0.043	5	50	Coastal	6	199	1.3	-48.9	1757	15	5.6	50.4	-
29 Jun 2013	04:24:11.550	0.038	4	40	Front	17	-169	1.7	-32.9	732	14	7.0	89.7	-
29 Jun 2013	04:24:11.614	0.038	4	40	Front	17	-233	1.7	-32.9	164	4	3.0	31.6	-
13 Sep 2013	18:11:13.263	0.019	5	50	Coastal	39	403	1.4	-35.3	1539	18	6.2	40.9	-

3. TETRA II

TETRA provided evidence that negative polarity lightning strikes accelerate particles downward and produce gamma rays with energies of at least 2 MeV. To improve on this, TETRA-II was designed to measure more abundant small TGFs from the ground with better statistics and a higher energy range. TETRA-II consists of individual detector boxes each with six 1 inch x 1 inch x 10 inch BGO scintillators from the ATIC cosmic ray balloon experiment [10]. The BGO are viewed by 1.5 inch PMTs at either end, and are spring outted into a PVC housing, as seen in figure 3. The PMTs are read out by National Instruments PCIe 6351 high speed data acquisition (1 Msample/sec) cards, and the data are pushed to a server at LSU for analysis (Figure 4).

Two TETRA-II boxes (12 BGO scintillators) are located on the rooftop of the Physics building at Louisiana State University, and have been operational since the Summer of 2016 together with one of the boxes from the original TETRA-I experiment. In December 2015, 10 boxes were mounted on the roof of Building B at the University of Puerto Rico in Utuado, a location chosen because of its high lightning rate, good infrastructure, and its location sufficiently far south that the Fermi orbit passes overhead. The 10 Utuado boxes have been calibrated and running since Fall of 2016 (Figure 5).



Figure 3. PVC assembly containing a BGO scintillator and 2 PMTs to view either end. Six of these are placed in each TETRA-II box.

Two boxes are installed at the Severe Weather Institute and Radar & Lightning Laboratories in Huntsville, Alabama and have been taking data since October 2016. Five more boxes were installed at the Centro Nacional de Metrologia de Panama (CENAMEP) in Panama City, Panama, in January 2017, in a location near where Fermi has detected high rates of TGFs (Fig 6). In all three TETRA-II locations, typical box separations are 5-15 m.

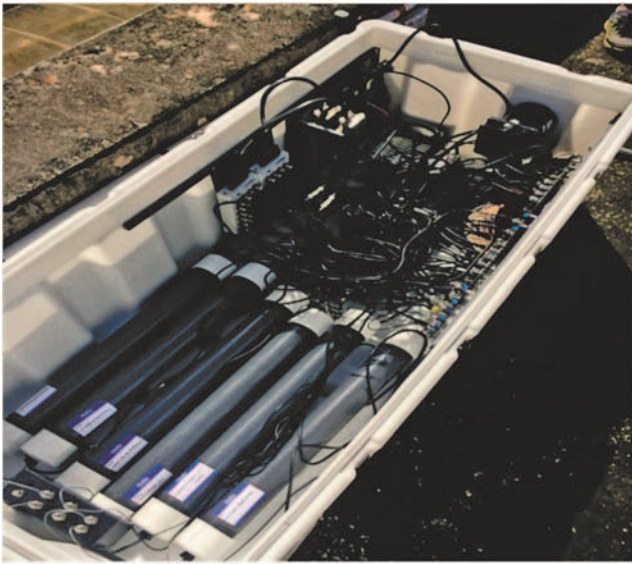


Figure 4. Detector box during assembly, showing 6 PVC BGO assemblies and fast electronics.

In each box (Figure 4), the readout and electronics are split into 2 separate devices for redundancy. 3 PVC assemblies send their 6 PMT output signals to a single front end board. In each PMT channel, signals above a threshold are fed to a peak stretcher, which holds the signal for 13 sec.



Figure 5. Four of 10 TETRA-II detector boxes on roof of Building B, UPR-Utuado.

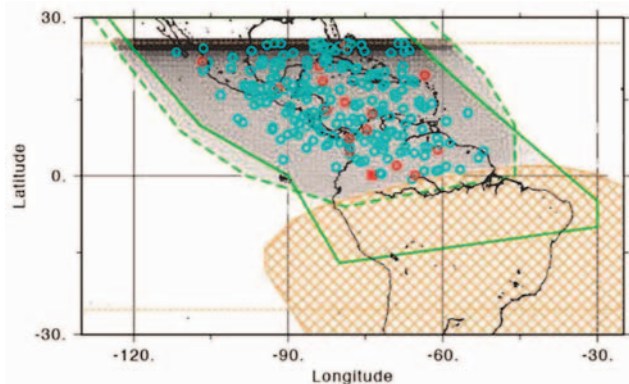


Figure 6. Map of TGFs seen by GBM onboard Fermi in the Americas. [11]

An FPGA selects coincidence events in which both PMTs on a single BGO fire. If a trigger is seen from one PMT pair, then the analog pulse heights from all 6 PMT channels on that device are read out together with timestamp information for each BGO (based on a 20 MHz clock) as well as the GPS pulse per second (PPS). Data are accumulated into 10-minute files.

The data collection software is written in Labview with the data pushed to the server at LSU every hour.

An event candidate from 24 August 2016 at LSU is shown in Figure 7, where the count rates for three BGO in a single detector box are plotted over 24 hrs in 2 millisecond bins. Each BGO sees a consistent rate at or below ~ 5 -7 counts/2 msec until around 21:00 UTC when each BGO sees a spike up to 18 – 20 counts/2 msec. (As a comparison with TETRA-I, note that in TETRA-I, a typical total of 20 counts was seen in three NaI in a box for a single event.)

Figures 8 and 9 show the same event in a single BGO. Figure 8 shows a ± 300 msec window with 20 sec bins in which the event clearly stands out above the background. Figure 9 shows the event over ± 100 μ sec.

CONCLUSION

The TETRA-I experiment successfully detected bursts of gamma rays associated with thunderstorms from the ground with a small array of NaI scintillators in Louisiana. The TETRA II array of BGO scintillators has been designed with improved sensitivity and resolution, and installed at four separate locations where lightning rates are high. These include Utuado, Puerto Rico and Panama City, Panama, both below the Fermi orbit.

Initial data analysis has begun, observing one candidate event at Louisiana State University on August 24, 2016 and one candidate at the University of Puerto.

Rico in Utuado on September 19, 2016. Both of these triggers show a range of 17-40 photons detected within a single BGO in 2 msec, an increase from the average of ~ 20 photons seen by three NaI detectors in a TETRA box. Further work looking at lightning, weather, and radar data at the time of these events is underway.

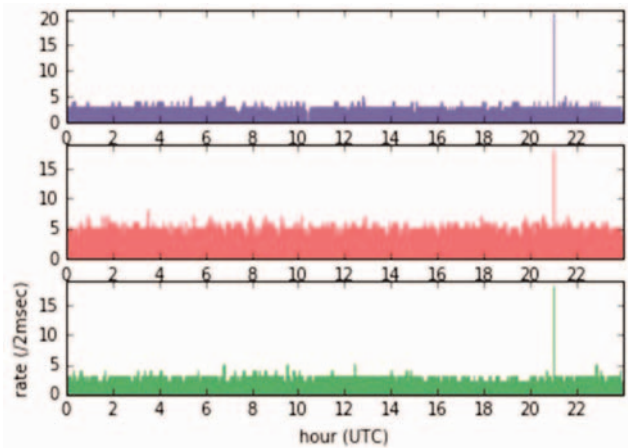


Figure 7. Count rate/2 msec in three BGO for 24 August 2016 at LSU.

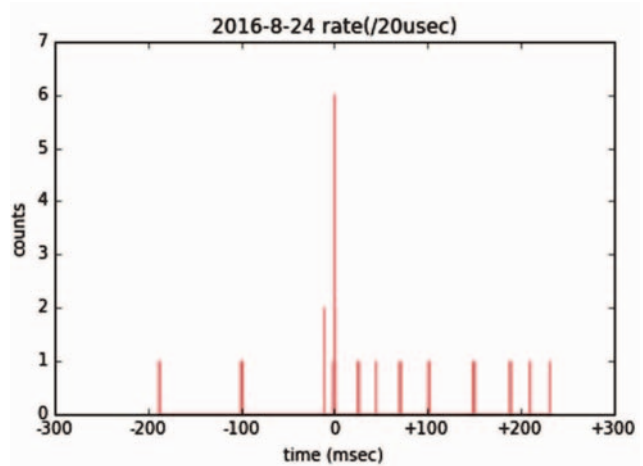


Figure 8. 24 August 2016 event for a single BGO in ± 300 msec window.

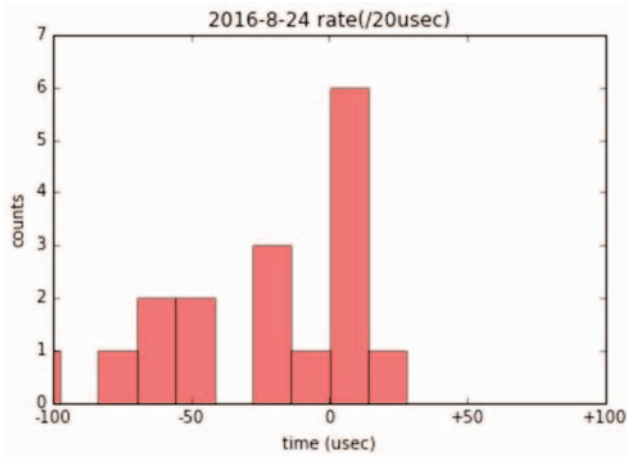


Figure 9. 24 August 2016 event for a single BGO in ± 100 μ sec window.

ACKNOWLEDGEMENT

We gratefully acknowledge funding from the US National Science Foundation (Office of Atmospheric and Geospace Sciences and Research Initiation Award), NASA EPSCoR, the Louisiana Board of Regents, and Louisiana Space Consortium for the development and operation of TETRA-II. We appreciate the valuable contribution of ATIC BGO scintillators by J. Wefel and the very helpful support of Edgar del Toro and Milton Riutort at Univ. of Puerto Rico-Utuado. DJP expresses his thanks to the organizers and gracious hosts of the TEPA meeting.

REFERENCE

[1] Fishman, G.J. et al. (1994), Discovery of intense gamma ray flashes of atmospheric origin. *Science* 264, 5163, 1313.

[2] Gjesteland, T. et al. (2012), A new method reveal more TGFs in the RHESSI data. *Geophys. Res. Lett.* 39, L05102.

[3] Grefenstette, B. W., D. M. Smith, B. J. Hazelton and L. I. Lopez (2009), First RHESSI terrestrial gamma ray flash catalog. *J. Geophys. Res.* 114, A02314.

[5] Marisaldi, M. et al. (2010), Gamma-ray localization of terrestrial gamma-ray flashes. *Phys. Rev. Lett.* 105, 128501.

[6] Marisaldi, M. et al. (2011), AGILE observations of terrestrial gamma-ray flashes. *Nuovo Cimento C034N3*, 279.

[7] Tavani, M. et al. (2011), Terrestrial gamma ray flashes as powerful particle accelerators. *Phys. Rev. Lett.* 106, 018501.

[8] Fishman, G. J. et al. (2011), Temporal properties of the terrestrial gamma-ray flashes from the Gamma-ray Burst Monitor on the Fermi Observatory. *J. Geophys. Res.* 116, A07304.

[9] Chilingarian, A. et al. (2010), Ground-based observations of thunderstormcorrelated fluxes of high-energy electrons, gamma rays, and neutrons, *Phys. Rev. D* 82, 043009.

[10] Ringuette, R. et al, (2013), TETRA observation of gamma-rays at ground level associated with nearby thunderstorms. *J. Geophys. Res. Space Phys.* 118, 7841.

[11] Chang, J. et al. (2008), An excess of cosmic ray electrons at energies of 300-800 GeV. *Nature* 456, 362.

[12] Briggs, M.S. et al. (2013), Terrestrial Gamma ray Flashes in the Fermi Era: Improved Observations and Analysis Methods. *J. Geophys. Res. Space Phys.* 118, 3805.

Cosmic ray short time increases during intervals with strong electric field at Lomnický štít: first experience.

J. Baše¹, J. Chum¹, M. Kollárik², K. Kudela^{2,3}, R. Langer², I. Strhářský², S. Štefánik²,

1. Institute of Atmospheric Physics, Czech Academy of Sciences, Prague, Czech Republic

2. Institute of Experimental Physics, Slovak Academy of Sciences, Košice, Slovakia

3. Nuclear Physics Institute of the Czech Academy of Sciences, Řež, Czech Republic

Abstract. Since March 2014 there is a continuous measurement of secondary cosmic rays (CR) with use of detector system SEVAN (Space Environmental Viewing and Analysis Network, described by Chilingarian et al., 2007) at Lomnický štít, altitude 2634 m asl. Starting from June 2016 the count rates (1s resolution) obtained from the three detectors and from their coincidences are available. Measurements during the interval with increased vertical component of electric field observed at the same site (June – September 2016) are presented and discussed. It is shown that the increases of count rates measured by SEVAN correspond to the periods of high electric field, usually with the negative polarity, rather than with the individual discharges (lightning).

1. INTRODUCTION

CR and energetic particles in the surrounding of Earth play important role in several atmospheric processes. One of them is lightning/thunderstorms relations to secondary CRs, namely TGE. The TGEs are often called gamma-ray glows or emissions and are usually several minutes long. The enhancement of the radiation measured on the ground mostly does not exceed 10% of the background values. Our earlier paper (Kollárik et al., 2015) was devoted to comparison of 1 min records of the upper scintillator of SEVAN device at Lomnický štít (LS) in 2014-2015 with the data from lightning network described by Betz et al. (2009).

Here we report the three month comparison of 1 sec data of SEVAN at LS with new electric field (EF) measuring equipment installed at LS by the Institute of Atmospheric Physics, Prague. Selected intervals with increases of count rate at SEVAN that coincide with large, usually negative EF measured at the same site, are discussed.

2. MEASUREMENTS OF EF AT LS.

Electrostatic measurement (Electric Field Mill EFM 100, Figure 1) at LS started from end of May 2016. EFM100 is mounted in inverted position to minimize the rain noise, EFM100 was calibrated with temporary reference EFM100 located at several places that have approximately flat surface (locally). The estimated uncertainty of calibration (sigma value) is=33%. The EF is positive (negative) if the ground is negative (positive) with respect to the atmosphere above.

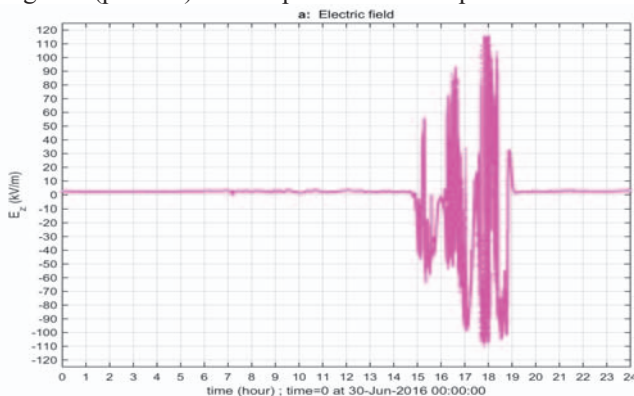


Figure 1. An example of the daily profile of EF including the intervals with fair weather (until ~ 1445 UT on June 30, 2016) and with the thunderstorm (since ~ 1450 until ~1900 UT).

3. SELECTED EVENTS.

About 20 events of increased count rates in 1 sec data of the first channel of SEVAN system were observed since June 9 until September 17, 2016. The absolute value of electric field at LS during these events was usually larger than about 60 kV/m. Figures 2 – 4 show selected intervals with such type of events.

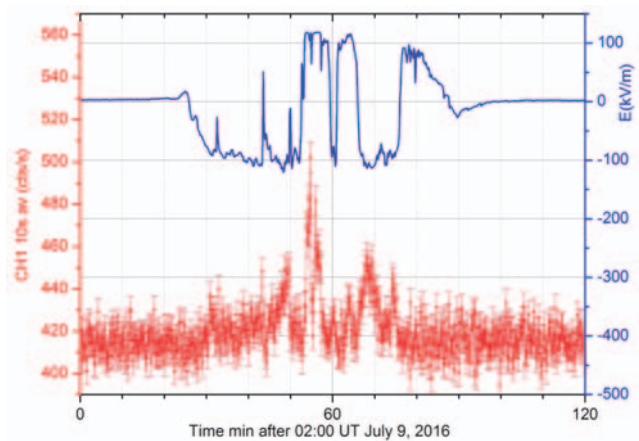


Figure 2. Example when the increase on chan1 of SEVAN is during positive EF polarity. Middle peak of increased SEVAN counts is in the period of large positive EF values. Only about 15% of the so far recorded SEVAN events have been observed for positive EF values.

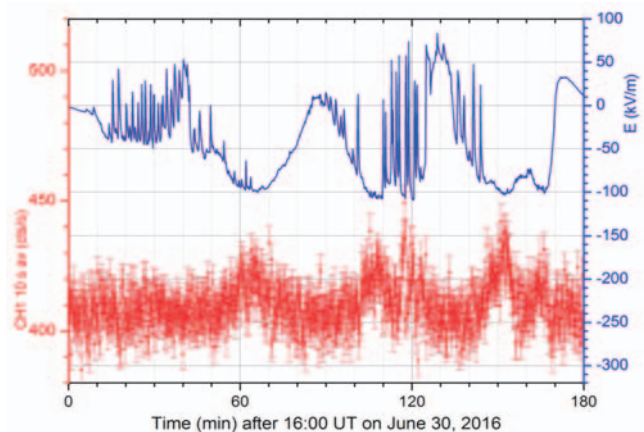


Figure 3. Example from June 30, 2016. Increased counts in the SEVAN chan1 are mainly during periods of large negative EF values. They do not correlate with the lightning strokes. Sometimes, nearby lightning may terminate the increased counts. Large spikes on EF signal correspond to nearby lightning that occurred at distance usually less than about 5 km from LS. Humidity was > 87%.

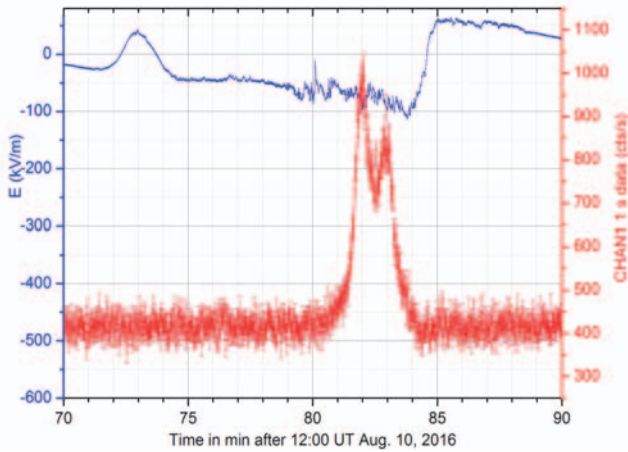


Figure 4. Event from August 10, 2016. One of two strongest increases observed by SEVAN. Humidity was >98.7% during the whole time period. The double-peak structure is statistically significant even in 1 sec resolution data in comparison with the intervals before and after. No corresponding channel 2 nor NM count rate increased during the whole interval.

4. DISCUSSION AND SUMMARY

The increases of count rates at first channel of SEVAN were usually observed (not in all cases) during the large EF at LS. This channel is mainly sensitive to muons and electrons at the altitude of LS. However, the detection of gamma-rays cannot be excluded. Our observations confirm the main characteristics of high mountain events in secondary CR in the relation to atmospheric EF and to thunderstorms as reported recently by Chilingarian et al. (2016). The important point is that the increases were observed mainly during the intervals when EF had negative polarity (LS is positive with respect to the atmosphere above). Some events were also observed for negative polarity of EF. The increases of count rates measured by SEVAN usually corresponded with periods of high EF rather than with the individual discharges (lightning). Regarding neutron monitor increases (NM response is mainly to the nucleonic component of secondary CR) we are not yet sure

about the coincidence with glow events at SEVAN and more detailed checking of data is needed.

Examination of relations between the observed glows and atmospheric parameters measured at LS as temperature, humidity, strength, direction of the wind, and pressure will be performed. As there may be short spikes inside the increases of counts, recording time of each pulse, as well as anticoincidence between different channels of SEVAN, now in progress, may help in clarification. Also, more detailed comparison with lightning detected around LS by the lightning detection network (Betz et al. , 2009; Schulz et al., 2016) will be useful.

ACKNOWLEDGEMENT

This work was supported by the Slovak Research and Development Agency under the contract No. APVV-15-0194 and under the mobility project SAV 16-19 by the Czech Academy of Sciences and partly also under the project 15-07281J by the Czech Science Foundation. This publication was supported by OP RDE, MEYS, Czech Republic under the project CRREAT, CZ.02.1.01/0.0/0.0/15_003/0000481.

REFERENCE

- Chilingarian, A., Hovsepyan, G., Arakelyan, K. et al.: 2007, Central European Astrophysical Bulletin, 31, 1, 259-272.
- Kollárik, M., Kudela, K., Langer, R., Strhárský, I.: 2016, Proc. Internat. Symp. TEPA 2015, ed. A. Chilingarian, Published by Cosmic Ray Division, Yerevan Physics Institute Alikhanyan Brothers Street 2, Yerevan, Armenia, available at <http://crd.yerphi.am/Conferences/tepa2015/files/tepa-2015-21march-low.pdf>, p. 31 – 34.
- Betz, H.D. et al. : 2009, in Lightning: Principles, Instruments and Applications, 115-140, Springer.
- Chilingarian, A., Hovsepyan, G., and Kozliner, L.: 2016, Astroparticle Physics, 82, 21-35 Schulz, W. et al. : 2016, Nat. Hazards Earth Syst. Sci. , 16, 595–605

Gamma-Ray and Energetic Electron Flux Short-time Variations Observed in Vernov and Lomonosov Missions

M. Panasyuk, S. Svertilov, V. Bogomolov, G. Garipov, V. Barinova, A. Bogomolov, A. Iyudin, V. Kalegaev, M. Kaznacheeva, V. Morozenko, I. Myagkova, P. Klimov, V. Petrov, A. Prokhorov, I. Yashin

*M.V. Lomonosov Moscow State University, Physics Department,
D.V. Skobel'syn Institute of Nuclear Physics, Moscow, Russia*

Abstract . The short-time ($10^{-4} - 10^2$ s) variations of gamma-quantum (0.02 – 3.0 MeV) and relativistic (0.3 – 10.0 MeV) electron fluxes were observed during Vernov and Lomonosov missions. The similar detectors based on NaI(Tl)/CsI(Tl) phoswich of 13.0 cm diameter and 2.0 cm total thickness (0.3 cm NaI(Tl) plus 1.7 cm CsI(Tl)) were used in both missions for study different kinds of transient phenomena, such as GRBs, TGFs, Solar Flares and magnetosphere electron precipitation.

Four gamma-ray detectors on-board Vernov satellite had a total area of about 480 cm², and were directed toward to the Earth atmosphere (in local Nadir). They were used especially for TGF observations. These detectors were also able to detect precipitated and quasi-trapped sub-relativistic and relativistic electrons. Several dozens of TGF candidates were selected as satisfied the trigger condition, i.e. more than 5 gamma-quanta detected for a 400 mcs exposure time in one detector with 120 cm² area. Possible connection of these events with TLEs detected by DUV instrument and lightning observed by WWLN is discussed. Quasi-trapped and precipitated electron flux short-time variations (burst-like) were observed regularly in different areas of the near-Earth space. The time and energy spectrum parameters of such events observed in Vernov mission are presented.

The first results of Lomonosov mission on TGF-like events and electron flux short-time variations are also discussed.

1. INTRODUCTION

Study of short-time ($10^{-4} - 10^2$ s) variations of gamma-quantum (0.02 – 3.0 MeV) and relativistic (0.3 – 10.0 MeV) electron fluxes during the Vernov (Panasyuk et al., 2016a) and Lomonosov (Sadovnichii et al., 2012) space experiments was one of the main goals of these missions because it gives opportunity in progress of understanding of Transient Energetic Phenomena (TEP) in the Atmosphere and its possible connection with magnetosphere relativistic electron precipitation. By TEP we mean the Terrestrial Gamma Flashes (TGF) and the Transient Luminous Events (TLE), which are the well-known effects possible connected with high altitude electric discharges, such as sprites, elves and blue jets as well as discovered in Tatiana-Universitetskii and Tatiana-2 missions flashes of ultraviolet (UV) and red emission (Sadovnichii et al., 2011).

The Vernov spacecraft was launched in 2014 July, 8 at polar (640×830 km) solar-synchronous orbit with 98.4° inclination and ~100 min period. RELEC complex of scientific instruments included gamma quantum and electron (0.01-3.0 MeV) spectrometer DRGE, UV (240 – 400 nm) and red (610 – 800 nm) photometer DUV, UV imager Telescope-T, low frequency (0 – 40 kHz) NChA (PSA-SAS3) and radio frequency (0.05 – 15.0 MHz) RFA analyzers and electronic unit BE. The satellite orbit allows observations in different areas of the near-Earth space including near Geomagnetic Equator and high latitude regions. This gives a good opportunity to study TGFs as well as electron precipitations. The main instrument for these purposes is DRGE spectrometer (Panasyuk et al., 2016b). It consisted of three units, i.e. two identical DRGE-1(2) and one DRGE-3 boxes. Each DRGE-1(2) box contained two identical detector units, which were based on the large area (13 cm in diameter) NaI(Tl)/CsI(Tl) phoswich detectors, each with thin (0.3 cm) NaI(Tl) and more thick (1.7 cm) CsI(Tl) crystals both viewed by photomultiplier tube (PMT) Hammamatsu R877. During the experiment detector axes were directed constantly to the Nadir, the total area of four

detectors was about 500 cm², which is enough to detect TGF at appropriate sensitivity level. The DRGE-3 unit was used mainly for electron precipitation study. It consisted of three identical detectors with axes normally directed to each other. First one was directed to the local Zenith, the second one was directed mainly against the satellite velocity vector, and the third one was directed normally to the plane formed by two other detectors axes. Each DRGE-3 detector unit consisted of CsI(Tl)/BGO/plastic phoswich with 0.3 cm thick CsI(Tl) and 1.7 cm thick BGO putted in the anticoincidence cup from plastic scintillator with 0.5 cm walls. The diameter of both CsI(Tl) and BGO scintillators was 1.5 cm. The cylindrical copper collimator with height of 1.0 cm and a 0.1 cm thickness was arranged above the CsI(Tl) crystal. The output data from all DRGE detectors were received in two modes. One is so-called monitor mode, in which mean count rates in given energy channels separate for gammas and electrons, were measured continuously for chosen exposure time (1.6 s mainly) during all observations. The other is “event by event” mode, in which for every detected gamma quantum or electron its energy and time of detection were fixed. It is very effective to study short events such as TGFs with time resolution limited only by detector dead time (~15 mcs).

The same observation technique was used in the Lomonosov mission, which was successively launched in 2016 April, 28. The Lomonosov instruments include the BDRG gamma ray burst monitor (GBM), which consists of three identical boxes with the same NaI(Tl)/CsI(Tl) phoswich detectors as DRGE-1(2). The BDRG instrument boxes are mounted on the spacecraft instrumental panel in such a way, that detector axes are directed normally to each other and detector fields of views (FOVs) cover a half of the sky. Despite the BDRG detectors are oriented to the opposite direction relatively to the Earth, they are also able to study precipitation electrons via bremsstrahlung and to detect TGFs by the use of “bottom” CsI(Tl) crystals, which are not totally screened by satellite constructions.

The results of TGF and electron flux short-time variations are discussed in this paper.

2. TGF OBSERVATIONS IN THE VERNOV MISSION

The DRGE-1 and DRGE-2 large area detectors with axes directed toward the Earth are the main instruments for TGFs observations during the operation of RELEC Vernov in space. As it was mentioned above, the DRGE instrument produces two types of data i.e. “Monitor” and “Event” or gamma by gamma. In the “Monitor” data average counts for exposure time 1.6 s were recorded for each detector unit in the energy channels as well as the integral counts for separate scintillators (NaI(Tl), CsI(Tl) for DRGE-1(2), CsI(Tl), BGO, plastic for DRGE-3) and summary counts in all scintillators of given detector package. The energy thresholds obtained in preflight calibration tests were about 10 keV for NaI(Tl) and about 30 keV for CsI(Tl) of DRGE-1(2) detectors and about 50 keV for CsI(Tl) and about 100 keV for BGO of DRGE-3 detectors. In the case of “gamma by gamma” data the time of each gamma-quantum detection as well as the amplitude determining the energy release in each part of the detector was fixed for every detected gamma-quantum.

To the extent that the TGFs are very short (<0.5 ms), “gamma by gamma” data taking mode was chiefly used for their selection. Due to the limited volume of data transfer the number of recorded events in a row is restricted such that not more than 800 events per second in one detector can be recorded in the case of low background count (<800 pulses/s in both crystals). If background is over 800 pulses/s or 1500 pulses/s, then not more than first 200 events or 50 events, respectively, can be recorded consequently event by event for every second. In the near-equatorial regions, the total background of each of the detector was less, than 800 pulses/s, so data on all detected gammas were stored. In the polar cap regions, the background exceeded 800 pulse/s, and only one fifth of the events detected per second was stored. Thus, in the near-equatorial regions, gammas were detected without losses. It is very favorable for a TGF search, because these events are observed mainly in equatorial thunderstorm regions.

At the background on average near the equator not more than 1 noise event is detected every few milliseconds. Because the majority of TGFs have a rather hard energy spectrum, only events with energy release over 500 keV inside both (NaI (Tl) & CsI(Tl)) scintillators were selected for triggering. Consequently, the trigger was chosen to have simultaneous detection of more than 5 hard energy gammas/ms by two detectors or 3 or more hard gammas by three detectors. That criterion corresponds to the 12σ significance level. Really it was not determined by the number of counts for a specified time interval, but by the duration of the set of successively recorded events. I.e. specified criteria meets the requirements that for the sequence of 5 recorded events the duration of interval between first and last of them should not exceed 1 ms. Besides, an additional condition was utilized in order to lower the trigger rate caused by charged particles background in the trapped radiation areas. This condition limits average background per second before firing trigger at 1 kHz.

The huge number of events which satisfied the trigger criterion was obtained. However, most of them were caused by cosmic rays, particularly heavy charge particles, passing through the scintillation crystals. Such events can be selected

effectively from the “energy-time” diagrams which reflect the energy release values pointed against the time of detection (see Figure 1). Events originated by heavy charged particles have a typical form of very high energy release at the beginning and specific tail. Such time profile may be caused by very high ionization density produced by heavy charged particle in scintillator crystal that leads to a sharp increase of PMT output current overloading sensitive input circuits as well as PMT itself.

To exclude the charged particle events additional criterion of specific tail determination was elaborated. It bases on the demands of consequence energy release decreasing for event by event after the point of maximal energy value. The optimal condition was that the number of such event points with decreasing energy should be no less than 5.

The limit corresponding to the low energies is caused by non-zero energy threshold chosen some above the noise of scintillator crystals and PMT. The “line” limiting the maximal energy values is caused by overload of amplifiers when particles or quanta with very high energies out of instrument dynamical range were detected. These limits are slightly different for different detector units.

The sample of TGF candidates was selected after excluding events caused by heavy charged particles. During the observation period from July 20 to December 10, 2014, six events which satisfied the discussed above criterion were found (Bogomolov et al., 2017). The times of their detection were 08.08.2014 22:20:55 UTC, 08.08.2014 00:31:07 UTC, 16.08.2014 13:06:55 UTC, 18.09.2014 10:15:34 UTC, 11.10.2014 06:46:20 and 02.11.2014 03:34:14 UTC. One of them (11.10.2014) was identified as very short cosmic gamma-ray burst (GRB). The most intensive flash was detected at 18.09.2014. The “energy release – time” diagram for this event is shown in Figure 2. As it could be seen from the figure, in the case of TGF-like event the point array on the diagram is quite different than in the case of heavy charge particle event that confirms the efficiency of proposed method of such event separation.

The sub-satellite point positions for the times of TGF candidate detection are marked on the map presented in Figure 3. The detector axes were directed in these sub-satellite points, when TGF-like events were detected.

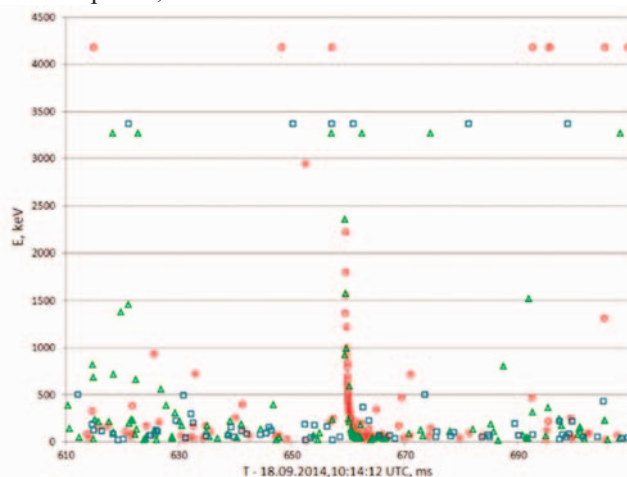


Figure 1. Example of “energy release – time” diagram with heavy charged particle detection events. The energy release values vs time (in the part of second) is plotted. Circles are corresponding to the events detected by DRGE-11, triangles – by DRGE-12, squares – by DRGE-21.

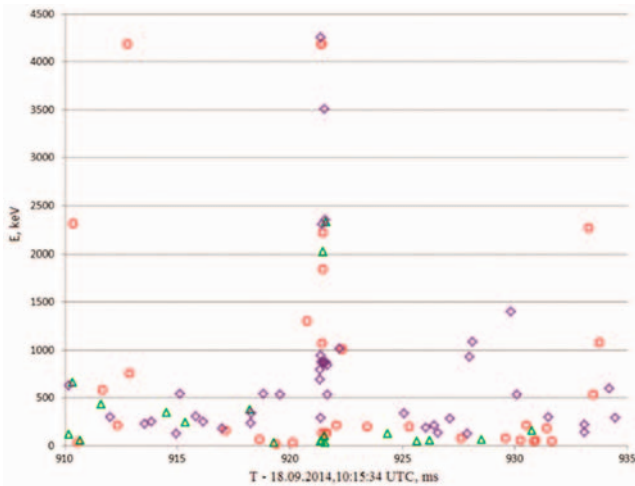


Figure 2. "Gamma by gamma" record for TGF 18.09.2014. Circles are corresponding to the events detected by DRGE-11, triangles – by DRGE-12, diamonds – by DRGE-22.

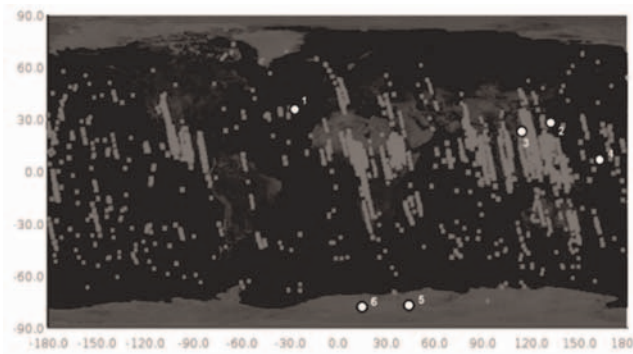


Figure 3. The map presented the sub-satellite point positions at the times of detection of UV flashes and TGF candidates (numbered).

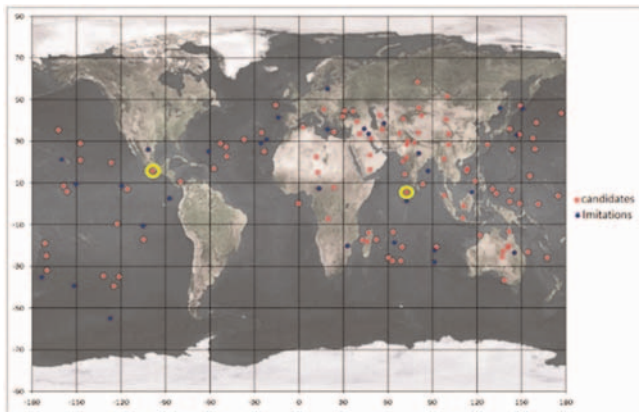


Figure 4. The map of distribution of TGF candidates selected by the soft criterion in the Equatorial region (red points) and imitations by heavy charged particles (blue points). Yellow rings mark the TGF-like events coincided with UV flashes.

Among the chosen TGF-candidates event number 5 detected in the polar region under Antarctica 02.11.2014 at 03:34:14.051 UT is of special interest. This burst is longer (~2.5 ms) than other events, which duration (<400 mcs) is typical for TGFs usually connected with thunderstorm activity. If take into account this burst source position, its connection with thunderstorm is very unlikely.

TGF candidates were also selected with softer criterion, which did not assume the requirement of coincidence of significant intensity increasing in different detectors. The new method of cleaning data from TGF imitations by heavy charged particles was used. This method is based on more accurate analysis of the time profile of TGF candidate. It

allows conducting a search of TGF candidates from the separate detector data without coincidence. According to this soft criterion those events were selected, for which no less than 5 gamma quanta were detected for a 400 mcs interval in the given detector in the Equatorial region and no less than 7 gamma quanta in the Polar Cap region. This increased the analyzed observation time of almost 2 times

The expected number of selected random events in dependence on the number of counts detected over 0.4 ms interval was estimated. This dependence was calculated by multiplying the probability of accidental imitation on a single time interval defined by Poisson distribution for taken background level on the time of observations. Thus, the expected number of random events detected with the DRGE-11 detector, for which the exposure time was the largest, in the Equatorial region is about 70, and in the Polar Cap region less than 0.1. Really, after the soft criterion was applicate about 110 events were selected in the Equatorial region and only one was selected in the Polar Cap region.

The map of selected in the Equatorial region TGF-candidate source position is presented in Figure 4. For comparison the distribution of burst-like events imitated by charged particles is also presented there. Despite that the most of selected events are random, about 40 of them may be the real TGF candidates. This is also confirmed by concentration of corresponding points in the regions with high thunderstorm activity, i.e. India, South-East Asia etc. It is interesting to compare selected TGF candidates with UV and red flashes detected from the Atmosphere by DUV instrument. About a several thousands of such bursts were detected during the Vernov mission. The sub-satellite points at the time of flash detection are presented in the map in Figure 3. The burst time profiles are very various. Single peak events were observed as well as the flushes with very complicated time structure. The last may be caused by flashing of large areas contained excited nitrogen and oxygen molecules. The series of UV flashes previously discovered in Tatiana-2 mission (Sadovnichii et al., 2011) were also observed by DUV Vernov. It is necessary to note, that despite that the most of events both single and series were observed above the continents in the active thunderstorm regions, quite a few bursts were detected above the ocean and at high latitudes up to Antarctic, rather far from thunderstorm active regions. The most of them have a single peak time profiles both in UV and in red channels. Only two UV and red flashes coincided in time with TGF candidates. The points of its detection are marked in Figure 4 by yellow rings. As it could be seen from the Figure 4, the sources of these flashes are located not far from thunderstorm regions. However, it is surprising that both events are characterizing by single peak profiles (see Figure 5), which are typical for high latitude events.

As for TGF-like events observed in Polar Caps the most of them were imitations by heavy charged particles and only one can be the real gamma ray flash, which was detected 22.11.14 at 5:05:03 UT. This event was observed above the Antarctic. It is marked on the map presented in Figure 3 as number 6. As the other high latitude gamma ray flash, i.e. event number 5, this one also very unlikely can be connected with thunderstorm activity. From the other hand both of these flashes were detected near the areas of magnetosphere electron precipitation.

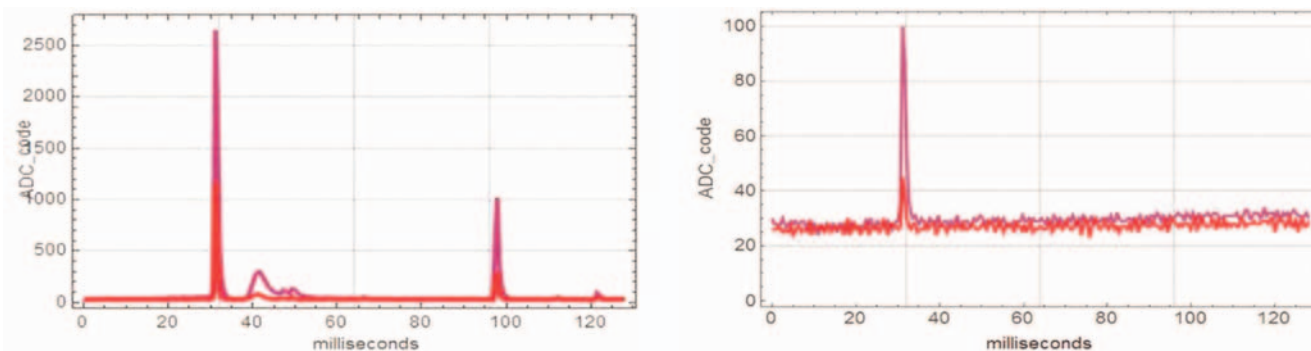


Figure 5. Time profiles of UV (blue curves) and red (red curves) flashes coincided with TGF candidates. The left panel presents profiles for event detected 16.10.2014 at 03:27:58 UT, the right panel presents profiles for event detected 05.09.2014 at 16:10:19 UT. The system is used for the digitizing observed signals and to control the LIDAR system, including:

3. ELECTRON PRECIPITATION AND SHORT-TIME FLUX VARIATIONS.

As it is well-known, electron precipitations from the Earth radiation belts are caused mainly by electromagnetic wave activity in the different bands from about 0.1 Hz to 15 MHz. Such precipitations were observed repeatedly during the Vernov and Lomonosov missions in the different regions of the near-Earth space including polar areas by the crossing of drift shells at the inner edge of the outer belt. The example of such precipitation from the Vernov data is presented in Figure 6. As it seen from the figure, local in time count rate increase is observed at the times corresponding to the crossing of L-shells ~8.3, 6.9, 5.9 in the South hemisphere. The increase amplitude is approximately equal for the all

three detectors unlike the backing count, which corresponds to the outer belt electron flux measurements, when detector (DRGE-31), which axis was directed along the magnetic field line, gave significantly lower count rate in comparison with two others, which axes were directed preferably normally to the magnetic field line. It is the natural sequence of that trapped particles have less isotropic fluxes in comparison with precipitated. By this the peaks noted in the figure probably connected with detection of precipitated electrons in the isotropisation area at the inner edge of the outer belt, which can be caused by the electron scattering on electromagnetic low frequency waves, in particular, on the ion-cyclotron (EMIC) waves (Yahnin et. al., 2016).

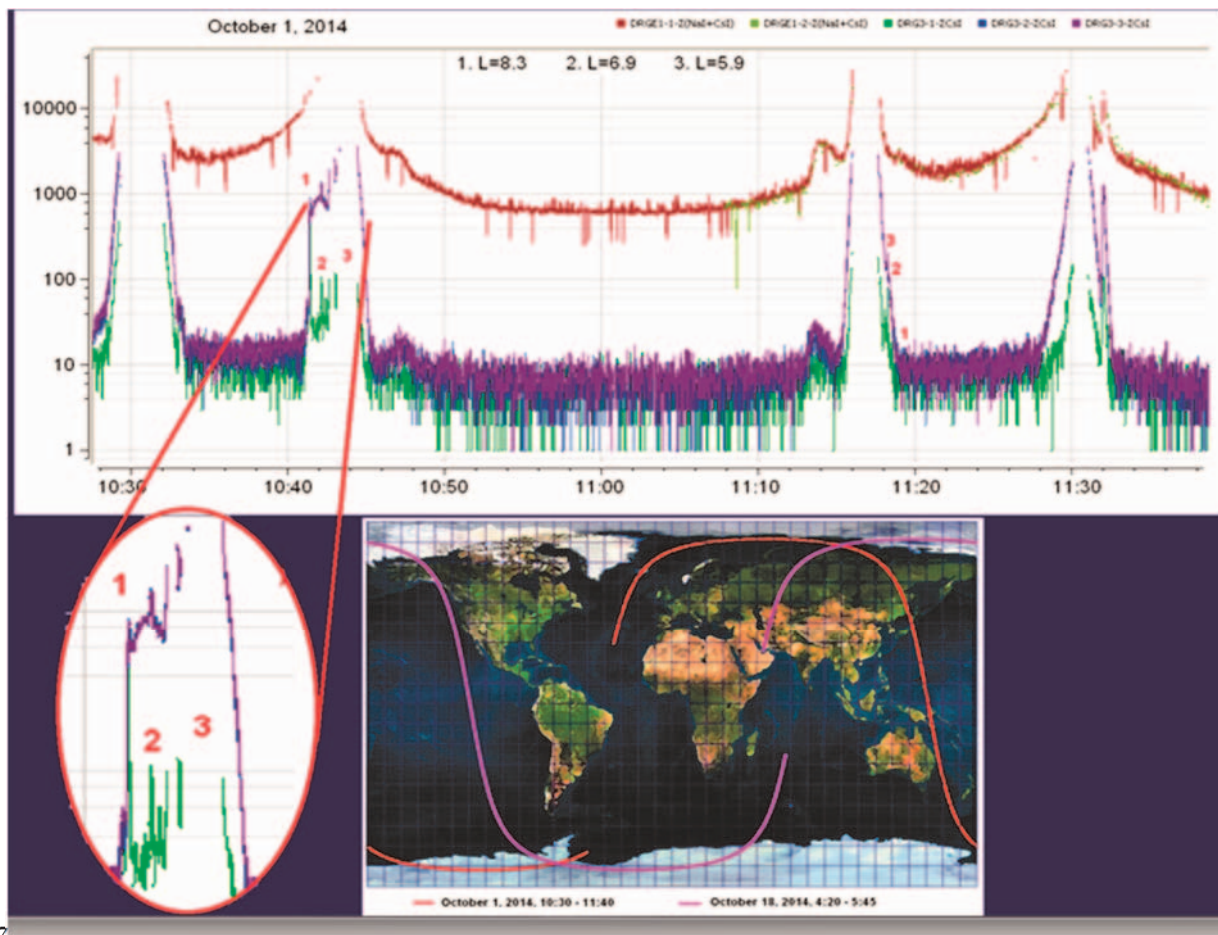


Figure 6. The time profiles of electron counts along one Vernov orbit. Time scale means universal time UT. Green, blue and violet lines mark the counting rate in the range 150-300 keV of DRGE-31, DRGE-32 and DRGE-33 detectors, respectively. Red and light green lines mark the time profiles of integral ($E > 15$ keV) counting rates of bremsstrahlung from the DRGE-11 and DGE-12 outputs. The more detailed part of profiles with peaks corresponding to the precipitation is shown in the bottom left part of the panel. The Vernov satellite orbit projections on the Earth map are shown in the bottom part of the panel. The orbit, which corresponds to the presented profiles is marked by red.

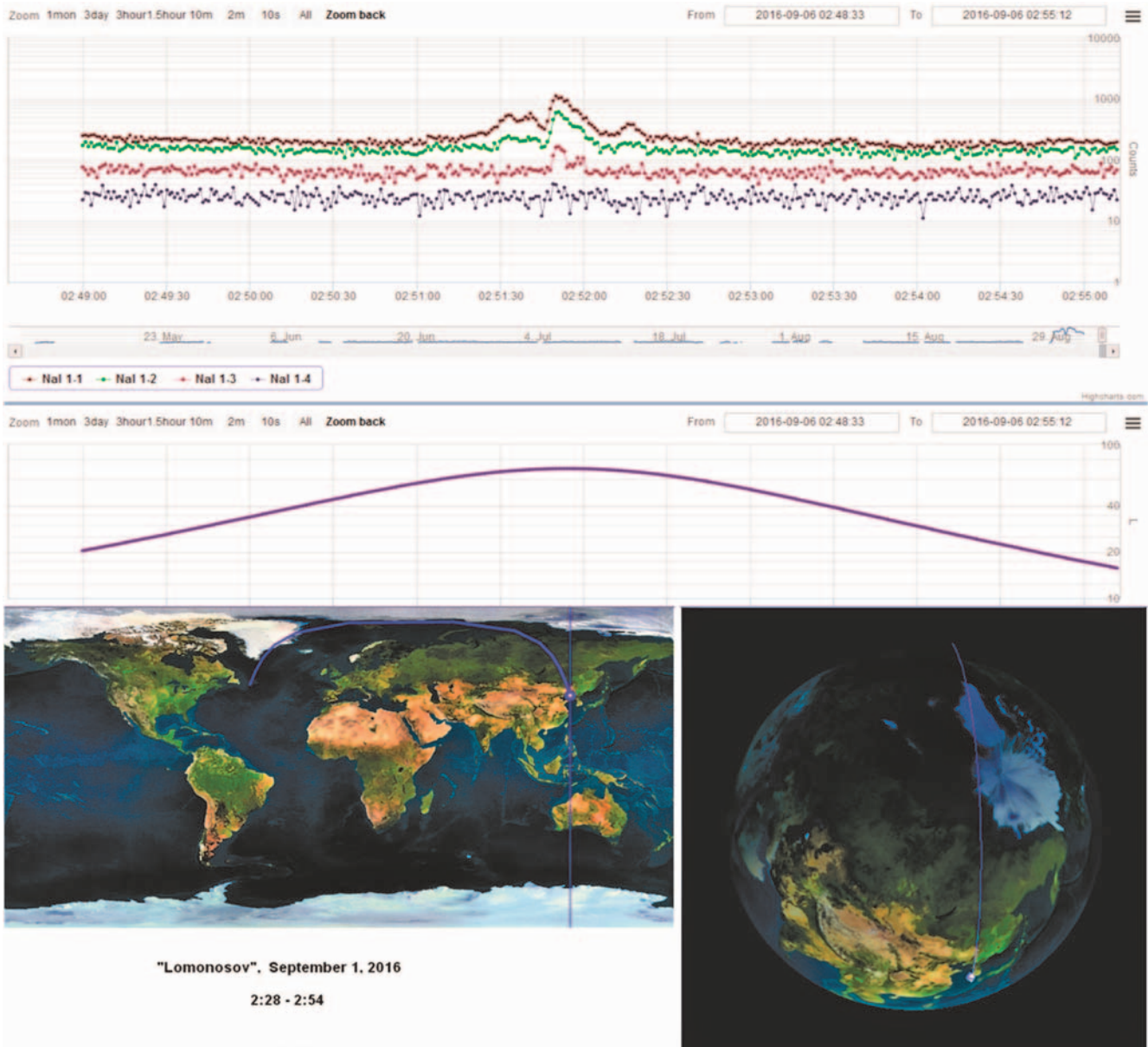


Figure 7. The top panel: the time profiles of counting rates in BDRG channels, BDRG-1 20 – 35 keV (green line), BDRG-3 20-35 keV (lilac line), BDRG-1 60 – 100 keV (blue line), BDRG-3 60 – 100 keV (brown line). Time scale means universal time UT. The middle panel: the time profile of L values at the same times as on the top panel. The left bottom panel: the satellite orbit projection on the map, the right bottom panel: 3D projection of the satellite orbit.

The left bottom panel: the satellite orbit projection on the map, the right bottom panel: 3D projection of the satellite orbit. Similar precipitation-like short-time electron flux variations were observed in Lomonosov mission. The example of such events is presented in Figure 7, in which the time profiles of counting rate in 20 – 35 and 60 – 100 keV energy ranges of two GBM monitor BDRG detectors are shown. Background in the BDRG channels is caused mainly by electron bremsstrahlung, thus, detected count rate variations really reflect the sub-relativistic electron flux variations. The rather short, with duration about a few seconds, count rate increase can be seen evidently at $L \sim 10$, i.e. at inner edge of outer belt.

As it could be seen from the Figure 7, the presented electron flux variations were observed at North Polar regions at some higher L values than precipitation observed in the Vernov mission. Nevertheless, we may assume that it is the

same phenomenon caused by electron scattering on the low frequency electromagnetic waves.

The other type of short-time electron flux variations also observed in the Lomonosov mission is presented in Figure 8. There are also plotted the counting rates in BDRG channels vs time together with corresponding L values and satellite orbit projection.

As it could be seen from the figure, the counting rate variations with duration about dozen seconds in 20 – 35 keV range and more short (with duration about a few seconds) in 60 – 100 keV are observed in the very middle part of the South Polar Cap. The time of its observation corresponds to the day side, thus these counting rate variations could be caused by sub-relativistic electron flux increasing due to electron penetration through the Cusp.

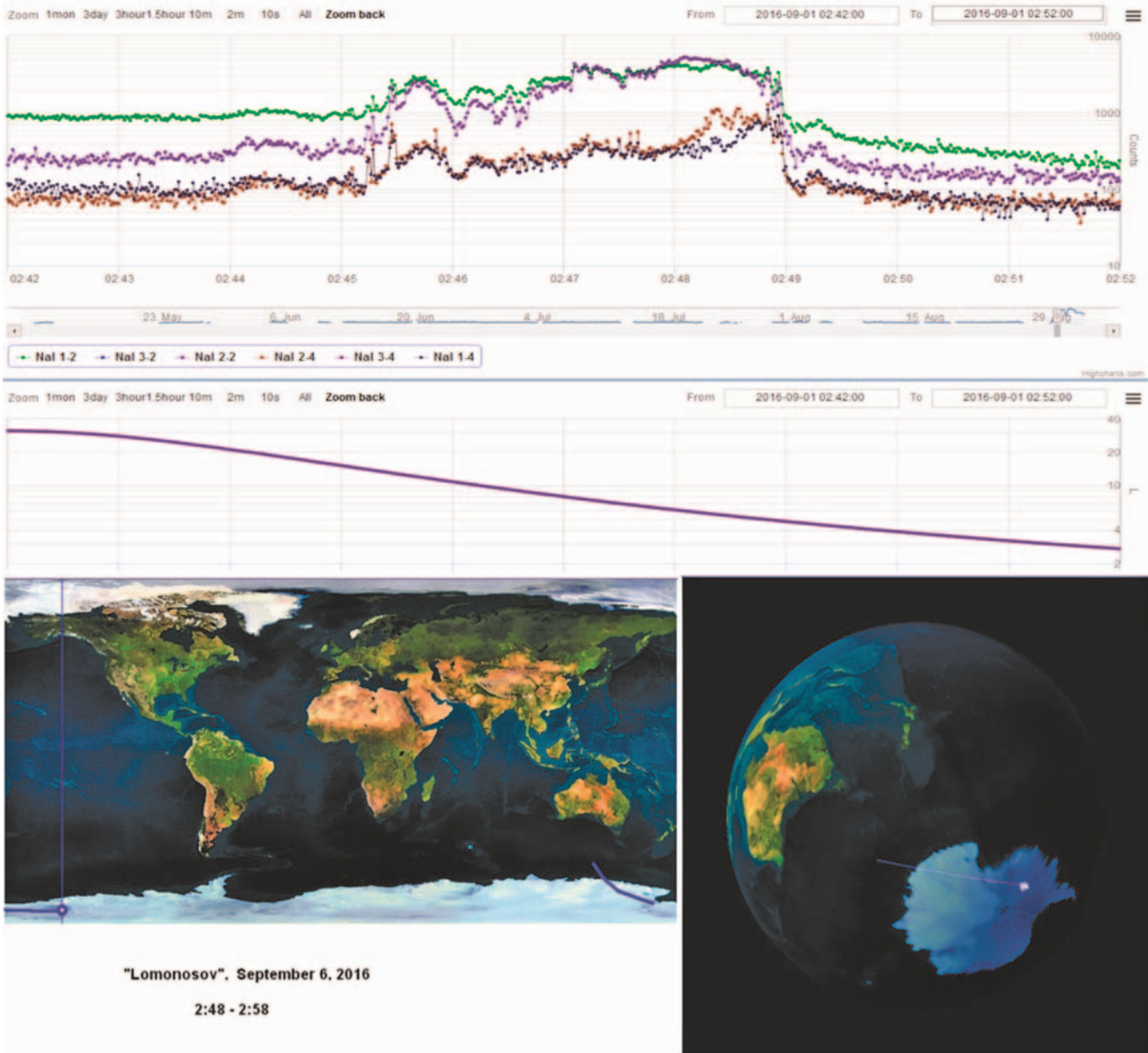


Figure 8. The top panel: the time profiles of counting rates in BDRG channels, BDRG-1 20 – 35 keV (green line), BDRG-3 20-35 keV (lilac line), BDRG-1 60 – 100 keV (blue line), BDRG-3 60 – 100 keV (brown line). Time scale means universal time UT. The middle panel: the time profile of L values at the same times as on the top panel.

CONCLUSION

Dozens of TGF candidates were detected during the Vernov mission. Two of them were observed in the Polar region above the Antarctic, i.e. far from the thunderstorm areas. Two of TGF candidates coincided with single peak UV flashes, which detected regularly at high latitudes near the magnetosphere electron precipitation zones. This let us assume that at least some kind of the Atmosphere gamma ray burst and UV flashes can be connected with electron precipitation.

The short-time variations of sub-relativistic electron fluxes were observed as in the Vernov as in the Lomonosov missions. There is electron precipitation at the inner edge of the outer belt due to the electron scattering on the low frequency electromagnetic waves. Also there were observed the electron flux variations in the Polar Cap, which may be connected with electron penetration through the Cusp. Principally, precipitated electrons can prepare the appropriate conditions for high altitude discharges in the Mesosphere. This assumption may be supported by the observation of gamma ray burst and UV flashes in the Polar Regions.

ACKNOWLEDGMENT

The RELEC experiment onboard the Vernov satellite was realized within the frames of Russia Federation Space Program with funding by the Russian Space Agency. The BDRG experiment onboard the Lomonosov satellite was realized with the partial financial support of M.V. Lomonosov Moscow State University within the framework of the “Prospects for Development” program (“Perspektivnye Napravleniya Razvitiya”).

REFERENCE

- Bogomolov V.V., Panasyuk M.I., Svertilov S.I. et al. Observations of Terrestrial Gamma Ray Flashes in the RELEC Space Experiment on-board Vernov Satellite. // Cosmic Research. 2017. In press.
- Panasyuk M.I., Svertilov S.I., Bogomolov V.V. et al. RELEC mission: Relativistic electron precipitation and TLE study on-board small spacecraft // Advances in Space Research 57 (2016) 835–849
- Panasyuk M.I., Svertilov S.I., Bogomolov V.V. et al. Experiment on the Vernov Satellite: Transient Energetic

Processes in the Earth's Atmosphere and Magnetosphere. Part I:Description of the Experiment // Cosmic Research. 2016. V. 54. № 4. P. 261-269.

Sadovnichii V.A., M.I. Panasyuk, A.M. Amelushkin et al. Study of Early Universe Extreme Phenomena on Lomonosov Space Mission, // Journal of Cosmology (2012), 18. ISSN 2159-063x.

Sadovnichii V.A., Panasyuk M.I., Yashin I.V. et al. Investigations of the space environment aboard the

Universitetsky-Tat'yana and Universitetsky-Tat'yana-2 microsatellites//Solar System Research. 2011. V. 45. № 1. P. 3–29.

Yahnin, A.G., Yahnina T.A., Semenova N.V., Gvozdevsky B.B., and Pashin A.B.. Relativistic electron precipitation as seen by NOAA POES // J. Geophys. Res. Space Physics. 2016. V. 121. doi:10.1002/2016JA022765.

Investigation of atmospheric high-energy phenomena onboard International Space Station: microsatellite "Chibis-AI" and VHF interferometer "Kite"

M. Dolgonosov, V. Gotlib, V. Karedin, A. Kosov, V. Nazarov, L. Zelenyi, S. Klimov

Space Research Institute of the RAS, Moscow, Russia

Abstract. Space Research Institute of the RAS is gradually developing its own program of the space-born experiments to study high-energy process in the terrestrial atmosphere. Terrestrial Gamma-ray Flashes (TGFs) and Compact Intracloud Discharges (CIDs) are among principal goals of the scientific research of the program. To conduct research is supposed to produce new «instruments»: microsatellite «Chibis-AI» and VHF interferometer «Kite» aboard International Space Station. Microsatellite "Chibis-AI" will be constructed on the platform originally designed at the Special Engineering Department of Space Research Institute of the Russian Academy of Sciences in 2011. It's forerunner «Chibis-M» was successfully launched in 2012. Expected date of «Chibis-AI» launch is 2019. The principal idea underlying design of the scientific payload of the microsatellite "Chibis-AI" is the joint observations of the TGF and CID emissions by different detectors installed onboard: Radio Frequency Analyzer (RFA) and Neutron and Gamma spectrometer (NGS). RFA contained two passbands in the range 15-26 and 26-48 MHz with a digitization at 96 megasamples/s. NGS is based on LaBr₃(Ce³⁺) crystal with the maximum achievable today spectral resolution and efficiency of gamma rays in the energy range 100 Kev – 10 MeV among scintillation crystals. The microsatellite orbit will be circular with inclination 51° with initial elevation above sea level around 550 km. VHF interferometer «Kite» to be installed in 2019-2020 aboard ISS. To implement interferometric scheme 4 antennas will be installed on the ISS surface. The passband of the instrument will be ~ 50-100 MHz. Technical details of both experiments, its current stage and features as well results of the previous experiment «Chibis-M» will be discussed.

1. INTRODUCTION.

Nature of gamma-ray flashes, bursts of powerful VHF radiation and lightning activity in the Earth's atmosphere at present is largely unclear. This problem of physics of high-energy processes, despite of the long history of studies of each of these events individually, currently does not have a comprehensive solution. To date, it was accumulated a significant amount of data on high-energy processes in the Earth's atmosphere such as Thunderstorm Ground Enhancements and Terrestrial Gamma-ray Flashes (TGE and TGF respectively). The greatest number of TGFs has been detected by the orbital mission RHESSI [Grefenstette *et al.*, 2009] and GBM/Fermi [Briggs *et al.*, 2010]. In addition, TGF was recorded in the space experiments «Agile» [Marisaldi *et al.*, 2010; Tavani *et al.*, 2011], LAT/Fermi [Grove *et al.*, 2013], as well as it was detected by DRGE detectors on the satellite "Vernov" [Bogomolov *et al.*, 2016]. With regard to Thunderstorm Ground Enhancements (TGE), on Aragats mountain stations (Yerevan Physics Institute, Armenia) the catalog of TGE was formed with typical characteristics of thunderstorm activity, as well as the model of TGE was proposed [Chilingarian, 2014]. However, many properties of TGE, important for the construction of self-consistent model of high energetic phenomena in the atmosphere have not yet been elucidated. In particular, it is not defined the electric structure of thunderstorm clouds during TGE/TGF events, and conditions that determine the intensity and the energy spectrum of gamma-ray bursts and their directional pattern, source size and frequency of occurrence. In addition, the open question is the mechanism of formation and relation TGF with the special powerful short bursts of VHF emission associated with compact intracloud discharges [Smith *et al.*, 1999a, 1999b].

The starting point of cosmic investigation described above phenomena in VHF range were projects ALEXIS/Blackbeard [Massey and Holden, 1995; Massey *et al.*, 1998] and FORTE [Jacobson *et al.*, 1999; Suszcynsky *et al.*, 2000]. The last satellite was designed at Los Alamos

National Laboratory in cooperation with the Laboratory of Sandia. Initially, the satellite was designed to detect nuclear weapon testing, and only later became also be used to study lightning activity from space. The main instrument of this satellite was the Radio Frequency Analyzer (range 30-300 MHz), having armed with two-polarization antenna, allowing to explore the "ordinary" and "extraordinary" modes of radio waves passing through the ionosphere. Triggering scheme implemented in RFA has been used to prevent its activation from artificial signals. One of the fundamental results on these satellites are detailed study of the so-called TIPP (Transitionospheric Pulse Pairs), discovered by satellite ALEXIS [Massey and Holden, 1995]. The name comes from the occurrence of two separated pulses, each a few microseconds long, separated by tens of microseconds. These emissions' instantaneous power was at least tenfold greater than that of VHF signatures ordinarily accompanying lightning. As it was shown in [Jacobson *et al.*, 1999, 2011; Suszcynsky *et al.*, 2000; Jacobson and Light, 2012] the origin of the pairs is closely related to the direct and reflected signal from an electrical breakdown in the upper atmosphere.

In recent years, opportunities for experimental research significantly expanded by successful launching into orbit a microsatellite "Chibis-M" (January 2012) [Zelenyi *et al.*, 2014; Dolgonosov *et al.*, 2015]. The set of scientific instrumentation consisted of the following devices:

- Roentgen-gamma detector (0.02-1 MeV);
- Ultraviolet and infrared detector (180-400 and 650-800 nm);
- RF analyzer (26-48 MHz);
- Digital optical camera (spatial resolution of 300 m);
- Magnetic wave complex (0.1-40 kHz): induction magnetometer and ferroprobe magnetometer.

A special role was assigned to RF analyzer (RFA) as a fast instrument aboard Chibis-M (~10 ns resolution). RFA played the role of a trigger to switch on all other instruments for event recording. It was also implemented triggering scheme similar to those used by RFA onboard FORTE. The

benefits of the scheme allowed to separate short (lasting a few microseconds) pulses of TIPP from signals of anthropogenic origin. During Chibis-M operations it was detected almost 400 TIPP-like events. But in spite of stable performance of Roentgen-gamma detector it was not accomplished no one simultaneous measurement of the TGF event in radio and gamma-ray ranges. One of the main methodological problems revealed in frame of Chibis campaign was inability to determine the location of TGF/TIPPs emitter by one-point measurement. To resolve these issues, it was proposed new payload of the microsatellite «Chibis-AI» and VHF interferometer «Kite» onboard International Space Station.

2. THE CHIBIS-AI MICROSATELLITE AND ITS PAYLOAD

As it was mentioned above, the «Chibis-AI» mission is devoted to the study of energetic mechanisms that generate compact intracloud discharges and gamma ray flashes in the terrestrial atmosphere above the thunderstorm areas. The science objectives include:

- Global mapping and occurrence rates of TGF and CID
- Relation of TGF and associated electromagnetic emission, especially in VHF range
- Study of explosive dissipation of the energy in the ionosphere

According to the decision of the Coordinating Scientific and Technical Council of the Russian Federal Space Agency (no. 03 of December 24, 2012), the «Chibis-AI» project was included in the Long-term program of scientific and applied studies and experiments on the Russian Segment of ISS. Delivery of the Chibis-AI into low Earth orbit should be carried out via the ISS infrastructure. The transport and launch container (TLC) (see Figure 1) have been already developed and manufactured at the Special Design Bureau of the Space Research Institute of the Russian Academy of Sciences (IKI).

A longer discussion of the Chibis platform capabilities have been provided in [Zelenyi et al., 2014]. The project was in Phase B as of 2016. The Preliminary Design Review took place in October 2016.

Chibis orbit is low Earth orbit with inclination 51° and initial elevation ~ 550 km.

The scientific payload is constituted by electric and magnetic antennas, radio frequency analyzer and X-ray and γ -ray sensors. The onboard measurements will be complimented with ground-based observations and dedicated measurement campaigns by Taranis and onboard ISS (see below).

The sensor complement has a mass of ~ 12 kg and a power consumption of ~ 23 W. To maximize the scientific return of the data collected by «Chibis-AI», the scientific payload is operated as a single instrument. The strategy adopted is twofold: a continuous monitoring of low resolution RF and particle data is performed and transmitted. Under alert, all Chibis instruments should initiate a synchronized high resolution data mode. The relative time accuracy between the Chibis instruments is less than 10 ns, allowing meaningful intercomparison of the data sets.

To allow the comparison with ground based (WWLN data) and space-born measurements the absolute time accuracy onboard will be less than 10 μ s. All instruments include memory to store high resolution data for a time interval including the event detection time.

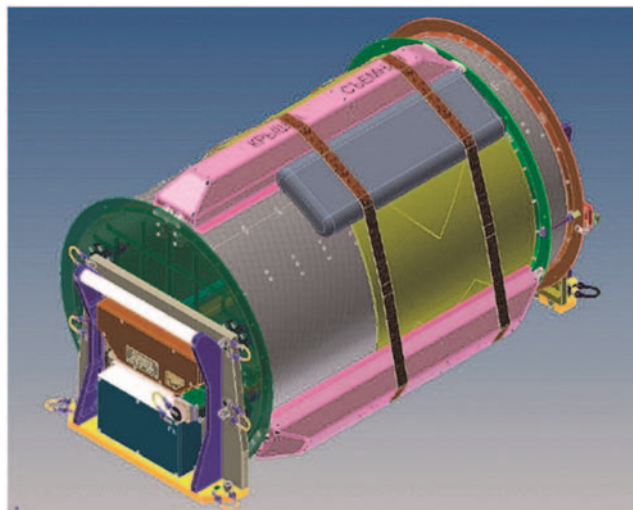


Figure 1. General view of the transport and launch container developed to launch satellites from Progress cargoship.

Below we provide technical details for instruments related only for high energy physics, namely, radio frequency analyzer (RFA) and neutron and gamma-ray spectrometer (NGS). NGS scientific instrument consists of neutron detectors module and gamma-ray spectrometer, joined by common electronics unit (Figure 2).

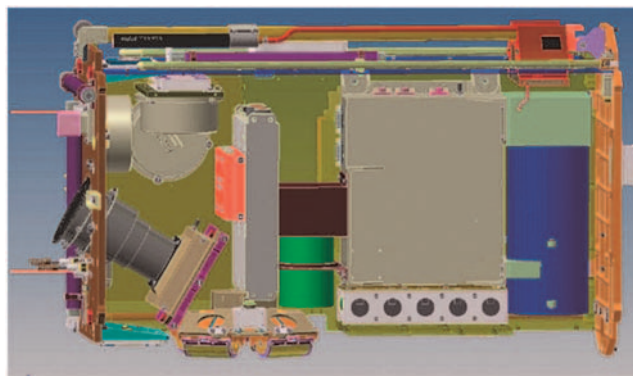


Figure 2. Mounting of assembled NGS instrument onboard "Chibis-AI" (green and brown boxes).

'Neutron' part of the instrument consists of high-energy neutron detector and thermal, epithermal, and fast neutron detectors. The former is a scintillation detector based of stilbene crystal of 21.5 inches diameter, surrounded by plastic anticoincidence shield that registers neutrons wenergies higher than 500 keV. Three detectors are based on He³ proportional counters (LND 25281 type):

- no shielded counter;
- counter shielded by cadmium foil 0.5–1 mm thick (for neutrons with energies of 0.4 eV-1 keV);
- counter shielded by cadmium foil 0.5–1 mm thick and polyethylene (for neutrons with energies 0.1 keV — 500 keV).

Cadmium shields allow separating neutrons relative to their energy. Cadmium effectively absorbs thermal neutrons with energies less than 0.4 eV, so that by deducting counts registered by cadmium-shielded detector from number of counts registered by unshielded detector, one can obtain thermal neutron flux. Gamma-ray spectrometer registers gamma-ray with high sensitivity and energy resolution not worse than 3.5% at the energy 662 keV. It is supposed to use the LaBr₃ (Ce³⁺) crystal, which has to date the highest spectral resolution and efficiency of gamma-ray registration

in energy range 100 keV-10 MeV among scintillation crystals. Due to tight limits on mass and energy consumption, imposed by Chibis project on NGS instrument, germanium spectrometer, which has significantly better energy resolution (approximately 0.3% at the energy 662 keV), was not considered. NGS will be mounted onboard microsatellite with nadir orientation. NGS mount onboard «Chibis-AI» is shown on the Figure 2. Specification of the NGS instrument is provided in the Table 1.

Table 1. Specification of the NGS instrument

Measurements	in a range 0.1 – 10.0 MeV (LaBr3 or CeBr3 crystals) Area ~ 60 sm ² spectral resolution 3.5% (662 keV)
Operation mode	«Standby» regime without scientific measurements and «Science» mode generating «burst» frame ~ 60 kilobytes
Power	7.0 W («Science» mode) and 4.5 W («Standby» mode)
Telemetry	45 Mb/day
Dimensions	263 x 258 x 169 mm
Weight	5.6 kg

Table 2. Specification of the RFA instrument

Measurements	in range 15-26 and 26-48 MHz Time resolution <10 ns Length of the frame - 150 ms ADC dynamic range - 12 bit
Operation mode	Slow mode and fast mode (triggered)
Power	7.0 W
Telemetry	120 Mb/day
Dimensions	205 x 130 x 36,5 mm
Weight	1 kg

It was supposed that Chibis and ISS orbits should be similar. That is why it was decided to install similar instrument onboard ISS for assessing the fluxes of fast, epithermal and thermal neutrons to estimate neutron Earth albedo.

The new RFA proposed for «Chibis-AI» contained two pass bands in the range 15-26 MHz and 26–48 MHz with a digitization at 96 megasamples/s. The radio channel will be connected to a V-shape passive dipole-like antenna with length 2 m of each probe. The antenna was mounted at the bottom of the platform. Initial footprint of the antenna will be around 2300 km along longitude and latitude, or $h_{\max} \sim 68^\circ$ from the plumb line at the equatorial region. Specification of the RFA instrument is provided in the Table 2.

The Scientific Data Accumulation System (SDAS) contains 16 Gb of space qualified flash memory. Each record is triggered (see above) and has an adjustable pretrigger/post-trigger records. Position of the trigger in a frame could be varied.

The SDAS is capable of retriggering a new record within several microseconds after the end of the previous one. The S- and X-band downlink transmitters should provide a flexible high-speed downlink solution for Chibis missions,

offering rates between 2.0 Mbps (S-band) and 20 Mbps (X-band). To manage data downlink and mission control tracking headquarters were organized on the basis of the Space Research Institute of RAS. The scientific data downlinks should occur at different stations up to several downloads per day.

3. VHF INTERFEROMETER «KITE» ONBOARD ISS

As it was mentioned above data provided by one-point measurement (made by one satellite) could not resolve the question about location of RF and gamma-ray emitter in the Earth atmosphere. As a result, it seems impossible to evaluate the luminosity function of the emitter. A great achievement would be working together ground lightning detection network (NLDN, WWLN, etc.), as well as more sensitive scientific instruments on the Earth's orbit. In order to solve the puzzle, we would like to propose for consideration "Kite" experiment onboard ISS.

It is well known that TIPP/CIDs processes produce a broad and continuous spectrum of RF radiation, e.g. [Dolgonosov *et al.*, 2015]. If the radiation over a certain broad frequency band, say, from several tens to a few hundred MHz, is from the same source, the broad band signal could then be used to locate the radiation source. By recording over the entire bandwidth, different frequencies at a fixed separation of two antennas are equivalent to many baselines with respect to a narrow band interferometer. Lower frequencies correspond to shorter baselines and higher to longer baselines.



Figure 3. Installation points of "Kite" antennas is indicated by red arrows.

The phase differences at different frequencies can then be computed after Fourier integration of the time series data from the two antennas, which are then used to resolve the angle of arrival of the radiation source.

So, a broad band system requires fewer antennas than a narrow band system to achieve equivalent angular resolution. In addition, frequency dependent location of the radio emissions can be extracted for a more detailed look at the lightning breakdown processes. In the proposed «Kite» project it should be installed a set of up to 4 broadband VHF receivers in the range 20-50 MHz, similar to that used in the "Chibis-AI". Each radio channel will be connected to a passive dipole-like antenna (2 m long rod). The relative distance between antennas is estimated to be more than 8 m. The signals received by the antenna are transmitted through cables to the electronics. The cables for antennas are semirigid coaxial cables with the same length for tolerance to the exposed space environment. Expected «Kite» antennas positions on ISS surface are shown in Figure 3 by red arrows.

The project is in Phase A as of 2017. The expected launch of the project is 2020.

CONCLUSION

The «Chibis-AI» and «Kite» missions will be conducted on the ISS to observe global distributions of lightning and lightning-associated TGFs by combining observations with radio and gamma-ray sensors. This paper focuses on the payload devoted for investigation of high energetic processes (CIDs and TGFs) of the missions (i.e., RFA and NGS instruments) and serves as an initial overview. The «Kite» VHF receivers is a set of up to 4 of VHF broadband antennas and electronics to record VHF waveforms from lightning and lightning-associated discharges. It is designed to estimate the direction-of-arrival with about 10-km resolution, which is equivalent to the scale of a thundercloud. This means that the «Kite» is able to monitor thunderclouds with global lightning activity and effectively locate position of the emitter in the terrestrial atmosphere. Comprehensive analyses on the «Kite» and «Chibis-AI» observations during their campaigns are expected to provide us with new scientific insights and understanding.

REFERENCE

Bogomolov, V. et al. (2016), Observation of TGFs onboard Vernov'' satellite and TGEs in ground-based experiments, in EGU General Assembly Conference Abstracts, vol. 18, p. 8476.

Briggs, M. S. et al. (2010), First results on terrestrial gamma ray flashes from the Fermi Gamma-ray Burst Monitor, *J. Geophys. Res.*, 115(A7), A07323, doi: 10.1029/2009JA015242.

Chilingarian, A. (2014), Thunderstorm ground enhancements - Model and relation to lightning flashes, *J. Atmos. Solar-Terrestrial Phys.*, 107, 68–76, doi:10.1016/j.jastp.2013.11.004.

Dolgonosov, M. S., V. M. Gotlib, D. I. Vavilov, L. M. Zelenyi, and S. I. Klimov (2015), Solitary'' Trans-Ionospheric Pulse Pairs onboard of the microsatellite

Chibis-M'', *Adv. Sp. Res.*, 56, 1177–1184, doi:10.1016/j.asr.2015.06.009.

Grefenstette, B. W., D. M. Smith, B. J. Hazelton, and L. I. Lopez (2009), First RHESSI terrestrial gamma ray flash catalog, *J. Geophys. Res.*, 114, doi: 10.1029/2008JA013721.

Grove, J. ~E., A. Chekhtman, and Fermi LAT Collaboration (2013), A Four-Year Fermi LAT Survey of Terrestrial Gamma-ray Flashes, in *AAS/High Energy Astrophysics Division*, vol. 13, p. 127.27.

Jacobson, A. R., and T. E. L. Light (2012), Revisiting "Narrow Bipolar Event" intracloud lightning using the FORTE satellite, *Ann. Geophys.*, 30(2), 389–404, doi: 10.5194/angeo-30-389-2012.

Jacobson, A. R., S. O. Knox, R. Franz, and D. C. Enemark (1999), FORTE observations of lightning radio-frequency signatures: Capabilities and basic results, *Radio Sci.*, 34(2), 337, doi:10.1029/1998RS900043.

Jacobson, A. R., R. H. Holzworth, and X.-M. Shao (2011), Observations of multi-microsecond VHF pulsetrains in energetic intracloud lightning discharges, *Ann. Geophys.*, 29(9), 1587–1604, doi:10.5194/angeo-29-1587-2011.

Marisaldi, M. et al. (2010), Detection of terrestrial gamma ray flashes up to 40 MeV by the AGILE satellite, *J. Geophys. Res.*, 115, doi:10.1029/2009JA014502.

Massey, R. S., and D. N. Holden (1995), Phenomenology of transionospheric pulse pairs, *Radio Sci.*, 30(5), 1645–1659, doi:10.1029/95RS01563.

Massey, R. S., D. N. Holden, and X.-M. Shao (1998), Phenomenology of transionospheric pulse pairs: Further observations, *Radio Sci.*, 33(6), 1755–1761, doi:10.1029/98RS02031

Space-time analysis of the Seismic Waves propagation and World Wide Lightning Location Network data association with the Terrestrial Gamma-ray Flashes detected by the Fermi Gamma-ray Burst Monitor

L. Sorokin

Peoples' Friendship University of Russia, Miklukho-Maklaya str., 6, Moscow, 117198, Russian Federation

Abstract. The natural high intensity sub-millisecond electromagnetic pulses associated with seismic waves from earthquakes can trigger +CG, -CG and IC lightning discharges, transient luminous events (TLEs) and non luminous events as TGFs. The lightning discharges with higher peak currents are more probable during the moments when seismic waves from earthquakes pass through a place of lightning. Huge charge transfer of triggered +CG, -CG and IC lightning discharges can radiate powerful electromagnetic emission. Space-time analysis of the seismic wave's propagation and WWLLN data was done together with the second Fermi GBM Terrestrial Gamma-ray Flashes (TGF) Catalog. A total number of 1203 events from the WWLLN associations table were associated with the entrance the exact seismic waves from earthquakes in the place of lightning. Only 11 events from 1214 associations were rejected. After that the full list of 1049 TGFs has been checked out. As the result the 1038 TGFs has been associated with earthquakes. Among them 42 events with time difference exceeding ± 100 sec were found. As the result 996 events get inside the time interval for the space-time analysis ± 100 sec, they correspond to 95% from the total number of 1049 TGFs. The probability density function for the Time difference data was calculated and more preferably can be explained by the probability density functions of Cauchy distribution. The Phases of Seismic Waves and earthquakes magnitude associated with selected 996 TGFs from WWLLN associations table were studied.

1. INTRODUCTION

The TGFs were discovered during the Burst and Transient Source Experiment (BATSE) (Fishman et al., 1994). Since that time the lightning strokes have been studied together with the very low frequency (VLF) radio signals of lightning and gamma ray observations from both BATSE (Inan et al., 1996; Cohen et al., 2006), the Reuven Ramaty High-Energy Solar Spectroscopic Imager (RHESSI) (Cummer et al., 2005; Stanley et al., 2006; Inan et al., 2006; Lay, 2008; Hazelton et al., 2009; Cohen et al., 2010; Shao et al., 2010) and the Gamma-ray Burst Monitor (GBM) on the Fermi Gamma-ray Space Telescope (Briggs et al., 2010; Connaughton et al., 2010).

The WorldWide Lightning Location Network (WWLLN) (Rodger et al., 2009) based on acquisition and processing the VLF radio signals, provides lightning data with localization about 20 km and an average RMS timing accuracy of 30 ms. The WWLLN data was used for finding the correlations with RHESSI TGFs (Lay, 2008; Hazelton et al., 2009). The GPS absolute timing accuracy available bough for TGFs and lightning data are within several microseconds. Perfect timing with the satellite orbital measurements provide the coordinated information on TGFs position.

The associations between Fermi GBM TGFs and WWLLN sferics, with both simultaneous and nonsimultaneous cases was reported by Briggs et al. (2010).

WWLLN sferic correlations with TGFs have been reported on the distances up to 1000 km away from the satellite (Hazelton et al., 2009) and the statistical analysis (Brigs et al., 2013) demonstrate the uniform density up to 300 km, then the density decreases with increasing offset.

The research of Stanley et al. (2006), Cummer et al. (2005), Williams et al. (2006) and Shao et al. (2010) describe the TGFs association with intracloud (IC) lightning. With the help of Lightning Mapping Array the initial development of an IC lightning event (Lu et al., 2010) was associated with TGFs seen by RHESSI.

The Aragats Space Environmental Center of the Cosmic Ray Division (CRD) of the Yerevan Physics Institute provide the research on Thunderstorm Ground

Enhancements (TGEs) and observation flux of electrons and gamma rays correlated with thunderstorms (Chilingarian et al., 2010; Chilingarian et al., 2011; Chilingarian and Mkrtchyan, 2012).

In our previous papers we had done the space-time analysis of the lightning triggering (Sorokin, 2007b) by the seismic waves. On the base of actual data records, the cases of Electromagnetic Pulses generation at the big angular distances by exact seismic waves from earthquakes have been described (Sorokin, 2007a). Electromagnetic Pulses related with seismic waves can provoke positive polarity lightning (Sorokin, 2005a, 2005b, 2006). All these can be associated with triggering the High-Altitude Atmospheric Discharges (Sorokin, 2002, 2006) and transient luminous events (TLEs) (Sorokin, 2009).

In this paper an attempt to associate the entrance the exact seismic waves from earthquakes in the place of lightning with the occurrence of the non luminous events as TGFs were done.

2. TERRESTRIAL GAMMA-RAY FLASHES (TGF) DETECTED BY THE FERMI GAMMA-RAY BURST MONITOR (GBM)

The Fermi Gamma-ray Space Telescope was launched from Kennedy Space Center on 11, 2008 and supports two instruments: the Large Area Telescope (LAT) and the Gamma-ray Burst Monitor (GBM). The observed data are available from GBM Terrestrial Gamma-ray Flashes (TGF) Catalog (G. Fitzpatrick et al., in preparation) Website. The relevant information about the Fermi GBM TGF catalog is available by Briggs et al. (2013). This catalog contains 3356 TGFs, detected from GBM trigger enabled on 2008 July 11 through 2015 June 23 and 579 brighter TGFs are included in the Trigger Table. The correlation of the GBM and WWLLN signals was described in Connaughton et al. (2010, 2013) and these events were included in the WWLLN Associations Table. The WWLLN Associations Table contains accurate localizations of the 1049 TGFs with the 1214 WWLLN radio signals.

3. THE COMPUTATIONAL METHOD

The standard procedure of seismic wave definition is based on computational methods.

All evaluations for the definition of seismic wave possible phases (Pup, P, Pdiff, PKPab, PKPbc, PKPdf, PKiKP, pP, pPKPab, pPKPbc, pPKPdf, pPKiKP, sP, sPKPab, sPKPbc, sPKPdf, sPKiKP, PcP, ScP, SKPab, SKPbc, SKPdf, SKiKP, PKKpab, PKKpbc, PKKpdf, SKKpab, SKKpbc, SKKpdf, PP, P'P', Sup, S, Sdiff, SKSac, SKSdf, pS, pSKSac, pSKSdf, sS, sSKSac, sSKSdf, ScS, PcS, PKSab, PKSbc, PKSdf, PKKSab, PKKSbc, PKKSdf, SKKSac, SKKSdf, SS, S'S' SP, PS, PnS) and evaluations of their travel times were conducted with the use of model AK135 based IASPEI-91 (Kennett, 1991a, 1991b), (Buland and Chapman, 1983).

The AK135 model calculates the travel times for 57 possible phases of seismic waves. The travel times found from AK135 can be estimated with an accuracy of ± 10 seconds. The AK135 use an averaged crust model, and do not differ the oceanic and continental parts of the crust. This can be very important for the coastline areas and the travel times found from AK135 can be significantly different for the direction to the highlands area or to the ocean. Taking in an account the elliptical error for the Earth radius one can improve the accuracy on 3-4 sec. One more source for the more accurate travel time's calculation is the use of the local model of the Earth crust and this can be done in future research.

The range of Fermi Gamma-ray Burst Monitor (GBM) is about 1000 km (Hazelton et al., 2009). This means that the seismic waves propagating in the Earth crust can cover this distance within several minutes. From the other side the scale of the weather front or atmospheric cyclone can be the same dimension as the range of Fermi GBM. The lightning activity can also affect the accuracy. The positive polarity lightning (+CG) can propagate on huge distance up to 100-200 km. The negative polarity lightning (-CG) can force the delayed lightning discharge (+CG) or upward lightning on the huge distance from the first one. Taking in account all information we consider the time interval for the space-time analysis ± 100 sec (Sorokin, 2009).

Seismic waves scattering around the globe, propagating through the Earth's mantle, core and reflecting from the back of crust can trigger, with high efficiency, lightning (Sorokin, 2007b), including positive polarity lightning (Sorokin, 2005b, 2006), High-Altitude Atmospheric Discharges (Sorokin, 2002, 2006) and TLEs (Sorokin, 2009).

Using the U.S. Geological Survey Search Earthquake Catalog data (time UTC, geographical coordinates Latitude and Longitude, depth, magnitude) together with the WWLLN data (date and time UTC, geographical coordinates Latitude and Longitude) it is possible to establish the space-time coupling between exact seismic waves from the earthquake with WWLLN lightning's associated with TGFs. For this purpose we will calculate for the observed TGFs the Event Time in the coordinates of the earthquake (the difference between the WWLLN time stamp and earthquake occurrence time) and the computational Travel Time for exact seismic waves from this earthquake.

In the case if the exact seismic wave from the earthquake passing the place of lightning in the same time with the WWLLN detection we will have a "Zero" Time difference.

4. SPACE-TIME ANALYSIS OF THE EARTHQUAKE – TGF RELATION

The Trigger Table contains information for 579 brighter TGFs. We do not focus on the Trigger events, due to most of them are included in the WWLLN associations table.

The WWLLN associations table has data on the 1049 TGFs for which a close association between a GBM Terrestrial Gamma-ray Flashes (TGF) and WWLLN radio signal was found in the window of ± 3.5 ms (Connaughton et al., 2010). This table contains 1214 associations, including 1019 simultaneous ones.

A total number of 1203 events from the WWLLN associations table were associated with the entrance the exact seismic waves from earthquakes in the place of lightning. Only 11 events from 1214 associations were rejected. After that the full list of 1049 TGFs has been checked out. As the result the 1038 TGFs has been associated with earthquakes. Among them 42 events with time difference exceeding ± 100 sec were found. As the result 996 events get inside the time interval for the space-time analysis ± 100 sec, they correspond to 95% from the total number of 1049 TGFs.

The WWLLN associations table from the second Fermi GBM TGF Catalog is not homogeneous and can be divided into two periods. The first part from 1 October 2008 to 17 February 2013 consist 41 events with Time difference exceeding ± 100 sec and only one event can be seen in the second part of the catalog from 18 February 2013 to 23 June 2015. It looks like that in these two periods the different algorithms can be applied. We can use the second part of the catalog or skip 42 events with Time difference exceeding ± 100 sec for the whole WWLLN associations table with the same result.

The computational Travel Time for exact seismic waves it is possible to compare (Figure 1) with the Event Time in the coordinates of the earthquake.

The Event Time can be calculated as the difference between the WWLLN time stamp and earthquake occurrence time:

$$Event\ Time = T_{(WWLLN)} - T_{(Earthquake)}.$$

We can feel the linear regression (Event number=996, $R^2=0.99906$) for the dependence of calculated Event Times from the computational Travel Times (Figure 1).

The exact seismic wave from the Earthquake entering the place of lightning in the time ($T_{(Seismic\ Wave)}$) equal to the sum of earthquake occurrence time and the computational Travel Time:

$$T_{(Seismic\ Wave)} = (T_{(Earthquake)} + Travel\ Time).$$

Time difference between the WWLLN time stamp and entering of exact seismic wave from the earthquake to the place of lightning, can be calculated as:

$$t = Time\ difference = T_{(WWLLN)} - (T_{(Earthquake)} + Travel\ Time).$$

A small number of the events (42) are situated beyond the linear regression function (± 100 sec) and looks like random component ($-100\ sec < Time\ difference < +100\ sec$). For the selected 996 events the mean value of the Time difference distribution is -0.173 sec and the variance is 498 sec with the standard deviation 22.32 sec. We can plot the probability density function (amplification factor ($N=3522.89$) of the normal distribution for the estimated parameters (Figure 2). From the Figure 2 we can see that the probability density function of the normal distribution do not feel the probability density function of the Time difference between the WWLLN time stamp and entering of exact seismic wave from the Earthquake to the place of lightning.

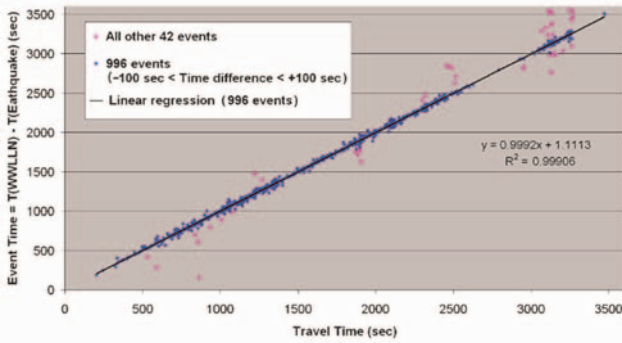


Figure 1. The comparison of calculated Event Times and computational Travel Times for 1038 TGFs associated with earthquakes
Data sources: GBM Terrestrial Gamma-ray Flashes (TGF) Catalog; Search Earthquake Catalog U.S. Geological Survey; WorldWide Lightning Location Network (WWLLN).

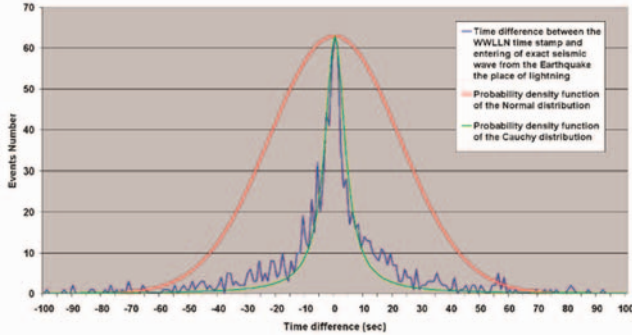


Figure 2. The probability density function for the calculated Time difference data in comparison with probability density functions of normal distribution and Cauchy distribution
Data sources: GBM Terrestrial Gamma-ray Flashes (TGF) Catalog; Search Earthquake Catalog U.S. Geological Survey; WorldWide Lightning Location Network (WWLLN).

We can check the Cauchy distribution conformity for the calculated Time difference data.

The Cauchy distribution is a continuous probability distribution and it is also known as Lorentz distribution or Cauchy-Lorentz distribution.

The Cauchy distribution has the probability density function (Feller, 1971):

$$f(t, t_0, \gamma) = \frac{1}{\pi\gamma} \left[\frac{\gamma^2}{(t - t_0)^2 + \gamma^2} \right],$$

where t_0 is the location parameter, specifying the location of the peak of the distribution, t is the Time difference and γ is the scale parameter which specifies the half width at half maximum (HWHM), alternatively 2γ is full width at half maximum (FWHM).

The maximum value of the Cauchy probability density function is $\frac{1}{\pi\gamma}$, located at $t = t_0$. Applying the method of least squares we can find the scale parameter ($\gamma = HWHM = 4.2$) and amplification factor ($C = 831.26$) to fit the probability density function of the Cauchy distribution (green line, Figure 2) to the observed data (blue line, Figure 2). In terms of interval estimation $FWHM = 8.4$ sec for the observed data the probability will be 0.3651 (383 TGFs from the total number 1049) see Table 1.

We can see that the Cauchy distribution more preferably to the calculated Time difference between the WWLLN time

stamp and entering of exact seismic wave from the Earthquake to the place of lightning.

Table 1. Interval estimation of the calculated Time difference for observed 1049 TGFs from WWLLN associations table

Time interval	TGFs observed in this Time interval	Probability
±4 sec	383	0.365
±5 sec	420	0.40
±10 sec	592	0.564
±25 sec	819	0.78
±30 sec	858	0.818
±50 sec	942	0.898
±100 sec	996	0.95

It is very difficult to compare the normal distribution (red line, Figure .2) with Cauchy distribution (green line, Figure 2) due to the fact that Cauchy distribution does not have a mean value and a variance is infinite value, so the rule of 3-sigma we could not apply. But we can compare them with in terms of HWHM and FWHM. The probability density function of the Cauchy distribution (HWHM=4.2) is the 6.25 times more narrow than for the normal distribution (HWHM=26.28).

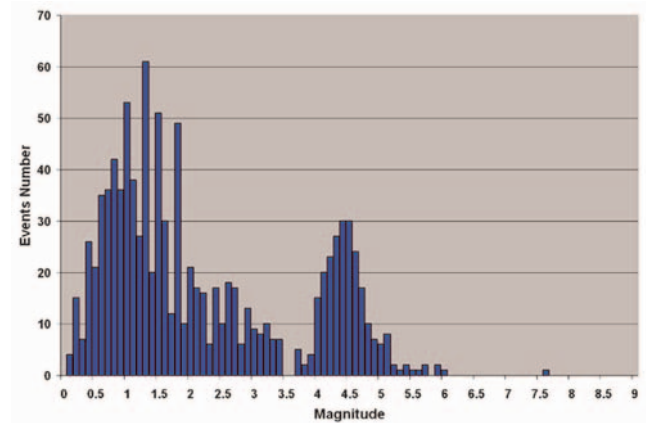


Figure 3. The earthquakes magnitude for selected 996 TGFs from WWLLN associations table
Data sources: GBM Terrestrial Gamma-ray Flashes (TGF) Catalog; Search Earthquake Catalog U.S. Geological Survey; WorldWide Lightning Location Network (WWLLN).

The Figure 3 contain the histogram of the 996 TGFs (Time difference inside the time interval ± 100 sec) associated with earthquakes. From Figure 3 we can see two parts of the distribution separated by magnitude $M = 3.5$.

The form factor of the first part of the distribution with the magnitude from 0 to 3.5 (Events number=755) can be explained by the multiplication of two functions: increasing a number of the earthquakes with lower magnitude and in the same time the lower probability to influence the atmosphere by them. This mechanism can be effective for the local seismicity. The next part of the distribution (Events number=241) can be the result of global seismicity due to the fact that the earthquakes with magnitude higher than 3.5 can emit the seismic waves traveling all over the globe within one hour. In some cases the seismic waves from the earthquakes can affect on the electric field of the atmosphere and trigger the lightnings (Sorokin, 2002, 2007b) and TLEs (Sorokin, 2006, 2009).

The propagation of the exact seismic waves through the earth's crust causes the significant changes in the atmosphere electric field protuberances and a different probabilities to trigger the +CG, -CG and IC lightnings. On the Figure 4 we

The CG lightning usually goes with lower rate of some events per second and choosing the new channel for the next stroke. But it can happen that CG lightning goes in the same channel within some ms twice. So for the CG lightning the probability of pinch effect is very low then for intracloud lightning. This fact can explain that a few CG lightning can produce X-rays and gamma-rays with neutrons and for the intracloud lightning the high energy photons and neutrons are common.

The production of high energy neutrons and protons in the D–T, D–D and D–³He fusion reaction together with proton capture reactions of type (*p*, γ), (*p*, α) and neutron capture reactions of type (*n*, *n*), (*n*, γ), (*n*, *p*), (*n*, α), (*n*, 2*n*) can explain the production of the radioactive materials, gamma-ray radiation and the air ionization during the lightning discharges (Sorokin, 2012). The X-ray and gamma-ray signatures from lightning can be explained due to the Compton scattering effect (Sorokin, 2012). The observation of the long period gamma-ray radiation during the thunderstorm can be due to the decay of isotopes.

So for the TGFs associations describe above relations can be very important: high intensity sub-millisecond electromagnetic pulses associated with seismic waves from earthquakes; triggered +CG, –CG and IC lightning discharges; powerful electromagnetic emission from triggered lightning; intracloud lightning repetition rate; pinch effect or hot plasma instability; the nuclear fusion reaction together with proton capture reactions and neutron capture reactions and Compton scattering effect.

ACKNOWLEDGEMENT

Author thanks M. Briggs for useful discussion during the TEPA-2015 Conference and remarkable work on the Fermi GBM Terrestrial Gamma-ray Flashes (TGF) Catalog. The author wish to thank the WorldWide Lightning Location Network, a collaboration among more than 50 universities and institutions, for providing the lightning location data and UTC time stamp used in this paper. Author thanks R. Buland (National Earthquake Information Centre, U.S. Geological Survey, Golden, Colorado) and Brian Kermett (Research School of Earth Sciences, Austrahan National University Canberra, Austraha) for the software IASPBI9I and AK135. The U.S. Geological Survey Search Earthquake Catalog data used for computational Travel Time.

REFERENCE

Briggs, M.S., et al. (2010), First results on terrestrial gamma ray flashes from the Fermi Gamma-ray Burst Monitor, *J. Geophys. Res.*, 115, A07323, doi: 10.1029/2009JA015242.

Briggs, M.S., et al. (2011), Electron-positron beams from terrestrial lightning observed with Fermi GBM, *Geophys. Res. Lett.*, 38, L02808, doi: 10.1029/2010GL046259.

Briggs, M.S., et al. (2013), Terrestrial gamma-ray flashes in the Fermi era: Improved observations and analysis methods, *J. Geophys. Res. Space Physics*, 118, 3805–3830, doi:10.1002/jgra.50205.

Buland, R., C.H. Chapman (1983), The computation of seismic travel times. *Bull. Seism. Soc. Am*, 1983, v. 73, pp. 1271-1302.

Carlson, B.E., N.G. Lehtinen, U.S. Inan (2009), Terrestrial gamma ray flash production by lightning current pulses. *J. Geophys. Res.*, 114, A00E08, doi:10.1029/2009JA014531.

Connaughton, V., et al. (2010), Associations between Fermi Gamma-ray Burst Monitor terrestrial gamma ray flashes and sferics from the World Wide Lightning Location Network, *J. Geophys. Res.*, 115, A12307, doi: 10.1029/2010JA015681.

Connaughton, V., et al. (2013), Radio signals from electron beams in terrestrial gamma ray flashes, *J. Geophys. Res. Space Physics*, 118, 2313–2320, doi:10.1029/2012JA018288.

Cohen, M.B., U.S. Inan, and G. Fishman (2006), Terrestrial gamma ray flashes observed aboard the Compton gamma ray observatory/burst and transient source experiment and ELV/VLF radio atmospheric, *J. Geophys. Res.*, 111, D24109, doi:10.1029/2005JD006987.

Cohen, M.B., U.S. Inan, R.K. Said, Gjestland, T. (2010), Geolocation of terrestrial gamma-ray flash source lightning, *Geophys. Res. Lett.*, 37, L02801, doi:10.1029/2009GL041753.

Cummer, S.A., Y. Zhai, W. Hu, D.M. Smith, L.I. Lopez, and M.A. Stanley (2005), Measurements and implications of the relationship between lightning and terrestrial gamma ray flashes, *Geophys. Res. Lett.*, 32, L08811, doi:10.1029/2005GL022778.

Feller, William, (1971), *An Introduction to Probability Theory and its Applications, Volume II (2ed.)*. New York: John Wiley & Sons Inc. p. 704. ISBN 978-0471-25709-7.

Fishman, G.J., et al. (1994), Discovery of intense gamma-ray flashes of atmospheric origin, *Science*, 264, 1313–1316, doi:10.1126/science.264.5163.1313.

Hazelton, B.J., B.W. Grefenstette, D.M. Smith, J.R. Dwyer, X.- M. Shao, S.A. Cummer, T. Chronis, E.H. Lay, and R.H. Holzworth (2009), Spectral dependence of terrestrial gamma-ray flashes on source distance, *Geophys. Res. Lett.*, 36, L01108, doi:10.1029/2008GL035906.

Inan, U.S., S.C. Reising, G.J. Fishman, and J.M. Horack (1996), On the association of terrestrial gamma-ray bursts with lightning and implications for sprites, *Geophys. Res. Lett.*, 23, 1017–1020, doi:10.1029/96GL00746.

Inan, U.S., M.B. Cohen, R.K. Said, D.M. Smith, and L.I. Lopez (2006), Terrestrial gamma ray flashes and lightning discharges, *Geophys. Res. Lett.*, 33, L18802, doi:10.1029/2006GL027085.

Kennett, B.L.N., E.R. Engdahl (1991), Traveltimes for global earthquake location and phase identification, *Geophys. J. Int.*, 1991, V105, 429-465.

Kennett, B.L.N. (1991), *IASPEI 1991 Seismological Tables*, Research School of Earth Sciences, Canberra, 1991.

Kolmašová I., O. Santolík (2012), The submicrosecond structure of unipolar magnetic field pulse trains generated by lightning discharges // 1st TEA – IS Summer School, June 17th – June 22nd 2012, Málaga, Spain, Pp. 132-133.

Krider, E.P., G.I. Radda, R.C. Noggle (1975), Regular radiation field pulses produced by intracloud lightning discharges, *J. Geophys. Res.*, Vol. 80, pp. 3801-3804, 1975, doi: 10.1029/JC080i027p03801

Lay, E.H. (2008), *Investigating lightning-to-ionosphere energy coupling based on VLF lightning propagation characterization*, Ph.D. thesis, Univ. of Wash., Seattle.

- Lu, G., R.J. Blakeslee, J. Li, D.M. Smith, X.- M. Shao, E.W. McCaul, D.E. Buechler, H.J. Christian, J.M. Hall, and S.A. Cummer (2010), Lightning mapping observation of a terrestrial gamma-ray flash, *Geophys. Res. Lett.*, 37, L11806, doi: 10.1029/2010GL043494.
- Østgaard, N., T. Gjesteland, J. Stadsnes, P. H. Connell, and B. Carlson (2008), Production altitude and time delays of the terrestrial gamma flashes: Revisiting the Burst and Transient Source Experiment spectra, *J. Geophys. Res.*, 113, A02307, doi: 10.1029/2007JA012618
- Rakov V.A., M.A. Uman, G.R. Hoffman, M.W. Masters, and M. Brook (1996), Burst of pulses in lightning electromagnetic radiation: observations and implications for lightning test standards, *IEEE Transactions on Electromagnetic Compatibility*, vol. 38, no. 2, pp. 156-164, May 1996, doi: 10.1109/15.494618
- Rodger, C.J., J.B. Brundell, R.H. Holzworth, and E.H. Lay (2009), Growing detection efficiency of the world wide lightning location network, in *Coupling of Thunderstorms and Lightning Discharges to Near-Earth Space*, edited by N. B. Crosby, T.- Y. Huang, and M. J. Rycroft, *AIP Conf. Proc.*, 1118, 15–20.
- Shao, X.- M., T. Hamlin, and D.M. Smith (2010), A closer examination of terrestrial gamma-ray flash-related lightning processes, *J. Geophys. Res.*, 115, A00E30, doi: 10.1029/2009JA014835.
- Chilingarian, A., A. Daryan, K. Arakelyan, A. Hovhannisyanyan, B. Mailyan, L. Melkumyan, G. Hovsepyan, S. Chilingaryan, A. Reymers, and L. Vanyan 2010: Ground-based observations of thunderstorm-correlated fluxes of high-energy electrons, gamma rays, and neutrons, *Phys. Rev. D* 82, 043009 (2010).
- Chilingarian, A., G. Hovsepyan, A. Hovhannisyanyan, 2011: Particle bursts from thunderclouds: natural particle accelerators above our heads. *Phys. Rev. D: Part. Fields* 83 (6), 062001.
- Chilingarian, A., H. Mkrtchyan (2012), Role of the lower positive charge region (LPCR) in initiation of the thunderstorm ground enhancements (TGEs). *Phys. Rev. D: Part. Fields* 86, 072003.
- Sorokin, L.V., (2002) Earthquake Space-Time Relations with Positive Lightning and High-Altitude Atmospheric Discharges // *Bulletin of Peoples' Friendship University of Russia. Series Physics*, 2002, No 10(1), Pp. 163–169, ISSN 2312-9735, (In Russian), <http://elibrary.ru/item.asp?id=11743084>.
- Sorokin, L.V. (2005a), Triggering of the Earthquakes by Seismic Waves// *Bulletin of Peoples' Friendship University of Russia. Series Physics*, 2005, No 1(13), Pp. 141-148, ISSN 2312-9735, (In Russian), <http://elibrary.ru/item.asp?id=11743126>
- Sorokin, L.V. (2005b), Triggering of Positive Lightning by Electromagnetic Pulses related with Seismic Waves // *Bulletin of Peoples' Friendship University of Russia. Series Physics*, 2005, No 1(13), Pp. 149–156, ISSN 2312-9735, (In Russian), <http://elibrary.ru/item.asp?id=11743127>.
- Sorokin, L.V. (2006), Triggering of Positive Lightning and High-Altitude Atmospheric Discharges. // *Proceedings of the NATO Advanced Study Institute on “Sprites, Elves and Intense Lightning Discharges”* Edited by Martin Fullenkrag, Eugene A. Mareev and Michael J. Rycroft. Corte, Corsica, France 24-31 July 2004, NATO Science Series II: Mathematics, Physics and Chemistry – Springer 2006, Vol. 225. – Pp. 384-385., ISBN-13 978-1-4020-4628-5 (PB). <http://www.springer.com/physics/book/978-1-4020-4628-5>
- Sorokin, L.V. (2007a), Anomalous seismo-electromagnetic emission related with seismic waves // *The proceedings of “7-th International Symposium on Electromagnetic Compatibility and Electromagnetic Ecology”*. Saint-Petersburg, June 26 – 29, 2007. – Pp. 293-296., IEEE Catalog Number 07EX1804C, ISBN 1-4244-1270-6, Library of Congress Catalog Card No. 2007925840, http://ieeexplore.ieee.org/xpl/freeabs_all.jsp?arnumber=4371715
- Sorokin, L.V. (2007b), Lightning triggering related with seismic waves // *The proceedings of 7-th International Symposium on Electromagnetic Compatibility and Electromagnetic Ecology”*. Saint-Petersburg, June 26 – 29, 2007. – Pp. 297-300., IEEE Catalog Number 07EX1804C, ISBN 1-4244-1270-6, Library of Congress Catalog Card No. 2007925840, http://ieeexplore.ieee.org/xpl/freeabs_all.jsp?arnumber=4371716
- Sorokin, L. V. (2009), Seismo-electromagnetic emissions related to seismic waves can trigger TLEs // *Coupling of thunderstorms and lightning discharges to Near-Earth Space*. Editors Norma B. Crosby, Tai-Yin Huang, Michael J. Rycroft. *Proceedings of the Workshop (Corte, France, 23-27 June 2008)*, Melville, New York, 2009, *AIP Conference proceedings*. – Vol. 1118. – Pp. 58-67., L.C. Catalog Card No. 2009924926, ISBN 978-0-7354-0657-5, ISSN 0094-243X, <http://scitation.aip.org/proceedings/confproceed/1118.jsp>
- Sorokin, L.V. (2012), High-Energetic Radiation from Gas Discharge Associated with the Maximum Rate of Current Change // *Bulletin of Peoples' Friendship University of Russia. Series Mathematics, Information Sciences, Physics*. No 4, 2012. Pp. 181–188., ISSN 2312-9735, <http://elibrary.ru/item.asp?id=17973322>
- Stanley, M.A., X.-M. Shao, D. M. Smith, L. I. Lopez, M. B. Pongratz, J. D. Harlin, M. Stock, and A. Regan (2006), A link between terrestrial gamma-ray flashes and intracloud lightning discharges, *Geophys. Res. Lett.*, 33, L06803, doi: 10.1029/2005GL025537.
- Williams, E., et al. (2006), Lightning flashes conducive to the production and escape of gamma radiation to space, *J. Geophys. Res.*, 111, D16209, doi: 10.1029/2005JD006447.
- The Aragats Space Environmental Center of the Cosmic Ray Division (CRD) of the Yerevan Physics Institute URL: <http://adei.crd.yerphi.am/adei>.
- GBM Terrestrial Gamma-ray Flashes (TGF) Catalog – URL: <http://fermi.gsfc.nasa.gov/ssc/data/access/gbm/tgf/>
- U.S. Geological Survey Search Earthquake Catalog – URL: <https://earthquake.usgs.gov/earthquakes/search/>
- WorldWide Lightning Location Network (WWLLN) – URL: <http://wwlln.net>

The First Sprite Observation from Moscow in the Direction of Tver Region Associated with Repetitive Lightning Discharge

L.V. Sorokin

Peoples' Friendship University of Russia, Miklukho-Maklaya str., 6, Moscow, 117198, Russian Federation

Abstract. The summer thunderstorms 2016 in the central part of Russia produced heavy precipitations and were accompanied by huge amount of lightning. During these events we provide the Sprite observation from Moscow. On the 18 August we caught two Sprites on the distance from 260 km to 290 km in the Tver region. It is important to underline that both Sprites occurred after the rare repetitive lightning discharge and the multiple lightning discharge. These types of lightning are rare in the Moscow region and more habitual for the tropical thunderstorms in Equator area. Due to the Climate Change and Global Warming the Sprites are common for the Russian Federation now..

1. INTRODUCTION

The first Sprite observation was done by Low-light Television (LLTV) camera in 1989 by Franz et al. (1990). The detailed research follow from ground observation (Lyons, 1994a,b, 1996a) and aircraft campaign (Sentman et al., 1995). From these remarkable events Sprites, Blue jets, Elves and other kinds of high altitude lightning become widely known as Transient Luminous Events (TLE).

INSTRUMENT

For the TLE observation we use the CCD camera WATEC WAT-902H3 ULTIMATE with the lens BOSCH 3-8 mm (f 1:1.0). This is a good solution for the low light observation. Video capture device CANOPUS ADVC-110 is compatible with all Widows computers with DV interface.

The video capture software UFOCaptureV2 (V2.24 2013/06/09) provides the 2.4 sec video record (60 frames) and the JPEG image of the trigger event.

The time synchronization was done over Time Server "time.windows.com" before starting the observation. It looks like the difference between the computer time and the UTC was $+400\pm 140$ msec. But it was possible to identify the exact lightning in the video record due to specific time interval between them. Each frame has duration of 40 msec and consists from even and odd half-frames. So we compare the UTC time stamp providing WorldWide Lightning Location Network together with the lightning location data for synchronization of the video record with accuracy of ± 40 msec.

The Blitzortung.org contributors lightning map is very useful for the estimation of the lightning activity in the real time all over the World. In the day time the high resolution satellite images and infrared images are available from Sat24.com and during the night they provide the infrared images of the clouds. With the help of these visualization maps together with Radar maps it is possible to target the camera on the thunderstorm and make a good image of TLE.

2. SPRITE OBSERVATION

During the EuroSprite-2008 Campaign providing by DTU Space and National Space Institute in the period from 1 to 8 September 2008 we participate in the observation from Pic du Midi and Corsican systems. During the heavy thunderstorm lasted from 2 till 5 September 2008 the Corsican systems observed 84 Sprites, two Elves and one

meteor (Sorokin, 2009). The observed Sprites (Sorokin, 2009) associated with the space-time coupling between seismic waves from earthquakes and triggered lightning (Sorokin, 2002, 2005, 2006, 2007b). This was a very successful experiment done during the period of high rate of seismic events.

The next successful Sprite observation was done 10 years later in the Russian Federation from Moscow. During the whole night 18 August 2016 only two Sprites were detected and the seismic activity was very weak in the period of observation. This was the first Sprite detection from the Moscow region, but it was not the first campaign in the Russian Federation, during the 2016 we provide the observations in July 17, 18, 30 and August 11, 12, 18, 19. The previous observations were not successful due to the bad visibility, experiments with the different cameras and lens, together with the software problems.

During the Conference Thunderstorms and elementary particle acceleration (TEPA – 2016) in Armenia with the help of Hripsime Mkrtychyan and Tigran Karapetyan the Sprite observation system was installed in the conference venue Nor Amberd, October 3-7, 2016. Due to the clear sky and absence of the thunderstorms in the range more then 600 km the Sprites in Armenia were not detected.

3. SPRITE OBSERVATION OVER TVER REGION ON 18 AUGUST 2016

At 18 August 2016 the Moscow weather was fine with clear sky and perfect visibility. This fact is seen from the Figure 1 and the red pointer demonstrates the destination from the place of observation (Moscow) to the Sprite location. In the evening the heavy thunderstorm was passing near Moscow over Tver region (Figure 1) and it was possible to target the camera in the direction of the most intensive lightning activity of the thunderstorm (Figure 2). From the Blitzortung.org contributors lightning data we can see that the maximum of the lightning activity in Europe produced the 3265 flashes within 20 minutes, just before the Sprites were detected. The Sprites occurred when the lightning activity reduced two times.

The observation was done from Moscow and the camera was situated in the place with coordinates: Latitude 55.6451 and Longitude 37.5176 with Elevation 36 m under the ground. From this direction we have a nice view on the North from Moscow

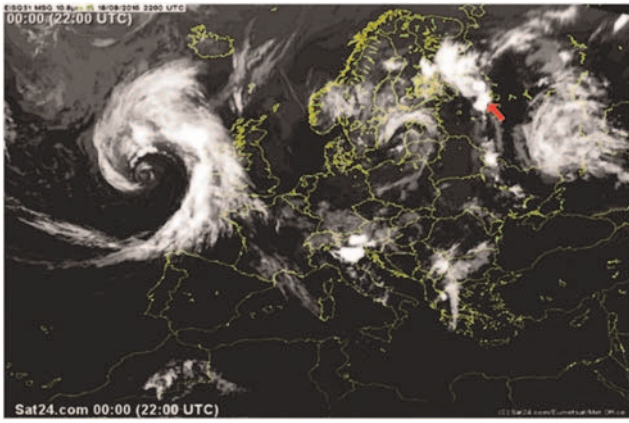


Figure 1. The Sat24.com infrared image of the clouds over Europe at 22:00 UTC, 18 August 2016. The red pointer demonstrates the destination from the place of observation (Moscow) to the Sprite location.

Source: Weather Europe Sat24.com – <http://en.sat24.com/en>

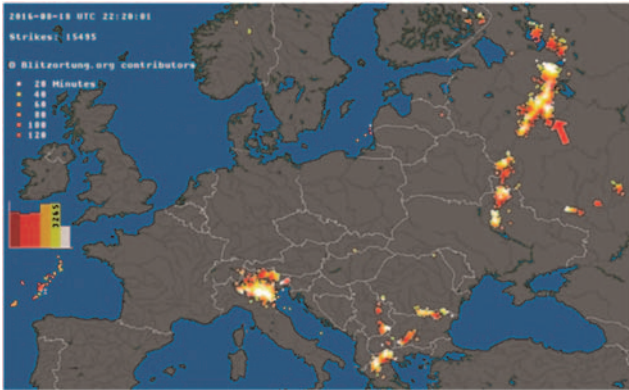


Figure 2. The crop image of the Blitzortung.org contributors lightning map of Europe. The red pointer demonstrates the destination from the place of observation (Moscow) to the Sprite location.

Source: Blitzortung.org contributors lightning map – <http://blitzortung.org>

Table 1. WorldWide Lightning Location Network Data associated with the first Sprite.

Date UTC Year/M/Day	Time UTC Hour:Min:Sec	Latitude Degrees	Longitude Degrees	Error μ s	Stat. Num.	Event Type
2016/08/18	22:09:10.066566	56.2453	34.2695	6.9	5	Lightning
2016/08/18	22:09:11.235464	57.7133	35.5068	15.6	6	Lightning
2016/08/18	22:09:11.235475	57.7487	35.5481	15.1	6	Lightning + Sprite
2016/08/18	22:09:11.698913	58.0151	35.0644	16.0	8	Lightning

Table 2. WorldWide Lightning Location Network Data associated with the second Sprite.

Date UTC Year/M/Day	Time UTC Hour:Min:Sec	Latitude Degrees	Longitude Degrees	Error μ s	Stat. Num.	Event Type
2016/08/18	22:18:19.898741	60.0752	36.5959	5.6	5	Lightning
2016/08/18	22:18:20.048457	60.1294	36.6468	12.9	7	Lightning
2016/08/18	22:18:20.714342	58.0644	35.7196	11.8	5	Lightning
2016/08/18	22:18:20.744765	58.0306	35.6983	9.4	5	Lightning
2016/08/18	22:18:20.766665	58.0576	35.7276	7.6	5	Lightning + Sprite
2016/08/18	22:18:21.426445	58.1337	35.1113	21.4	13	Lightning
2016/08/18	22:18:21.513607	58.2094	34.8091	17.0	5	Lightning

In Figure 3 we can see the frame with the Sprite event from UFO video capture software. The first Sprite was observed in between of repetitive lightning discharge and the delayed lightning (Table 1). It looks like the first Sprite was follow after the repetitive lightning discharge and can be seen on the next frame together with the lightning flash halo. The distance from the place of observation to the repetitive lightning discharge was 260 km. Usually the Sprite occur



Figure 3. The first Sprite was follow after the repetitive lightning discharge and can be seen together with the lightning flash halo.



Figure 4. The second Sprite occurs after the multiple lightning discharge.

close to the lightning discharge so we can consider this distance as the characteristic for this event.

This thunderstorm lasted from the evening up to the midnight and produces only two Sprites. The next Sprite image we can see on the Figure 4. A group of three lightning was observed just before the second Sprite occurs (Table 2). This three lightning's were visible in two different frames and the second Sprite happened the next frame after them.

This Sprite is slightly visible one frame more and has a longer duration than the first one. The distance from the place of observation to the multiple lightning discharge was 290 km, but the second Sprite was shifted to the direction of the first Sprite.

With the help of only one Sprite observations system we could not make the triangulation. But we can estimate the distance of 40 km between the repetitive lightning discharge (the first event) and the multiple lightning discharge (the second event). In the both cases (Figure 3 and Figure 4) we can see that the Sprites were localized in the compact area in comparison with their dimension.

CONCLUSION

On 18 August 2016, two Sprites were detected in the central part of the Russian Federation, Tver region. So the Sprites are common for Russia now. It is important to underline that both Sprites occurred after the rare repetitive lightning discharge and the multiple lightning discharge. These types of lightning are rare in the Moscow region and more habitual for the tropical thunderstorms in Equator area. The repetitive lightning discharge due to the pinch effect can produce the high energy radiation on the altitude of 4-5 km (Sorokin, 2012). The source of the high energy radiation inside the cloud can launch the particle acceleration (Chilingarian et al., 2010), (Chilingarian et al., 2011) and nuclear reactions (Sorokin, 2012) these can cause the conditions for Upward lightning, Blue jets and Sprites.

The heavy thunderstorm (18 August 2016) over Tver region produce about 10000 lightning discharges within 3 hours and only two Sprites. Probably the Sprites were detected in the central part of the Russian Federation due to the Global Warming and the climate became more tropical. From the other side the top of the tropical thunderstorms can reach the higher altitudes of 16 – 18 km and produce more upward lightning that can initiate the Sprites.

ACKNOWLEDGEMENT

The authors thank the staff of the Aragats Space Environmental Center for the uninterruptible operation of Aragats research station facilities.

The author wish to thank the WorldWide Lightning Location Network, a collaboration among more than 50 universities and institutions, for providing the lightning location data and UTC time stamp used in this paper.

REFERENCE

- Chilingarian, A., Daryan, A., Arakelyan, K., Hovhannisyanyan, A., Mailyan, B., Melkumyan, L., Hovsepyan, G., Chilingaryan, S., Reymers, A. and Vanyan, L., 2010: Ground-based observations of thunderstorm-correlated fluxes of high-energy electrons, gamma rays, and neutrons, *Phys. Rev. D* 82, 043009 (2010).
- Chilingarian, A., Hovsepyan, G., Hovhannisyanyan, and A., 2011: particle bursts from thunderclouds: natural particle accelerators above our heads. *Phys. Rev. D: Part. Fields* 83 (6), 062001.
- Lyons, W. A., 1994a: Characteristics of luminous structures in the stratosphere above thunderstorms as imaged by low-light video. *Geophys. Res. Lett.*, 21, 875–878.
- Lyons, W. A., 1994b: Low-light video observations of frequent luminous structures in the stratosphere above thunderstorms. *Mon. Wea. Rev.*, 122, 1940–1946.
- Lyons, W. A., 1996a: Sprite observations above the U.S. high plains in relation to their parent thunderstorm systems. *J. Geophys. Res.*, 101, 29 641–29 652.
- Sentman, D. D., E. M. Wescott, D. L. Osborne, D. L. Hampton, and M. J. Heavner, 1995: Preliminary results from the Sprites94 aircraft campaign: 1, Red sprites. *Geophys. Res. Lett.*, 22, 1205–1208.
- Sorokin L.V., 2002: Earthquake Space-Time Relations with Positive Lightning and High-Altitude Atmospheric Discharges // *Bulletin of PFUR. Series Physics*. No 10(1), 2002. Pp. 163–169., ISSN 2312-9735, (In Russian), <http://elibrary.ru/item.asp?id=11743084>
- Sorokin L.V., 2005: Triggering of Positive Lightning by Electromagnetic Pulses related with Seismic Waves // *Bulletin of PFUR. Series Physics*. No 1(13), 2005. Pp. 149–156., ISSN 2312-9735, (In Russian), <http://elibrary.ru/item.asp?id=11743127>
- Sorokin. L.V., 2006: Triggering of Positive Lightning and High-Altitude Atmospheric Discharges. // *Proceedings of the NATO Advanced Study Institute on “Sprites, Elves and Intense Lightning Discharges”* Edited by Martin Fullenkruug, Eugene A. Mareev and Michael J. Rycroft. Corte, Corsica, France 24-31 July 2004, NATO Science Series II: Mathematics, Physics and Chemistry – Springer 2006, Vol. 225. – Pp. 384-385., ISBN-13 978-1-4020-4628-5 (PB). <http://www.springer.com/physics/book/978-1-4020-4628-5>
- Sorokin. L.V., 2007b: Lightning triggering related with seismic waves // *The proceedings of 7-th International Symposium on Electromagnetic Compatibility and Electromagnetic Ecology*”. Saint-Petersburg, June 26 – 29, 2007. – Pp. 297-300., IEEE Catalog Number 07EX1804C, ISBN 1-4244-1270-6, Library of Congress Catalog Card No.2007925840, http://ieeexplore.ieee.org/xpl/freeabs_all.jsp?arnumber=4371716
- Sorokin L. V., 2009: Seismo-electromagnetic emissions related to seismic waves can trigger TLEs // *Coupling of thunderstorms and lightning discharges to Near-Earth Space*. Editors Norma B. Crosby, Tai-Yin Huang, Michael J. Rycroft. *Proceedings of the Workshop (Corte, France, 23-27 June 2008)*, Melville, New York, 2009, AIP Conference proceedings. – Vol. 1118. – Pp. 58-67., L.C. Catalog Card No. 2009924926, ISBN 978-0-7354-0657-5, ISSN 0094-243X, <http://scitation.aip.org/proceedings/confproceed/1118.jsp>
- Sorokin L.V., 2012: High-Energetic Radiation from Gas Discharge Associated with the Maximum Rate of Current Change // *Bulletin of PFUR. Series Mathematics, Information Sciences, Physics*. No 4, 2012. Pp. 181–188., ISSN 2312-9735, <http://elibrary.ru/item.asp?id=17973322>
- Blitzortung.org contributors lightning map – <http://blitzortung.org>
- Weather Europe Sat24.com – <http://en.sat24.com/en>
- WorldWide Lightning Location Network – <http://wwlln.net>

Muon Flux Monitoring in the YerPhI Underground Laboratory

A. Aleksanyan, S. Amirkhanyan, T. Kotanjyan, L. Poghosyan, V. Pogosov

Yerevan Physics Institute, Alikhanyan Brothers 2, Armenia, 0036

Abstract. We have organized the muon flux monitoring in the YerPhI underground laboratory. Muon detector system consists of two pairs of plastic scintillators 50x50x5cm³ size. The data acquisition system registered and stored 1-sec, 1-minute and 1-hour time series of the detector counts. Time series are transferred to the Cosmic Ray Division database via 1 km long cable and then radio-modems and are accessible on-line via ADEI multivariate visualization platform.

1. INTRODUCTION

Yerevan Physics Institute performs experiments in the underground low-background laboratory with a developed scientific infrastructure including fast Internet connections (that is nontrivial for the deep underground location). The laboratory is placed in the Avan salt mine, which is located in within Yerevan limits, at the depth of 240 m (650 m w.e.). The laboratory has an important advantage, compared to other known underground laboratories, as it is located in close vicinity of a large city with the corresponding infrastructure and communication system and near to a well-known scientific center.

The laboratory has had several remarkable achievements during its lifetime. For example, there was an experiment performed earlier together with the Institute of Theoretical and Experimental Physics (Moscow), in which, for the first time, two-neutrino double-decay of ⁷⁶Ge has been observed, and the most stringent limit on a half-life of neutrinoless double beta-decay in this germanium isotope was set [1]. The subject of the latest experiments performed by our group was the search for the rare decays of californium nuclei [2, 3].

Figures 1-4 show historical picture of the start of measurements taking and current work in the underground lab. An old HPG detector (P-type Coaxial High Purity Germanium Detector GEM15P4, Ortec) represented in Figure 5 is surrounded by a radio-pure lead and covered by a polyethylene bag. Nitrogen is blown into the bag to displace the radioactive radon from around the detector. Figure 6 represents a background spectrum measured by the HPGe detector on the surface and in the underground laboratory with and without shielding during equal time intervals (22 hours). This figure demonstrates obvious advantages of underground measurements of the rare processes.

Very low background counts due to low-radioactivity of the salt give a big advantage to the research of the rare nuclear processes. The new purchased High Purity Germanium Detector (HPG - GCD-20180, Figure 7) with its multi-channel analyzer BOSON (both are products of Baltic Scientific Instruments, Latvia) will highly enlarge the scientific potential of the underground laboratory. We plan to use the developed scientific infrastructure for the started nuclear physics research program on the IBA 18-MeV proton cyclotron located on premises of Yerevan Physics Institute. We are now developing a low background setup for the future experiments. Due to its special construction, the new HPGe detector will allow us to achieve an even higher level of background suppression.

2. CONSTRUCTION OF THE MUON DETECTOR

The main subject of this paper is the description of the muon detector on the base of plastic scintillators for future monitoring of muons with the energies higher than 150 GeV, which are generated in the atmosphere by the galactic cosmic rays. The depth of our laboratory determines this rather high-energy threshold. High energy muon monitoring should give us additional information in the synchronized measurements with other muon detectors located on Aragats research station of YerPhI where monitoring of a flux of muons with energies ranging from 1 MeV to 5 GeV is continued for tenths of years [4]. The investigation of muon flux variations depending on the season, temperatures of the high layers of the atmosphere, is important from the applied point of view, as well as from the point of view of fundamental physics. It is worth to mention that large muon detectors also can detect violent explosions in Universe.

Muon detecting system consists of two pairs of 50x50x5cm³ scintillators. Each pair is registering coinciding muon traversals to eliminate the environmental noise. Figure 8 presents one of the detector pairs. Top and bottom scintillators have the different type of light collection system for choosing an optimal one. The estimated value for mean muon flux at the depth of our laboratory is about 0.05/m²/s. Thus, operated detector will observe daily variations down to the level of a few percent. The further buildup of muon detector should substantially increase its sensitivity.

The Internet connections established in salt mine allows on-line correlation analysis between highest energy muon events and muons registered on the Aragats high-mountain stations (energy range 1 – 5000 MeV). The muon count rates from the salt mine on-line enter the Cosmic Ray Division's database and are assessable for the analysis via user-friendly multivariate visualization platform ADEI [5]. Figure 9 represents the time series of the muon flux measured by one of the pairs of plastic scintillators during 445 hours. Figure 10 represents the statistical analysis of this data: first and second moments and goodness of fit criteria. The mean value of muon flux of a pair of scintillators equals to ~47 per hour.



Figure 1. A railway transportation system to underground laboratory.



Figure 2. Three decades ago: the installation of the first Germanium detector for searching for double beta decay of ^{76}Ge nuclei. From left to right: V.Pogosov (YerPhi) and A.Starostin (ITEP, Moscow)



Figure 3. S. Amirhanyan is checking DAQ system before starting the data collection



Figure 4. The staff of underground laboratory. From left to right: S. Amirkhanyan, A. Aleksanyan, T. Kotanjyan, L. Poghosyan



Figure 5. An old Germanium detector (surrounded by shielding to decrease environmental background).

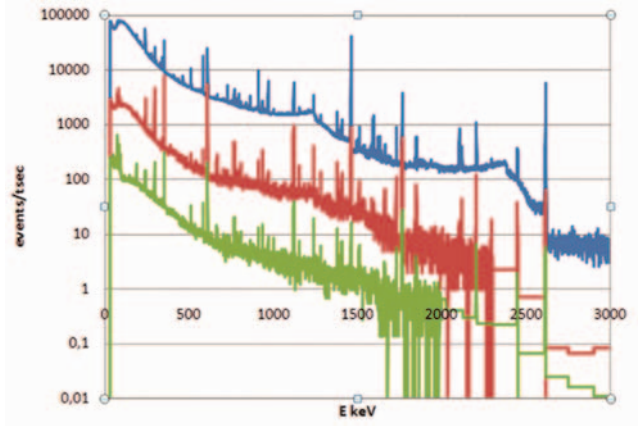


Figure 6. Background spectrum measured by the HPGe detector during equal time intervals (22 hours): blue – on the surface; red - in the underground laboratory; green – in the underground laboratory with radioactive lead shielding.

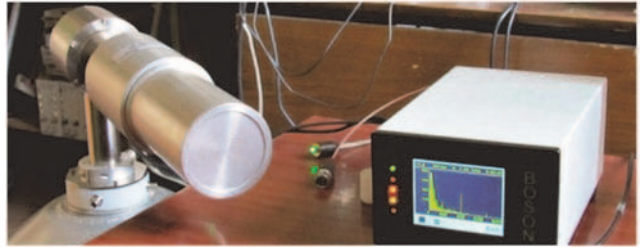


Figure 7. The new HPGe-detector with its analyzer BOSON

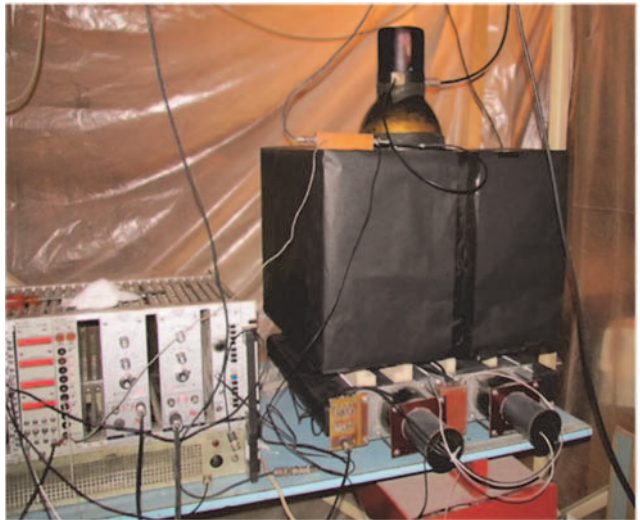


Figure 8. The muon detectors consisted of a pair of plastic scintillators each of $50 \times 50 \times 5 \text{ cm}^3$ size.

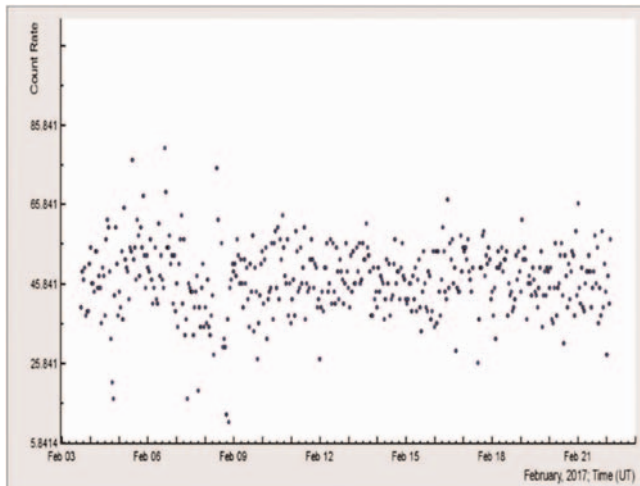


Figure 9. Hourly count rates measured by a pair of plastic scintillators

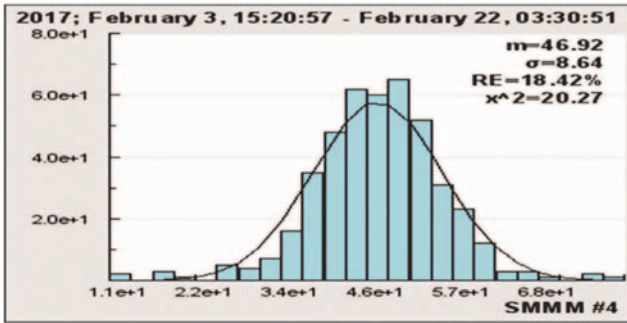


Figure 10. Incident muons hourly count rate distribution

CONCLUSION

We started the muon flux monitoring in the YerPhI underground laboratory. The data transfer to the YerPhI's web page (ADEI) in real time has been organized as well. Muon detector system based on two pairs of plastic scintillators $50 \times 50 \times 5 \text{ cm}^3$ has been constructed. The further increasing of the detector will allow us to achieve the desirable sensitivity. For instance, a daily count rate of 10 m^2 detector will have statistical variations down to the one percent. This will allow to investigation of the correlation between the underground muon flux and the upper air temperature, including, so called, sudden stratospheric warming (SSW, [6]). The muon-induced events are one of the main concerns regarding background in deep underground facilities where modern neutrino experiments are located. The careful estimation of the muon flux created by cosmic rays in the atmosphere and penetrated deep underground is of crucial importance for the neutrino experiments [7].

ACKNOWLEDGMENT

We appreciate prof. A. Chilingarian efforts, which initiated this work and supported it during its implementation.

REFERENCE

- [1] Vasenko A.A., et al., New Results In The ITEP / YerPI Double Beta Decay Experiment With Enriched Germanium Detector. Mod.Phys.Lett. A5 (1990) 1299-1306
- [2] A. Aleksanyan, S. Amirkhanyan, H. Gulkanyan, T. Kotanjyan, L. Poghosyan, V. Pogosov, Searching for Long-Living Rare Products of the ^{252}Cf Spontaneous Fission. Armenian Journal of Physics 8 (3), 103 (2015).
- [3] Ayvazyan, H. Gulkanyan, V. Pogosov, L. Poghosyan. Search for Rare Decay Modes of Californium. Proceedings of National Academy of Sciences of Armenia, 51, N1, 3-14 (2016).
- [4] S. Chilingaryan, A. Beglarian, A. Kopmann, and S. Voćking, Advanced data extraction infrastructure: Web based system for management of time series data, J. Phys. Conf. Ser. 219, 042034 (2010).
- [5] Chilingarian A., A. Daryan, K. Arakelyan, A. Hovhannisyan, B. Mailyan, L. Melkumyan, G.Hovsepyan; Ground-based observations of thunderstorm-correlated fluxes of high-energy electrons, gamma rays, and neutrons (2010),Phys Rev D. 82.043009.
- [6] C.A. Varotsos, A.P. Cracknell & C. Tzanis (2010) Major atmospheric events monitored by deep underground muon data, Remote Sensing Letters, 1:3, 169-178.
- [7] Abrahão T., Almazan H., dos Anjos J.C., et al., Cosmic-muon characterization and annual modulation measurement with Double Chooz detectors, Journal of Cosmology and Astroparticle Physics, JCAP02 (2017) 017.

Muon Hodoscope URAGAN as a New Meteorological Tool

N. Barbashina, A. Petrukhin, I. Yashin,

National Research Nuclear University MEPhI (Moscow Engineering Physics Institute), Moscow, Russia

Abstract. Muon diagnostics is a new direction in the development of the global environment observation system based on the analysis of variations of the penetrating component of cosmic rays. The approach is based on the simultaneous detection of muon fluxes from all directions of the upper hemisphere (hodoscopic mode). It allows to get an overall picture of the processes in the upper troposphere, as well as to follow the dynamics of their changes, in particular, to identify disturbed areas, to determine the direction and the speed of their movement, and to estimate the time of their appearance in a given point. The method is sensitive to large-scale atmospheric processes, as well as to the rapidly changing local phenomena and, in addition, allows to explore the characteristics of wave processes, generated by strong turbulent events, including potentially dangerous (storms, squalls, tornadoes, hurricanes, etc.). Method of muon diagnostics has been implemented with the wide aperture muon hodoscope (MH) URAGAN with a high spatial and angular accuracy, which was constructed in MEPhI. In the paper, a short description of MH URAGAN is given and the results of investigation of various atmospheric processes are discussed

1. INTRODUCTION

The Earth's atmosphere is an open system, in which the basic processes are regulated by the activity of the Sun. Also, the atmosphere is irradiated by cosmic rays (of solar, galactic and extragalactic origin) which are the main source of ionization in air. The changes of global climate, the growth of the number of atmospheric phenomena of a catastrophic character stimulate the development of systems for early observation of meteorological hazards. This is a problem not only for the atmosphere, but also for the near-terrestrial space, since existing satellite monitoring system for space weather does not carry out remote scan and is located either at the Lagrange point (ACE, SOHO) [1,2], or at certain low-Earth orbit (GOES) [3]. Primary cosmic rays are a constant source of penetrating radiation that reach the Earth's surface, and contain information about the state of near-Earth space and the Earth's atmosphere.

Along with the integral modulation of muon flux at the Earth's surface - the barometric and temperature effects - there are more sophisticated modulation mechanisms of ground level muon flux associated with the proliferation of various waves in the upper atmosphere, which are generated during the formation of cells of turbulence - future hurricanes and tornadoes.

Creating a global network of neutron monitors, the formation of the world's data centers [4] made it possible to analyze variations of cosmic rays simultaneously recorded in different parts of the globe. Important information also can be obtained from measurements of variations of muon flux of cosmic rays by muon telescopes. However, variations of cosmic rays of geophysical origin are considered as an undesirable factor which should, if possible, be excluded from the physical analysis. A new type of detectors is large area muon hodoscopes able to simultaneously detect muon fluxes from any direction of the entire celestial hemisphere in real time mode. Creating of large area precise muon hodoscope URAGAN [5,6] was the basis for the development of the muon diagnostics - a new method of remote monitoring based on the simultaneous registration of the muon flux from all directions in order to study dynamic processes in the near-terrestrial space and the Earth's atmosphere.

The physical principle of the muon diagnostics of the atmosphere consists in a close connection of various atmospheric phenomena with processes of generation and propagation of muons in the atmosphere [7, 8].

2. MUON HODOSCOPES

Practical realization of the muon diagnostics requires a new type of detectors - muon hodoscopes, which should provide real-time simultaneous registration of muon fluxes from all directions in the frame of the aperture (up to 80° in zenith angle), have a high angular accuracy ($<1^\circ$) and a large area ($> 10 \text{ m}^2$) to provide the required statistical accuracy of the data in all angular directions. Unlike muon telescopes which detect particles that come in some solid angle at a certain zenith angle, muon hodoscopes reconstruct tracks of every registered muon in real-time. Therefore, its aperture is continuous within all directions of the upper hemisphere. This makes it possible to study angular variations of the muon flux from all available directions. The first in the world large area muon hodoscope URAGAN [6, 7] is currently operating at the National Research Nuclear University MEPhI in Moscow (55.7° N , 37.7° E , 173 m a.s.l.). It is a coordinate-tracking detector, which detects muon flux at the Earth's surface in a wide range of zenith angles ($0-80^\circ$) with a high angular resolution ($\sim 1^\circ$) and is able to study the variations of the angular distribution of the muon flux caused by atmospheric and extra-atmospheric processes and detected in real time-mode. The range of the detection threshold energies is 0.2 to 0.6 GeV . URAGAN consists of four independent supermodules (SM). Each SM (Figure 1) represents an assembly of eight layers of streamer tube chambers consisting of discharge tubes with size $9 \times 9 \times 3500 \text{ mm}^3$ enclosed in one plastic container with 16 pieces in each. Every layer contains 320 tubes with an external two-coordinate X-Y strip readout system. The sensitive area of the one SM is $\sim 10.5 \text{ m}^2$.



Figure 1. The muon hodoscope URAGAN. In the foreground one of the supermodules is seen. On the left and behind, the other three SM can be seen.

Exposure process is divided into equal one-minute intervals within which monitoring of detection channels (2 s) and the actual detection (~58 s) are carried out. Thereby, total operational "live" time is the sum of actual detection time fractions of all one-minute intervals of measurement exposition except intervals of traffic of one-minute frame data. The fraction of events with reconstructed tracks is ~ 91 % of the total intensity of 1700-1900 triggers per second. Synchronization of all SMs operation is provided by GLONASS /GPS [9].

3. DATA FORMAT

The angular distributions of the tracks detected during 1 minute intervals are stored in three types of binary arrays-matrices with dimensions 91×91 cells: by zenith and azimuth angles, $M_a = [\theta_i, \varphi_j]$, by projection angles, $M_{pa} = [\theta X_i, \theta Y_j]$ and tangents of projection angles $M_{tg} = [tg\theta X_i, tg\theta Y_j]$. The sequence of such matrices gives unique possibility to study the temporal changing of muon angular distributions. Depending on the analysis to be performed, matrices can be collected in different time intervals Δt . For the study the dynamics of rapidly developing atmospheric processes that cause variations in the intensity of muons, five-minute matrices are analyzed.

As a quantitative characteristics of the muon flux angular variations in a real-time, a vector of local anisotropy A is used. A is the sum of the unit vectors of particle tracks, normalized by the total number of tracks [9]. Starting from the angular distribution matrices M_a , the projections (A_S , A_E , A_Z) and the length A of the anisotropy vector A are calculated as [9]:

$$A_x = \frac{1}{N} \sum_{\theta} \sum_{\varphi} M_a \cos \varphi \sin \theta ,$$

$$A_y = \frac{1}{N} \sum_{\theta} \sum_{\varphi} M_a \sin \varphi \sin \theta ,$$

$$A_s = A_x \cos \varphi_0 + A_y \sin \varphi_0 ,$$

$$A_e = -A_x \sin \varphi_0 + A_y \cos \varphi_0 ,$$

$$A_z = \frac{1}{N} \sum_{\theta} \sum_{\varphi} M_a^{cor} c \cos \theta ,$$

$$A = \sqrt{A_s^2 + A_e^2 + A_z^2} .$$

where A_x and A_y are projections of the vector A in the laboratory coordinate system, A_s is the projection on the North-South axis and A_e is the projection on the West-East axis; A_z is the vertical component; $\varphi_0 = 34.726^\circ$ is the azimuth angle between the local and geographic coordinate systems; θ , φ are zenith and azimuth angles at the middles of the cells of the matrix M_a ; N is the total number of events in the analyzed range of angles ($\theta = 0 \div 75^\circ$, $\varphi = 0 \div 360^\circ$); $N = \sum_{\theta} \sum_{\varphi} M_a$; $N^{cor} = \sum_{\theta} \sum_{\varphi} M_a^{cor}$, M_a^{cor} is the corrected for atmospheric pressure matrix M_a . Additional real-time information is the difference between the current anisotropy vector A and its mean value \bar{A}_N , calculated from the previously accumulated data. The relative anisotropy vector can be defined: $r = A - \bar{A}_N$. The horizontal projection of this vector: $r_h = \sqrt{r_s^2 + r_e^2}$ indicates the side shift of the angular distribution of the muon flux.

4. MUONOGRAPH

Muonograph is a graphical representation of the matrix of variations of the angular distribution of the counting rate over the last 5 minutes (current matrix) with respect to the normalization matrix the preceding 24 hours in statistical error units [9]. Data from SMs are used to form different types of muonographs: non-smoothed, smoothed with a Gaussian filter, corrected to the shape of the angular distribution (a bell shape), and in the East–North coordinate system. If the current and normalization angular distributions are approximated using a function in the form $C \cos^{\alpha} \theta d\Omega$ and (C , α) and (C_N , α_N) coefficients are obtained, respectively, the shape of the normalization distribution can then be matched to the shape of the current distribution. The bell shape is corrected in order to improve image resolution when there are relatively high variations in the current and normalization counting rates.

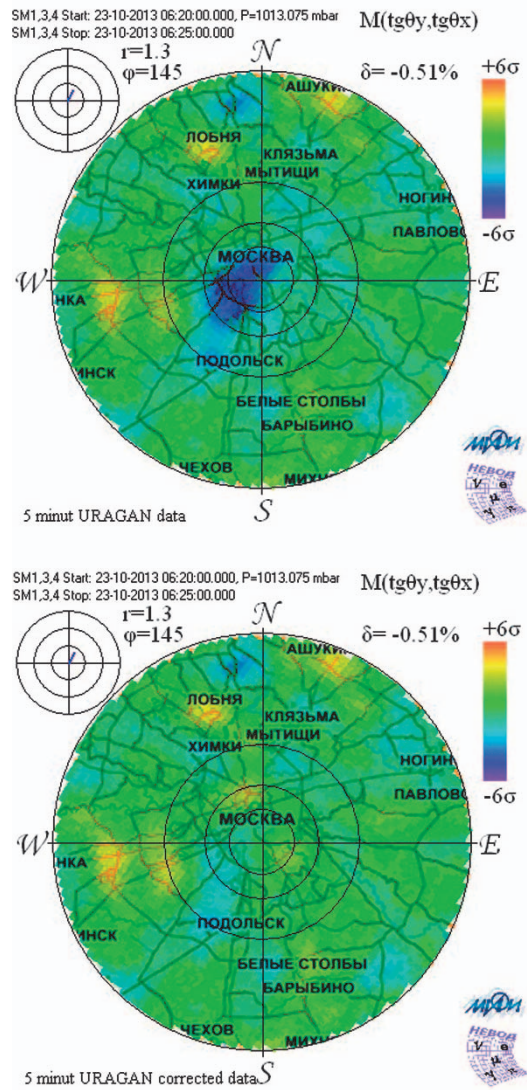


Figure 2. An example of a smoothed 5-minute matrix of changes of the angular distribution of the detected particle flux in terms of statistical errors. Down: without correction on the shape of the angular distribution; right: with correction.

For formation of a muonograph, five-minute series of matrices M_{tg} are used. To apply a "muon snapshot" to the local map, from the point of the detector location in directions corresponding to cells of the angular matrix, straight lines, are drawn and the points of intersection of these lines with the level of generation of muons (16 km) are determined. After that, the points of intersection are projected onto the surface of

the Earth. Thus, the position of the angular cell on the map is a projection of the spatial region in which muons were generated and detected in this cell.

An example of such an image is shown in Figure 2, where one of the images represents 5-minute matrix without correction on the shape of the angular distribution, and the other with correction. The figure displays: δ , a change in the counting rate in %; r , value r_{h5m} ; φ – the azimuth direction of the vector r_{5m} in degrees (0 – direction to the South, 90° – direction to the East). Top left, inside of the small circle with radii, 2 and 3 (in units of $\sigma_{tat}(rh5m)$), the length and direction of the horizontal projection of the vector r_{5m} are displayed.

5. MONITORING OF VARIOUS ATMOSPHERIC PROCESSES

For comparison and correlation analysis of characteristics of muon flux variations at Earth's surface with various large-scale and local meteorological processes in the area of muon hodoscope location, the weather history was used, which was formed on the basis of weather data from several independent sources of information available at the various internet sites and the results of the processing of synoptic maps and satellite images.

6. MONITORING OF LARGE SCALE BARIC FORMATIONS PASSING OVER MOSCOW

Large baric formation, such as cyclones and anticyclones, are convenient atmospheric phenomena to explore the possibilities of URAGAN hodoscope to implement the monitoring of the atmosphere over the Moscow region. To find regularities which connect angular variations of muon flux and parameters of cyclones and anticyclones movement, the anisotropy vector projections A_S and A_E are used.

With arriving of large baric formation, the flux of muons is changed and therefore the vector of anisotropy is changed, too: on the arrival of an anticyclone, the length of the vector of local anisotropy decreases and with the arrival of the cyclone increases. However, at considering of projections it is needed to take into account the direction of muon flux arrival. Figure 3 shows the projections of A_S and A_E for anticyclone (a) and the cyclone (b), which came from the same direction (from the West).

The behavior of the average values of the projections is shown by broken lines. When anticyclone is coming, the projection of anisotropy vector in the eastern direction A_E increases due to the fact that the flux of muons from the western direction is reduced; therefore, the anisotropy vector deviates in the opposite (east) direction. When cyclone is coming, the opposite process occurs. At the same time, the projection to the southern direction A_S does not change (only visible diurnal variation), since in this direction muon flux is not changed.

Figure 4 shows the comparison of the periods of passages of large-scale atmospheric processes over the location of the URAGAN hodoscope and of variations of muon flux registered in July 2009. The year 2009 was chosen because of low solar activity, corresponding to the solar cycle minimum. Periods of the passage of baric formations (cyclones and anticyclones) over the Moscow region were selected. List of cyclones and anticyclones was based on the analysis of synoptic maps.

In the figure 4 blue areas shaded with line correspond to the periods of cyclones, red areas, shaded crosswise, to anticyclones. The pressure and muon counting rate series are also given. The graphs clearly show that when a cyclone

arrives the muon counting rate increases due to the pressure decreasing. When a cyclone starts to go away, the pressure starts to increase and the counting rate of the muons falls. With the passage of the anticyclone, there is a inverse process: firstly the counting rate falls due to rising pressure, and when the anticyclone leaves, the pressure falls, and the rate of muon registration increases.

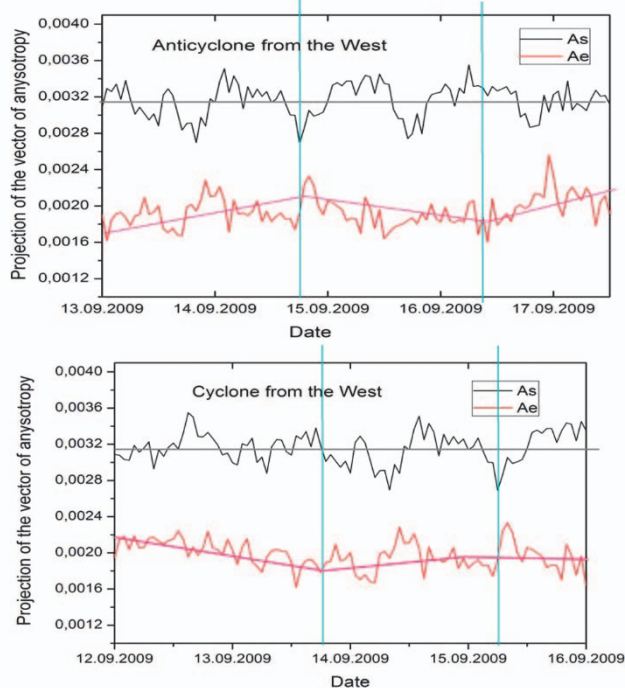


Figure 3. Variations of the projections of the local anisotropy vector A_S (black curve) and A_E (red curve) during the passage of the anticyclone (a) and cyclone (b) from the West to the East (marked by blue vertical lines). Broken lines indicate the behavior of observed average value.

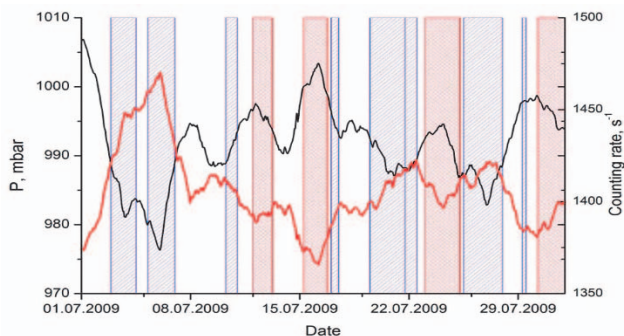


Figure 4. Variations of the muon flux (red line) and behavior of the atmospheric pressure (black line) during the passage of baric formation, July 2009. Blue areas: periods of the passage of cyclones. Red areas: periods of the passage of anticyclones.

7. MONITORING OF ATMOSPHERIC FRONTS PASSING OVER THE MOSCOW

Atmospheric fronts represent adjacent air masses separated by a relatively narrow transition zones, strongly inclined to the Earth's surface. In cold fronts, air masses flow like a wedge under the warm air, forcing it to traverse up along the separating surface.

In this case, cold air undergoes friction on the Earth's surface, and its lower layers are behind the upper, which leads to the steepening of the front surface. When warm front comes, it moves above of a wedge of cold front and goes up along this wedge, adiabatically cooled during this movement.

On the basis of data obtained with the muon hodoscope URAGAN, the correlations of parameters of the integral muon flux and anisotropy of the angular distribution of the muon flux during the passage of fronts over the Moscow

region in the period 2010 - 2011 were studied. The list of atmospheric fronts was formed on the basis of analysis of synoptic maps. In Figures 5 – 8, the correlations between temperature and atmospheric pressure and characteristics of registered muon flux variations during the passage of cold and warm fronts are presented.

From the analysis of the distributions it follows that the muon counting rate anti-correlates well with pressure and temperature in the case of cold and warm fronts. Parameter A (the magnitude of the anisotropy vector) anti-correlates with pressure and has a good correlation with temperature in the case of cold fronts. For the warm fronts the dependence is less certain.

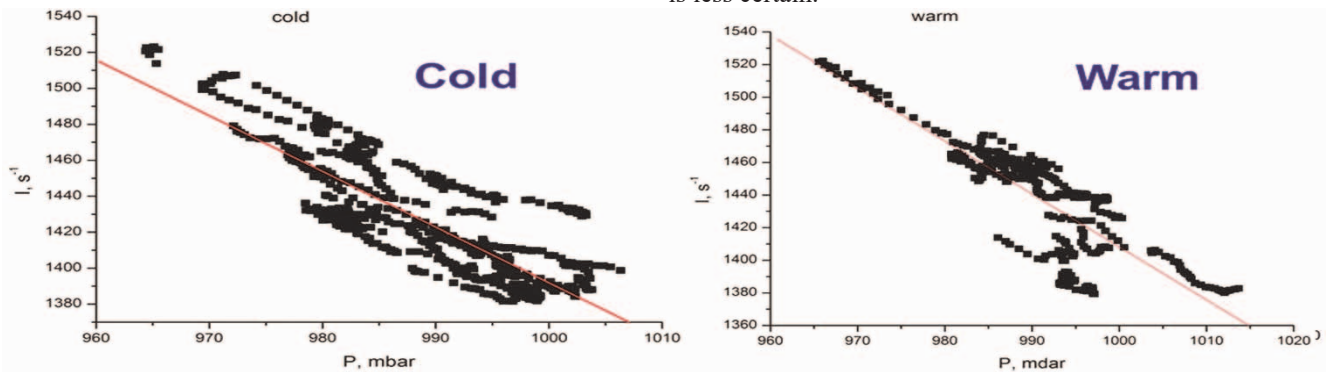


Figure 5. The dependence of the integral counting rate of MH URAGAN on atmospheric pressure during the passage of fronts over the Moscow region. Left: cold fronts; right: warm.

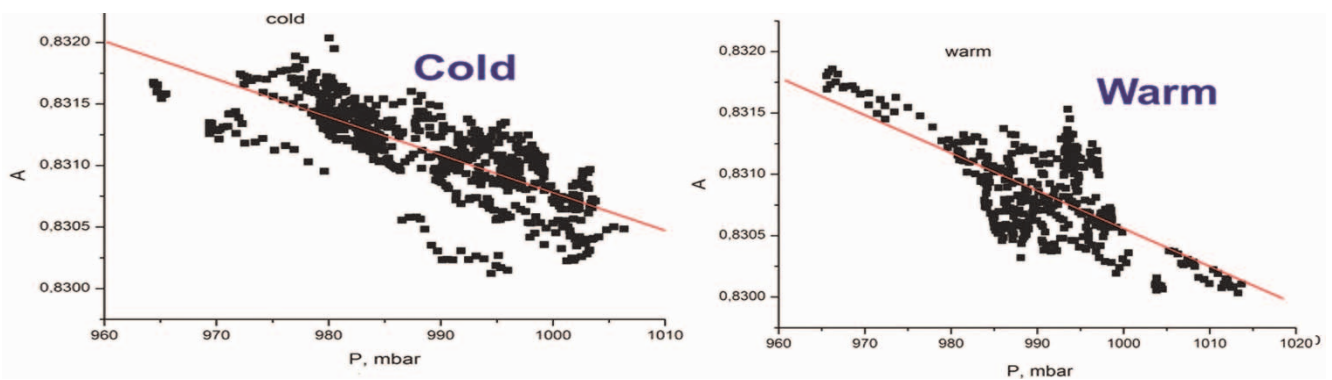


Figure 6. The dependence of the length of the vector of anisotropy of muon flux detected by MH URAGAN on atmospheric pressure during the passage of fronts over the Moscow region. Left: cold fronts; right: warm.

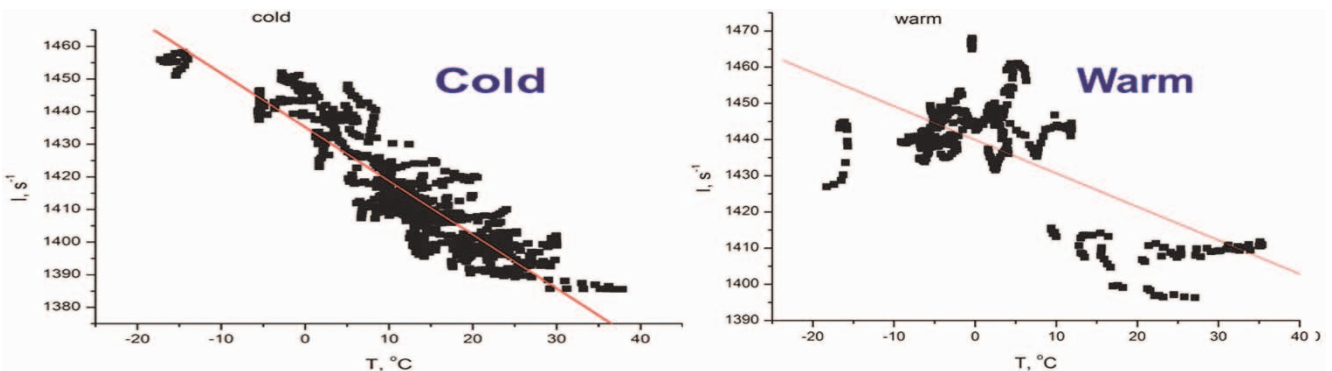


Figure 7. The dependence of the integral counting rate of MH URAGAN on surface temperature during the passage of fronts over the Moscow region. Left: cold fronts; right: warm.

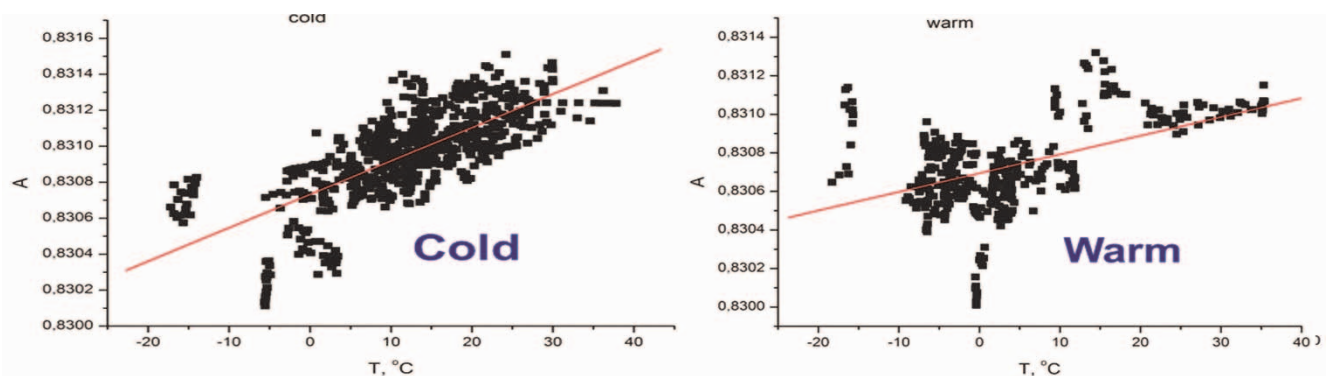


Figure 8. The dependence of the length of the vector of anisotropy of muon flux detected by MH URAGAN on surface temperature during the passage of fronts over the Moscow region. Left: cold fronts; right: warm.

8. MONITORING OF THUNDERSTORMS

The study of rapidly changing non-stationary processes of a local origin in the atmosphere, in particular the powerful thunderstorms, are a very important task of muon diagnostics. The earlier performed analysis of URAGAN data obtained during observation of thunderstorms passing over Moscow in summers 2009 and 2010 indicated promising perspectives of application of cosmic ray muons as a tool for monitoring and forecasting of atmospheric

phenomena [10]. The useful opportunity to test of the approaches based on muon diagnostics appeared in connection with the development in Russia of the technology of application of Doppler radar for the meteorological purposes. Spatial and angular parameters of the muon flux detected by the URAGAN muon hodoscope during thunderstorms in Moscow area in 2014 and 2015 were analyzed together with data of the DMRL-C Doppler weather radar (Russian Federal Service for Hydrometeorology and Environmental Monitoring) [11].

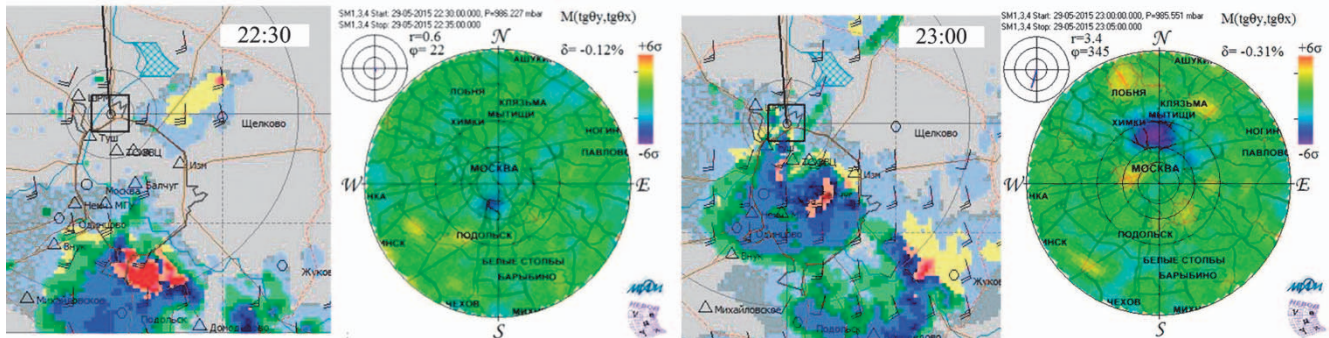


Figure 9. Maps of radiolocation observations using Doppler weather radars (on the left) and muonographs (on the right) at moments 22:30 and 23:00 UTC for the thunderstorm occurred on May 29, 2015.

Radio locator determines the radio beam reflectivity from various hydrometeors (droplets, snowflakes, etc.). According to the arrival time and intensity of returned radiation, various meteorological parameters which are then used in the synoptic practice are calculated. Instrumental range of radio beam is 250 km, maximum detection height is 20 km. Zenith angle range is from 0.1° to 86° . Operating frequency range of DMRL-C is from 5.6 to 5.65 GHz. Locator performs cyclical monitoring with a period of 10 minutes in a 24-hour automated mode and provides data with high spatial resolution (0.5 - 1 km) on the area of 200 thousand sq. km. The information obtained with a locator is in the form of 3D maps of radiolocation observations (maps of events). For the analysis, information collected by DMRL-C Doppler weather radars at Moscow's Vnukovo and Sheremetyevo airports was used.

Analysis of storm phenomena according to URAGAN and DMRL-C data includes several basic steps:

1. analysis of the situation in the heliosphere and magnetosphere;
2. study of the meteorological situation;
3. visual comparison of meteorological maps and muonographs;
4. study of muon flux integral characteristics;
5. study of temporal characteristics of muon flux relative anisotropy;
6. study of muon flux azimuthal distributions, including in geographical directions.

The analysis of the DMRL-C Doppler weather radar data and additional meteorological sources for the period 2014–2015 allowed to select 71 thunderstorm events detected in the Moscow region. Rejection of disturbances caused by the solar activity in the interplanetary and terrestrial magnetic fields, reduced the number of thunderstorms for the physical analysis to 47 [12]. These events were classified according to their meteorological parameters: atmospheric fronts (warm, cold, occluded, no front); types of thunderstorm cells (single- and multi-cell); intensity of precipitation; velocity of air mass motion; altitudes of the tropopause and the upper boundary of cloudiness. For each thunderstorm event, maps of

radiolocation observations and muonographs were visually compared, and the behavior of the characteristics of muon flux and different meteorological parameters were estimated.

Figure 9 shows maps of observations made with the DMRL-C Doppler weather radars and muonographs of the event that occurred on May 29, 2015, (22:30–23:10). This thunderstorm was classified as single-cell against the background of a warm atmospheric front. Maps are presented for two moments in time: approaching of the thunderstorm to the location point of the hodoscope (22:30) and the passage of the thunderstorm over the hodoscope (23:00). Areas that corresponds to the thunderstorm (on the left) and to the area of deficit of muon flux (on the right), are heavily shaded in the maps. The figure shows that when thunderstorm came and passed over, a prior reduction of the muon flux was observed, which can be explained by the movement of the area of high pressure ("pressure nose") before the storm.

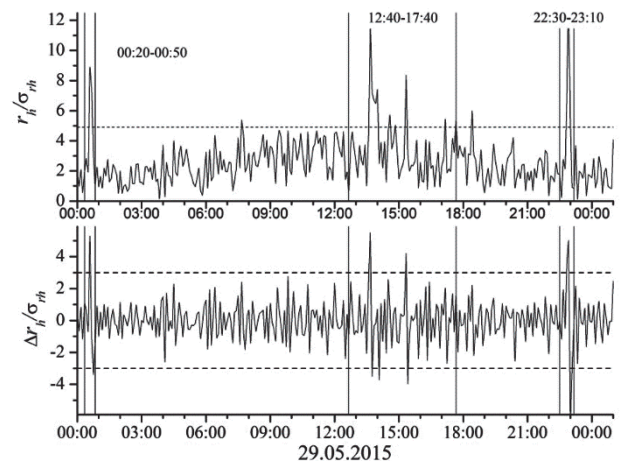


Figure 10. Time dependence of parameters r_h/σ_{rh} and $\Delta r_h/\sigma_{rh}$ on May 29, 2015.

Figure 10 shows variations in parameters r_h/σ_{rh} and $\Delta r_h/\sigma_{rh}$ during the day of May 29, 2015. In addition to the thunderstorm shown in Figure 9, there were two other thunderstorm events on May 29, 2015, at 00:20 and 12:40 (the periods are marked by vertical lines). From the figures, sharp variations in the anisotropy parameters of the muon flux during thunderstorms are clearly seen. The maximum value of

r_h/σ_{r_h} is 8.8 for the thunderstorm occurring at 00:20–00:40; for the thunderstorm occurred at 12:40–17:40, $r_h/\sigma_{r_h}=11.8$; and for the thunderstorm occurred at 22:30–23:10, $r_h/\sigma_{r_h} = 13.4$. The rate of anisotropy variation for these events is $\Delta r_h/\sigma_{r_h} > 5$.

The parameters of the muon flux anisotropy (r_h, r_s, r_E) are more sensitive to atmospheric disturbances which generally allow the identification of thunderstorm with an efficiency of about 70%. If thunderstorm is accompanied by warm and cold fronts, its identification efficiency is more than 80%. During the passage of thunderstorm over the URAGAN, it can be identified using not only r_h but also the rate of its variation (Δr_h) which efficiency is about 85%.

Finally, the efficiency of thunderstorm phenomena registration with the MH URAGAN was estimated using the variations in the characteristics of the muon flux with different meteorological parameters for all 47 selected thunderstorms

With anisotropy parameters $r_h, r_s,$ and $r_E,$ the hodoscope URAGAN provides identification of thunderstorm events occurring in its vicinity with an efficiency of $\sim 70\%$. If a thunderstorm event is accompanied by warm and cold fronts, the average efficiency becomes greater than 80%. When a thunderstorm is passed above the URAGAN muon hodoscope, it is possible to use the rate of its variation Δr_h in addition to projection r_h to identify the event, that make it possible to raise the efficiency of detection to $\sim 85\%$. The comparison of the muon flux parameters and the velocity of air mass motion shows that anisotropy appears more frequently at high velocities than at low velocities. Muon flux anisotropy is observed at tropopause altitudes higher than 10.5 km and cloudiness upper boundaries of more than 9.5 km. This is in good agreement with the altitude of muon generation in the atmosphere (from 10 to 20 km).

CONCLUSION

The use of cosmic ray muons as the penetrating radiation, and muon hodoscopes as peculiar tool to make "muon snapshots" of the atmosphere and near-terrestrial space, gives a unique possibility to locate disturbed areas and to trace the dynamics of their development and direction of movement. The analysis of data obtained with the muon hodoscope URAGAN at detection of various atmospheric processes demonstrated its ability to reveal active atmospheric phenomena on the basis of the analysis of variations of various characteristics of muon flux (integral counting rate, zenith-angular anisotropy, wave parameters). Variations in the characteristics of the muon flux, represented by 5-minute data, are mainly due to the atmospheric causes. Cyclones (anticyclones) cause clear identifying reaction in a flux of cosmic-ray muons in the integral intensity as well as in the zenith-azimuthal distribution. The influence of atmospheric fronts has a more

complex character, and the analysis of variations of muon flux related with atmospheric fronts requires taking into account additional meteorological information. However, to obtain quantitative evaluations concerning large scale atmospheric processes, each case of passing of the pressure atmospheric formation over the Moscow region should be carefully studied with the involvement of additional meteorological information.

ACKNOWLEDGMENT

The work was performed at the unique NEVOD experimental complex. It was supported by the RF Ministry of Education and Science (government task).

REFERENCE

- [1] <http://www.srl.caltech.edu/ACE/>
- [2] <https://sohowww.nascom.nasa.gov/>
- [3] <http://www.goes.noaa.gov/>
- [4] <http://www.nmdb.eu/>
- [5] D.V. Chernov et al., "Experimental setup for muon diagnostics of the Earth's atmosphere and magnetosphere (the URAGAN project)", Proc. 29th ICRC (Pune), 2005, 2, pp. 457-460.
- [6] N.S. Barbashina et al., "The URAGAN wide-aperture large-area muon hodoscope", Instrum. Experim. Techn., 2008, 51, 2, pp. 180-186.
- [7] D.A. Timashkov et al., "Muon diagnostics of the Earth's atmosphere, near-terrestrial space and heliosphere: First results and perspectives", Proc. 30th ICRC (Merida), 2007, vol. 1, pp. 685-688.
- [8] I.I. Yashin et al., "Muon diagnostics: present status", Bull. Russ. Acad. Sci.: Phys., 2013, 77, 5, pp. 554–557.
- [9] I.I. Yashin, et al., "Real-time data of muon hodoscope URAGAN", Advances in Space Research, 56, 12, 2015, pp. 2693-2705.
- [10] A.S. Mikhaylenko et al., Bull. Russ. Acad. Sci.: Phys., 2011, 75, 6, pp. 827–830.
- [11] Yu.B. Pavlyukov et al., "Vremennye metodicheskie ukazaniya poispol'zovaniyu informatsii doplerovskogo meteorologicheskogo radiolokatora DMRL-S v sinopticheskoi praktike (Provisional methodology guidelines for the use of the DMRL-S Doppler meteorological radar data in synoptic practice)", Moscow, 2014. <http://map.meteorad.ru/static/VMU-DMRL-140701.pdf>.
- [12] N.S. Barbashina et al., "Muon flux variations detected by the URAGAN muon hodoscope during thunderstorms" Bull. Russ. Acad. Sci.: Phys., 2017, 81, 2, pp. 230–233

Muon Telescope Planned for Operation in Israel Cosmic Ray Observatory on Mount Hermon

L. Kozliner^{1,3}, L. Pustynnik^{1,2}, D. Shtivelman¹

1. Cosmic Ray Center of Tel Aviv University, Israel,

2. Shamir Research Institute, Israel,

3. Yerevan Physics Institute, Armenia

Abstract. The results of observation of the muon component of cosmic rays give us information on the direction of primary cosmic rays; this is essential for the study of cosmic-ray anisotropy and cosmic ray propagation from solar flares. In this report, we propose a program for construction of a muon telescope in the Cosmic Ray Observatory on the Mount Hermon, Israel, and present specific details of its registration system.

1. INTRODUCTION

The cosmic rays observed at the Earth's surface have different components. The first component is represented by high-energy, 10^9 - 10^{20} eV, cosmic rays that penetrate the solar system from outside, from the Galactic space. Its sources are explosions of Supernova stars [1]. Due to Galactic magnetic fields, these high-energy particles get scattered and change their direction at random. As a result, the cosmic ray propagation in the Galaxy is diffusive by nature. So, one should forget about identifying the primary sources of these particles as they enter the solar system as an almost isotropic flux. This property of cosmic rays is opposite to the angular distribution of the electromagnetic emission from the same supernovas and their remnants observed as points or local extended sources on the sky. The second component of the observed cosmic rays [2] is solar cosmic rays - sporadic cosmic rays caused by acceleration in sporadic solar flares. The energy of solar cosmic rays is relatively lower than that of the galactic component (10^6 - 10^{10} eV). These particles scatter on the magnetic inhomogeneity of the solar wind and their distribution is anisotropic for a short time, but in the first ten minutes after ejection, the scattering is not too effective and the diffusion is anisotropic either. Another possible source of cosmic rays with low-amplitude anisotropy is the scattering of galactic cosmic rays that penetrate the solar system primarily from outside the heliosphere. These particles are scattered on regular magnetic field of shock wave on the head of massive coronal mass ejection, propagated in solar wind from solar flare to the Earth.

The basic piece of equipment of a standard cosmic ray observatory is a set of neutron detectors (monitors or super monitors) that detect secondary neutrons – the product of the nuclear reactions of primary high-energy cosmic ray particles at their propagation through the Earth's atmosphere [1]. Neutron monitors are optimal instruments for the study of temporary cosmic ray variations caused by their interaction with the atmosphere, magnetosphere and the solar wind. However, they cannot measure the cosmic ray flux distribution on the sky as they integrate the intensity of cosmic rays coming from all directions. In principle, by combining all neutron monitors existing on the globe into an international network it is possible to obtain the distribution of the cosmic ray flux detected at different stations and from different directions in the sky. It would make it possible to restore the primary anisotropy, partly preceded by the impact of coronal mass ejection on the Earth.

As opposed to neutron monitors, muon telescopes use two sets of scintillators (top and bottom) with a system of registration of coincidence events in both. Such technique gives the observer the secondary cosmic ray muon arrival directions. By muon observations, one can restore the angular distribution of cosmic rays in the sky and measure the angular anisotropy of primary cosmic rays [3]. So most of the cosmic ray observatories in the world supplement the standard neutron monitors in their station with a complex of muon telescopes.

In this report, we propose a program for construction of a muon telescope in the Cosmic Ray Observatory on the Mount Hermon, Israel [4], and present specific details of its registration system.

2. USE OF AMPLITUDE ANALYZER

Charged particles passing through the scintillator create in him photons of light. This light is recorded photomultiplier (PMT) tube and converted into electrical impulses. The PMT output pulse amplitude is proportional to the energy deposited by the particle in the bulk of the scintillator; this is why ADCs are used. ADCs are necessary for separation of useful pulse from noise, for adjustment of electronic channels and other tasks. However, the high cost of ADCs is a serious hindrance to their use in government-funded experiments. Analyzers capable to operate at 5-10 MHz cost several thousands of dollars and it is, as a rule, impossible to purchase them. Cosmic ray experiments deal with relatively low fluxes. For instance, the intensity of a vertical flux of charged particles at the sea level is 110-150 particles/m²·sec. The count rate for our used 0.5×0.5m² scintillators should be 30-40 particles per second. Considering this fact, we have designed and made a stretcher unit, which employs the technique of the pulse amplitude's conversion into a time interval and a code [5], which makes it possible to measure pulses with a width of 20-200 nsec and amplitude from 20 mV to 5.0 V. The unit is compatible with standard NI PCI- 6221B 16-Bit, 250kS/s, 16 Analog Inputs ADC that costs a few hundred dollars (<http://sine.ni.com/nips/cds/view/p/lang/en/nid/14132>). The operating frequency of the ADC we used is 250 kHz for one channel and 125 kHz for two channels. The data acquisition and registration program for that device has been written at LabVIEW 2014. Use of two analyzer channels makes it possible to measure the noise and the wanted pulse signals as well as to compare and analyze the registered amplitudes.

3. PRINCIPLE OF OPERATION OF THE STRETCHER UNIT

The positive pulses from the preamplifier (1) assembled on the PMT base, are fed to the amplifier A1. Further the output signal is integrated in the R5C2(2) chain and then the pulse widens 2-3 times (3) but its amplitude reduces in proportion with the pulse energy. After the second amplifier stage, the signal through the high-frequency diode V1 is fed to the selection and storage circuit C4, D4.1, A-3.1(4). Pulse storage authorization is granted based on the threshold, which can be adjusted in a wide range by the potentiometer R11 on the comparator. When the set threshold is overshoot, the capacitor C4 is charged. To ensure signal registration, the storage time should exceed 10 μ sec in order to keep the

signal for 11 μ sec. At the same time, this signal is fed to the programmable functional input (PFI0) of ADC NI PCI-6221B and triggers its internal counter. When two channels are used, the ADC operating rate is 100 kHz, i.e. the inner counter's rate is 10 μ sec. In such case, the triggering pulse width varies within 15 and 32 μ sec. This is necessary to ensure full discharge of capacitor C4. After the signal passes through the unit and is read by the ADC, capacitor C4 is zeroed and the circuit is ready to register the next PMT signal. The key D4.1 ensures resetting. The threshold unit of comparator D1 and univibrator D2 are used to control this key. Figure 1 shows the simplified circuit diagram of our designed unit.

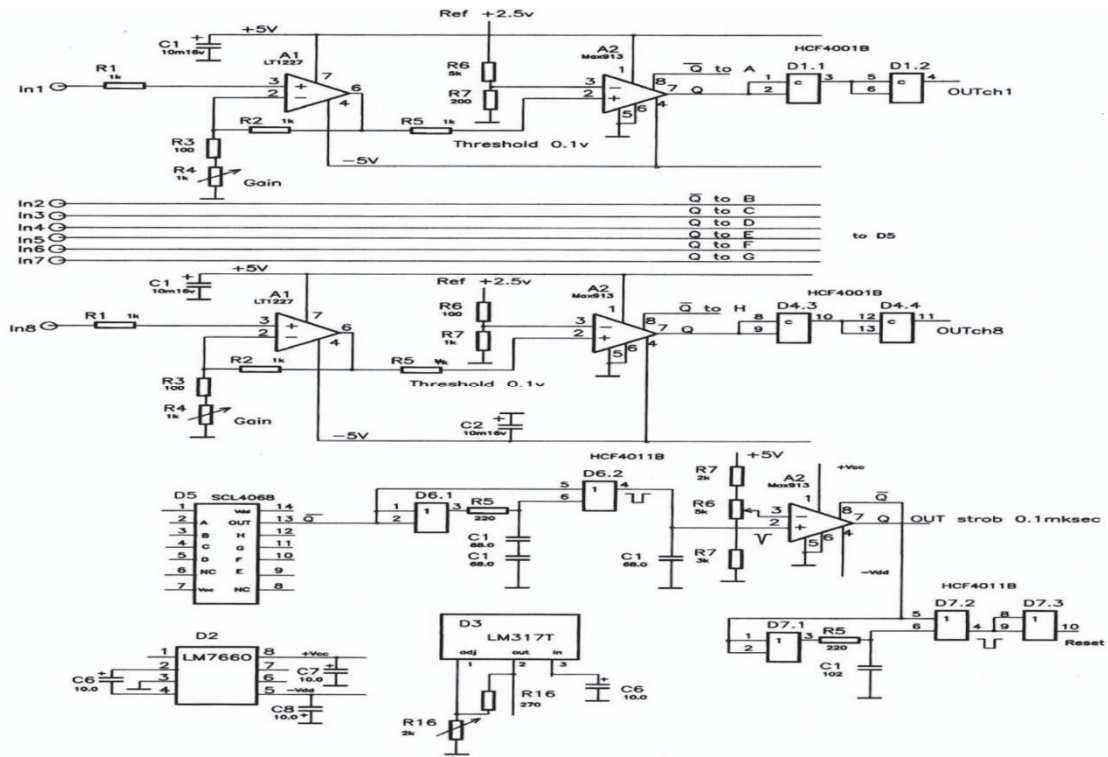


Figure 1. Circuit diagram of our designed unit.

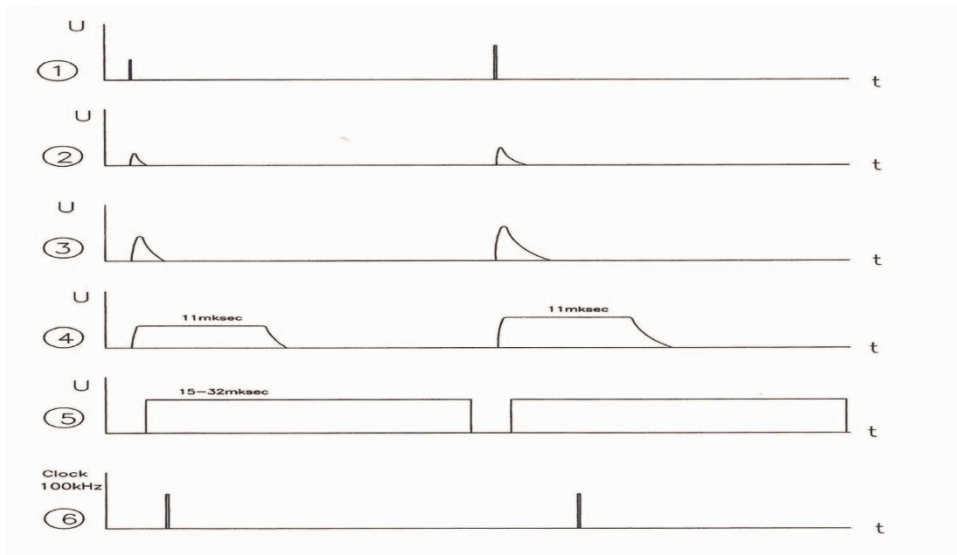


Figure 2. The shapes of the signals taken at the designed unit's check points.

- (1) pulse signals on the input.
- (2) amplifier signal after the first integrating circuit.
- (3) amplifier signal after the second integrating circuit.
- (4) signal on the selection and storage circuit's capacitor C4.
- (5) window of authorization for reading out of the signal.
- (6) pulses of NI PCI-6221B ADC's internal counter.

As the input (PFI0) of ADC cannot tolerate pulses with amplitudes higher than 5 V, the output signal of the stretcher unit is fed through the divider R38-R39, ensuring the required voltage.

Figure 2 shows the shapes of the signals taken at the designed unit's checkpoints.

The technique offered for the measurement of pulses with the help of a stretcher unit and an ADC permits to measure the PMT pulse amplitudes from 0.02 to 5.0 V at a rate of 30 kHz. The results of our measurements give an idea what blocks in what configuration should comprise the electronics of the muon telescope to be constructed.

4. TECHNICAL DETAILS OF THE MUON DETECTOR SET UP AT HERMON OBSERVATORY.

The scintillation spectrometer for registration of the muon component of cosmic rays is designed to work with the neutron monitor set up at 2000 m asl on the Mount Hermon. The main aim of the complex is registration of cosmic ray muons at different zenith angles. Specific of our registration system is the use of QUANTOCHRON – registration of each

flash event in each scintillator by detecting both the number (location) of element and time of registration of the flash with maximal high time accuracy (in our case it is 100 nanoseconds). In such manner, one can save the primary information about all events in the computer memory with a following real time identification of coincidence of different events and restoration of their angular distribution.

The QUANTOCHRON approach can be useful in studying the ultrafast processes of particles acceleration in the electric field of atmospheric discharges [6,7] – a problem studied very intensively in the last years and discussed during TEPA-2016 symposia.

The scintillation detectors are arranged so as to ensure the best possible amplitude and time resolution of the detectors. The choice of the shape and material of the detector housing were limited by the space between the floor and the bottom of the neutron monitor where the muon detectors were to go. With regard to the size of scintillator blocks (50×50×10 mm³), the housings were made of 2 mm thick sheet of aluminum shaped into 730×540×100 mm³ rectangular boxes (Figure 3)

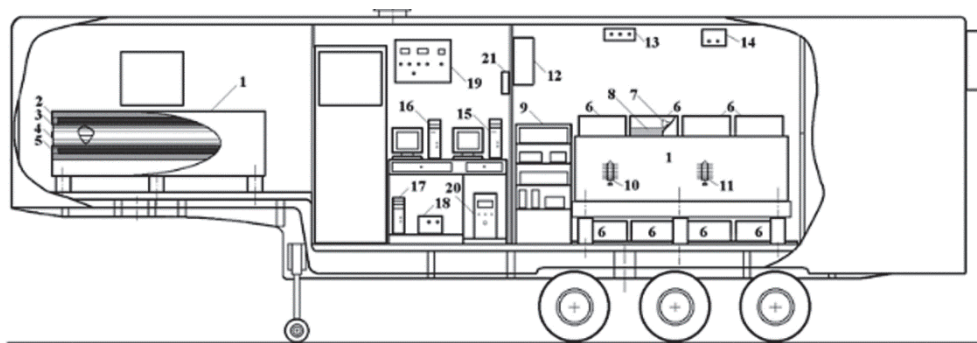


Figure 3. 1 – neutron monitor, 6 – boxes of muon telescope with scintillators and PMT

The electronics was designed for direct monitoring of the time of arrival of signal from each detector. Figure 4 shows the complex during laboratory testing.

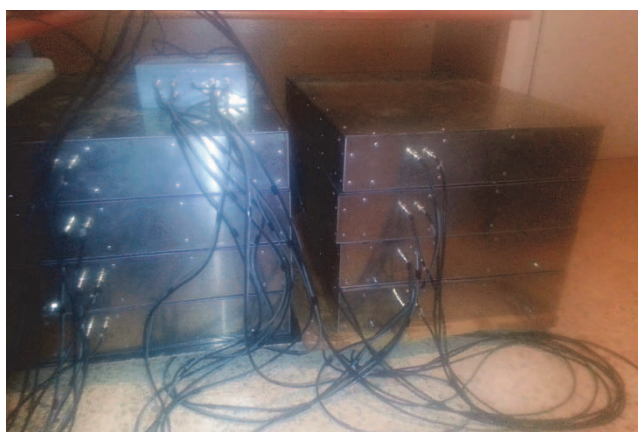


Figure 4. Testing of muon telescope detectors in laboratory.

Using QUANTOCHRON, we obtain from all flashes from all detectors two parameters: t_i – time moment of the flash with high time accuracy (at least 1 microsecond) and n_i – number (coordinate) of scintillator. This registration principle differs from the standard one, when the observer accumulates a number of different directions of the cosmic rays having arrived during a chosen time interval. In the standard approach, all information about individual pulses (flashes) during that time interval (time resolution) is lost and cannot be restored. In our approach, we save all moments of

all flashes and the coordinates of scintillators that have “flashed”. We can use these data in the next analyses, such as analysis of calculation coincidences and their dynamics, flashes from the electron component of CR in the upper layer of scintillators, flashes from natural emission of charged particles or pulses from the particles accelerated by atmospheric discharges.

The signal registration rate should be better than 100 μ sec and the arrival time determination accuracy should be 1 μ sec. High frequency amplifiers A 1 followed the PMT preamplifier with adjustable amplification from 1 to 3; this allowed us to set the same amplitude at the output of each PMT. The signals were then fed to comparators A that put out logical 1, which was then counted by the digital counter. With the help of stabilizer D3, the voltage was adjusted within the range from 0.08 V to 0.13 V. The comparator signals were fed to the delay units for synchronization with the reading capture window. From the inverse comparator output, the signal was fed to the logic unit D5. There were made 8 (16) channels in all. Should a signal from the scintillator of one of the channels arrive, the data from all the channels are read out. From the inverse output of D5 unit, $\sim 0.1 \mu$ sec signal is synchronously fed to the pulse shaper D6 (1,2). The output signal of D6 has trapezoidal shape that is why it is fed to the comparator A3 via potentiometer R6 to adjust the pulse width within 0.09-0.115 μ sec. The signal is then fed to the programmable functional input PFI1 of counter 6535 allowing reading out from the port. The counting rate of 6535 counter is 10 MHz and the real number of arriving events is 300-400 per second. The problem of

measuring the real time between the events was solved as follows. From a quartz generator, microsecond pulses were fed through two twelve-bit binary splitters SD4040 to 24 free inputs of the 6535 counter. Should a signal arrive from a detector to the corresponding port, the counter was reset and a new count would start until a new signal arrived. In such manner, there were registered the signals as well as the time of their arrival. The inter-event lengths of time are read out as binary codes. Figure 5 shows the muon registration circuit diagram.

The pulse discrimination is arranged to maximally get rid of the inherent noise of the electronics. As the PMT

signals vary in a wide range by both the width and amplitude, the system is blocked for 300 nsec after having registered the signal. In such a way, repeat count of the same pulse with a width of more than 100 nsec is excluded. The shaped pulses are fed to PCI 6535b module which is coupled with a computer through PCIe interface and has 32 digital input channels. This module's specifications are available at: <http://sine.ni.com/nips/cds/view/p/lang/en/nid/205627>.

The data acquisition and registration program for that device was written at LabVIEW 2014, allowing registration of the counter number and time of arrival of each signal.

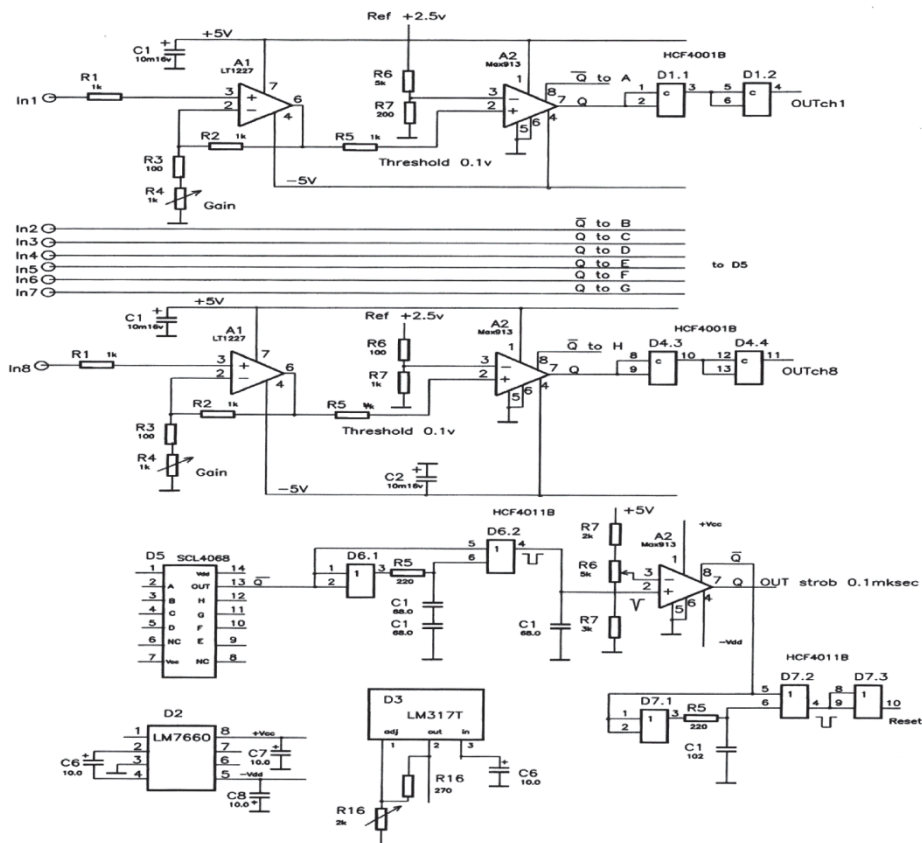


Figure 5. Muon registration circuit diagram

CONCLUSION

We give the description of a new muon telescope that can register muon traversal through the scintillator plates. The applied QUANTOCHRON registration technique allows us to use this system for not only identification of CR muons, but also for the study of particles accelerated in thunderclouds and, as well, perform the analysis of the pulses of CR electrons identified only in the upper layer of detector above the neutron monitor and possible emission of the natural radiation from the ground in the lower layer of detector under neutron monitor.

REFERENCE

- [1] Dorman L., Cosmic Rays in the Earth's Atmosphere and Underground, , Chapter 1 “, Cosmic Rays as an Object of Research”, Springer, page 3-5, 2004
- [2] Miroshnichenko L., “Solar Cosmic Rays: Fundamental and Applications”, Springer, Chapter 8, “Solar Cosmic Rays in Interplanetary Space”, second edition, 2015
- [3] Dorman L., “Cosmic Rays in the Earth's Atmosphere and Underground”, Chapter 4. Experimental Basis of Cosmic Ray Research, Springer, p.205-214, 2004
- [4] Dorman L.I., Applbaum D.S., Pustil'nik L.A., Sternlieb A., Zukerman I.G. and V.G. Yanke, “New multi-directional muon telescope and EAS installation on Mt. Hermon (Israel) in combination with NM-IQSY”, 29th International Cosmic Ray Conference Pune (2005), 469-472
- [5] А.П.Цитович «Ядерная электроника», Москва энергоатомиздат 1984, гл.5.5.4 стр.272
- [6] Chilingarian A., Hovsepyan G., and Kozliner L., Thunderstorm ground enhancements: Gamma ray differential energy spectra, Physical Review D 88, 073001 (2013).
- [7] Chilingarian A., Hovsepyan G., Kozliner L., Extensive Air Showers, Lightning, and Thunderstorm Ground Enhancements, Astroparticle Physics 82 (2016) 21–35.

GEANT4 Simulations of Electromagnetic Showers Initiated by 30MeV γ -Rays Entering the Atmosphere at Different Altitudes

N. Akopov, A. Grigoryan, G. Karyan

A.I. Alikhanyan Scientific Laboratory (Yerevan Physics Institute)

Abstract. The aim of this paper is to investigate the GEANT4 simulation for electromagnetic showers initiated by 30 MeV photons entering into the atmosphere at different altitudes (h). Charged and neutral components of the shower have been studied in various radial slices (R) with the detecting level corresponding to the altitude of Aragats mount, where the experimental setups of Cosmic Ray Division (CRD) of Yerevan Physics Institute (YerPhI) are operating. Qualitative observations of the energy spectra, as well as the tabulated parameters describing the fluxes at different values of h and R are used to make a comparison with those from the experimental data. The experimental data on particle fluxes are considered to be correlated with the atmospheric conditions such as pressure, temperature, presence of the charged clouds initiating the lightnings etc.

1. INTRODUCTION

The High Energy Atmospheric Physics (HEAP) is one of the fastest developing subjects during the last decade [1, 2, 3, 4]. There are many centers for cosmic ray detection over the world including the Aragats and Nor-Amberd cosmic rays stations. The huge thunderstorms that took place at Aragats (usually during the spring and autumn) allow simultaneous detection of all the relevant data to reveal the temporal pattern of the storm development and to investigate the atmospheric discharges and particle fluxes [5, 6]. The well known typical complications with the experimentally observed energy spectra of photons and electrons are :

- In general, unknown location of the shower origin (both h and R)
- Wide energy spectra for the initial photons/electrons/hadrons entering the atmosphere
- Possible correlations of the particles fluxes with the atmospheric conditions, i.e. pressure, temperature, presence of the charged clouds initiating the lightnings etc.

To address these issues we use the GEANT4 simulations in the following way: Initial photons are entering into the atmosphere with the energy $E_\gamma = 30$ MeV without any angular spread (perpendicularly to the atmospheric layer). The GEANT4 Physics List includes only the ElectroMagnetic (EM) interactions:

- For photons: Photo-Electric Effect, Compton Scattering, Gamma-Conversion
- For electron: Bremsstrahlung, Ionization, Multiple Scattering
- For positron: + Annihilation

The minimal energy cutoff is selected to be equal to 300 keV in order to decrease the simulation time. At fixed altitude (h) the air box has a size along the X-axis equal to h determined in the range of $[-h/2, h/2]$ m surrounded by the vacuum. For present studies $h(m)$ is taken with the values: 200 m, 500 m, 1000 m, 2000 m, 3000 m, 4000 m and 5000 m above the observation level, i.e. 3200 m. The Y and Z coordinates of the absorber box are both changing in the range $[-5000$ m, 5000 m]. For a fixed h ten different radial slices R (m) are introduced in the following manner: [0-100 m], [100-300 m], [300-600 m], [600-900 m], [900-1200 m], [1200-1500 m], [1500- 1800 m], [1800-2100 m], [2100-2400 m] and [2400-2700 m].

We also introduce into our model a dependence of the air density ρ ($\frac{g}{cm^3}$) on altitude h (m) by dividing the air box mentioned above on several sub-layers and using the following parameterization form for each of those sub-layers:

$$\rho = (1.215 - 0.983 \times 10^{-4} \times h) \times 10^{-3} \quad (1)$$

2. RESULTS AND DISCUSSION

We classify the obtained results from the GEANT4 simulations in the following way:

- Integrated fluxes as a function of h and R
- Energy spectra integrated over radial slices at different values of h
- Energy spectra at various h and R

We parameterize the observables, i.e. the particle fluxes and the energy spectra by using three different functional forms:

$$f(x) = \alpha E^\beta \quad (2)$$

$$f(x) = \alpha \exp(\gamma x) \quad (3)$$

$$f(x) = \alpha E^\beta \exp(\gamma x) \quad (4)$$

and tabulate the outcome of the fits in Tables 1-6 (see Appendix). The most effective (as to reduced χ^2 values) parameterization form to describe both, the fluxes and the energy spectra is given by the function (4).

3. FLUXES AS A FUNCTION OF h AND R

On Figure 1 and Figure 2 the h dependence for the fluxes (number of particles integrated over the energy of the corresponding spectrum) of photons and electrons normalized per primary particle are shown. It should be noted that for photon fluxes we see a clear turn around ≈ 420 m which is the mean free path of 30 MeV photons in air. There is more than three times lower fluxes observed for electrons in comparison with those of photons.

On Figure 3 one can see similar dependences of flux vs. altitude done at different radial slices. The shape of these dependences is quite different for various radial slices reflecting a complicated angular behaviour of involved electromagnetic processes at different values of h and R .

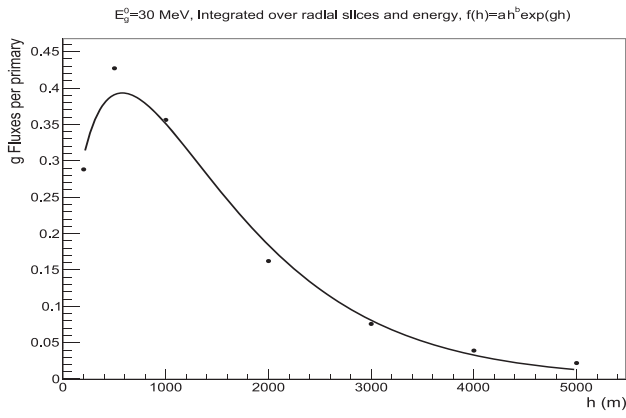


Figure 1. Fluxes of photons as a function of altitude

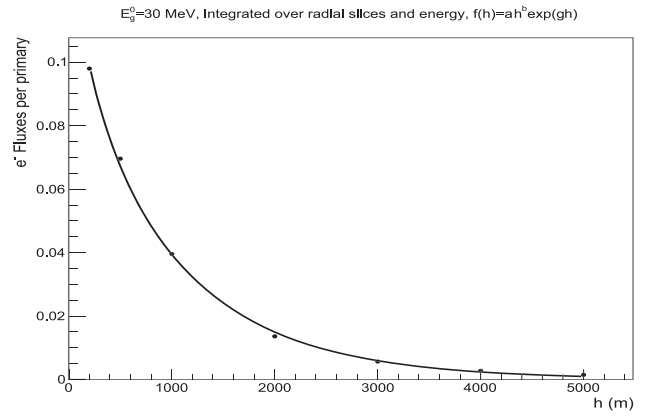


Figure 2. Fluxes of electrons as a function of altitude

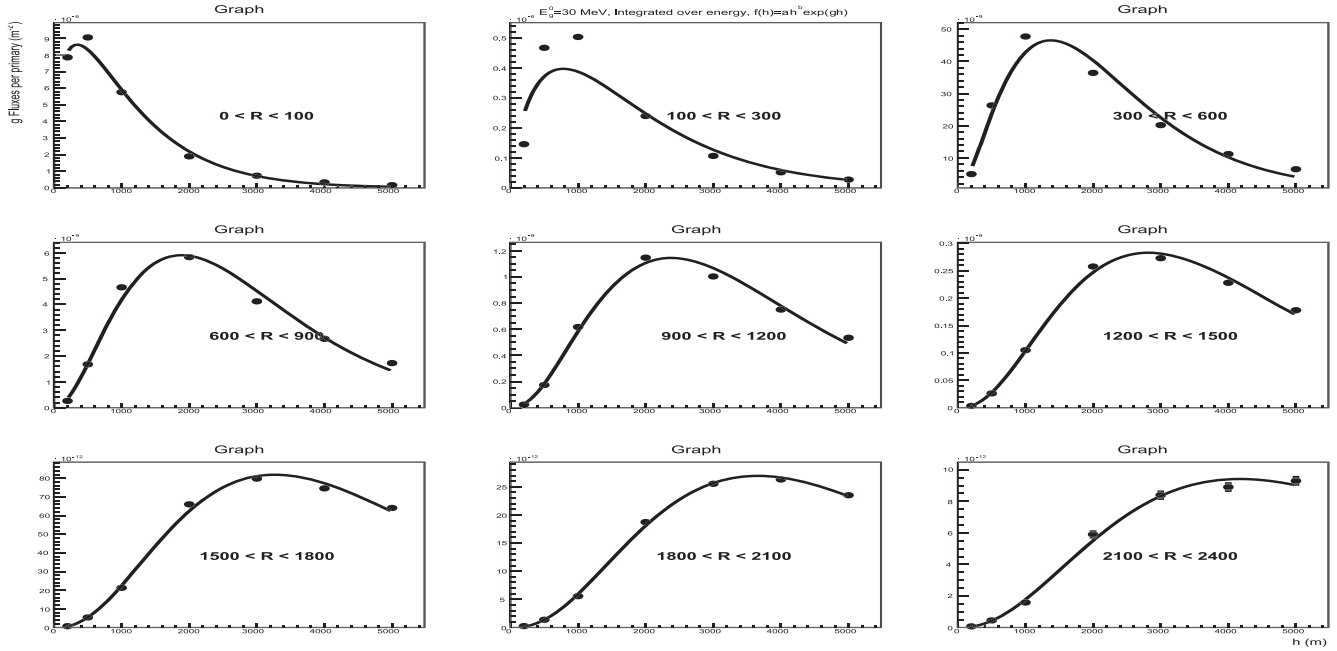


Figure 3. Fluxes of photons as a function of altitude at different radial slices normalized on primary and square of the corresponding slice. The curves correspond to the fitting function (4)

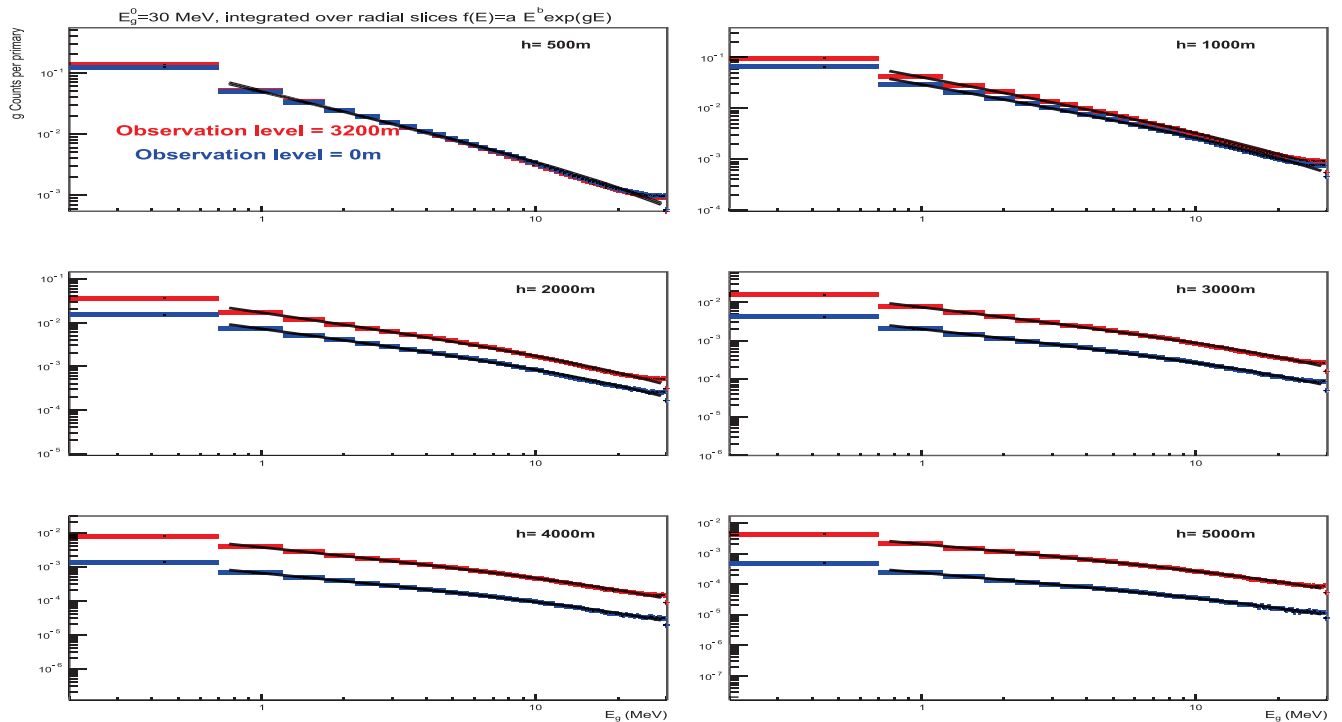


Figure 4. Photon energy spectra integrated over radial slices (see explanation in text).

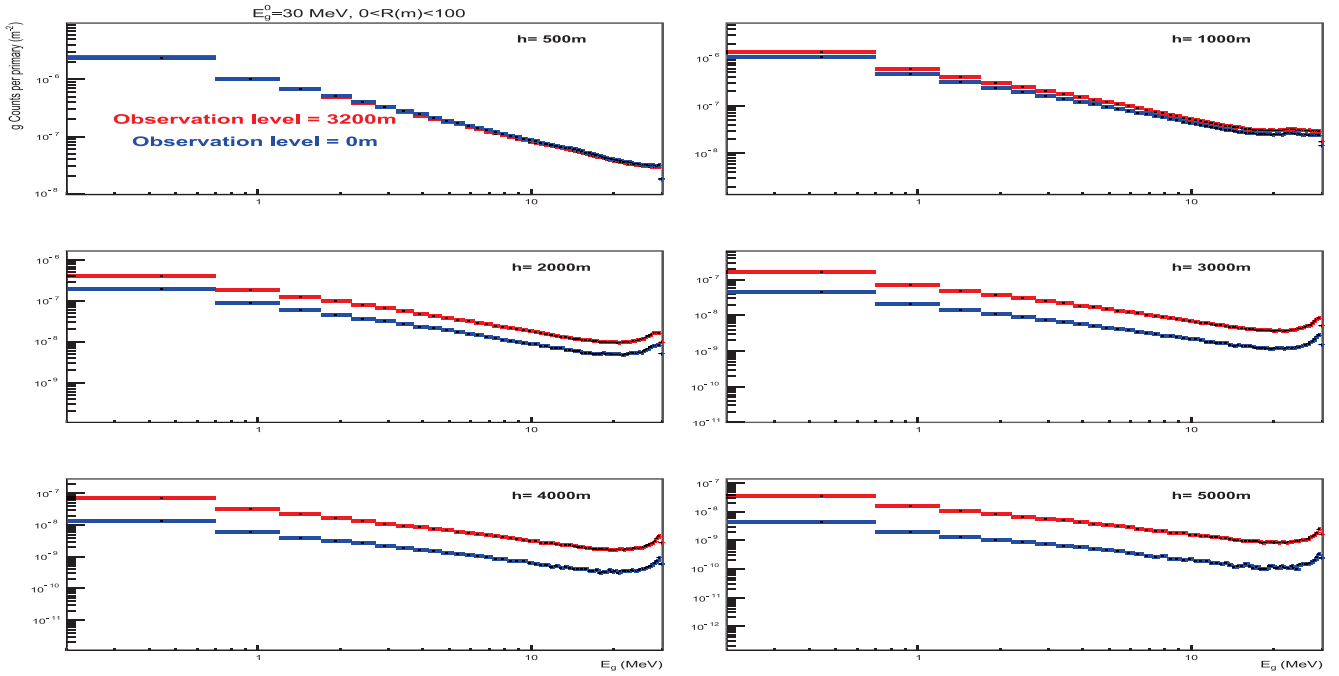


Figure 5. Photon energy spectra at first radial slice (see explanation in text).

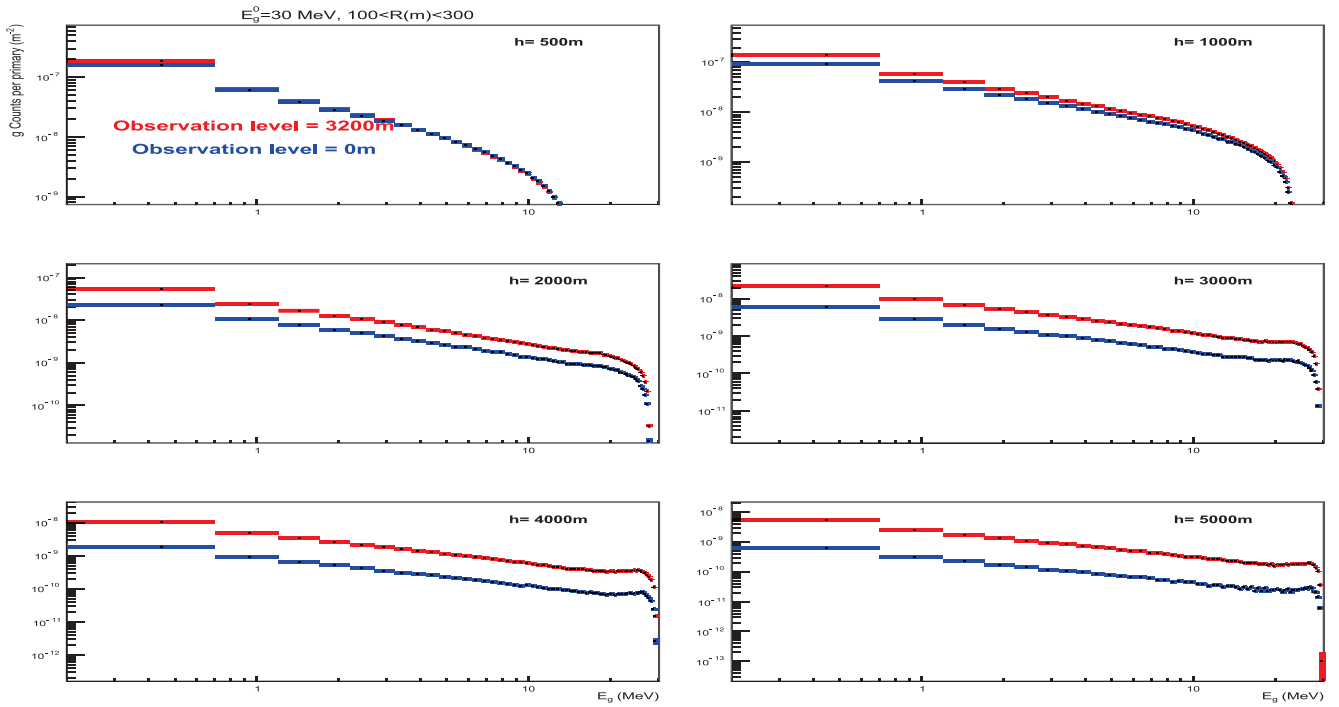


Figure 6. Photon energy spectra at second radial slice (see explanation in text).

On Figure 4 the energy spectra of photons detected at Aragats level (3200 m) and also at ground level are shown for initial 30 MeV photon entering into the atmosphere at different values of altitude (h). Besides of altitude equal to 500 m, where both spectra with different observation altitude (h). Besides of altitude equal to 500 m, where both spectra with different observation levels are quite close to each other, starting the altitude equal to 1000 m we can note that the number of photons at observation level equal to 3200 m is greater than at ground level. On Figure 5 the energy spectra for different values of h are shown for the first radial slice - $0 < R(m) < 100$. The interesting behaviour is seen at central radial slice for energy spectra corresponding to values of $h > 500$ m. Here we can note the enhancement of the high energy photons, which is a reaction of inverse energy-angle dependence typical for all involved electromagnetic processes. Such behaviour is not observed

at higher radial slices, which can be seen on Figs. 6 and 7. Another reaction of mentioned inverse energy-angle dependence is clearly seen, particularly for higher radial slices softening of the energy spectra. One more observed complication with the energy spectra fitted with the best (in sense of minimal values for reduced χ^2) selected 5 function done in (4) is different behaviour at different parts of spectra. In order to improve the description of obtained energy spectra with the expression (4), the whole range of [0-30] MeV was divided on three subranges: [0:7.5 - 5:5] MeV, [5:5 - 16:5] MeV and [16:5 - 29:5] MeV, and fitting procedure with the form (4) was performed separately for each of subranges. In Tables 1-6 (see Appendix) one can see the corresponding values of obtained fit parameters for each of mentioned subranges marked with $\alpha 1; 2; 3$; $\beta 1; 2; 3$ and $\gamma 1; 2; 3$ respectively.

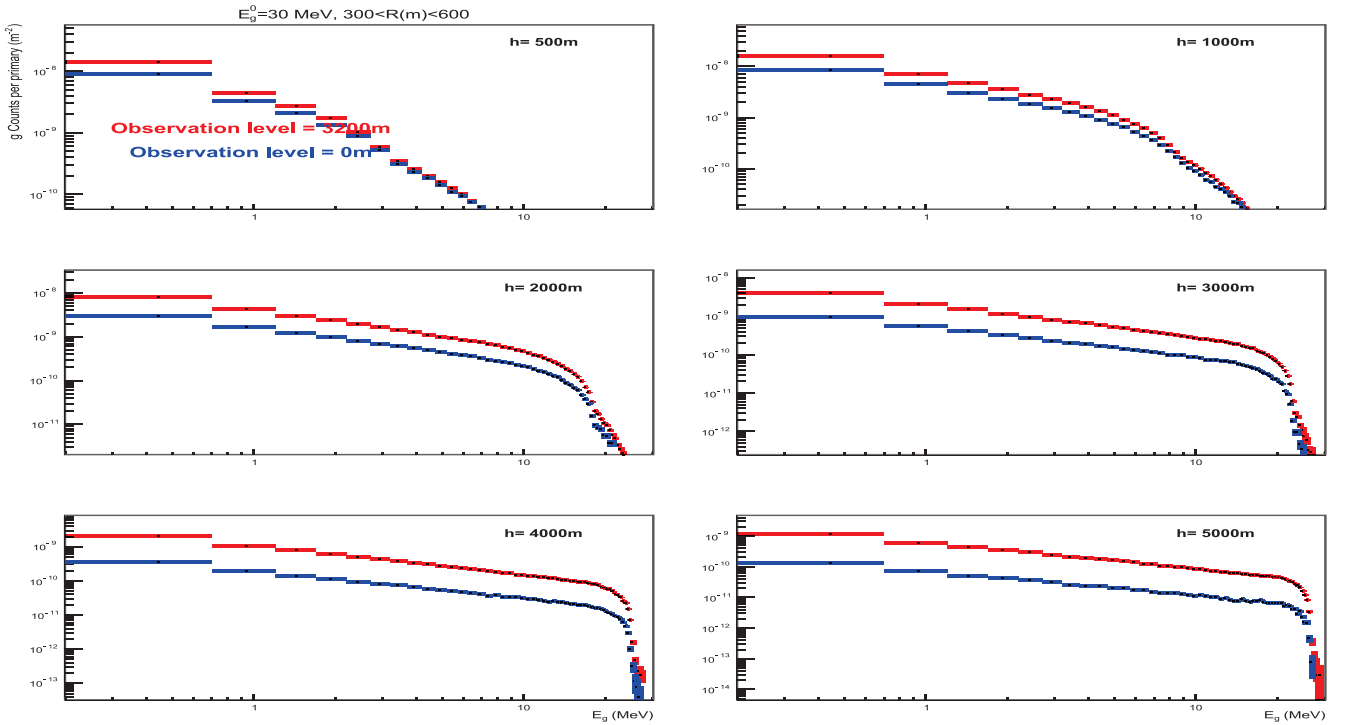


Figure 7. Photon energy spectra at third radial slice (see explanation in text).

CONCLUSION

The simulations done with GEANT4 using a simple model which includes the electromagnetic processes and barometric dependence of air density on altitude provide many interesting observations partly discussed in present paper. The obtained results will be very useful for further comparison with experimentally observed spectra (fluxes). Tabulated data with parameters corresponding to the fitting function (4) to describe the photons energy spectra at observation level equal to 3200 m at different values of h and R are included in Tables 1-6 (see Appendix).

ACKNOWLEDGEMENT

We thank A. Chilingarian for initiating of these studies, as well as for many useful discussions.

REFERENCE

- [1] A. Chilingarian, G. Hovsepian, and E. Mnatsakanyan, Phys. Rev. D 93, 052006 (2016).
- [2] A. Chilingaryan et al., Phys. Rev. D 82, 043009 (2010).
- [3] A. Dubinova et al., Phys. Rev. Lett., 115, 015002 (2015).
- [4] H. Tsuchiya et al., Phys. Rev. Lett., 99, 165002 (2007).
- [5] A. Chilingarian, S. Chilingarian, A. Reimers Geophys. Res. Space Physics 120, 021259 (2015).
- [6] A. Chilingarian, L. Vanyan, B. Mailyan Astroparticle Physics 48, 1-7 (2013)

APPENDIX

Table 1. Parameters describing the photon energy spectra detected at any of radial slices initiated by 30 MeV photon entering into the atmosphere at different h fitted with (4).

$h(m)$	200	500	1000	2000	3000	4000	5000
$\alpha_1 \pm \Delta\alpha_1$	$3.6e-02 \pm 4.7e-05$	$5.3e-02 \pm 5.5e-05$	$4.2e-02 \pm 4.6e-05$	$1.7e-02 \pm 2.8e-05$	$7.6e-03 \pm 1.8e-05$	$3.8e-03 \pm 1.2e-05$	$2.0e-03 \pm 9.1e-06$
$\beta_1 \pm \Delta\beta_1$	$-1.0e+00 \pm 3.2e-03$	$-9.6e-01 \pm 2.6e-03$	$-8.7e-01 \pm 2.8e-03$	$-8.1e-01 \pm 4.2e-03$	$-7.9e-01 \pm 6.2e-03$	$-7.9e-01 \pm 8.6e-03$	$-8.0e-01 \pm 1.2e-02$
$\gamma_1 \pm \Delta\gamma_1$	$-6.3e-02 \pm 1.4e-03$	$-6.7e-02 \pm 1.1e-03$	$-6.3e-02 \pm 1.2e-03$	$-4.5e-02 \pm 1.7e-03$	$-3.4e-02 \pm 2.6e-03$	$-2.4e-02 \pm 3.6e-03$	$-1.3e-02 \pm 4.8e-03$
$\alpha_2 \pm \Delta\alpha_2$	$4.8e-02 \pm 1.2e-03$	$7.2e-02 \pm 1.4e-03$	$5.6e-02 \pm 1.1e-03$	$2.1e-02 \pm 5.6e-04$	$8.9e-03 \pm 3.5e-04$	$3.7e-03 \pm 2.0e-04$	$1.8e-03 \pm 1.3e-04$
$\beta_2 \pm \Delta\beta_2$	$-1.4e+00 \pm 2.0e-02$	$-1.3e+00 \pm 1.6e-02$	$-1.2e+00 \pm 1.6e-02$	$-9.5e-01 \pm 2.1e-02$	$-8.9e-01 \pm 3.1e-02$	$-7.2e-01 \pm 4.2e-02$	$-6.3e-01 \pm 5.6e-02$
$\gamma_2 \pm \Delta\gamma_2$	$-2.8e-04 \pm 2.1e-03$	$-1.2e-02 \pm 1.6e-03$	$-2.1e-02 \pm 1.6e-03$	$-3.2e-02 \pm 2.2e-03$	$-3.1e-02 \pm 3.1e-03$	$-4.4e-02 \pm 4.2e-03$	$-4.8e-02 \pm 5.7e-03$
$\alpha_3 \pm \Delta\alpha_3$	$5.1e-01 \pm 1.3e-01$	$1.2e+00 \pm 2.4e-01$	$1.2e+00 \pm 2.2e-01$	$8.6e-01 \pm 2.3e-01$	$3.7e-01 \pm 1.3e-01$	$1.2e-01 \pm 5.7e-02$	$7.8e-02 \pm 4.7e-02$
$\beta_3 \pm \Delta\beta_3$	$-2.7e+00 \pm 1.2e-01$	$-2.9e+00 \pm 9.4e-02$	$-2.9e+00 \pm 9.2e-02$	$-3.0e+00 \pm 1.3e-01$	$-2.9e+00 \pm 1.7e-01$	$-2.7e+00 \pm 2.3e-01$	$-2.7e+00 \pm 2.9e-01$
$\gamma_3 \pm \Delta\gamma_3$	$8.4e-02 \pm 5.3e-03$	$8.9e-02 \pm 4.3e-03$	$8.8e-02 \pm 4.2e-03$	$9.3e-02 \pm 5.9e-03$	$8.8e-02 \pm 7.7e-03$	$7.8e-02 \pm 1.0e-02$	$7.7e-02 \pm 1.3e-02$

Table 2. Parameters describing the photon energy spectra detected at $0 < R(m) < 100$ radial slice initiated by 30 MeV photon entering into the atmosphere at different h fitted with (4).

$h(m)$	200	500	1000	2000	3000	4000	5000
$\alpha_1 \pm \Delta\alpha_1$	$9.1e-07 \pm 1.2e-09$	$1.0e-06 \pm 1.3e-09$	$6.0e-07 \pm 9.7e-10$	$1.9e-07 \pm 5.3e-10$	$7.1e-08 \pm 3.2e-10$	$3.2e-08 \pm 2.2e-10$	$1.6e-08 \pm 1.5e-10$
$\beta_1 \pm \Delta\beta_1$	$-1.0e+00 \pm 3.4e-03$	$-9.4e-01 \pm 3.2e-03$	$-8.7e-01 \pm 4.1e-03$	$-8.6e-01 \pm 7.2e-03$	$-8.6e-01 \pm 1.2e-02$	$-8.7e-01 \pm 1.7e-02$	$-8.7e-01 \pm 2.5e-02$
$\gamma_1 \pm \Delta\gamma_1$	$-3.1e-02 \pm 1.5e-03$	$-4.4e-02 \pm 1.4e-03$	$-4.7e-02 \pm 1.7e-03$	$-3.9e-02 \pm 3.0e-03$	$-3.7e-02 \pm 4.9e-03$	$-2.9e-02 \pm 7.3e-03$	$-2.6e-02 \pm 1.0e-02$
$\alpha_2 \pm \Delta\alpha_2$	$1.4e-06 \pm 3.5e-08$	$1.3e-06 \pm 3.0e-08$	$9.7e-07 \pm 2.6e-08$	$2.6e-07 \pm 1.3e-08$	$1.1e-07 \pm 9.0e-09$	$4.8e-08 \pm 5.5e-09$	$1.9e-08 \pm 3.2e-09$
$\beta_2 \pm \Delta\beta_2$	$-1.4e+00 \pm 2.0e-02$	$-1.3e+00 \pm 1.7e-02$	$-1.4e+00 \pm 2.1e-02$	$-1.2e+00 \pm 3.8e-02$	$-1.3e+00 \pm 6.6e-02$	$-1.2e+00 \pm 9.2e-02$	$-1.1e+00 \pm 1.3e-01$
$\gamma_2 \pm \Delta\gamma_2$	$-3.6e-03 \pm 2.1e-03$	$2.5e-02 \pm 1.7e-03$	$2.7e-02 \pm 2.1e-03$	$9.8e-03 \pm 3.8e-03$	$1.5e-02 \pm 6.7e-03$	$1.2e-02 \pm 9.2e-03$	$-3.9e-03 \pm 1.3e-02$
$\alpha_3 \pm \Delta\alpha_3$	$1.6e-05 \pm 4.0e-06$	$2.2e-05 \pm 4.4e-06$	$6.9e-09 \pm 1.8e-09$	$1.0e-01 \pm 1.8e-03$	$2.2e+00 \pm 1.6e-01$	$3.6e+00 \pm 1.5e-01$	$8.0e-01 \pm 4.8e-02$
$\beta_3 \pm \Delta\beta_3$	$-2.7e+00 \pm 1.2e-01$	$-2.7e+00 \pm 9.7e-02$	$7.5e-01 \pm 1.2e-01$	$-8.1e+00 \pm 7.7e-03$	$-1.0e+01 \pm 3.7e-02$	$-1.1e+01 \pm 1.8e-02$	$-1.0e+01 \pm 2.6e-02$
$\gamma_3 \pm \Delta\gamma_3$	$8.4e-02 \pm 5.4e-03$	$8.0e-02 \pm 4.4e-03$	$-3.7e-02 \pm 5.5e-03$	$4.0e-01 \pm 5.3e-04$	$4.9e-01 \pm 2.0e-03$	$5.2e-01 \pm 1.3e-03$	$5.0e-01 \pm 1.8e-03$

Table 3. Parameters describing the photon energy spectra detected at $100 < R(m) < 300$ radial slice initiated by 30 MeV photon entering into the atmosphere at different h fitted with (4).

$h(m)$	200	500	1000	2000	3000	4000	5000
$\alpha_1 \pm \Delta\alpha_1$	$5.3e-08 \pm 3.0e-10$	$6.5e-08 \pm 1.2e-10$	$5.8e-08 \pm 1.1e-10$	$2.3e-08 \pm 6.3e-11$	$9.7e-09 \pm 4.0e-11$	$4.6e-09 \pm 2.7e-11$	$2.4e-09 \pm 2.0e-11$
$\beta_1 \pm \Delta\beta_1$	$8.0e-03 \pm 1.2e-02$	$-9.0e-01 \pm 4.7e-03$	$-9.0e-01 \pm 4.6e-03$	$-8.4e-01 \pm 7.0e-03$	$-8.2e-01 \pm 1.1e-02$	$-8.3e-01 \pm 1.6e-02$	$-8.6e-01 \pm 2.1e-02$
$\gamma_1 \pm \Delta\gamma_1$	$-9.5e-01 \pm 5.9e-03$	$-9.5e-02 \pm 2.0e-03$	$-3.1e-02 \pm 1.9e-03$	$-2.0e-02 \pm 2.9e-03$	$-1.8e-02 \pm 4.5e-03$	$-1.1e-02 \pm 6.5e-03$	$3.0e-03 \pm 8.9e-03$
$\alpha_2 \pm \Delta\alpha_2$	$1.3e-08 \pm 4.3e-09$	$1.4e-09 \pm 1.0e-10$	$2.2e-08 \pm 7.1e-10$	$3.6e-08 \pm 1.5e-09$	$1.4e-08 \pm 1.0e-09$	$6.0e-09 \pm 5.9e-10$	$2.6e-09 \pm 3.5e-10$
$\beta_2 \pm \Delta\beta_2$	$-9.9e-01 \pm 2.8e-01$	$3.1e+00 \pm 6.0e-02$	$2.4e-02 \pm 2.5e-02$	$-1.2e+00 \pm 3.3e-02$	$-1.1e+00 \pm 5.9e-02$	$-1.0e+00 \pm 7.7e-02$	$-8.8e-01 \pm 1.0e-01$
$\gamma_2 \pm \Delta\gamma_2$	$-3.3e-01 \pm 3.1e-02$	$-6.7e-01 \pm 6.5e-03$	$-1.5e-01 \pm 2.6e-03$	$2.5e-02 \pm 3.3e-03$	$1.6e-02 \pm 5.9e-03$	$4.6e-03 \pm 7.7e-03$	$-8.0e-03 \pm 1.0e-02$
$\alpha_3 \pm \Delta\alpha_3$	$1.6e-11 \pm 1.6e-11$	$9.0e-17 \pm 2.0e-17$	$2.4e-21 \pm 6.7e-23$	$2.1e-25 \pm 3.1e-27$	$9.9e-12 \pm 2.2e-13$	$2.2e-15 \pm 1.3e-16$	$1.7e-12 \pm 8.7e-14$
$\beta_3 \pm \Delta\beta_3$	$2.0e+00 \pm 4.1e-01$	$1.1e+01 \pm 9.9e-02$	$1.8e+01 \pm 1.5e-02$	$2.1e+01 \pm 9.9e-03$	$3.1e+00 \pm 1.2e-02$	$6.1e+00 \pm 2.8e-02$	$2.4e+00 \pm 2.2e-02$
$\gamma_3 \pm \Delta\gamma_3$	$-4.5e-01 \pm 4.2e-02$	$-1.0e+00 \pm 7.5e-03$	$-1.4e+00 \pm 1.5e-03$	$-1.3e+00 \pm 9.3e-04$	$-2.6e-01 \pm 1.0e-03$	$-3.1e-01 \pm 1.7e-03$	$-1.2e-01 \pm 1.6e-03$

Table 4. Parameters describing the photon energy spectra detected at $300 < R(m) < 600$ radial slice initiated by 30 MeV photon entering into the atmosphere at different h fitted with (4).

$h(m)$	200	500	1000	2000	3000	4000	5000
$\alpha_1 \pm \Delta\alpha_1$	$3.0e-10 \pm 6.6e-12$	$9.0e-09 \pm 6.7e-11$	$8.1e-09 \pm 2.4e-11$	$4.3e-09 \pm 1.5e-11$	$2.0e-09 \pm 9.9e-12$	$1.1e-09 \pm 7.2e-12$	$5.9e-10 \pm 5.3e-12$
$\beta_1 \pm \Delta\beta_1$	$-4.1e+00 \pm 4.8e-02$	$-3.6e-01 \pm 1.5e-02$	$-7.2e-01 \pm 7.4e-03$	$-7.8e-01 \pm 8.9e-03$	$-7.8e-01 \pm 1.3e-02$	$-7.6e-01 \pm 1.7e-02$	$-7.9e-01 \pm 2.3e-02$
$\gamma_1 \pm \Delta\gamma_1$	$6.3e-01 \pm 2.2e-02$	$-7.5e-01 \pm 7.6e-03$	$-1.7e-01 \pm 3.2e-03$	$-3.9e-02 \pm 3.7e-03$	$-2.0e-02 \pm 5.2e-03$	$-2.5e-02 \pm 7.2e-03$	$-6.0e-03 \pm 9.6e-03$
$\alpha_2 \pm \Delta\alpha_2$	$3.3e-09 \pm 5.9e-09$	$1.7e-09 \pm 5.9e-10$	$1.7e-07 \pm 2.2e-08$	$4.4e-10 \pm 3.6e-11$	$1.5e-09 \pm 1.2e-10$	$1.2e-09 \pm 1.3e-10$	$6.7e-10 \pm 9.3e-11$
$\beta_2 \pm \Delta\beta_2$	$-3.6e+00 \pm 1.5e+00$	$-2.3e-01 \pm 3.0e-01$	$-2.5e+00 \pm 1.1e-01$	$1.4e+00 \pm 6.4e-02$	$-5.3e-01 \pm 6.2e-02$	$-9.0e-01 \pm 8.2e-02$	$-8.6e-01 \pm 1.1e-01$
$\gamma_2 \pm \Delta\gamma_2$	$-4.2e-02 \pm 1.7e-01$	$-4.1e-01 \pm 3.4e-02$	$-1.5e-01 \pm 1.2e-02$	$-3.2e-01 \pm 6.5e-03$	$-5.0e-02 \pm 6.2e-03$	$-3.5e-03 \pm 8.2e-03$	$-8.4e-03 \pm 1.1e-02$
$\alpha_3 \pm \Delta\alpha_3$	$1.8e-19 \pm 1.6e-18$	$1.1e-06 \pm 1.0e-06$	$1.4e-14 \pm 3.0e-15$	$1.2e+01 \pm 1.3e+00$	$4.5e-21 \pm 2.9e-22$	$1.2e-22 \pm 7.1e-24$	$2.0e-25 \pm 1.1e-26$
$\beta_3 \pm \Delta\beta_3$	$6.8e+00 \pm 4.6e+00$	$-3.7e+00 \pm 3.9e-01$	$7.7e+00 \pm 1.8e-01$	$-8.0e+00 \pm 4.7e-02$	$1.6e+01 \pm 4.0e-02$	$1.7e+01 \pm 3.3e-02$	$2.0e+01 \pm 3.5e-02$
$\gamma_3 \pm \Delta\gamma_3$	$-4.0e-01 \pm 3.5e-01$	$-2.2e-01 \pm 4.1e-02$	$-9.0e-01 \pm 1.9e-02$	$-1.9e-01 \pm 5.1e-03$	$-1.3e+00 \pm 4.3e-03$	$-1.3e+00 \pm 2.8e-03$	$-1.3e+00 \pm 3.2e-03$

Table 5. Parameters describing the photon energy spectra detected at $600 < R(m) < 900$ radial slice initiated by 30 MeV photon entering into the atmosphere at different h fitted with (4).

$h(m)$	200	500	1000	2000	3000	4000	5000
$\alpha_1 \pm \Delta\alpha_1$	$1.9e-11 \pm 1.4e-12$	$2.4e-10 \pm 4.6e-12$	$1.6e-09 \pm 1.5e-11$	$8.8e-10 \pm 5.4e-12$	$4.9e-10 \pm 3.7e-12$	$2.8e-10 \pm 2.7e-12$	$1.7e-10 \pm 2.1e-12$
$\beta_1 \pm \Delta\beta_1$	$-2.2e+00 \pm 1.6e-01$	$-2.4e+00 \pm 4.2e-02$	$-2.8e-01 \pm 2.1e-02$	$-6.5e-01 \pm 1.6e-02$	$-6.8e-01 \pm 2.0e-02$	$-7.2e-01 \pm 2.6e-02$	$-7.0e-01 \pm 3.3e-02$
$\gamma_1 \pm \Delta\gamma_1$	$1.9e-02 \pm 7.4e-02$	$1.3e-01 \pm 1.9e-02$	$-6.2e-01 \pm 9.9e-03$	$-1.0e-01 \pm 6.6e-03$	$-4.6e-02 \pm 8.2e-03$	$-1.7e-02 \pm 1.1e-02$	$-2.7e-02 \pm 1.3e-02$
$\alpha_2 \pm \Delta\alpha_2$	$7.3e-07 \pm 3.0e-06$	$2.6e-10 \pm 3.1e-10$	$2.0e-10 \pm 9.1e-11$	$1.8e-08 \pm 4.2e-09$	$1.4e-12 \pm 3.1e-13$	$1.2e-11 \pm 1.8e-12$	$1.0e-10 \pm 2.1e-11$
$\beta_2 \pm \Delta\beta_2$	$-1.1e+01 \pm 3.4e+00$	$-9.1e-01 \pm 1.1e+00$	$5.3e-01 \pm 3.9e-01$	$-2.2e+00 \pm 1.9e-01$	$5.2e+00 \pm 1.8e-01$	$2.2e+00 \pm 1.2e-01$	$-2.5e-01 \pm 1.6e-01$
$\gamma_2 \pm \Delta\gamma_2$	$8.5e-01 \pm 3.5e-01$	$-3.8e-01 \pm 1.2e-01$	$-4.6e-01 \pm 4.4e-02$	$-1.5e-01 \pm 2.2e-02$	$-8.2e-01 \pm 1.9e-02$	$-3.7e-01 \pm 1.2e-02$	$-7.7e-02 \pm 1.6e-02$
$\alpha_3 \pm \Delta\alpha_3$	$7.0e-04 \pm 1.0e-02$	$2.1e+05 \pm 6.2e+05$	$7.5e-10 \pm 2.5e-09$	$1.6e-15 \pm 9.8e-16$	$1.6e-15 \pm 1.5e-15$	$6.1e-05 \pm 1.8e-05$	$1.1e-15 \pm 3.6e-16$
$\beta_3 \pm \Delta\beta_3$	$-1.1e+00 \pm 4.8e+00$	$-2.1e+01 \pm 2.6e+00$	$-1.1e-01 \pm 1.7e+00$	$8.1e+00 \pm 3.4e-01$	$7.6e+00 \pm 4.3e-01$	$-3.6e+00 \pm 1.3e-01$	$1.0e+01 \pm 1.7e-01$
$\gamma_3 \pm \Delta\gamma_3$	$-1.0e+00 \pm 7.0e-01$	$9.6e-01 \pm 3.9e-01$	$-4.3e-01 \pm 1.1e-01$	$-9.2e-01 \pm 3.1e-02$	$-8.2e-01 \pm 2.4e-02$	$-3.6e-01 \pm 1.3e-02$	$-1.1e+00 \pm 1.4e-02$

Table 6. Parameters describing the photon energy spectra detected at $900 < R(m) < 1200$ radial slice initiated by 30 MeV photon entering into the atmosphere at different h fitted with (4).

$h(m)$	200	500	1000	2000	3000	4000	5000
$\alpha_1 \pm \Delta\alpha_1$	$2.9e-12 \pm 4.9e-13$	$2.5e-11 \pm 1.1e-12$	$1.4e-10 \pm 3.1e-12$	$2.7e-10 \pm 3.1e-12$	$1.4e-10 \pm 1.7e-12$	$8.9e-11 \pm 1.3e-12$	$5.7e-11 \pm 1.0e-12$
$\beta_1 \pm \Delta\beta_1$	$-1.9e+00 \pm 3.6e-01$	$-2.0e+00 \pm 1.1e-01$	$-1.3e+00 \pm 4.7e-02$	$-1.4e-01 \pm 3.0e-02$	$-5.4e-01 \pm 3.2e-02$	$-6.3e-01 \pm 3.9e-02$	$-6.0e-01 \pm 4.8e-0$
$\gamma_1 \pm \Delta\gamma_1$	$-1.1e-01 \pm 1.8e-01$	$5.0e-02 \pm 4.9e-02$	$-1.8e-01 \pm 2.2e-02$	$-4.2e-01 \pm 1.3e-02$	$-9.7e-02 \pm 1.3e-02$	$-4.3e-02 \pm 1.6e-02$	$-4.9e-02 \pm 2.0e-02$
$\alpha_2 \pm \Delta\alpha_2$	$1.0e-08 \pm 1.9e-08$	$6.4e-10 \pm 2.1e-09$	$5.2e-11 \pm 1.1e-10$	$4.0e-11 \pm 2.0e-11$	$3.0e-09 \pm 1.3e-09$	$3.8e-13 \pm 1.5e-13$	$9.5e-14 \pm 8.8e-14$
$\beta_2 \pm \Delta\beta_2$	$-9.3e+00 \pm 1.6e+00$	$-3.7e+00 \pm 2.8e+00$	$1.1e-01 \pm 1.8e+00$	$8.3e-01 \pm 4.2e-01$	$-2.1e+00 \pm 3.7e-01$	$5.2e+00 \pm 3.4e-01$	$5.4e+00 \pm 7.4e-01$
$\gamma_2 \pm \Delta\gamma_2$	$7.8e-01 \pm 2.1e-01$	$-3.0e-02 \pm 3.2e-01$	$-4.4e-01 \pm 2.0e-01$	$-4.2e-01 \pm 4.5e-02$	$-1.5e-01 \pm 4.1e-02$	$-8.8e-01 \pm 3.8e-02$	$-7.8e-01 \pm 7.6e-02$
$\alpha_3 \pm \Delta\alpha_3$	$2.3e-05 \pm 3.4e-04$	$4.1e-11 \pm 3.7e-10$	$2.4e+04 \pm 1.4e+05$	$2.6e-04 \pm 6.9e-04$	$1.2e-16 \pm 1.4e-16$	$4.6e-11 \pm 3.1e-11$	$9.4e-15 \pm 7.7e-15$
$\beta_3 \pm \Delta\beta_3$	$-1.2e+00 \pm 5.2e+00$	$-4.3e+00 \pm 3.6e+00$	$-2.0e+01 \pm 3.7e+00$	$-6.2e+00 \pm 1.6e+00$	$8.3e+00 \pm 5.6e-01$	$1.6e+00 \pm 2.8e-01$	$5.9e+00 \pm 4.7e-01$
$\gamma_3 \pm \Delta\gamma_3$	$-1.0e+00 \pm 8.4e-01$	$2.4e-01 \pm 4.6e-01$	$8.4e-01 \pm 3.3e-01$	$-1.8e-01 \pm 1.2e-01$	$-8.9e-01 \pm 4.7e-02$	$-5.1e-01 \pm 2.9e-02$	$-7.4e-01 \pm 4.6e-02$

First Results on Transient Atmospheric Events from Tracking Ultraviolet Set-Up (TUS) on Board the Lomonosov Satellite

P. Klimov, B. Khrenov, S. Sharakin, M. Zotov, N. Chirskaya, V. Ereemeev, G. Garipov, M. Kaznacheeva, M. Panasyuk, V. Petrov, A. Shirokov, I. Yashin

M.V. Lomonosov Moscow State University, D.V. Skobeltsyn Institute of Nuclear Physics, Moscow, Russia

Abstract. Study of transient atmospheric events (TAE) is started by a new space instrument TUS, an imaging detector equipped with a large area mirror-concentrator ($\approx 2 \text{ m}^2$) and 256 photomultipliers in the focal plane. Its covering area in the atmosphere is $80 \text{ km} \times 80 \text{ km}$. TUS was launched on 28 April 2016, and several hundred of TAE were measured during the first months of its flight. The detector has several modes of operation with different temporal resolution, which allow measuring TAE at various time scales. In comparison with earlier experiments, the instrument measures orders of magnitude less bright transient luminous events due to a large optical aperture. TUS has a spatial resolution (5 km from orbit height 500 km), which gives an opportunity for a reliable classification of TAE types basing on their temporal dynamics and spatial structure. Data on lightning are compared with data from ground-based networks and examples of TAE images are discussed.

1. INTRODUCTION. DESIGN OF THE TUS DETECTOR

The TUS detector is accommodated on board of the Lomonosov satellite (international designation MVL 300, or 2016-026A). It was launched on April 28, 2016, on a polar sun-synchronous orbit with inclination of $97^\circ.3$, a period of ~ 94 min, and a height around 500 km. Description of TUS and its main characteristic were published elsewhere [1-3]. Optical parameters (focusing power of mirror-concentrator, coefficient of photon-electron conversion at photomultiplier tube (PMT) cathode, PMT gain coefficient) were measured before the flight [4, 5]. In preliminary measurements by Tatiana satellites, the background atmosphere UV photon intensity was measured for various regions of the Earth and various moon phases [6-8] and was taken into account during the TUS experiment preparation.

It was a-priori known (and confirmed by Tatiana experiments) that moon UV light scattered in the atmosphere is the main source of background noise in the TUS experiment. At nights with the Moon above the horizon, the most of measured UV radiation are photons scattered in the atmosphere. An important result of the observation was a higher intensity of the Moon UV light in the presence of clouds in the field of view (FOV) than from the clean atmosphere-roughly twice larger. At moonless nights, the background intensity is constant at scales of thousands km above oceans and has two regions of higher intensity: in aurora regions and above equatorial ionospheric anomaly. This feature and lower noise at moonless nights make operation of TUS much safer at moonless nights.

The TUS detector consists of two main parts: a parabolic mirror-concentrator of the Fresnel type and a square-shaped 256-pixel photodetector in the focal plane of the mirror. The mirror has an area of about 2 m^2 with a focal distance of 1.5 m. In control measurements of the mirror quality, the size of the focal spot was found to be less than the detector pixel size (15 mm). A pixel field of view equals 10 mrad, which results in space resolution at the atmosphere 5 km with the area of TUS FOV approximately $80 \text{ km} \times 80 \text{ km}$ at sea level. It was also found that the focusing part of the mirror area is accompanied by a diffuse mirror scattering part with its percentage of $\sim 40\%$ of the total mirror area. This diffuse scattering part is important in observation of large radiating

objects, like clouds lit by the Moon. It also adds background to pixels and produces signals from events outside the FOV.

Pixels of the TUS photodetector are photomultiplier tubes Hamamatsu R1463 with multialkali cathode of 13 mm diameter. The pixel wavelength band 240-400 nm is limited by a UV filter cutting the band at upper wavelength of 400 nm and by PMT quantum efficiency (QE) at wavelengths lower than 240 ($QE < 10\%$). Average QE in the UV band is 20%. Light guides with square entrance apertures ($15 \text{ mm} \times 15 \text{ mm}$) and circular outputs were employed to fill uniformly the detector's FOV. Each pixel has a black blend with the height of 1 cm above the light guide to protect it from side irradiation. An UV filter of 13 mm diameter and 2.5 mm thick is placed in front of each PMT. The pixels are grouped in 16 identical photodetector modules. Each cluster has its own digital data processing system for the first-level trigger, based on a Xilinx field-programmable gate array (FPGA), and a high voltage power supply, controlled by the FPGA. The central processor board gathers information from all modules, controls their operation, and implements the second-level trigger algorithm.

It is important that the TUS electronics can operate in four modes intended for detecting various fast optical phenomena in the atmosphere at different time scales with different time sampling. The main mode is aimed at registering extensive air showers (EASs) born by extreme energy cosmic rays and has a time sampling of $0.8 \mu\text{s}$. This mode is also efficient for elves measurements, the most common type of transient luminous events. Three other modes have time sampling of $25.6 \mu\text{s}$ and 0.4 ms for studying TLEs of different kinds slower than elves: sprites, blue jets, gigantic jets, etc., and 6.6 ms for detecting micrometeors, space debris and thunderstorm activity at a longer time scale ($\sim 1.7 \text{ s}$). Waveforms in each mode (a "record") consist of 256 time samples. The trigger algorithm consists of two levels. The first level trigger decision is based on a comparison of the simple moving average of analog-to-digital converter (ADC) counts calculated for each pixel with a threshold level that depends on the mean value of the background noise. At the second level trigger, the geometry and number of hit pixels are analyzed. In case of EAS and meteors it is a search for a track, i.e., adjacent pixels lined up within a certain time.

Two processes in the photodetector electronics affect the event selection by TUS. These are the trigger algorithm itself and the PMT gain control. During normal operation, the detector measures the UV background level and adjusts the sensitivity of the PMTs to avoid their saturation under conditions of increased UV intensity during moonlit nights. This leads to a lower sensitivity and a higher trigger threshold. The high voltage correction occurs once every 100 ms.

TUS on board the Lomonosov satellite and during preflight preparations at cosmodrome Vostochny is shown in Figure 1.

An important addition to the space detector data on lightning and related events gives use of data from ground based lightning detection networks (WWLLN, Vaisala) generously presented to us by prof. R. Holzworth, the head of the World Wide Lightning Location Network, and Vaisala Inc. company.

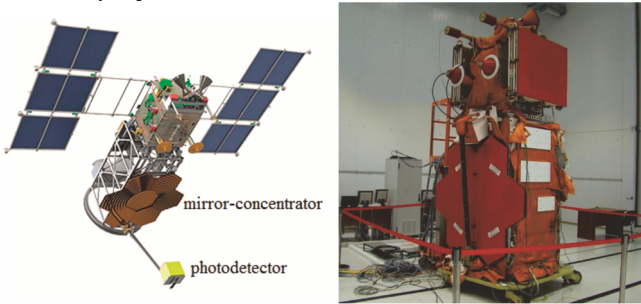


Figure 1. Artist's view of the TUS detector on board the Lomonosov satellite (left panel). TUS on board the Lomonosov satellite covered with a protective cover during preflight preparations at cosmodrome Vostochny (right panel).

2. THE MAIN RESULTS

In what follows, we present the preliminary results of an analysis of data obtained with TUS in various modes of operation to demonstrate that different phenomena can be measured in UV range from orbit by one detector. All these events are related to UV background (airglow, city lights) and thunderstorm activity. First we discuss events in the EAS mode of operation (0.8 μ s temporal resolution), then in the TLE mode (0.4 ms) and finally we present a thunderstorm measurement in the METEOR mode (6.6 ms).

2.1 EVENTS WITH NOISE-LIKE WAVEFORMS IN THE EAS MODE AND CITY LIGHTS

The majority of events registered thus far by TUS have noise-like waveforms with ADC counts of all PMTs fluctuating around some average values, which are close to each other if rescaled according to the individual PMT gains. A typical waveform (recorded in a full moon night) in one pixel is shown in Figure 2. The trigger is caused by random fluctuations of the background.

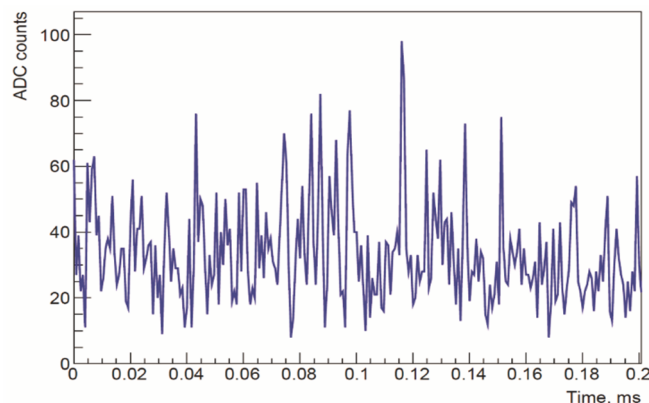


Figure 2. Typical waveform in one pixel of a noise-like event.

Within the group, there is a subset of events with noise-like waveforms but strongly non-uniform illumination of the focal plane. An event of this kind is shown in Fig. 3 when TUS was near Erevan, Armenia. One can see a strong localized signal in the group of pixels. Interesting to note that pixel signals above USA cities are modulated with 120 Hz while Europe and Russia ones- with 100 Hz. An example of waveform measurements above the USA with 0.4 ms temporal resolution with well seen periodical structure and the results of Fourier analysis are shown in Figure 4.

There are numerous other events of this kind but a preliminary analysis reveals that only a part of them can be directly related to city lights or other anthropogenic sources. These data are under analysis.

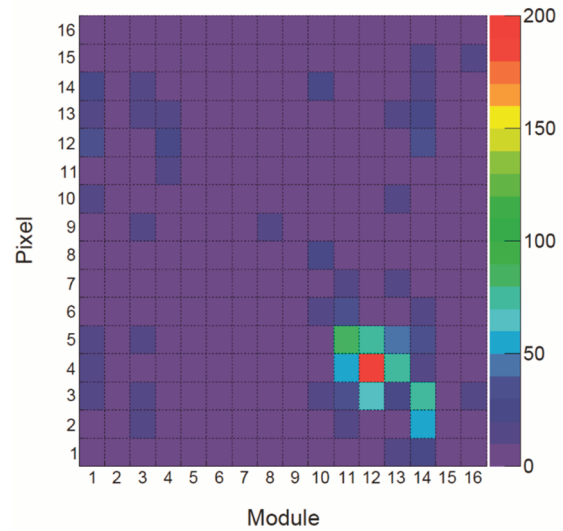


Figure 3. Snapshot of the focal plane of the event registered above Erevan, Armenia.

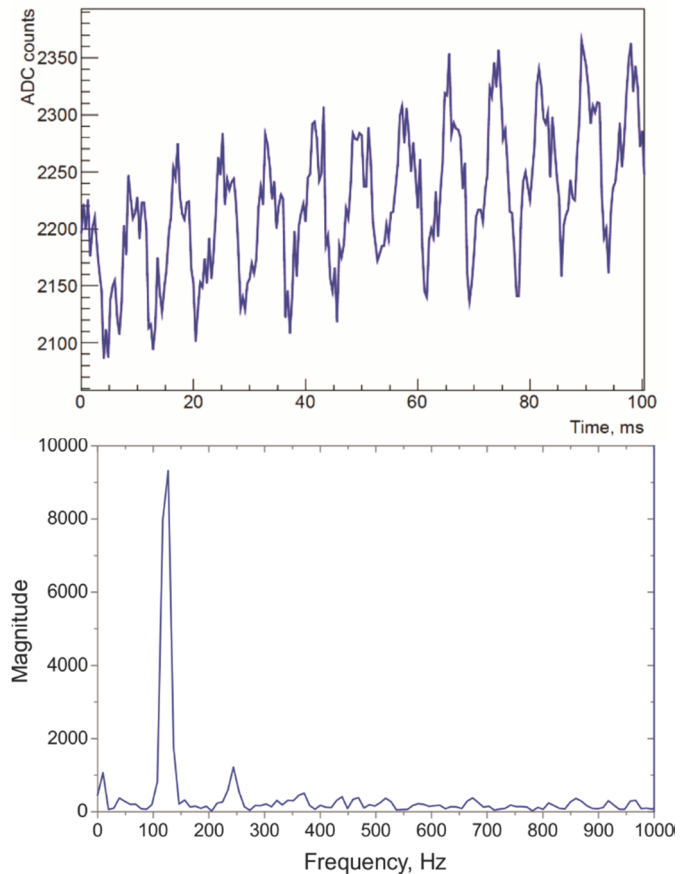


Figure 4. Example of a waveform measured above the USA on June 11, 2016, 04:56 UTC in the mode with 0.4 ms temporal resolution (top panel) and results of the Fourier analysis with a peak at 120 Hz (bottom panel).

2.2 INSTANT TRACK-LIKE FLASHES IN THE EAS MODE

One of surprises of the TUS operation in space is a big number of instant (i.e., happening in one or, rarely, two time samples of $0.8 \mu\text{s}$) and as a rule intensive flashes that produce tracks or, sometimes, small spots in the focal surface. They were called “track-like events.” They are likely to be caused by low energy cosmic ray particles (mainly protons of hundred MeV energy). These events and results of their simulation in GEANT4 are described in paper [9]. Those events comprise approximately 14% of all events. An example of a track-like-event is shown in Fig. 5. One can see a flash that occurs during one time frame simultaneously in a group of PMTs lined up in a track.

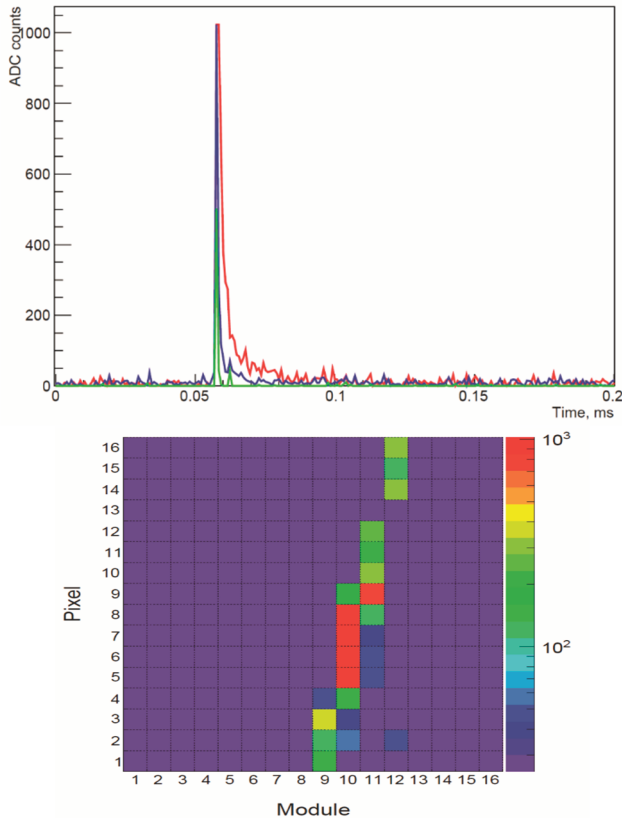


Figure 5. Track-like event registered on October 25, 2016. Left: waveforms of ten PMTs that demonstrated the biggest ADC counts. Colors denote different pixels. Right: snapshot of the focal surface at the moment of maximum ADC counts.

2.3 EVENTS WITH UNIFORMLY MONOTONOUSLY INCREASING PIXEL COUNTS

Another distinct group of events consists of ADC counts monotonously increasing in comparatively slow rise time ($100 \mu\text{s}$). We shall call them “monotonous flashes.” Such a flash typically evolves simultaneously in majority of pixels presenting an almost uniform illumination of the focal plane. An example of a waveform of a monotonous flash is shown in Fig. 6. In most cases, the global maximum of a flash is not passed prior to the end of the recorded trace ($200 \mu\text{s}$).

An analysis of geographical distribution of these flashes demonstrates their correlation with well known regions of thunderstorm activity. A comparison with lightning flashes measured by the WWLLN has been performed. It demonstrated that the majority of them occur in more than 400 km from the TUS FOV within 1 s time interval (see [10] for details).

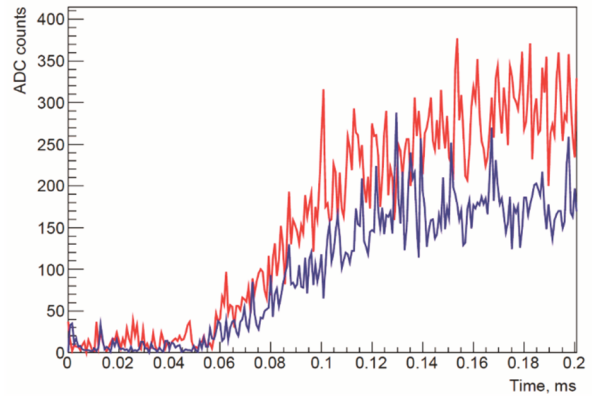


Figure 6. Example of a “monotonous flash” waveform in two pixels.

These flashes can be explained as follows. The TUS diffuse scattering mirror part has much wider FOV than the focusing mirror part and the probability of lightning detection (or related to them transient events) outside the actual FOV could be higher if energy distribution of lightning is hard. Let us make a simple estimation of the signal in one pixel for a point-like source out of the focusing mirror FOV. A point-like source radiating Q photons at distance of R to nadir direction of the TUS produces $q(Q, R)$ photons reflected by plane rough mirror of area S :

$$q(Q, R) = Q S \cos(\delta(R))^2 / 4\pi(R^2 + h^2),$$

where $\delta(R) = \arccos(h / (h^2 + R^2)^{0.5})$ is the angle between nadir and the direction from TUS to the light source. The light is scattered from the mirror to a focal plane pixel, having the FOV of 10^{-4} sr, and produces $P(Q, R) = q(Q, R) 10^{-4} 0.2 / 2\pi$ photoelectrons in one pixel.

For a distance $R=1000$ km (much out of focusing mirror FOV), a source of $Q=10^{23}$ photons (a typical UV flash measured by Tatiana and Vernov satellites) produces a number of photo electrons in one pixel of the order $P=10^4$. Taking into account that duration of a lightning is thousand times longer than the TUS time sample (in the EAS mode of operation) one should expect a signal of dozen photoelectrons in one pixel—too small for detecting above the background. For distances close to the focusing mirror FOV ($R=100$ km), the plane mirror may produce a monotonous flash with total number of photo electrons more than $P=10^5$ (or 10^2 per pixel per time sample). Snapshots inside the FOV of the focusing mirror become very much different, showing lateral characteristics of the source with pixel signals per time sample two order of magnitude higher than from the plane mirror.

2.4 ELVES MEASURED BY THE TUS DETECTOR

During the first months of operation, the TUS detector measured numerous UV transient flashes in the EAS mode with different temporal dynamics and spatial structure. The most common type of TLEs with a specific geometry of the development in the ionosphere are so-called elves—the result of the ionosphere heating by an expanding electromagnetic wave from a powerful cloud-to-ground lightning. A number of such events were measured by the TUS detector.

The event presented here (see the snapshots of focal plane in Fig.7) was registered on September 18, 2016, above Africa. An arc-like shape of the track made by the brightest PMTs and the speed of development support the hypotheses that this was an elve. Waveforms of several pixels and the geographical location of the event are shown in Figure 8.

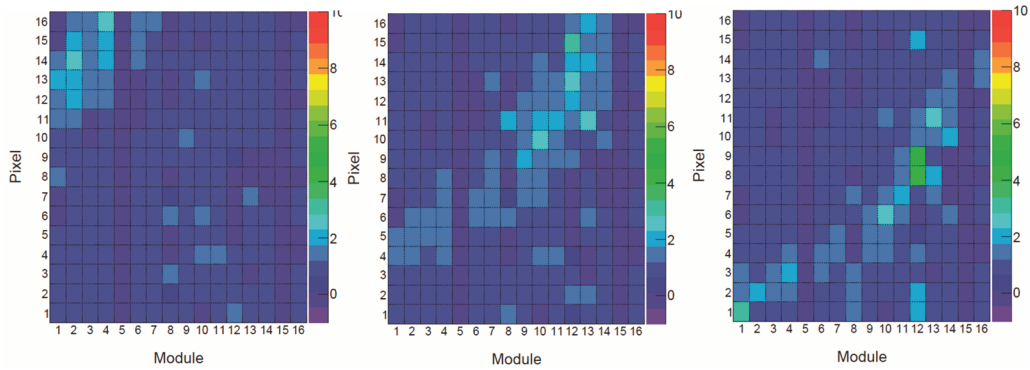


Figure 7. Snapshots of the focal plane show arc-like shape and movement of the object through the detector's field of view. The snapshots were taken at $t = 0.077$ ms, 0.182 ms, and 0.174 ms from the beginning of the record. Colors denote the signal amplitude in arbitrary units scaled to individual PMT gains.

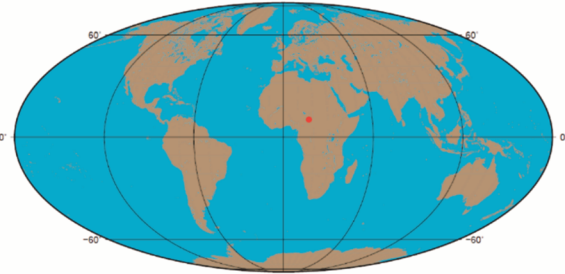
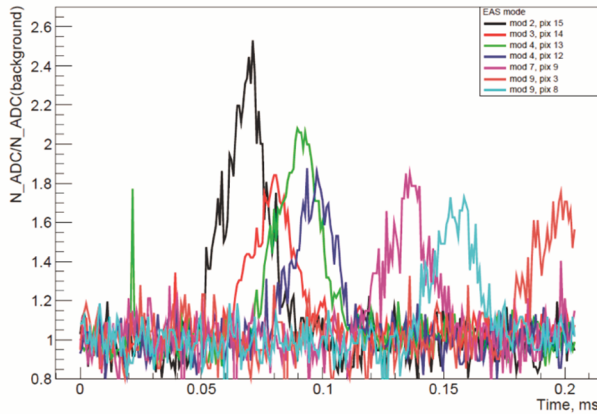


Figure 8. Waveforms of several hit pixels and geographical location of the elve event registered on September 18, 2016, above Africa. The Y-axis is a ratio of ADC counts and background signal for each pixel.

A comparison with Vaisala Global Lightning Dataset GLD360 was made for this event. Two lightning discharges of different polarity was found 120 km away from the TUS event. The direction to the lightning and the geometry and dynamics of the event support the elve hypothesis.

2.5 LIGHTNING AND TLE MEASUREMENTS WITH 0.4 MS TEMPORAL RESOLUTION

Several hundred of events were measured by the TUS detector in the TLE mode. Most of them represent huge flashes distributed over the entire photo detector. These flashes are lightning discharges under a thundercloud or outside the FOV. In the second case, the measured signal is a diffuse scattered light from the mirror as was discussed above.

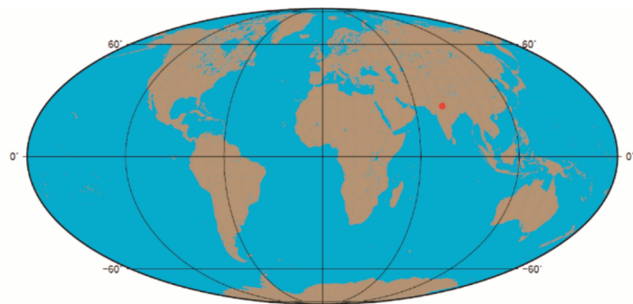
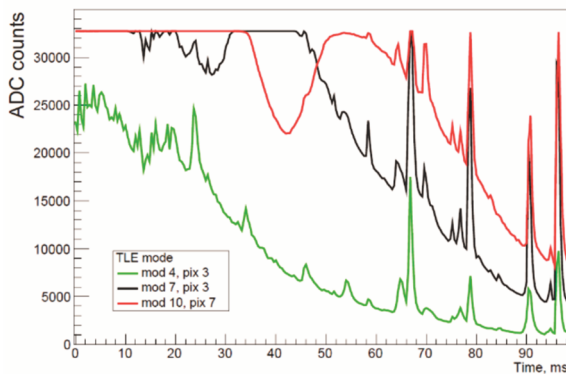


Figure 9. Waveforms of three pixels and the geographical location of the event registered on June 27, 2016, bott India ($25.^{\circ}3S$, $77.^{\circ}8E$).

We present an event that was measured on June 27, 2016, above India, as an example. It occurred in the field of view and produced a huge signal: several pixels in the center of the event are saturated, see Figs. 9 and 10.

A comparison with Vaisala Global Lightning Dataset GLD360 was made for this event as well. Several lightning strikes were found in this region for the time of the TUS measurements and two of them (negative cloud-to-ground) took place exactly in the FOV.

Different events have various temporal structure and most probably occurred in the active thunderstorm regions. The same was observed in previous measurements that were made by Vernov and Tatiana MSU satellites.

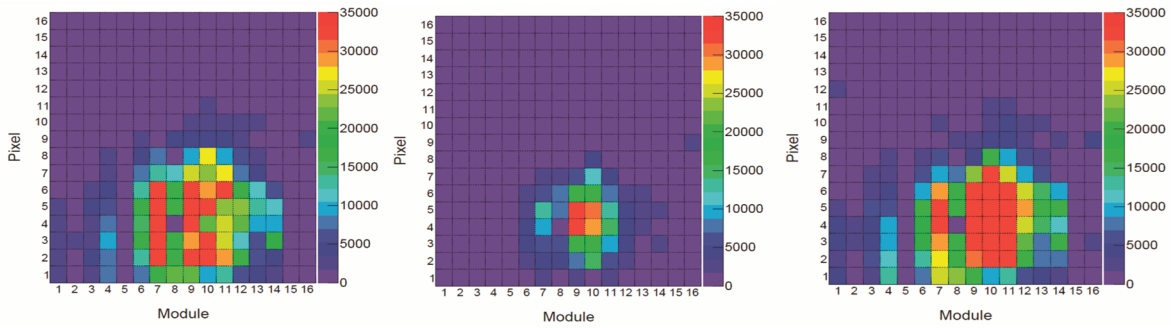


Figure 10. Snapshots of the focal plane. Snapshots were made at $t = 40$ ms, 88 ms, 96.4 ms from the beginning of the record. Colors denote real ADC counts.

2.6. THUNDERSTORM MEASUREMENTS WITH 6.6 MS TEMPORAL RESOLUTION

The TUS detector was operating in so called the METEOR mode with 6.6 ms temporal resolution for 13 days at the very beginning of 2017. This mode allows measuring slow events with a duration up to 1.7 s. A number of bright meteors were measured during this period of time, which confirms the multi-functionality of such orbital observatory. (These events are out of the focus of the paper, so we do not provide an example.) The most important point is that the majority of events was measured above thunderstorm regions and represent very long waveforms of lightning and TLEs inside the TUS FOV or nearby. These sequence of flashes have very complicated temporal structure with numerous peaks. An analysis of this data is in progress.

As an example we present an event which was measured on January 4, 2017, 03:23:27 UTC, above South America ($17^{\circ}.7S$, $66^{\circ}.5W$). It is a sequence of spikes lasting in the field of view during nearly **one second** (Figure 11).

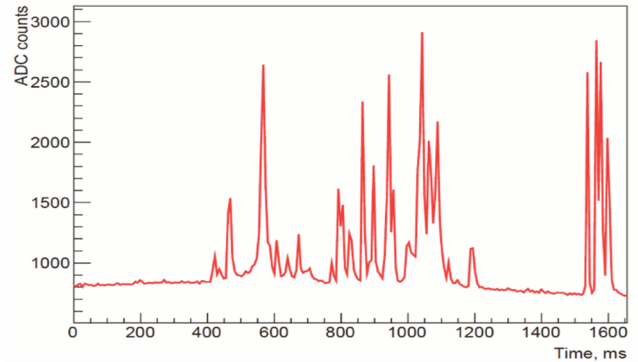


Figure 11. Waveforms of a pixel for an event measured on January 4, 2017, 03:23:27 UTC, above South America. Time tick = 6.6 ms.

On-line data of South America lightning location network StarNet indicates a presence of a thunderstorm in the region of measurements (shown in Figure 12 by the red circle).

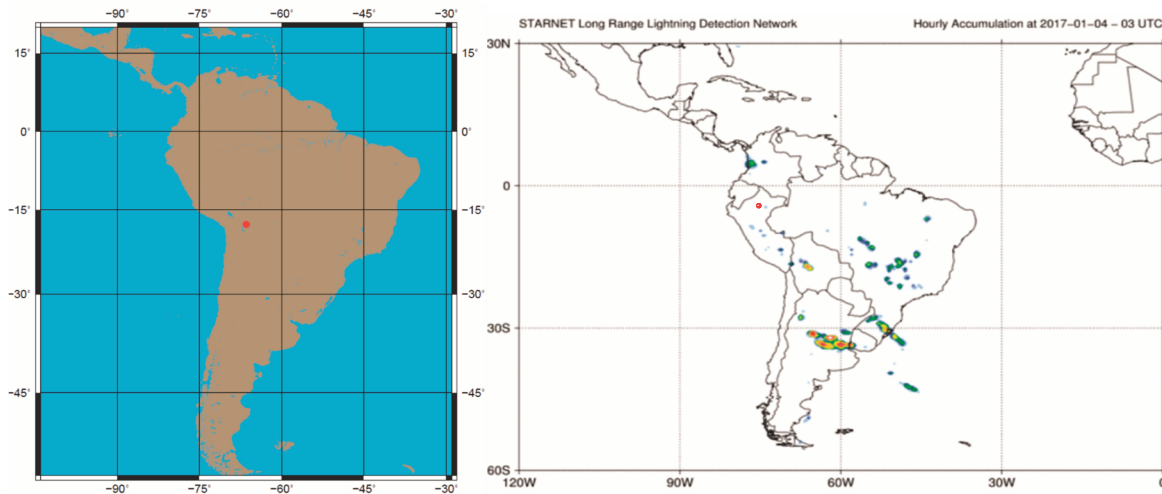


Figure 12. Left panel: location of the TUS event registered on January 4, 2017, 03:23:27 UTC, above South America ($17^{\circ}.7S$, $66^{\circ}.5W$). bottom panel: map of lightning activity for the January, 4, 2017, 03 a.m. UTC from the STARNET Sferics Timing and Ranging Network (<http://www.starnet.iag.usp.br/>).

CONCLUSION

The diversity of transient events recorded by TUS in the UV range of wavelengths has improved significantly our earlier understanding of transient atmospheric events. Numerous measurements obtained in three temporal scales (temporal resolutions: 0.8 μ s, 0.4 ms, 6.6 ms) have demonstrated the multi-functionality of the orbital telescope. We believe TUS marks a big step in the development of the technique of detecting extreme energy cosmic rays from space, and its data is important for the development of much

more advanced instruments like KLYPVE and JEM-EUSO [11, 12].

ACKNOWLEDGMENT

The authors thank Robert Holzworth, the head of the World Wide Lightning Detection Network, and Vaisala Inc. company for providing the data on lightning strikes employed in the present study. The work was done with partial financial support from the Russian Foundation for Basic Research grants No. 15-35-21038 and No. 16-29-13065.

REFERENCE

- [1] B. A. Khrenov et al., Nucl. Phys. B (Proc. Suppl.) 112 (2002) 115.
- [2] B. A. Khrenov et al., Phys. Atom. Nucl. 67(11) (2004) 2058.
- [3] Abrashkin et al., Advances in Space Research 37 (2006) 1867.
- [4] M.I. Panasyuk et al., Journal of Physics, 632(1) (2015) 012097.
- [5] A. Grinyuk et al., NIMA 763 (2014) 604-609.
- [6] L.G. Tkatchev et al., 34th ICRC2015, Beijing, (2015) 616.
- [7] N.N. Vedenkin et al JETP , 113 (2011)1063–7761..
- [8] G.K. Garipov et al. JGR 118, (2013) 370–379, doi:10.1029/2012JD017501/
- [9] P.A. Klimov et al, Bulletin of the RAS: Physics, 81, N4, (2017) 442.
- [10] B.A. Khrenov et al., Astroparticle Physics, 2017 (submitted)
- [11] M. I. Panasyuk, et al. Journal of Physics Conference Series, 632(1):012097, 2015.
- [12] Jr. Adams, J.H., et al., Experimental Astronomy, 40(1):19–44, 2015.



List of Participants

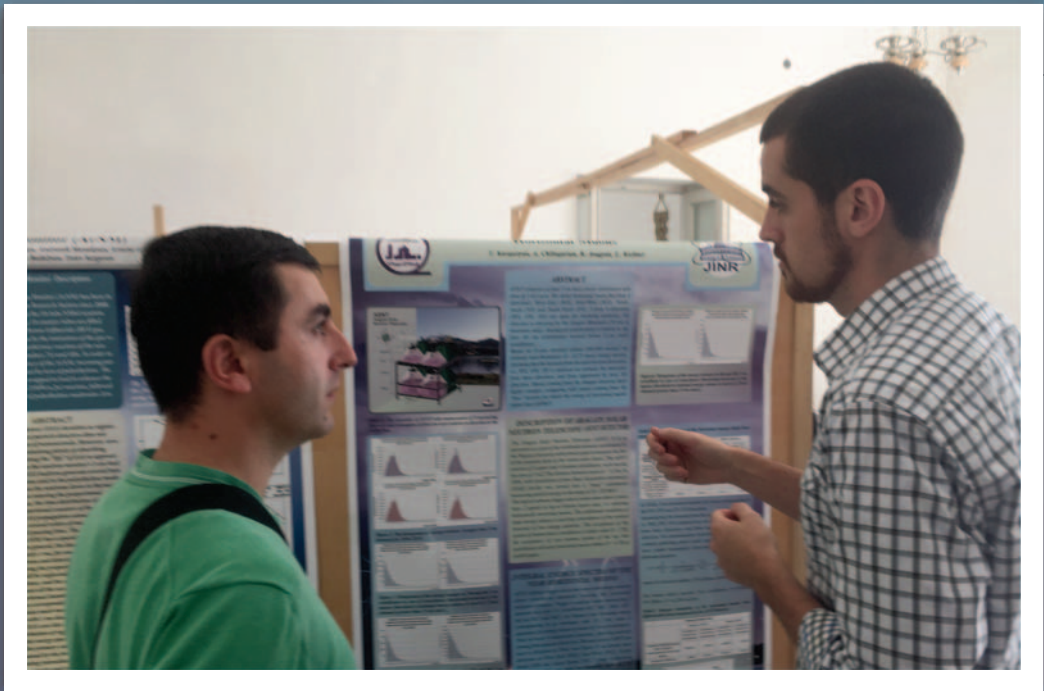
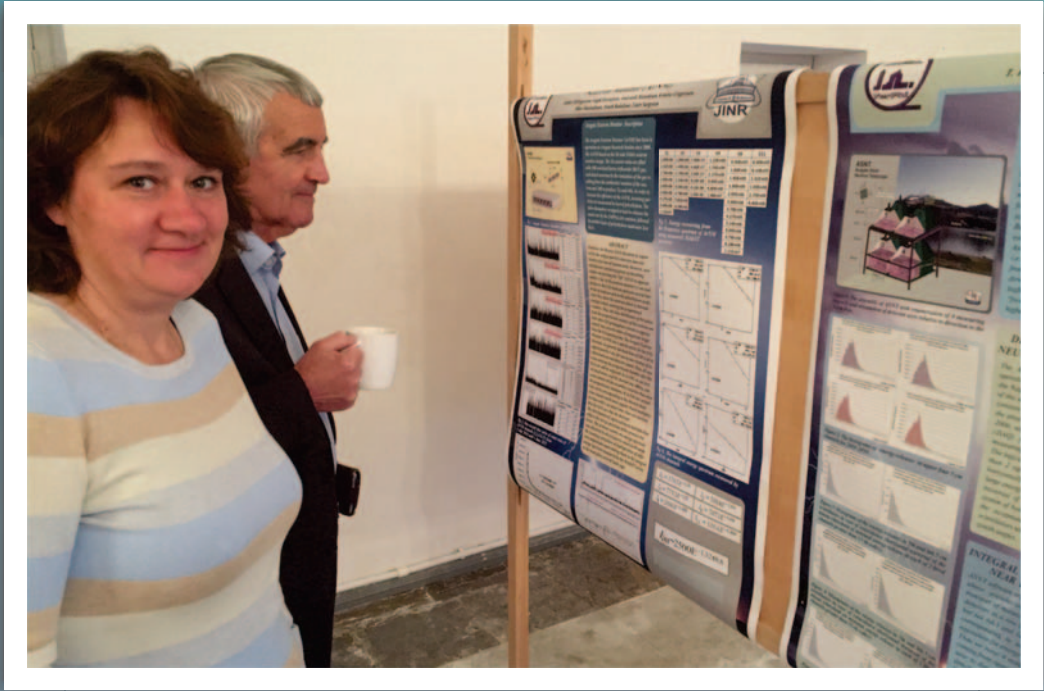
1.	Donald Pleshinger, University of Louisiana, USA	djplshinger@gmail.com
2.	Bagrat Mailyan, The University of Alabama, Huntsville, USA	bagrat.mailyan@uah.edu
3.	Shaolin Xiong, Institute of High Energy Physics, Chinese Academy of Sciences	xiongsli@ihep.ac.cn
4.	Roy Yaniv, Department of Geosciences, Tel Aviv University, Israel	royyaniv@gmail.com
5.	Razmik Mirzoyan, Max-Planck-Institute for Physics, Munich, Germany	mirzoyan.razmik@gmail.com
6.	Johannes Knapp, DESY, Zeuten	johannes.knapp@.de
7.	Leonid Sorokin, People's Friendship University of Russia	leonid.plasma@gmail.com
8.	Vitaly Bogomolov, Physical Department of Skobeltsyn Institute of Nuclear Physics, MSU, RF	bogovit@gmail.com
9.	Pavel Klimov, Skobeltsyn Institute of Nuclear Physics, MSU, RF	pavel.klimov@gmail.com
10.	Svertilov Sergey, Skobeltsyn Institute of Nuclear Physics, MSU, RF	sis@coronas.ru
11.	Gali Garipov, Skobeltsyn Institute of Nuclear Physics, MSU, RF	ggkmsu@yandex.ru
12.	Anton Chernenko, Space Research Institute, RAS, RF	anton.chernenko@gmail.com
13.	Maxim Dolgonosov, Space Research Institute of RAS, RF	russia.on.mars@gmail.com
14.	Vladimir GoUib, Space Research Institute of RAS, RF	gotlib@iki.rssi.ru
15.	Alexei Pozanenko, Space Research Institute, RAS, RF	grb123@mail.ru
16.	Alexander Shepetev, P. N. Lebedev Physical Institute of RAS, RF	ashep@tien-shen.org
17.	Inna Gubenko, Hydrometeorological Research Centre of Russian Federation (Hydrometcentre of Russia)	img0504@yandex.ru
18.	Anatoliy Petrukhin, National Research Nuclear University MEPHI, RF	AAPetrukhin@mephi.ru
19.	Igor Yashin, National Research Nuclear University MEPHI, RF	iiyashin@mephi.ru
20.	Natalia Barbashina, National Research Nuclear University MEPHI, RF	nsbarbashina@mephi.ru
21.	Dmitry Iudin, Institute of Applied Physics of Russian Academy of Science, Nizhny Novgorod, RF	Idiot64@gmail.com
22.	Stanislav Davidenko, Institute of Applied Physics of Russian Academy of Science, Nizhny Novgorod, RF	chili@aragats.am
23.	Ashot Chilingarian, Yerevan Physics Institute, Yerevan, Armenia	chili@aragats.am
24.	Tigran Karapetyan, Yerevan Physics Institute, Yerevan, Armenia	ktigran79@gmail.com
25.	Karen Avagyan, Yerevan Physics Institute, Yerevan, Armenia	avagyan.karen@gmail.com
26.	Gagik Hovsepyan, Yerevan Physics Institute, Yerevan, Armenia	hgg@yerphi.am
27.	David Pokhsroryan, Yerevan Physics Institute, Yerevan, Armenia	davitpo@gmail.com
28.	Eduard Mnatsakanyan, Yerevan Physics Institute, Yerevan, Armenia	eduardmnats@gmail.com
29.	Lev Kozliner, Yerevan Physics Institute, Yerevan, Armenia	kozliner@yerphi.am
30.	Hripsime Mkrtychyan, Yerevan Physics Institute, Yerevan, Armenia	hripsime@yerphi.am
31.	Suren Soghomonyan, Yerevan Physics Institute, Yerevan, Armenia	surensog@gmail.com
33.	Yeghia Khanikyants, Yerevan Physics Institute, Yerevan, Armenia	khanikync@yerphi.am
	Zaruhi Asaturyan, Yerevan Physics Institute - Yerevan, Armenia	zara@mail.yerphi.am

TEPA 2016

PHOTOGALLERY





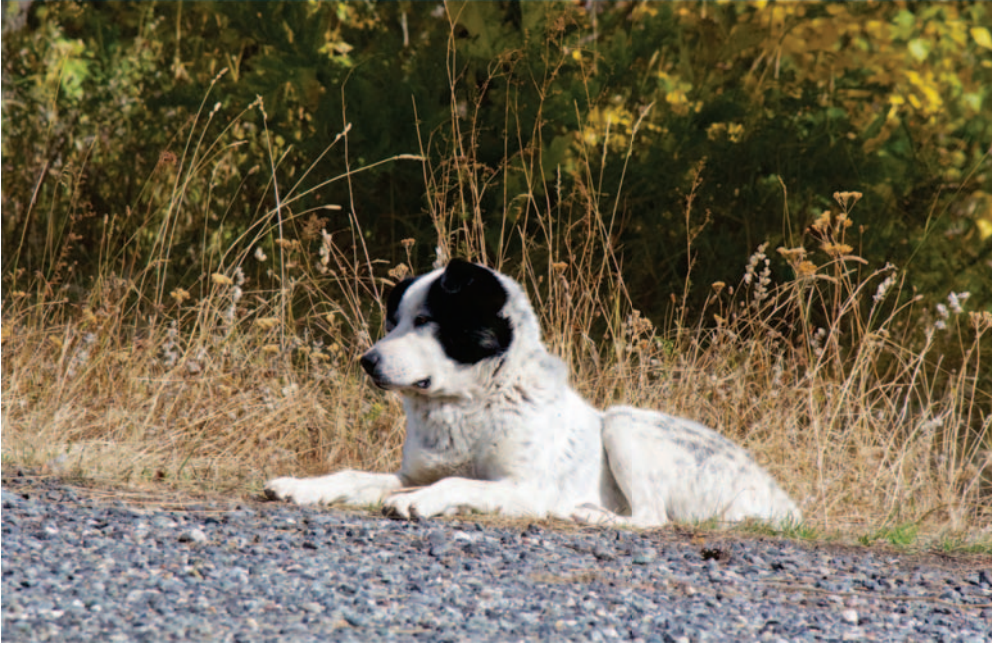




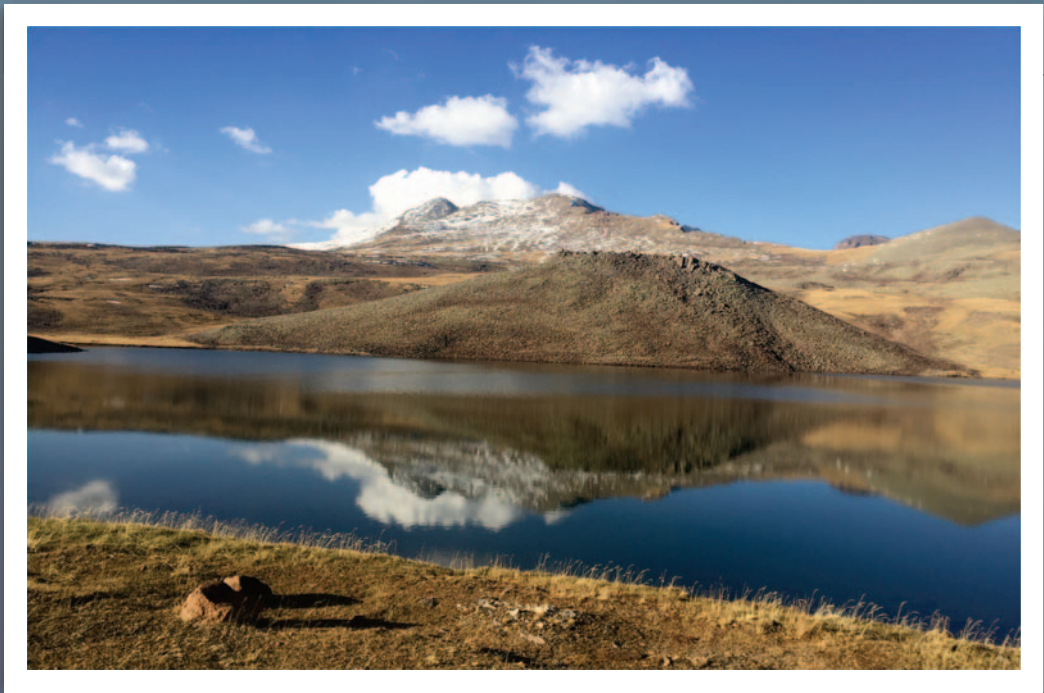




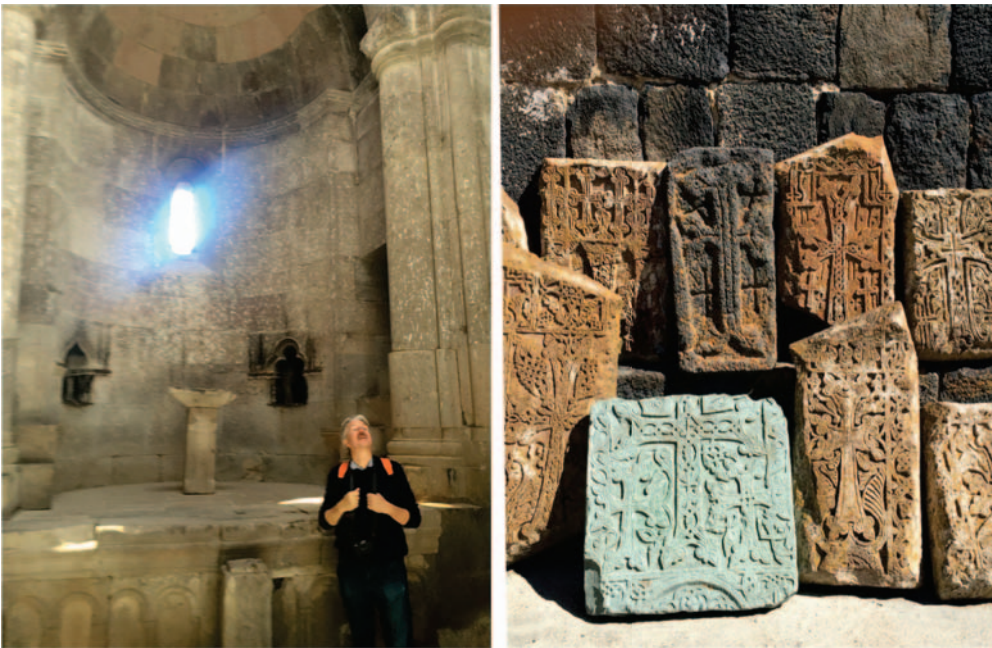


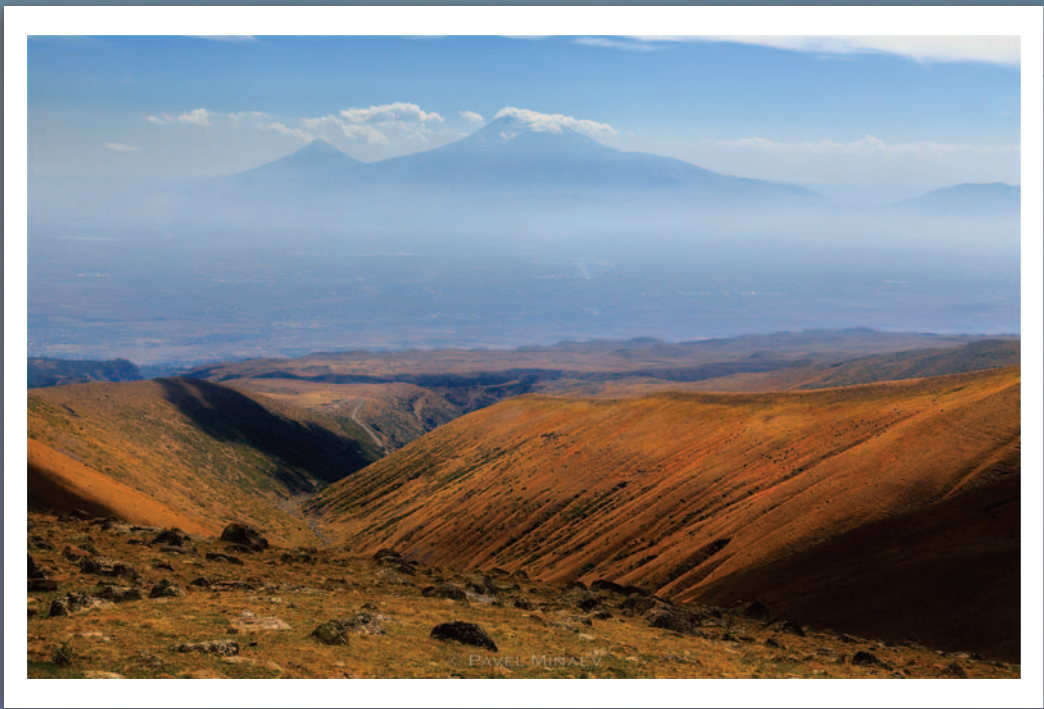




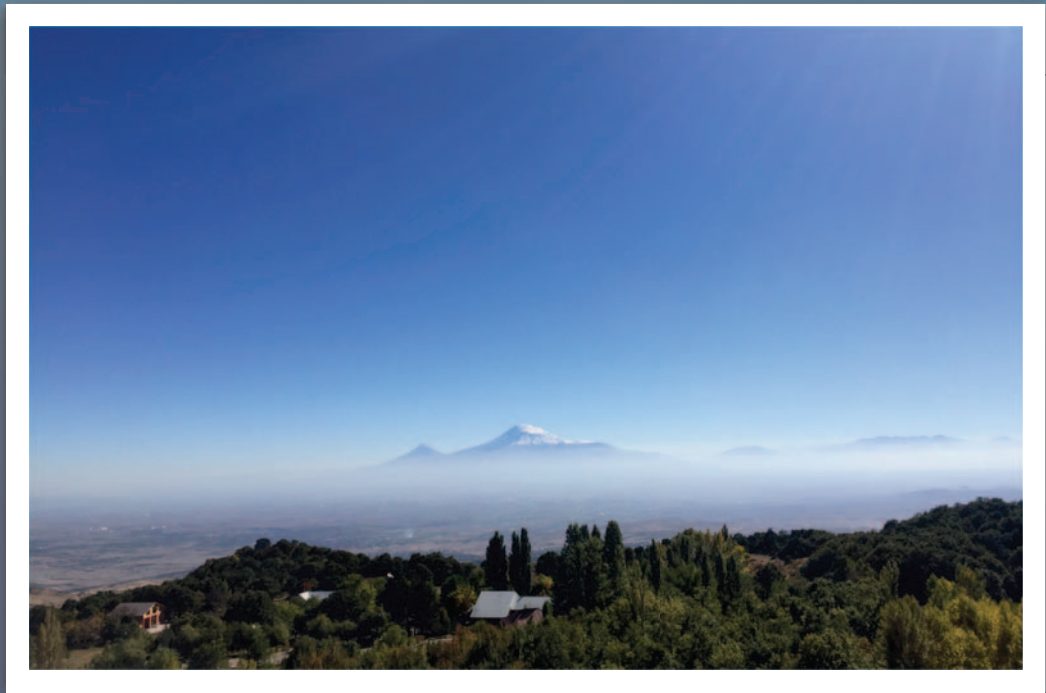
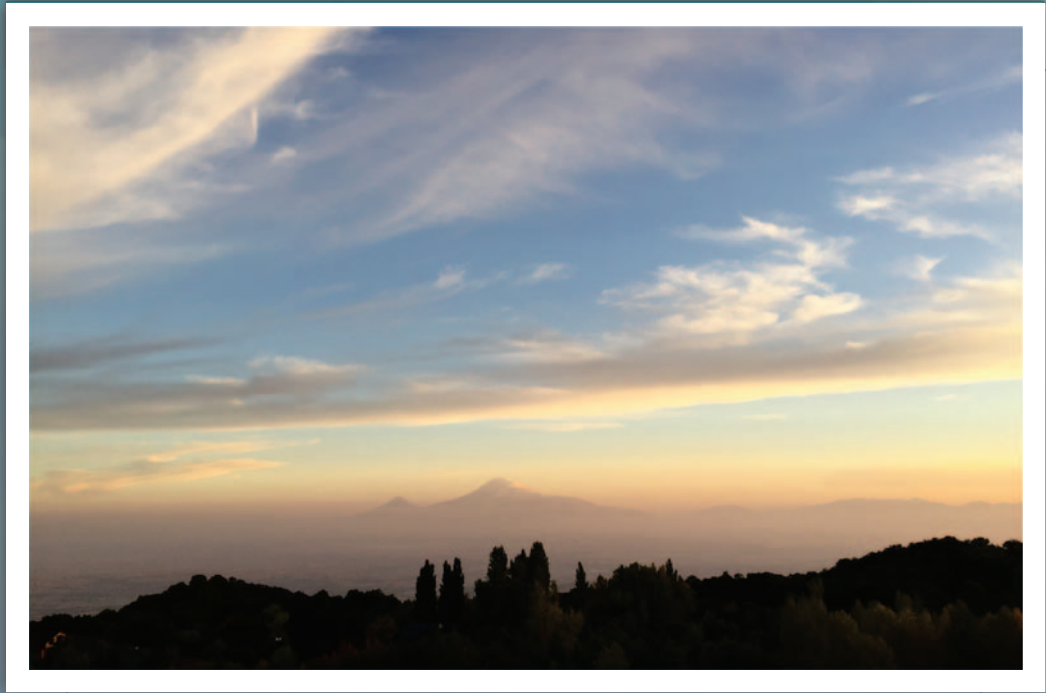






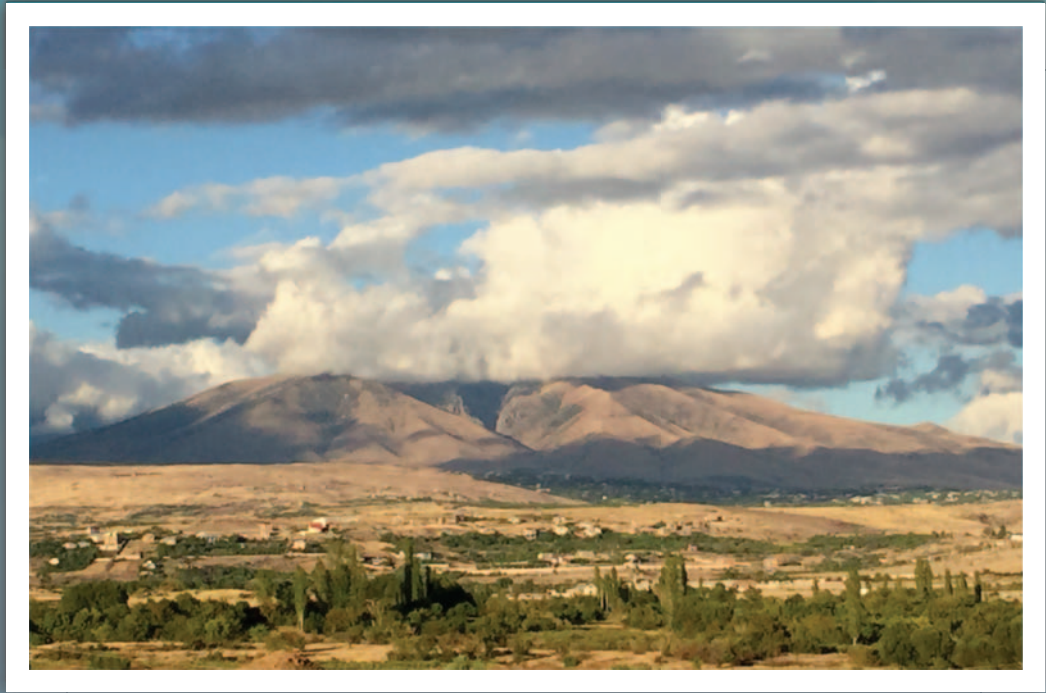












<http://crd.yerphi.am/Conferences/tepa2016/home>